UNIVERSIDAD
NACIONAL
DE COLOMBIA

Injection Locked VCSEL Based Oscillator –ILVBO

Juan Fernando Coronel Rico

Universidad Nacional de Colombia
Facultad de Ingeniería, Departamento de Ingeniería
Eléctrica y Electrónica
Bogotá, Colombia
2016

INJECTION LOCKED VCSEL BASED OSCILLATOR – ILVBO

By

Juan Fernando Coronel Rico

A dissertation submitted in partial satisfaction of the requirements
for the degree of
Doctor
in
Engineering – Electrical Egineering
in the
Doctoral School
of the
National University of Colombia at Bogota

Directed by
Dr. Gloria Margarita Varón Durán
Departamento de Ingeniería Eléctrica y Electrónica. Universidad Nacional de Colombia,
sede Bogotá. Bogotá, Colombia

Co-Directed by
Dr. Angélique Rissons
Département Électronique, Optonique et Signal. Institut Supérieur de l'Aéronautique et
de l'Espace. Toulouse, France

Members of Jury:
Professor Anne-Laure Billabert
Univeristé Paris-Est Marne-la-Vallée – Laboratoire Electronique, Systèmes de
Communication et Microsystèmes

Professor Yannis Le Guennec
Institut Polytechnique de Grenoble – Institut de Microélectronique, Electromagnetisme
et Photonique et Laboratoire d'Hyperfrequences et Caractérisation (IMEP-LaHC)

Professor Juan Domingo Baena Doello
Departamento de Física, Universidad Nacional de Colombia, sede Bogotá

June 2016

When you are smiling

ocurre que tu sonrisa es la sobreviviente

la estela que en ti dejó el futuro

la memoria del horror y la esperanza

la huella de tus pasos en el mar

el sabor de la piel y su tristeza

when you are smiling

the whole world

que también vela por su amargura

smiles with you

Mario BENEDETTI (1920 -2009)

Remerciements - Agradecimientos

> "…Everything you want's a dream away
>
> Under this pressure under this weight
>
> We are diamonds taking shape…"

Resumen

Los osciladores están presentes en todos los sistemas de comunicaciones que utilizamos a diario. Estos permiten hacer la sincronización entre el emisor y receptor de un mensaje. La calidad de esta sincronización depende de la estabilidad del oscilador. Con el fin de caracterizar la estabilidad del oscilador en el dominio de la frecuencia, el ruido de fase es utilizado como parámetro de referencia. Un oscilador que entrega una señal con un bajo ruido de fase es un oscilador de alta pureza espectral.

Los osciladores electrónicos presentan un buen desempeño a baja frecuencia. A medida que la demanda de tasa de transmisión de los sistemas de comunicaciones aumenta, los osciladores electrónicos logran la generación de señales en alta frecuencia utilizando multiplicadores de frecuencia, los cuales adjuntan elementos adicionales a la cadena de comunicaciones. Los sistemas híbridos permiten tomar ventaja del buen desempeño de los componentes ópticos en alta frecuencia con el fin de integrarlos en los sistemas electrónicos y de esta maneja mejorar su desempeño.

Este trabajo utiliza la técnica *optical injection locking* que consiste en la inyección de un haz láser de un láser maestro hacia un láser esclavo. Esta técnica permite mejorar el ancho de banda en modulación directa del láser bajo modulación. El ruido de intensidad relativa del láser bajo *optical injection locking* es mejorado, teniendo en cuenta las medidas realizadas. Al utilizar el láser bajo condición de *optical injection locking* en el oscilador optoelectrónico, es posible implementar osciladores basados optoelectrónicos basados en VCSEL a más alta frecuencia y menor ruido de fase.

Palabras clave: Oscilador, inyección óptica, ruido de fase, VCSEL, fibra óptica, optoelectrónica.

Abstract

Oscillators are present in all telecommunication systems. They synchronize the emitter and receiver of a message. The quality of the synchronization depends on the oscillator stability. To characterize the frequency domain oscillator stability, the phase noise of the carrier is used as figure of merit. An oscillator delivering a low phase noise carrier is a high spectral purity oscillator.

Electronic oscillators are high performing at low frequencies. As communications systems require high data rate transmission, the electronic oscillators uses frequency multipliers that degrades the spectral purity of the carrier. The hybrid systems take advantage of the good performance of optical components at high frequency with the goal to be integrated in the electronic systems to overcome frequency limitation issues.

This work use the optical injection locking technique by injecting the laser beam of a master laser inside the cavity of a VCSEL under direct modulation. The optical injection locking technique enlarges the direct modulation bandwidth of the VCSEL and reduces the Relative Intensity noise of the laser (RIN). The RIN reduction has as side effect the reduction of the additive noise inside the oscillator and, in consequence, reducing the oscillator phase noise.

Keywords: Oscillator, optical injection, phase noise, VCSEL, optical fiber, optoelectronics.

Index

Table Index

Figure Index

VCSEL	Vertical Cavity Surface Emitting Laser
MOCVD	Metalorganic Chemical Vapor Deposition
EOM	Electro-Optical Modulator
MZM	Mach-Zender Modulator
VCO	Voltage Controlled Oscillator
VBO	VCSEL Based Optoelectronic Oscillator
OIL	Optical Injection Locking
OILVBO	Optically Injection Locked VCSEL Based Optoelectronic Oscillator
ESA	Electrical Spectrum Analyzer
OEO	Optoelectronic Oscillator
SSB	Single Side Band
Q	Quality Factor
RIN	Relative Intensity Noise
MCEF	Modulation Current Efficiency Factor
FSR	Free Spectral Range
SBD	Stimulated Brillouin Diffusion
SRD	Stimulated Raman Diffusion
VNA	Vector Network Analyzer
DFB	Distributed Feedback Laser
SOA	Semiconductor Optical Amplifier
ADS	Advanced Design Systems (Keysight simulation suite)

Introduction

Oscillators are present in all communication systems since the beginning of the electronics era to synchronize emitter and receiver. In a world that is connected everywhere and with an insatiable requirement of information, communication systems are demanded to be high performing.

With the advent of high speed communications era, the telecommunications channels are moving towards the optical frequencies thanks to their high bit rate transference capability. The upcoming communication satellite generation will use the free space optical communication technology by the implementation of modulated optical sources. This is why low-power consumption and efficient systems are required to be placed onboard the satellites.

In the beginning of the 80's the optoelectronic oscillator was proposed to generate stable reference signals to synchronize antenna arrays for radio telescopes thanks to its simplicity and high spectral purity compared to complex atomic oscillators used before to do the synchronization [1]. The spectral purity reported for the signal generated first optoelectronic oscillator was -140 dBc/Hz at 10 kHz offset [2].

The development of semiconductor lasers gave the possibility to build compact and efficient oscillators. At the beginning of the 2000's, it did appearance a low cost, low power consumption and miniaturized generation of lasers, the Vertical Cavity Surface Emitting Lasers (VCSELs). The VCSEL was rapidly implemented in short haul optical communications at low wavelengths. A second long wavelength generation of VCSELs was developed at standard communication devices operation (1.3 and 1.5 µm).

Thanks to the long wavelength VCSEL implementation, it was possible in 2008 to implement a VCSEL Based Optoelectronic Oscillator (VBO) with a direct modulated laser source at the S-band of the microwave spectrum as performing as electronic oscillators at the same frequency [3]. From the development of the VBO, the scientific community is interested in increasing the carrier frequency of the VBO that is limited by the relatively low direct modulation bandwidth (around 5 GHz). To overcome this issue, the Optical Injection Locking technique (OIL) was proposed. It has been already shown that the OIL enhances the microwave performance of the VCSELs [4], [5].

In this work it is proposed the implementation of the OIL technique in the VCSEL Based Optoelectronic oscillator with the purpose of the enhancement of the oscillator spectral purity. The prediction of the frequency stability prediction of the VCSEL Based Optoelectronic oscillator is approached.

The results of this research work through this document are presented in five chapters as follows:

The First Chapter is named "*Optoelectronic Oscillators: Review and State-of-the-Art*". In this chapter, the most performing optoelectronic oscillators are recalled and described with the purpose of defining a departure point for this research.

The Second Chapter is titled "**Long Wavelength VCSEL Characterization**". This Chapter presents the characterization of VCSELs at 1.3 and 1.5 µm. The Relative Intensity Noise (RIN) and frequency response of the VCSELs are measured. From the characterization the design of the VCSEL Based Optoelectronic Oscillator is derived.

The Third Chapter is titled "*VCSEL Based Optoelectronic Oscillator*". This Chapter presents the implementation, characterization and modelling of the VBO using 1.3 and 1.5 µm VCSELs. The VCSEL frequency response, Relative Intensity Noise (RIN) and their influence on the oscillator spectral purity are discussed along this Chapter.

The Fourth Chapter is titled "*Optical Injection Locking of VCSELs*". In this Chapter it is presented the implementation study of the Optically Injection Locking technique in the VCSEL (OIL-VCSEL). The OIL effects in the frequency response and RIN of the OIL-VCSEL are discussed.

The Fifth Chapter is titled "*Optical Injection Locked VCSEL Based Optoelectronic Oscillator*". In this Chapter, the implementation of the Optically Injection Locked VCSEL Based Optoelectronic Oscillator (OILVBO) is presented. The OILVBO is implemented at frequencies beyond the VCSEL *free running* direct modulation cut-off frequency. The optoelectronic oscillator spectral purity is measured and modelled with the goal to validate the presented results.

Objectives

General Objective

To build and characterize the optical injection locked VCSEL based optoelectronic oscillator.

Specific Objectives

- To validate different VCSEL Based Oscillators (VBO) with the latest VCSEL technology available.
- To implement a VCSEL by VCSEL optical injection locking setup.
- To evaluate the injection locking range conditions for the proposed setup.
- To build an optical injection locked VCSEL based optoelectronic oscillator – ILVBO.
- To characterize the generated signal behavior as a function of the system temperature to determine the need of a temperature control.
- To compare the performance parameters (generated frequency, phase noise and size) between the implemented VBOs and ILVBOs.
- To model the phase noise in the ILVBO including the VCSEL by VCSEL Injection Locking effects.

Chapter 1

Optoelectronic Oscillators: Review and State-of-the-Art

Introduction

The optical generation of microwave signals has been studied since the 90's. The growing needs of higher bandwidth to send and receive increasing data volume, like data centers, smartphones, and navigation systems have pushed the development of optical communication technologies.

In this context, the hybrid field of optoelectronics appears to take advantage of the possibility given by the electronics and optical systems. When operating high data rate systems, the quality of the information sent and delivered is a key factor, especially when they are related to high precision systems (radar, navigation systems, data rate microwave link). The quality of the performance of such systems comes, basically, from the quality of their synchronization. The synchronization of a telecommunication system is given by a stable signal generated by an oscillator.

In the middle of the 90's, it was proposed an optoelectronic oscillator as a high quality signal generator [2]. From this milestone, several different configurations have been proposed in order to adapt this technology to different application fields.

This chapter will present a description and the state-of-the-art of optoelectronic oscillators.

1.1   Optoelectronic Oscillator

The optoelectronic oscillator (OEO) was developed in 1995 by Yao and Maleki [6]. This architecture was inspired by that one presented in 1982 by Neyer and Voges [7]. This hybrid technology used electronic and optic components to convert optical energy into electrical signals with an excellent spectral purity. This is composed of a laser source, a Mach-Zender modulator (MZM), an optical fiber that acts as a delay line, a photodetector, a RF amplifier and a RF filter. Figure 1 presents the setup proposed by Yao and Maleki [8].
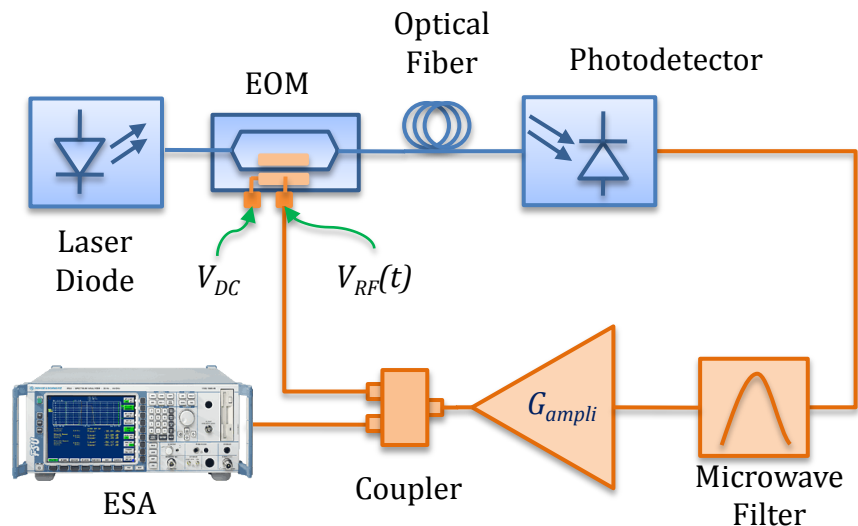
Figure 1 Optoelectronic oscillator.

1.1.1   System Description

In an OEO, the laser diode sends an optical signal through an electro-optical modulator (EOM). The EOM is a Mach-Zender modulator (MZM). The EOM output is connected to the optical fiber delay line. The optical signal is then detected by a photodetector. In electrical domain, this signal is filtered by a bandpass filter and finally it is amplified.
To achieve an oscillation with this loop, it is necessary to accomplish the Barkhausen condition, the phase and gain condition. To make a further analysis of this subject, an open loop analysis of the oscillator will be performed in the next section.

1.1.2   Open Loop Analysis of the Optoelectronic Oscillator [3][9][10]

The open loop oscillator is presented in Figure 2. Let us consider a signal $V_{RF(t)}$ injected at the loop input, this means, at the RF port of the EOM. From this, it is possible to find the open loop transfer function.
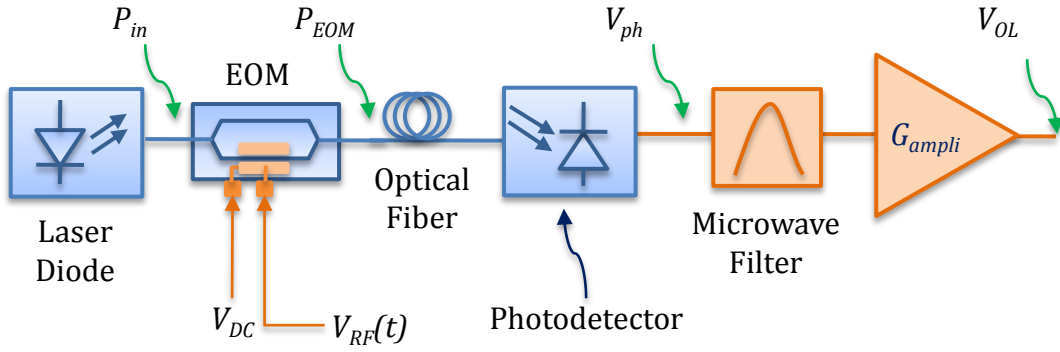
Figure 2 Optoelectronic oscillator in open loop configuration.

1.1.2.1   Electro-Optical Modulator Transmission

The transfer function of the electro-optical modulator (EOM) is given by:

$$H_{mod} = \frac{P_{EOM}}{P_{in}} = \alpha cos^2 \left[\frac{1}{2} \left(\frac{\pi V_{DC}}{V_{\pi DC}} + \frac{\pi V_{RF(t)}}{V_{\pi RF}} + \theta_{RF} + \theta_{DC} \right) \right] \tag{1}$$

$$H_{mod} = \frac{\alpha}{2} \left[1 + M * cos \left(\frac{\pi V_{DC}}{V_{\pi DC}} + \frac{\pi V_{RF(t)}}{V_{\pi RF}} + \theta_{RF} + \theta_{DC} \right) \right] \tag{2}$$

Where, P_{EOM} is the output power of the MZM, P_{in} is the input power of thw MZM, M is the modulation index that is assumed as 1 in our analysis, α represents the insertion losses of the modulator, θ_{RF} represents the phase mismatch between the optical and microwave signals, θ_{DC} represents the autopolarization, $V_{\pi DC}$ and $V_{\pi RF}$ represent the half-wave voltage DC and RF respectively. The modulator is assumed to have an actual autopolarization equal to $\frac{V_{\pi DC}}{2}$, from this, it is possible to say that $\theta_{DC} = \frac{\pi}{2}$. We will use the following notations:

- R_{ph}: load impedance of the photodetector [Ω].

- $\bar{S} = Se^{j\phi_S}$: responsivity of the photodetector [A/W].

- $\bar{F} = Fe^{j\phi_F}$: filter transmission [-].

- $\overline{G_A} = G_A e^{j\phi_A}$: Voltage gain of the microwave amplifier [-].

- $\bar{A} = Ae^{-j\omega\tau_{FO}}$: transfer function of the optical fiber [-].

- $\overline{\alpha_E} = \alpha_E e^{j\phi_E}$: electric losses [-].

- P_{opt} is the optical detected power [W].

Using this notation, it is possible to present the photodetected current and voltage as follows,

$$I_{ph} = \bar{S} * \bar{A} * \overline{H_{mod}} * P_{opt} = \bar{S} * \bar{A} * \frac{\alpha}{2} \left[1 + M * cos \left(\frac{\pi V_{DC}}{V_{\pi DC}} + \frac{\pi V_{(t)}}{V_{\pi RF}} + \theta_{RF} + \theta_{DC} \right) \right] * P_{opt} \tag{3}$$

$$\overline{V_{ph}} = R_{ph} * \overline{S} * \overline{A} * \overline{H_{mod}} * P_{opt} \tag{4}$$

The output voltage after the microwave amplifier, just before the feedback to the EOM is given by,

$$\begin{aligned} \overline{V_{OL}} &= \overline{G_A} * \overline{\alpha_E} * \overline{F} * R_{ph} * \overline{S} * \overline{A} * \overline{H_{mod}} * P_{opt} \\ &= \overline{G_A} * \overline{\alpha_E} * \overline{F} * R_{ph} * \overline{S} * \overline{A} \\ &\quad * \frac{\alpha}{2} \left[1 + M * cos\left(\frac{\pi V_{DC}}{V_{\pi DC}} + \frac{\pi V_{(t)}}{V_{\pi RF}} + \theta_{RF} + \theta_{DC} \right) \right] * P_{opt} \end{aligned} \tag{5}$$

1.1.2.2   Linearization of the EOM's Transfer Function

The transmission of the EOM can be modeled by using Bessel's series, making by this way the different frequency components of the signal. Before going further, the following properties of sine and cosine functions are considered:

$$cos(m \sin \omega t) = J_o(m) + 2 \sum_{p=1}^{\infty} J_{2p}(m) \cos(2p\omega t) \tag{6}$$

$$\sin(m \sin \omega t) = 2 \sum_{p=1}^{\infty} J_{2p-1}(m) \sin[(2p-1)\omega t] \tag{7}$$

$$cos(m \cos \omega t) = J_o(m) + 2 \sum_{p=1}^{\infty} -1^p J_{2p}(m) \cos(2p\omega t) \tag{8}$$

$$\sin(m \cos \omega t) = 2 \sum_{p=1}^{\infty} -1^p J_{2p-1}(m) \cos[(2p-1)\omega t] \tag{9}$$

Let us consider a microwave signal at the modulator input as follows,

$$V(t) = V_o \sin(\omega_e t + \phi_o) \tag{10}$$

And we define,

$$\overline{V_c} = \overline{G_A} * \overline{\alpha_E} * \overline{F} * R_{ph} * \overline{S} * \overline{A} * \frac{\alpha * P_{in}}{2} \tag{11}$$

Then, the voltage at the amplifier output (V_{OL}) is given by,

$$\overline{V_{OL}} = V_c \left[1 + M * cos\left(\frac{\pi V_{DC}}{V_{\pi DC}} + \frac{\pi V_o \sin(\omega_e t + \phi_o)}{V_{\pi RF}} + \theta_{RF} + \theta_{DC} \right) \right] \tag{12}$$

$$\begin{aligned} \overline{V_{OL}} &= \overline{V_c} + \overline{V_c} * M * cos\left(\frac{\pi V_{DC}}{V_{\pi DC}} + \theta_{RF} + \theta_{DC} \right) * cos\left(\frac{\pi V_o}{V_{\pi RF}} + \theta_{RF} + \theta_{DC} \right) - \overline{V_c} * M \\ &\quad * \sin\left(\frac{\pi V_{DC}}{V_{\pi DC}} + \theta_{RF} + \theta_{DC} \right) * \sin\left(\frac{\pi V_o}{V_{\pi RF}} + \theta_{RF} + \theta_{DC} \right) \end{aligned}$$

From equations (7) and (8), it is possible to write:

$$cos\left(\frac{\pi V_o}{V_{\pi RF}}\sin(\omega_e t + \phi_o)\right) = J_o\left(\frac{\pi V_o}{V_{\pi RF}}\right) + 2\sum_{p=1}^{\infty} J_{2p-1}\left(\frac{\pi V_o}{V_{\pi RF}}\right)\cos[(2p(\omega_e t + \phi_o)] \quad (13)$$

$$sin\left(\frac{\pi V_o}{V_{\pi RF}}\sin(\omega_e t + \phi_o)\right) = 2\sum_{p=1}^{\infty} J_{2p-1}\left(\frac{\pi V_o}{V_{\pi RF}}\right)\sin[(2p-1)(\omega_e t + \phi_o)] \quad (14)$$

Finally,

$$\overline{V_{OL}} = \overline{V_c} + \overline{V_c} * M$$
$$* \cos\left(\frac{\pi V_{DC}}{V_{\pi DC}} + \theta_{RF} + \theta_{DC}\right)\left[J_o\left(\frac{\pi V_o}{V_{\pi RF}}\right)\right.$$
$$+ 2\sum_{p=1}^{\infty} J_{2p}\left(\frac{\pi V_o}{V_{\pi RF}}\right)\cos[(2p(\omega_e t + \phi_o)]\right] - \overline{V_c} * M$$
$$* \sin\left(\frac{\pi V_{DC}}{V_{\pi DC}} + \theta_{RF}\right.$$
$$+ \theta_{DC}\left)\left[2\sum_{p=1}^{\infty} J_{2p-1}\left(\frac{\pi V_o}{V_{\pi RF}}\right)\cos[(2p-1)(\omega_e t + \phi_o)]\right]$$

$$(15)$$

To take into account:

- The output signal has several harmonics due to the non-linear nature of the EOM.

- If the speed mismatch between the optical and electrical signals is very small, it can be neglected by setting $\theta_{RF} \cong 0$.

- If the previous condition is satisfied, we consider:

  o For the autopolarization $\theta_{DC} = \frac{\pi}{2}$ and $V_{DC} = 0$ (2π), all harmonic even modes are zero.

  o For the autopolarization $\theta_{DC} = \frac{\pi}{2}$ and $V_{DC} = \frac{\pi}{2}$ (2π), all harmonic odd modes are zero.

Equation (15) is the expression for the actual voltage available at the amplifier's output without the signal filtering. To simplify this, it will be taken into account just the first harmonic (with angular frequency ω_e) and the DC components will be kept as well. ϕ_o will be neglected for this analysis. Let us consider τ the total delay of the loop. So, the voltage at the output of the amplifier is given by:

$$\overline{V_{OL}} = \overline{V_c} + \overline{V_c} * M * \cos\left(\frac{\pi V_{DC}}{V_{\pi DC}} + \theta_{RF} + \theta_{DC}\right)\left[J_o\left(\frac{\pi V_o}{V_{\pi RF}}\right)\right] - \overline{V_c} * M$$
$$* \sin\left(\frac{\pi V_{DC}}{V_{\pi DC}} + \theta_{RF} + \theta_{DC}\right)J_1\left(\frac{\pi V_o}{V_{\pi RF}}\right)\sin\omega_e\tau * e^{(-j\omega_e\tau)} \quad (16)$$

After filtering the signal, the DC component is removed. Then, Equation (16) becomes,

$$\overline{V_{OL}} = -2\,V_c * M * sin\left(\frac{\pi V_{DC}}{V_{\pi DC}} + \theta_{RF} + \theta_{DC}\right)\left[J_1\left(\frac{\pi V_o}{V_{\pi RF}}\right)\right] sin\,\omega_e \tau * e^{(-j\omega_e \tau)} \qquad (17)$$

From the Equation (17) it is possible to compute the actual voltage at the loop output. From this, we compute the open loop gain $\overline{V_{OL}} = \overline{G_{OL}} * V_{(\tau)}$,

$$\overline{G_{OL}}(Vo) = -2\,\frac{V_c}{V_o} * M * sin\left(\frac{\pi V_{DC}}{V_{\pi DC}} + \theta_{RF} + \theta_{DC}\right)\left[J_1\left(\frac{\pi V_o}{V_{\pi RF}}\right)\right] * e^{(-j\omega_e \tau)} \qquad (18)$$

The gain presented in Equation (18) is not linear. It can be linearized using Taylor series to model the Bessel's function to find the small signal gain. When the index n of the Bessel's function is fixed and z is close to zero, we have [11],

$$J_n(z) = \left(\frac{1}{2}z\right)^n \sum_{k=0}^{\infty} \frac{\left(-\frac{1}{4}z^2\right)^k}{k!\,\Gamma(n+k+1)} \qquad (19)$$

If n is a natural number: $\Gamma(n+1) = n!$. We can rearrange as,

$$J_1\left(\frac{\pi V_o}{V_{\pi RF}}\right) = \frac{\pi V_o}{2V_{\pi RF}} - \frac{\left(\frac{\pi V_o}{2V_{\pi RF}}\right)^3}{2} + \frac{\left(\frac{\pi V_o}{2V_{\pi RF}}\right)^5}{12} \qquad (20)$$

And for third order,

$$J_1\left(\frac{\pi V_o}{V_{\pi RF}}\right) \cong \frac{\pi V_o}{2V_{\pi RF}} - \frac{\left(\frac{\pi V_o}{2V_{\pi RF}}\right)^3}{2} \qquad (21)$$

And the small signal gain $\overline{G_{OL-SS}}$ is given by,

$$G_{OL-SS} = \frac{\partial \overline{G_{OL}}}{\partial \overline{V}}(V=0) = -\frac{\pi V_c M}{V_{\pi RF}} sin\left(\frac{\pi V_{DC}}{V_{\pi DC}} + \theta_{RF} + \theta_{DC}\right) \qquad (22)$$

The open loop small signal gain is expressed as a function of the input voltage is as follows,

$$\overline{G_{OL}}(Vo) = G_{OL-SS} * \left(1 - \frac{1}{2}\left(\frac{\pi V_o}{2V_{\pi RF}}\right)^2 + \frac{1}{12}\left(\frac{\pi V_o}{2V_{\pi RF}}\right)^4\right) * e^{(-j\omega_e \tau)} \qquad (23)$$

1.1.3 Closed Loop Analysis of the Optoelectronic Oscillator [12][3], [10]

The closed loop of the OEO is shown in Figure 3. The loop is composed by and RF amplifier with transfer function defined as $\overline{G_A} = G_A e^{j\phi_A}$, and the resonant network transfer function is $\overline{H_{react}} = \frac{\overline{G_{OL}}}{G_A}$, this network is composed by the EOM, a microwave filter and a photodiode. This is an open loop network closed by a microwave amplifier.
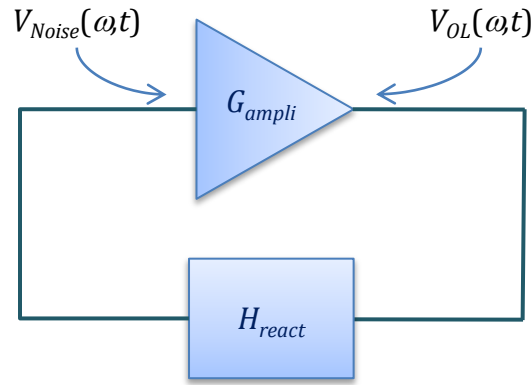
Figure 3 Closed loop oscillator diagram.

There are several noise sources linked to the laser and photodectector. For the laser, the relative intensity noise (RIN) due to laser power fluctuations, the noise linked to optical fiber reflections and perturbations is present in the OEO. In the photodetector there is the schottky noise due to the optical/electrical discrete process conversion.

If we assume a sinusoidal noise signal, $V_{noise}(\omega, t)$, this is as follows,

$$V_{noise}(\omega, t) = V_{noise}(\omega) * e^{j\omega t} \tag{24}$$

The noise signal inside the loop starts the oscillation process. Because of the phase coherence inside the loop, there is a constructive feedback inside the oscillator. When the amplitude of the signal reaches the open loop gain (oscillation threshold), the oscillation is achieved. Once the system is oscillating, the output signal is represented as $V_{RF}(t)$. From this, it is possible to stablish a closed-loop OEO transfer function,

$$\frac{V_{RF}}{V_{noise}} = \frac{\overline{G_A}}{1 - \overline{G_{OL}}} = \frac{G_a \, e^{j\phi t}}{1 - \overline{G_{OL}}^2 - 2\overline{G_{OL}} * \cos(\omega_e \tau + \pi)} \tag{25}$$

1.1.3.1 Oscillation Condition

To achieve an oscillation, it is necessary to satisfy the two Barkhausen conditions. The first one is the gain condition and the second one is the phase condition.

$$|G_{OL}| = 1$$

$$\omega_{RF}\tau + \phi_0 = 2k\pi \tag{27}$$

Where k is an integer.

1.1.3.2 Oscillation Voltage and Power

Let us consider the term V_{RF} representing the oscillation amplitude. Replacing it into Equation (18), this leads to:

$$|G_{OL}| = |G_{OL-SS}| \frac{2V_{\pi RF}}{\pi V_{RF}} J_1\left(\frac{\pi V_{RF}}{V_{\pi RF}}\right) = 1 \tag{28}$$

If we consider the situation when $V_{RF} \ll V_{\pi RF}$, we are able to develop a first order Bessel transfer function expressed in Taylor's series:

$$J_1\left(\frac{\pi V_{RF}}{V_{\pi RF}}\right) \approx \frac{\pi V_{RF}}{2V_{\pi RF}} - \frac{\left(\frac{\pi V_{RF}}{2V_{\pi RF}}\right)^3}{2} + \frac{\left(\frac{\pi V_{RF}}{2V_{\pi RF}}\right)^5}{12} \tag{29}$$

We replace Equation (28) in (29) and we have,

$$|G_{OL}| = |G_{OL-SS}|\frac{2V_{\pi RF}}{\pi V_{RF}}\left(\frac{\pi V_{RF}}{2V_{\pi RF}} - \frac{\left(\frac{\pi V_{RF}}{2V_{\pi RF}}\right)^3}{2} + \frac{\left(\frac{\pi V_{RF}}{2V_{\pi RF}}\right)^5}{12}\right) = 1 \tag{30}$$

Where we obtain the following expression for the third order oscillation voltage:

$$V_{RF} = \frac{2\sqrt{2}V_{\pi RF}}{\pi}\sqrt{1 - \frac{1}{|G_{OL-SS}|}} \tag{31}$$

For the fifth order,

$$V_{RF} = \frac{2\sqrt{3}V_{\pi RF}}{\pi}\left(1 - \frac{1}{\sqrt{3}}\sqrt{\frac{4}{|G_{OL-SS}|} - 1}\right)^{\frac{1}{2}} \tag{32}$$

From Equations (31) and (32) it is found the oscillation power of the OEO.
For the third order it is:

$$P_{oscillator} = \frac{V_{RF}^2}{2R_{amp}} = \frac{1}{R_{amp}}\left(\frac{2V_{\pi RF}}{\pi}\right)^2\left(1 - \frac{1}{|G_{OL-SS}|}\right) \tag{33}$$

For the fifth order the oscillation power is given by:

$$P_{oscillation} = \frac{V_{RF}^2}{2R_{ch}} = \frac{6}{R_{amp}}\left(\frac{V_{\pi RF}}{\pi}\right)^2\left(1 - \frac{1}{\sqrt{3}}\sqrt{\frac{4}{|G_{OL-SS}|} - 1}\right) \tag{34}$$

Where R_{amp} is the amplifier load impedance.

1.1.3.3   Photodetected Current

To compute the photodetected current, it is necessary to consider the voltage of the photodetected signal. It is given by:

$$\tilde{V}_{ph} = H_{MZM}\tilde{\alpha}_O P_{in}\tilde{S}R_{ph} \tag{35}$$

Where,
- R_{ph} represents the photodetector resistance load.

- $\tilde{\alpha}_O$ represents the optical losses inside the loop, these losses are defined as:

$$\tilde{\alpha}_O = \frac{\tilde{\alpha}_{MZM}}{2}\tilde{\alpha}_{FO}$$

Where, $\tilde{\alpha}_{FO} = \alpha_{FO}e^{-j\omega\tau_d} = \alpha_{FO}e^{-j\omega\phi_{FO}}$ represent the optical fiber losses and α_{FO} the optical fiber delay.

- S represents the photodetector responsivity.

And the photodetected current is given by,

$$\tilde{I}_{ph} = \frac{\tilde{V}_{ph}}{R_{ph}}$$

(36)

$$\tilde{I}_{ph} = \tilde{\alpha}_O P_{in}\tilde{S}\left\{1 + M\cos\left(\frac{\pi V_{DC}}{V_{\pi DC}} + \frac{\pi V_{RF}(t)}{V_{\pi RF}} + \theta_{DC} + \theta_{RF}\right)\right\}$$

This expression can be manipulated as previously done to the open loop voltage. From the manipulation, we obtain,

$$\left|I_{ph}\right| = \alpha_O P_{in}S \cdot |1 + MJ_0(Y)\cos(X) - 2MJ_1(Y)\sin(X)\sin(\omega_0 t)|$$

(37)

Where,

$$X = \frac{\pi V_{DC}}{V_{\pi DC}} + \theta_{DC} + \theta_{RF}$$

$$Y = \frac{\pi V_{RF}}{V_{\pi RF}}$$

From Equation (37), it is possible to see two different operation states of the oscillator:

- The first one corresponds to the situation when there is not enough optical power to achieve the oscillation. In this case the second term of Equation (37) is neglected and the expression is reduced to

$$\left|I_{ph}\right| = \alpha_O P_{in}S \cdot |1 + MJ_0(Y)\cos(X)|$$

(38)

- The second situation occurs when the power threshold is achieved and the expression remains the same as Equation (37).

1.1.3.4   Oscillation Frequency

The oscillation frequency is given by,

$$f_{osc,k} = \frac{k}{\tau} - \frac{\phi_0}{2\pi\tau}$$

(39)

The frequency space between the modes is given by the free spectral range (FSR). This is given by,

$$FSR = \frac{1}{\tau} = \frac{1}{\tau_F + \tau_C}$$

(40)

Where τ_C represents the time delay due to the electrical system components of the oscillator and τ_F is the time delay due to the optical fiber that is defined as:

$$\tau_F = \frac{n_F L}{c}$$

(41)

n_F represents the refractive index of the optical fiber, c is the speed light.

Due to the presence of the RF filter inside the oscillator loop, there will be just one mode that will oscillate inside the loop. The other modes will be rejected by the RF filter. Figure 4 presents the oscillation mode selection.
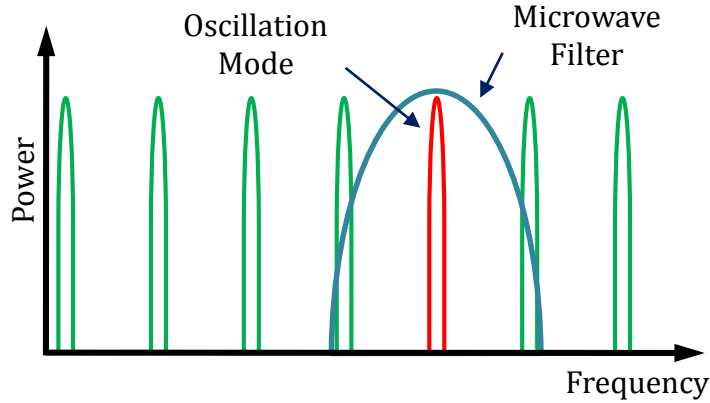
Figure 4 Oscillating mode of the OEO.

1.1.3.5   Oscillation Quality

The noise voltage, V_{noise}, has been described in previous sections. From this, it is possible to compute the noise power in a given bandwidth Δf at frequency ω:

$$P_{noise}(\omega) = \frac{|V_{noise}(\omega)|^2}{2R_{ampli}} = S_{noise} * \Delta f \tag{42}$$

Where, R_{ampli} represents the amplifier load impedance.

The white noise is injected to the amplifier, then, it is possible to find the spectral power density of the noise signal normalized with regard to the oscillation power,

$$S_{RF}(f) = \frac{P_{RF}(f)}{P_{osc}\Delta f}$$

$$\frac{P_{RF}(f)}{P_{noise}(f)} = \frac{G_a^2}{1 + |G_{OL}|^2 - 2|G_{OL}|\cos(\omega\tau + \pi)} \tag{43}$$

Where f is the fourier frequency defined as $\omega = \omega_{osc} + 2\pi f$.

The power spectral density of the oscillating signal is given by the following equation,

$$S_{RF}(f) = \frac{G_a^2 S_{noise}/P_{osc}}{1 + |G_{OL}|^2 - 2|G_{OL}|\cos(\omega\tau + \pi)} \tag{44}$$

Considering the situation when $f \ll 1/\tau$, we can convert the cosine expression as follows,

$$\cos(x) = 1 - \frac{x^2}{2} \tag{45}$$

With this, the spectral power density of the oscillating signal is as follows,

$$S_{RF}(f) = \frac{G_a^2 S_{noise}/P_{osc}}{(1 + |G_{OL}|\ )^2 - |G_{OL}|(2\pi f\tau)^2} \tag{46}$$

This calculations was done just taking into account the phase term. Now, to calculate the spectral linewidth and the quality factor, we must take into account the following considerations to precisely compute those parameters.

$$f \ll 1/\tau$$

$$\cos(2\pi f\tau) \cong 1$$

$$\int_{-\infty}^{\infty} S_{RF}(f).df \approx \int_{-1/2\tau}^{1/2\tau} S_{RF}(f).df = 1 \tag{47}$$

Now, it is possible to write:

$$\frac{G_a^2 S_{noise}/P_{osc}}{\tau(1 + |G_o|)^2} = 1 \tag{48}$$

The open-loop gain at the amplifier output can be written as a function of the Noite to signal ratio (NSR), as follows,

$$|G_{OL}| = 1 - \sqrt{\frac{NSR}{\tau}} \tag{49}$$

Where the NSR is defined as,

$$NSR = \frac{G_{a\ noise}^2 S}{P_{osc}} \tag{50}$$

1.1.3.6 Half-Power Spectral Linewidth (HPSL)

The half-power spectral linewidth is defined as the carrier linewidth measured at 3 dB from the carrier peak. This is expressed as,

$$S_{RF}(\Delta f_{HPSL}) = \frac{S_{RF}(f = 0)}{2} = \frac{NSR}{2(1 - |G_{OL}|)^2} \tag{51}$$

When integrating the HPSL,

$$\Delta f_{HPSL} = \frac{\sqrt{NSR/\tau}}{\pi\tau}\left(1 - \sqrt{NSR/\tau}\right)^{-1/2} \approx \frac{\sqrt{NSR/\tau}}{\pi\tau} \tag{52}$$

1.1.3.7 Quality Factor of the Resonator (Q)

The quality factor (Q) or selectivity factor measures the relation between the energy received and dissipated in a signal cycle by the resonator. The quality factor has an inverse relation in comparison with the half-poser spectral linewidth. Q is expressed as follows,

$$Q = \frac{f_{osc}}{\Delta f_{HPSL}} = \frac{\pi f_{osc}\tau}{\sqrt{NSR/\tau}} \tag{53}$$

1.1.4 Optoelectronic Oscillator Performance Parameters

The oscillator stability has a key role in the performance of the applications, such as, radar target discrimination, time reference, etc. There are two reference work frames in oscillators. The first one is the court term stability and the long term stability. Figure 5 presents each of them.
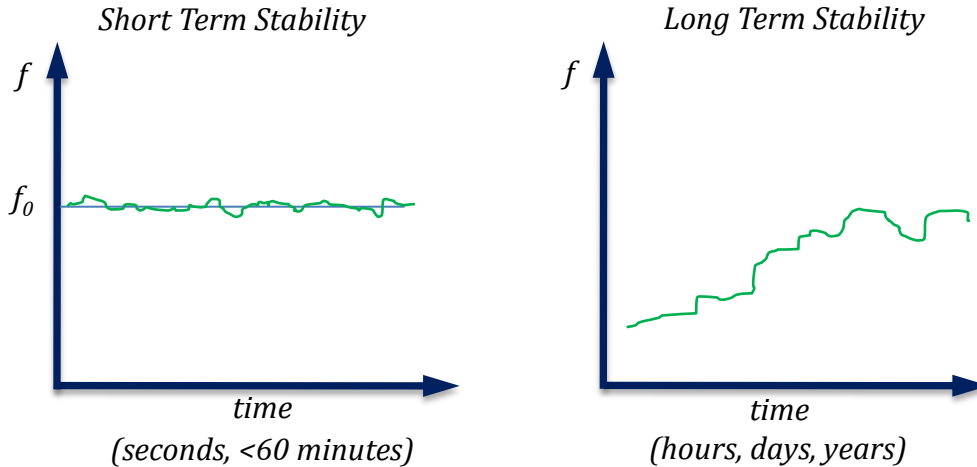
Figure 5 Long term and short term stability of an oscillator.

The short term stability is related to the oscillator phase noise. This is defined as the ability of the oscillator to keep the same frequency in a reduced period of time taking into account the frequency random variations due to the noise phenomena inside the system [13][14].

Amplifiers or any microwave active component inside the system is an intrinsic noise source. Most of the optoelectronic oscillator internal noise is contributed by the flicker noise that is introduced by the microwave amplifier and several perturbation sources such as mechanical vibrations, temperature variations.

1.1.4.1 *Phase Noise* [15], [16]

The output signal of an ideal oscillator can be modeled as a sinusoidal function as follows:

$$V_{(t)} = V_o \sin(2\pi v_o t)$$

(54)

In Equation (54) the terms V_o and v_o correspond to the signal amplitude and frequency. If a non ideal oscillating signal is going to be analyzed, it is necessary to take into account the amplitude ($\epsilon(t)$) and frequency variations ($\varphi(t)$). The Equation (55) represents this model as follows:

$$V_{(t)} = [V_o + \epsilon(t)] \sin(2\pi v_o t + \varphi(t))$$

(55)

Where, $\epsilon(t)$, represents the fluctuation random process around V_o, known as amplitude noise and $\varphi(t)$ represents the random noise process (phase noise) linked to the frequency random variations. The amplitude variations ($\epsilon(t)$,) are neglected in this analysis because of the fact they will not affect directly the frequency stability, unless the case where the non-linear dynamics of the oscillator converts the amplitude variations into phase variations. Consequently, to analyze the frequency stability, the frequency variations will be taken into account. The sinusoidal signal equation will be as Equation (56).

$$V_{(t)} = [V_o] \sin(2\pi v_o t + \varphi(t)) \tag{56}$$

The instantaneous frequency $v(t)$ is defined as,

$$v(t) = \frac{1}{2\pi} \frac{d}{dt} \left(2\pi v_o t + \varphi(t)\right) = v_o + \frac{1}{2\pi} \frac{d\varphi(t)}{dt}$$

$$v(t) = v_o + \Delta v(t) \tag{57}$$

From $\Delta v(t)$, it is possible to define the random process that fits the frequency noise as,

$$\Delta v(t) = \frac{1}{2\pi} \frac{d\varphi(t)}{dt} \tag{58}$$

This could be analyzed taking into account two variables of interest, the relative frequency variation $y(t)$ and the relative phase variation $x(t)$ that are described as follows.

$$y(t) = \frac{1}{2\pi v_o} \frac{d\varphi(t)}{dt}$$

$$x(t) = \frac{\varphi(t)}{2\pi v_o} \tag{59}$$

Finally, $y(t)$ and $x(t)$ can be related as,

$$y(t) = \frac{dx(t)}{dt} \tag{60}$$

1.1.4.2   *Frequency stability in frequency domain* [17][18]

Due to the random fluctuation of phase and frequency, it is necessary to make a statistical analysis to describe the frequency stability. These statistical methods are correlation function and spectral densities.

As it was defined in the previous section, $\Delta v(t)$ is the process that models the frequency noise. It is possible to define the noise spectral density, $S_{\Delta v}^{TS}(f)$, as the two sided noise power spectral density,

$$S_{\Delta v}^{TS} = \int_{-\infty}^{\infty} R_{\Delta v}(\tau) e^{-j2\pi f \tau} d\tau \ [Hz] \tag{61}$$

Where,

$$R_{\Delta v}(\tau) = \langle \Delta v(t) \Delta v(t - \tau) \rangle \tag{62}$$

The integration limits correspond to the two-sided (TS) calculation. At experimental level, the measurement is taken in a single band (SB). This can be expressed as,

$$S_{\Delta v}(f) = 2 S_{\Delta v}^{TS}(f) \tag{63}$$

With this consideration, Equation (61) is solved in the range $0 < f < +\infty$.

In the same way it is possible to express the Single Band (SB) phase noise spectral density as,

$$S_{\varphi}(f) = 2 \int_{0}^{\infty} R_{\varphi}(\tau) e^{-j2\pi f \tau} \ [Rad^2/Hz] \tag{64}$$

Where,

$$R_\varphi(\tau) = \langle \varphi(t)\varphi(t-\tau) \rangle \tag{65}$$

To define the spectral density functions relative to frequency $S_y(f)$ [Hz^{-1}] and phase $S_x(f)$ [s^2/Hz],

$$S_y(f) = \frac{1}{v_o^2} S_{\Delta v}(f)$$
$$S_{\Delta v}(f) = f^2 S_\varphi(f)$$
$$S_y(f) = \left(\frac{f}{v_o}\right)^2 S_\varphi(f) \tag{66}$$
$$S_y(f) = 4\pi^2 f^2 S_x(f)$$

The frequency noise power spectral density $S_y(f)$ has a key role in the frequency stability characterization because this gives a description of the noise processes in an actual oscillator. There is an asymptotic model that describes $S_y(f)$ as a component addition , where each noise source is represented by a different component [18]. $S_y(f)$ is described as follows:

$$S_y(f) = \begin{cases} \displaystyle\sum_{\alpha=-2}^{+2} h_\alpha f^\alpha & for\ 0 \leq f \leq f_c \\ 0 & for\ f > f_c \end{cases} \tag{67}$$

Where α represents each noise type contribution and constant h_α is the measurement of the noise level. f_c is the cut-off frequency of the actual elements in an oscillator.

In the same way it is introduced the single sideband (SSB) phase noise, $\mathcal{L}(f)$, defined as the half of the SSB phase noise spectral density. $\mathcal{L}(f)$ is the measurement of the noise energy related to the RF power measured with an electrical spectrum analyzer. $\mathcal{L}(f)$ presents the power inside a single band (power in a single sideband - P_{ssb}) with a bandwidth of 1 Hz related to the complete signal power.

$$\mathcal{L}(f) = \frac{1}{2} S_\varphi(f) = \frac{P_{ssb}(f)}{P_o} \tag{68}$$

$\mathcal{L}(f)$ is expressed in dBc/Hz. Figure 6 presents graphically this definition and Figure 7 presents a typical SSB phase noise measurement.
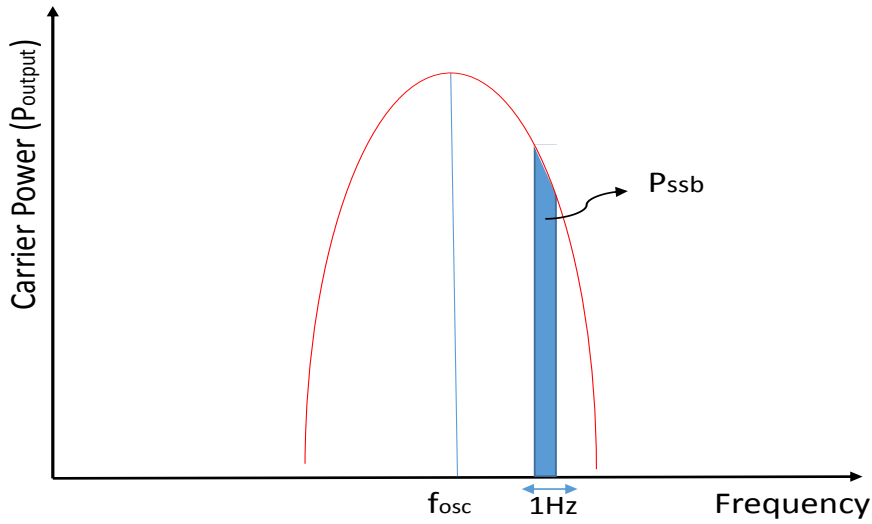
Figure 6 Single sideband phase noise.
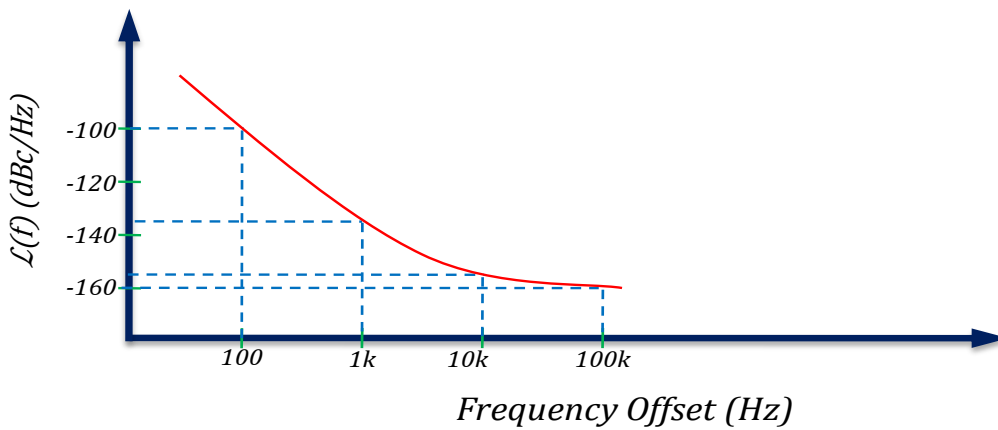
Figure 7 SSB phase noise typical measure representation.

1.1.4.3   Stability in Time Domain [18][17]

The oscillator time domain stability is used to characterize an oscillator in long term. According to the frequency given by Equation (69), it is necessary to define a time interval τ in order to characterize the temporal frequency stability of the oscillator. The average of $v(t)$ in a period time from t_k to $t_k + \tau$ is given by,

$$\langle v(t) \rangle_{t_{k,\tau}} = v_0 + \frac{1}{\tau} \int_{t_k}^{t_k+\tau} \Delta v(\theta) d\theta = \frac{n_k}{\tau} \tag{69}$$

Where n_k is the number of cycles of the signal inside the time range τ.

The normalized quantity $\overline{y_k}$ is defined as follows,

$$\bar{y}_k = \frac{1}{\tau} \int_{t_k}^{t_k+\tau} y(\theta) d\theta \tag{70}$$

From Equations (58) and (59), the Equation (69) becomes,

$$\langle \nu(t) \rangle_{t_k,\tau} = \nu_0(1 + \bar{y}_k) = \frac{n_k}{\tau} \tag{71}$$

And from this, it is possible to obtain

$$\bar{y}_k = \frac{\varphi(t_k + \tau) - \varphi(t_k)}{2\pi \nu_0 \tau} \tag{72}$$

The upper term of Equation (72) represents the phase error in time range of τ.

Using Equation (72) it is possible to obtain equally space time samples. From the measurement of several samples it is possible to find their dispersion, this means, to calculate a variance.
Using two samples it is possible to calculate a figure-of-merit variance, known as Allan's Variance [18], and it is defined as,

$$\sigma_y^2(\tau) = \frac{1}{2}\langle(\bar{y}_2 - \bar{y}_1)^2\rangle \tag{73}$$

1.1.4.4   *Transformations between frequency domain and time domain* [19]

There is a mathematical relation that can link the temporal and frequency domains. From the relative frequency spectral noise density, it is possible to find the Allan's variance:

$$\sigma_y^2(\tau) = \int_0^\infty S_y(f) \frac{2\sin^4 \pi\tau f}{(\pi\tau f)^2} df \tag{74}$$

To convert measurements from frequency domain to time domain there is an approximate model that represents the random fluctuations as five noise independent processes inside the oscillator. Each of the slopes represents a noise process as seen in Figure 8. In Table 1 it is presented the relation between the time and frequency domain for each noise source.
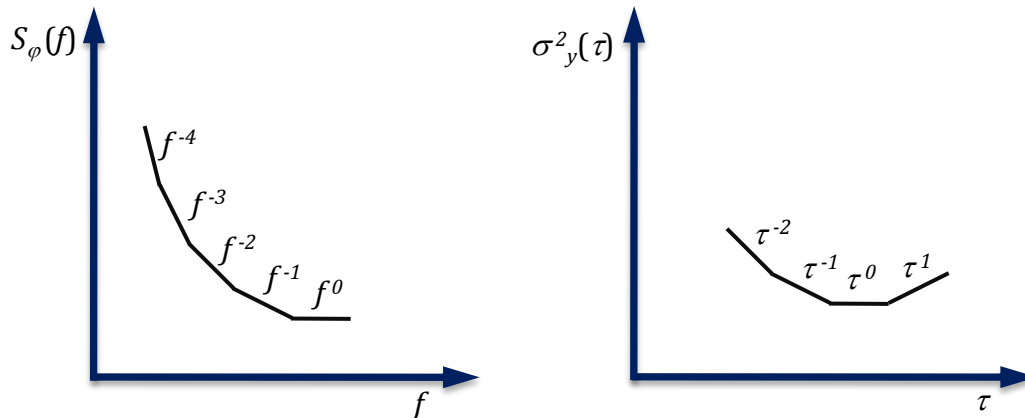
Figure 8 *Phase noise representation in frequency and time domain.*

Noise	$S_y(f)$	$S_\varphi(f)$	Allan's Variance $\sigma_y^2(\tau)$	Slope	
				$S_\varphi(f)$	$\sigma_y^2(\tau)$
Random Frequency	$h_{-2}f^{-2}$	$v_0^2 h_{-2} f^{-4}$	$\dfrac{2\pi^2 h_{-2}\tau}{3}$	-4	1
Frequency Flicker	$h_{-1}f^{-1}$	$v_0^2 h_{-1} f^{-3}$	$2ln(2)h_{-1}$	-3	0
White Noise	h_0	$v_0^2 h_0 f^{-2}$	$\dfrac{h_0}{2\tau}$	-2	-1
Flicker Phase	$h_1 f$	$v_0^2 h_1 f^{-1}$	$\dfrac{h_1}{4\pi^2\tau^2}\{1,038 + 3\cdot ln(2\pi f_h\tau)\}$	-1	≈-2
White Phase	$h_2 f^2$	$v_0^2 h_2$	$\dfrac{3h_2 f_h}{4\pi^2\tau^2}$	0	-2

Table 1 Noise processes in time and frequency domain

1.2   Oscillators State-of the-Art

A state-of-the-art of the optoelectronic oscillator in terms of frequency stability is shown in this section. Since the optoelectronic oscillator idea conception in the 80's, researchers are interested on the spectral purity of the oscillator in order to have an accurate reference source. Afterwards, with the integration of optoelectronic communications in commercial communications systems, the goal of the research is to increase the oscillation frequency while keeping the spectral purity.

The frequency stability of the oscillator varies according to the trade-off between the optical and electronic components. The use of high quality factor (Q) dielectric resonators [20] (Q=13000) reduces the phase noise value that means higher frequency stability. To compare the different high spectral purity optoelectronic oscillators, the following section presents the most relevant results.

1.2.1   High Spectral Purity Oscillators

Sapphire Oscillator
This oscillator configuration uses a Zaphire sample as a dielectric resonator. The quality factor achieved with this material moves from 10^4 at room temperature to 10^9 at -270 ºC. For a 9 GHz carrier the spectral density noise power is -165 dBc/Hz at 10 kHz offset [21]. A 10 GHz Sapphire oscillator with phase noise value of -127 dBc/Hz at 3 kHz offset [22].

Quartz Oscillator
The oscillators using a quartz resonators are widely used for frequency generation thanks to the good quality factor achieved with this technology, between 10^4 to 10^6. A quartz based oscillator at 2.11 GHz with a phase noise value of -136.5 dBc/Hz at 10 kHz offset[23]. The best result reported, from the best of our knowledge, it is a 10 GHz oscillator with

phase noise -145 dBc/Hz at 10 kHz offset reported by De Giovanni and Chomiki in 2010 [24].

Dielectric Resonator Oscillator

This kind of oscillator uses ceramic dielectric materials ($Q=10^4$) as resonant cavity and a microwave transistor as active element. The trade-off between the resonator quality factor, the microwave transistor performance and the transmission lines quality, it is possible to obtain oscillator at 10.2 GHz with phase noise of -118 dBc/Hz at 10 kHz offset [25].

Electrical Resonator Oscillator

The use of electrical resonator oscillator such LC networks, has permitted the development of several milestone results. For the C-Band of the spectrum, a tunable voltage controlled oscillator (VCO) has been reported with a phase noise value of -120 dBc/Hz at 1 MHz offset [26].

In 2008, a 21 GHz CMOS based VCO was presented by Wang et al with a phase noise of -106 dBc/Hz at 1 MHz, and a 24 GHz CMOS based VCO with -117 dBc/Hz at 10 MHz offset was presented by the same author [27].

A 9.34 GHz CMOS frequency synthesizer was presented by Tsai et al in 2012 with a phase noise of -75.1 dBc/Hz at 100 kHz offset.
The oscillators described in this category are summarized in Table 2.

Topology	Author	Frequency (GHz)	Phase Noise (dBc/Hz)
Sapphire Oscillator	Ivanov et al. [21]	9	-165 @ 10 kHz offset
Quartz Oscillator	Mosso et al. [22]	10	-127 @ 3 kHz offset
	El Aabbaoiu et al. [23]	2.11	-136.5 @ 10 kHz offset
	De Giovanni and Chomiki. [24]	10	-145 @ 10 kHz
Dielectric Resonator Oscillator	Regis et al. [25]	10.2	-118 @ 10 kHz
Electrical Resonator Oscillator	Wang [26]	3	-120 @ 1 MHz
	Wang [27]	24 GHz	-117 @ 10 MHz
	Tsai [28]	9.34	-75.1 @ 100 kHz

Table 2 High spectral purity oscillator state-of-the-art.

1.2.2   Optoelectronic Oscillators

The optoelectronic oscillator principles have been widely discussed in the previous sections. Different topologies have been suggested using different resonant elements with the goal of having the highest possible quality factor.

Whispering Gallery Mode Optoelectronic Oscillator

This technology uses passive optical resonators that have quality factor of 10^{11}. This thanks to the possibility of the light injection in a very small size cavity. The high quality factor of the whispering gallery mode resonator has a very high selectivity of the oscillation

modes. The best result reported using this technique for a 10 GHz carrier is reported by Merrer et al with a phase noise of -95 dBc/Hz at 10 kHz offset [29].

Fiber Ring Resonator Optoelectronic Oscillator

The optical fiber ring resonator has quality factor of order 10^{10}. The best result for this configuration has been reported by Saleh for a 10 GHz fiber ring optoelectronic oscillator with a phase noise of -130 dBc/Hz at 10 kHz offset [30].

Delay Line Optoelectronic Oscillator

The delay line optoelectronic oscillator architecture was the first one to be implemented by Yao and Maleki [6]. The optical fiber delay line acts as a resonant cavity according to its length. The higher the length higher the quality factor of the resonant cavity. The best reported results for this optoelectronic oscillator topology is that one reported by by Maleki and Matsko (OEWaves Inc.), a 10 GHz carrier generation is reported with a phase noise of -163 dBc/Hz at 7 kHz offset [31].

Topology	Author	Frequency (GHz)	Phase Noise (dBc/Hz)
Whispering Gallery Mode Optoelectronic Oscillator	Merrer et al. [29]	10	-95 @ 10 kHz offset
Fiber Ring Optoelectronic Oscillator	Saleh [30]	10	-130 @ 10 kHz offset
Delay Line Optoelectronic Oscillator	Maleki and Matsko [31]	10	-163 @ 10 kHz offset

Table 3 Optoelectronic oscillator state-of-the-Art.

Chapter 2

Long Wavelength VCSEL Characterization

Introduction

The Vertical Cavity Surface Emitting Laser (VCSEL) is a semiconductor laser that permits the long wavelength light emission with a reduced power consumption. In this work, long wavelength VCSELs at 1.3 and 1.5 μm are used. The optical spectrum of the lasers is analyzed to assure the single mode performance, the Relative Intensity Noise (RIN) is measured to characterize the noise contribution of the laser to the oscillator and the laser frequency response is analyzed be addressed in Chapter 3 for the VCSEL Based Optoelectronic Oscillator (VBO).

2.1 Vertical Cavity Surface Emitting Laser Description [51]

The Vertical Cavity Surface Emitting Laser (VCSEL) is a semiconductor laser that differs from other laser structures due to the fact that this is a surface emitting device instead of being an edge emitting device. Usually common semiconductor lasers, known as Edge Emitting Lasers (EELs) emit light along the junction, as shown in Figure 9. VCSELs emit their energy in perpendicular path with respect to semiconductor layers, as seen in Figure 10.
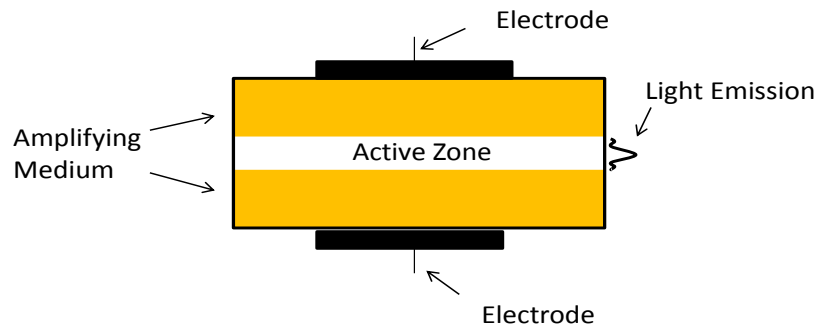
Figure 9 Edge Emitting Laser Structure [52].
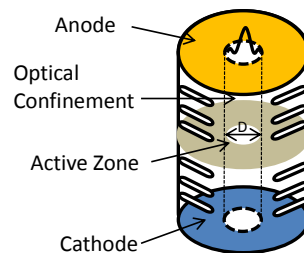
Figure 10 VCSEL Structure [33].

The first VCSEL idea was conceived in 1979 [33] to design a laser that could emit its energy perpendicular to the semiconductor junction. It was not until the end of 80's when Koyama [34] and Jewell [35] developed a microelectronic grown semiconductor epitaxial method that led to the birth of the 850 nm VCSEL.

2.1.1 VCSEL Structure

As shown in Figure 10, VCSELs are monolithic devices. These are relatively easy to manufacture [32]. Additionally, more detailed comparison between EEL and VCSEL structure is presented in Table 4. Some previously reported VCSEL structures are presented in Annex 2.

Parameter		EEL	VCSEL
Active Zone Volume	V_{act}	60 µm³	0.07 µm³
Active Layer Area	S	$3*300\mu m^2$	$5*5\mu m^2$
Active Layer Thickness	d	100 A° - 0.1µm	80A-0.5µm
Cavity Length	L_{act}	300 µm	1 µm
Mirrors Reflectivity	R_m	0,3	>0,99
Optical Confinement	ζ	3%	4%
Longitudinal Confinement	Γ	50%	3%
Photon Lifetime	τ_p	1 ps	>1 ps
Resonance Frequency at low bias current	F_r	8 GHz	3 GHz

Table 4 Comparison of parameters between stripe laser and VCSEL [32].

2.1.2   VCSEL Materials

Depending on desired emission wavelength, VCSELs use different materials like InGaAsP, InAlGaAs, GaInNAsSb on InP substrate [36]. Figure 11 presents different materials according to the emission wavelength use [33], [37]–[39].
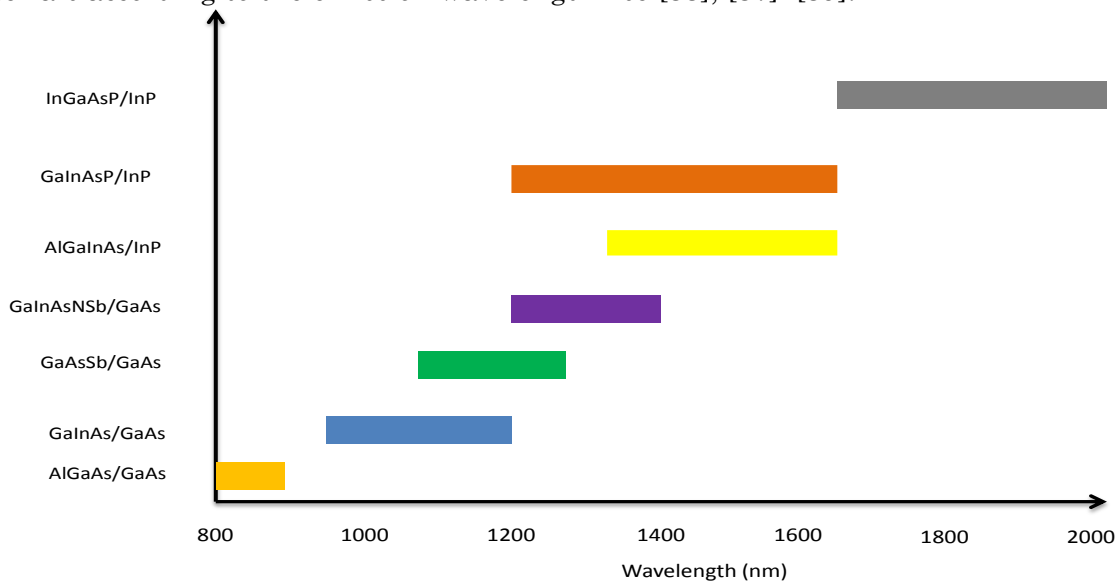
Figure 11 VCSEL materials and wavelengths.

2.1.3   Long Wavelength VCSELs

Long wavelength VCSELs were first demonstrated in 1993 with a 1.3 µm InGaAs-InP VCSEL [40]. The top distributed Bragg reflector (DBR) was made of 8.5 pairs of p-doped MgO-Si material with Au-Ni-Au layers and the top layer was made of 6 pairs of n-doped SiO-Si material, as shown in Figure 12.
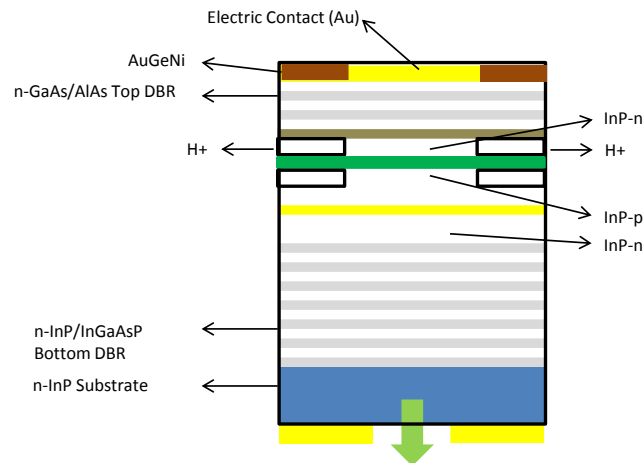
Figure 12 Long wavelength VCSEL structure with tunnel junction at 1.55 um.

Then, Salet et al, presented a 1227 nm wavelength InGaAs-InP VCSEL. This was composed by 50 DBR pairs with 500 mA threshold current. The top mirror was made using p-doped SiO_2-Si reflectors [41].

In 1999 Boucart et.al presented a 1.5um VCSEL [42] using 26.5 GaAs-AlAs layer pairs as top DBR and 50 layer pairs of n-doped InGaAsP-InP DBR as bottom mirror with 11mA threshold current. Table 5 presents long wavelength VCSEL fabrication development technology chronology [42].

The semiconductor lasers can be manufactured using different fabrication processes, a monolithic integrated circuit corresponds to that one that is made in the same semiconductor crystal as a single structure. The wafer fusion fabrication process consists on the direct bonding using chemical connections of two semiconductor materials [43]. And the epitaxy technique consists on deposition of semiconductor materials as several films on a substrate or crystal structure.

Active Region	DBRs	Fabrication Process	Research Group
InGaAsP-InP 1.3 µm	8.5 pairs of p-doped MgO-Si with Au/Ni/Au metal at the top and 6 pairs n-doped SiO/Si at the bottom	Monolithic	Baba et al. 1993 [44]
InGaAsP-InP 1.3 µm	P doped SiO_2-Si at the top 50 pairs of n-doped InGaAsP-InP at the bottom	Monolithic	Salet et al. 1997 [41]
GaInAsN-GaAs 1.8 µm	21 and 25.5 pairs of p and n-doped GaAs-AlAs layers at the top and at the bottom respectively	Monolithic	Larson et al. 1998 [45]
InGaAsP-InP 1.5 µm	30 pairs of p-doped GaAs-$Al_{0.67}Ga_{0.33}As$ at the top and	Wafer fusion	Margalit at. Al 1998 [46]

	undoped GaAs-AlAs at the bottom		
InGaAsP-InP 1.55 µm	26.5 pairs of n-doped GaAs-AlAs at top and 50 pairs of n-doped InGaAsP-InP at the bottom	Monolithic	Boucart et al 1999 [42]
InGaAsP-InP 1.55 µm	30 pairs of p-doped GaAs-Al$_{0.85}$As$_{0.15}$Ga at top and 50 pairs of n-doped InGaAsP-InPn at the bottom	Wafer fusion and epitaxy	Rapp et al 1999 [47]
InGaAlAs 1.56 µm	35 pairs of p doped InGaAlAs-InAlAs at the top and 43.5 pairs of n-doped InGaAlAs-InAlAs at the bottom	Monolithic	Kazmierski et al 1999 [48]
AlInGaAs 1.55 µm	45 and 35 pairs of n-doped Al$_{0.9}$Ga$_{0.38}$In$_{0.53}$As-Al$_{0.48}$In$_{0.52}$As at the top and at the bottom	Monolithic	Hall et al 1999 [49]
AlInGaAs 1.55 µm	30 and 23 pairs of n-doped AlAs$_{.0.56}$Sb$_{0.44}$-Ga0.$_8$As$_{0.58}$Sb$_{0.42}$ at the top and the bottom respectively	Monolithic	Hall et al 1999 [50]
GaAsSb 1.23 µm	19 and 30.5 pairs of p-doped and n-doped GaAs-AlAs at the top and at the bottom respectively	Monolithic	Yamada et al [51]
GaInNAs-GaAs 1.18 µm	24 and 35 pairs of p-doped and n-doped Al$_{0.7}$Ga$_{0.3}$As-GaAs at the top and bottom respectively	Monolithic	Kageyama et al 2001 [52]
AlInGaAs 1.55 µm	32 and 23 pairs of n-doped AlAs$_{0.56}$Sb$_{0.44}$-Al$_{0.2}$Ga$_{0.8}$As$_{0.52}$Sb$_{0.48}$	Monolithic	Hall et al 2001 [53]
BTJ 1.55 µm	CaF /ZnS 5 pairs	Monolitic	Amann et al. 2011 [54]

Table 5 Long wavelength VCSEL structures.

2.1.4 VCSEL Basic Parameters Description

Threshold Current

The threshold current of a VCSEL is expressed as a function of the threshold current density [34], as follows,

$$I_{th} = \pi \left(\frac{D}{2}\right)^2 J_{th} = \frac{qVN_{th}}{\eta_i \tau_s} \tag{75}$$

Where q represents the electron charge, V is the active region volume, N_{th} is the threshold carrier density, n_i is the internal quantum efficiency, τ_s is the recombination time and D is the active zone diameter.

Optical Power

The optical output power of a VCSEL is expressed as,
$$P_o = \eta_d \cdot \eta_{spon} \cdot \beta \cdot h \cdot v \cdot I, \qquad (I \leq I_{th})$$

$$\tag{76}$$

$$P_o = \eta_d \cdot h \cdot v \cdot (I - I_{th}) + \eta_d \cdot \eta_{spon} \cdot \beta \cdot h \cdot v \cdot I_{th}, \qquad (I \geq I_{th})$$

Where, η_d represents the quantum differential efficiency of the output mirror, η_{spon} is the spontaneous emission efficiency, β is the spontaneous emission factor, h is the planck constant, v is the optical emission frequency, and I is the driving current of the laser.

Modulation Frequency

The bandwidth of a VCSEL is the frequency range at which it can be modulated. Considering the approximation presented by Coldren [55], this is expressed as,

$$f_{3dB} \approx f_r \cdot \sqrt{1 + \sqrt{2}} \approx 1{,}55 \cdot f_r \tag{77}$$

Where, f_r is the resonance frequency of the VCSEL, given by,

$$f_r = \frac{1}{2\pi} \sqrt{\frac{v_g a}{qV_p} \eta_i (I - I_{th})} \tag{78}$$

Where, v_g is the group velocity, a is the differential gain, η_i is the laser internal efficiency, q is the electron charge, V_p is the cavity volume.

2.1.5   RayCan VCSELs

The Korean company RayCan has built long wavelength VCSELs using MOCVD technique. Figure 13 presents the structure of a MOCVD (Metalorganic Chemical Vapor Deposition) monolithically grown 1.3 and 1.5 µm wavelength VCSELs.
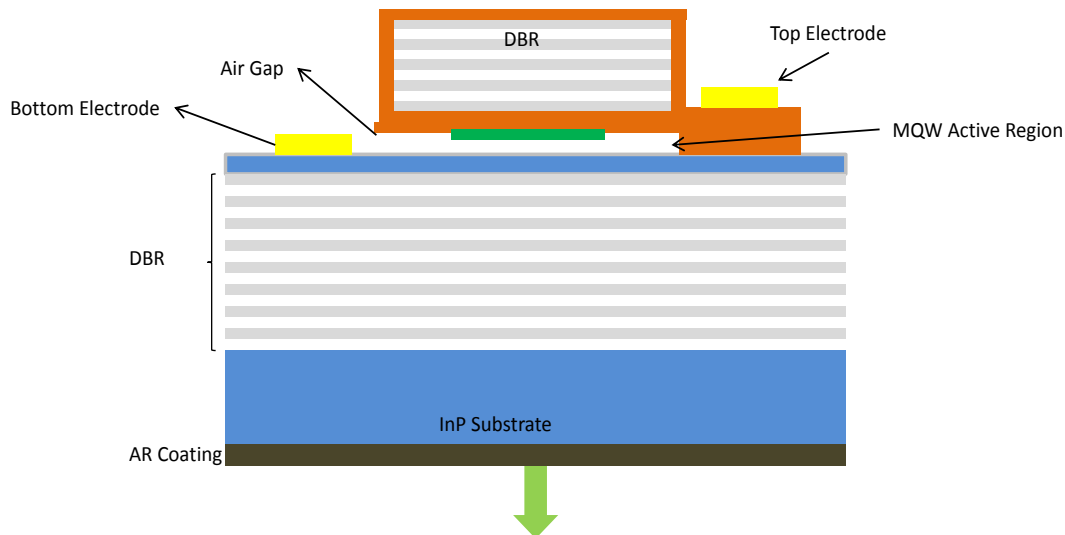
Figure 13 MOCVD grown monolithic structure of a 1.5 um VCSEL.

For the development of this research, Raycan pigtailed VCSELs were used at 1.3 and 1.5µm. Figure 14 presents a TO packaged VCSEL. In Annex 3, the datasheet of a Raycan VCSEL is presented.

Figure 14 Raycan pigtailed VCSEL.

2.2 RayCan VCSEL Characterization

The RayCan VCSELs are InP based lasers. RayCan VCSELs used are TO packaged as shown in Figure 14. This package has an optical fiber pigtail to facilitate the connection to the other optical components of the optoelectronic oscillator.

Two VCSELs were used to perform these test:
- 1.5 µm RC340541-FFP-1341607 RayCan pigtailed VCSEL.
- 1.3 µm RC220101-FFP-11423514 RayCan pigtailed VCSEL.

The VCSELs are temperature controlled at 20ºC. The threshold current for each one is:

$$I_{threshold} = 0.954 \ mA \ for \ 1.3 \ \mu m \ VCSEL$$
$$I_{threshold} = 1.192 \ mA \ for \ 1.5 \ \mu m \ VCSEL$$
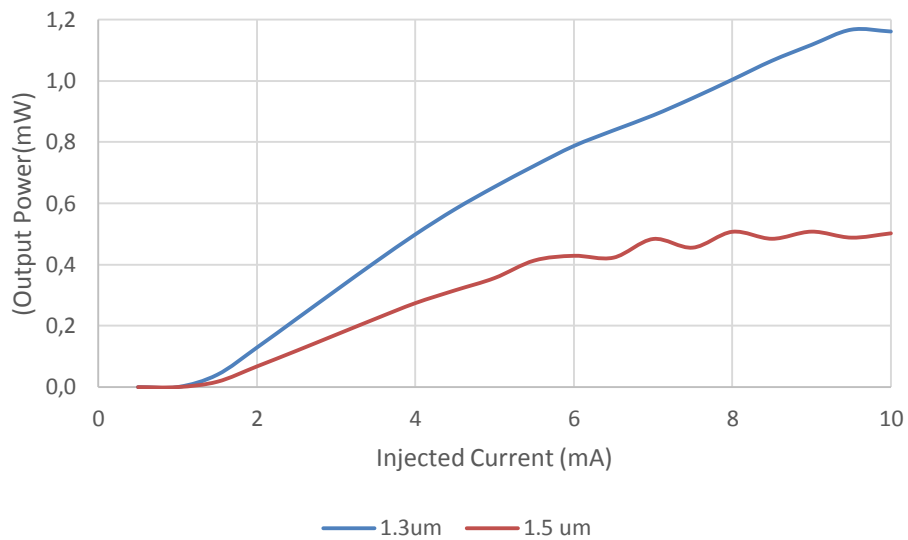
Figure 15 Output power vs injected current for 1.3 and 1.5 μm VCSELs.

2.2.1.1   VCSEL Optical Spectrum

The dominant mode of the single mode VCSEL was measured using the optical spectrum analyzer, as seen in Figure 16 for a 1.3 μm VCSEL and Figure 17 for a 1.5 μm VCSEL. From the optical spectrum shown in both figures, it is observed that the Side Mode Supression Ratio (SMSR) of the VCSELs is higher than 30 dB, this means that the second mode amplitude is 0.001 times that one of the dominant mode in linear scale.
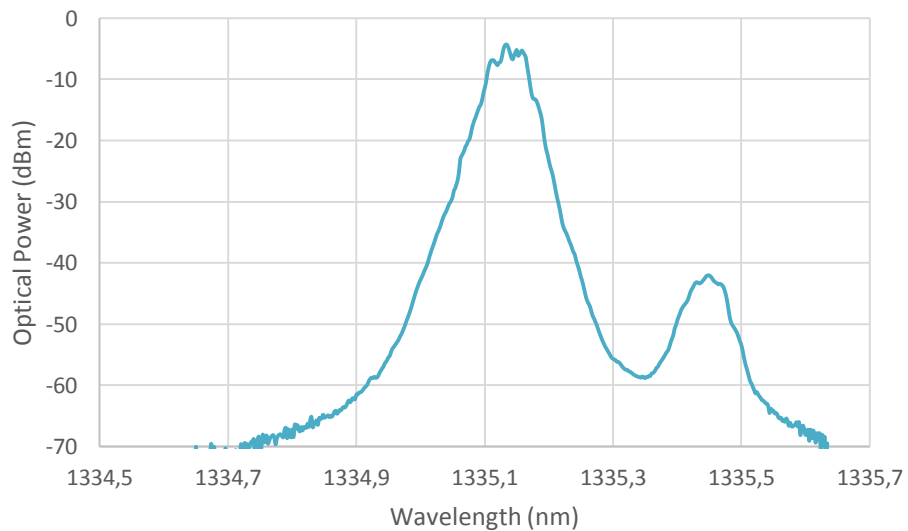
Figure 16 Optical spectrum for a 1330 nm VCSEL.
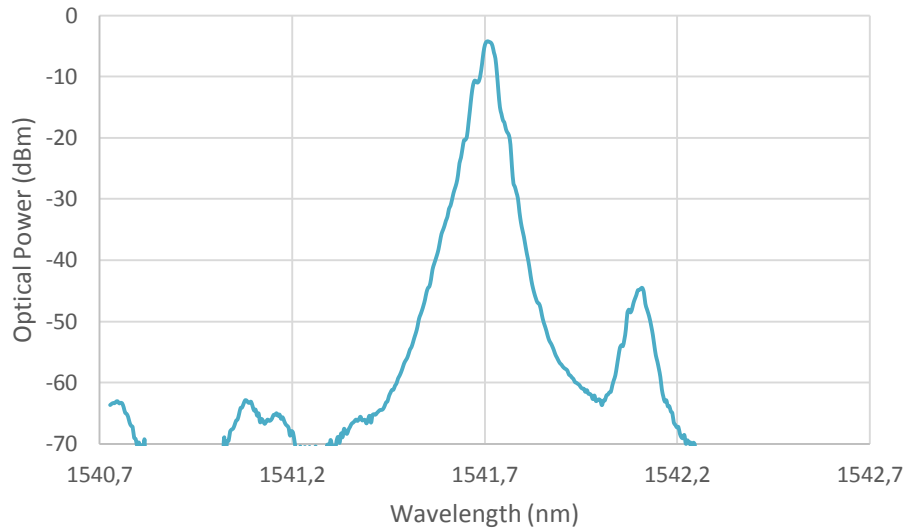
Figure 17 Optical spectrum for a 1550 nm VCSEL.

Influence of Temperature in VCSEL Wavelength

To perform the characterization of the temperature effect in VCSEL wavelength emission, a setup as shown in Figure 18 was implemented. The VCSEL under test is placed inside a metallic thermal controlled enclosure. The VCSEL output is connected to the optical spectrum analyzer (OSA).
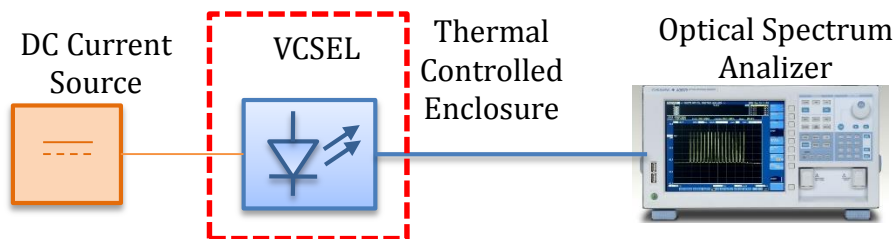
Figure 18 VCSEL Wavelength vs temperature setup.

There is a direct relation between the temperature and the emission wavelength in the VCSEL because of the lengthen of the laser cavity caused by the temperature increase. From the performed measurements it is observed a wavelength drift of 0.119 nm/°C, as shown in Figure 19.
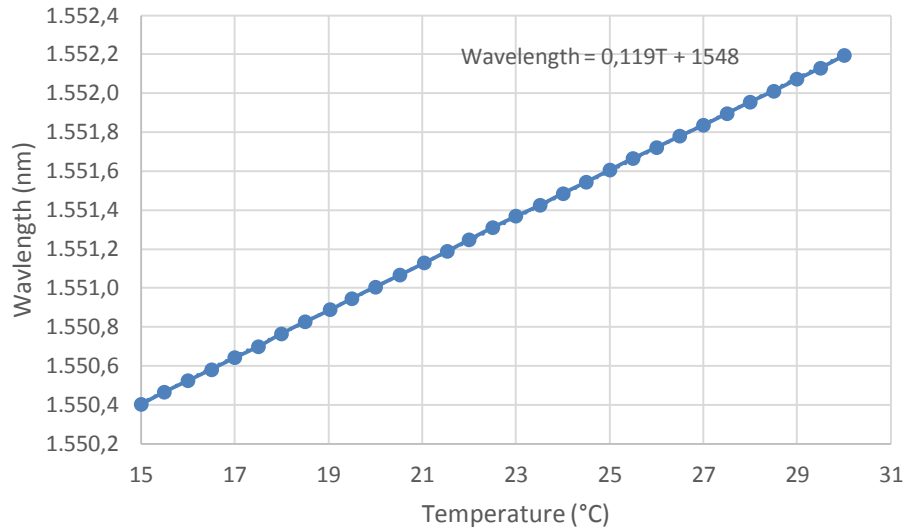
Figure 19 VCSEL wavelength vs temperature.

From this measurement it is concluded that thermal control must be applied to the VCSEL in order to assure the laser stability and repeatability of the measurements.

2.2.1.2   VCSEL Linewidth

The VCSEL linewidth is an important property for optical sources; this predicts the degree of the laser quality gradation in high speed optical communications. The linewidth of an optical source is known as Herny Factor (α_H) [56]. This factor is defined as relation between the laser gain and the refractive index variations as a function of carrier density, N. As follows,

$$\alpha_H = \frac{4\pi}{\lambda} * \frac{dn/dN}{dg/dN}$$

(79)

Where, n is the refractive index, g is the gain and λ is the emitted wavelength. It is important to mention that VCSELs linewidth larger than EELs due to the reflector losses and better coupling in the lasing mode [57].

For this research it has been chosen the chromatic dispersion of the optical fiber method to find the VCSEL Henry's Factor. Taking into account the technical resources of the laboratory, it is feasible to implement this method.

Optical Fiber Dispersion Method

Optical Fiber Dispersion Method Theory

This method consists on the optical fiber cut-off frequency detection, and from this, the extraction of the Henry factor is possible, as shown by Devaux [58]. The optical fiber chromatic dispersion is responsible of the optical signal deformation and from this, some characteristic frequencies appear. To give a better understanding of this phenomenon, it is necessary to perform an small signal analysis of a laser beam being propagated in a dispersive medium. The electric field of this wave is given by:

$$E = \sqrt{P}e^{j\phi(P)} \tag{80}$$

Where P corresponds to the optical emitted power and $\phi(P)$ to the phase of the electric field. The phase of the optical wave changes according to the light intensity as a function of the Henry's factor, as follows,

$$\Delta\phi(I) = \frac{\alpha_H}{2}\frac{\Delta P}{P} \tag{81}$$

When the VCSEL is under direct modulation, the modulating current is described as follows,

$$I = I_o(1 + m * \cos(2\pi f t)) \tag{82}$$

Where, I_o is the average, m is the modulation index (much lower than 1) and f is the modulation frequency of the optical signal. The electrical field of the optical wave can be assumed as a periodic signal, so it can be written as follows,

$$E = e^{j\omega_o t}\sum_{-\infty<p<\infty} A_p e^{j2\pi p f t} \tag{83}$$

Where, ω_o is the optical pulse. The Equation (80) can be developed as Fourier series using Equations (80) and (81). By developing E as a Fourier series of power m, we have the three first Fourier coefficients, they are:

$$A_{-1} = \sqrt{I_o}\,m\left(\frac{1+j\alpha_H}{4}\right) \tag{84}$$

$$A_0 = \sqrt{I_o} \tag{85}$$

$$A_0 = \sqrt{I_o}\,m\left(\frac{1+j\alpha_H}{4}\right) \tag{86}$$

These are the spectral components of electric field at the laser output. Each component will propagate through the optical fiber at different speed. The propagation constant is given by:

$$\beta_{\pm p} = \beta_o \pm \frac{2\pi p f}{v_g} - \frac{\pi\lambda^2 D p^2 f^2}{c} \tag{87}$$

Where, v_g is the group speed, c is the speed of light, and D is the chromatic dispersion of the optical fiber. The electric field of the optical wave after the optical fiber is given by,

$$E = e^{j\omega_o t}\sum_{-\infty<p<\infty} A_p e^{j(2\pi p f t - \beta_p L)} \tag{88}$$

Where, L is the optical fiber distance from its beginning. From this expression, it is possible to determine the light intensity at the fiber output at a frequency f as,

$$I_f = \frac{1}{2}\Re\left\{\sum_{p+q=1} A_p A_q e^{j(\beta_p+\beta_q)L}\right\} \tag{89}$$

From Equations (83) to (87) in (89), we have the following frequency response,

$$I_f = I_o m \sqrt{1 + \alpha_H^2} \left| \cos\left(\frac{\pi \lambda^2 D p^2 f^2}{c} + \arctan(\alpha_H) \right) \right| \tag{90}$$

There are several cut-off frequencies in the fiber given by,

$$I_f = \frac{c}{2D\lambda^2} \left(1 - \frac{2}{\pi} \arctan(\alpha_H) \right) \tag{91}$$

The expression for the Henry factor is given by,

$$\alpha_H = \tan\left(\frac{\pi}{2} - \frac{\pi \lambda^2 D p^2 f^2}{c} \right) \tag{92}$$

Measurement of the Optical Fiber Dispersion and VCSEL Henry Factor [59]

This test was performed using 60 km SMF-28 optical fiber. The laser source used was a 1.55 µm laser. The chromatic dispersion can be found using the following relation,

$$D = \frac{500c}{f_o^2 L \lambda^2} \tag{93}$$

The measurement of the S21 parameters using a Vectorial Network Analyzer (VNA) is as seen in Figure 20. The first frequency null is seen at 7.522 GHz. From this, the chromatic dispersion is D=17.91 ps/(nm*km).
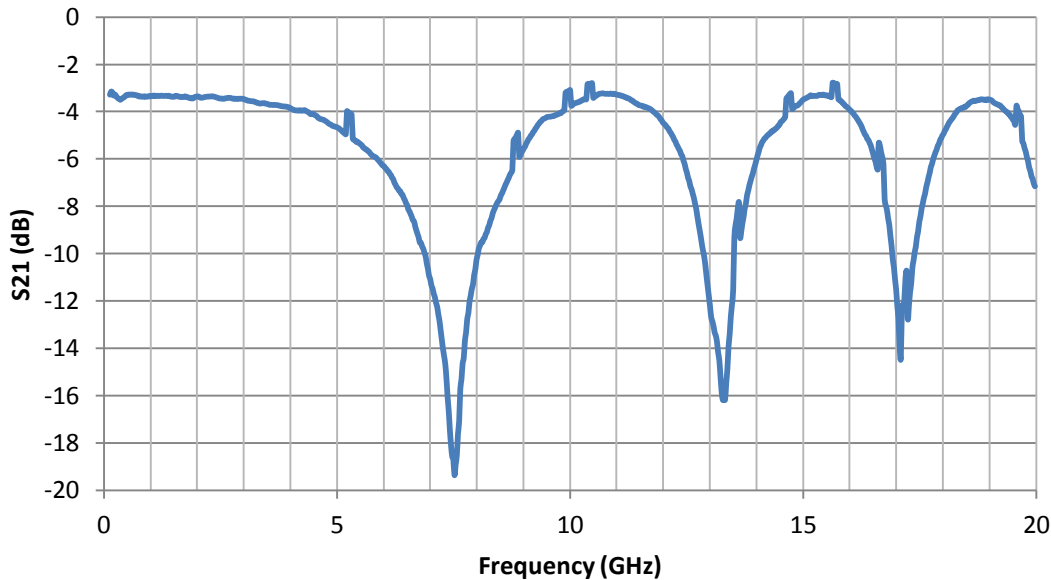
Figure 20 Optical Fiber S21 parameter measurement.

To measure the cut-off frequency taking into account the VCSEL, it was performed a test as described in Figure 21. The direct-modulated VCSEL is used in this second measurement instead of the optical source of the VNA. By comparing the measurement presented in Figure 20 to that one of Figure 22, it is possible to obtain the first cut-off frequency of the VCSEL.
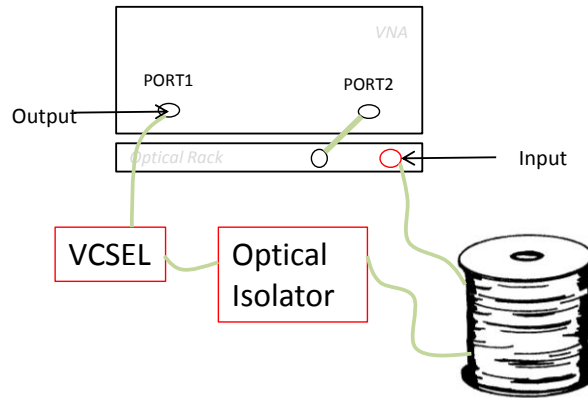
Figure 21 Chromatic dispersion optical fiber measurement.

From this measurement, the S_{21} curve is presented in Figure 22. It is observed that the first cut-off frequency of the 60 km optical fiber using this VCSEL is at 3.16 GHz. It is important to clarify that the null of the S_{21} curve at 1.3 GHz is linked to the resonance frequency of the interface between VCSEL electrical connection and the thermally controlled box due to transmitted electromagnetic interference linked to common grounding of the laser bias and VNA.
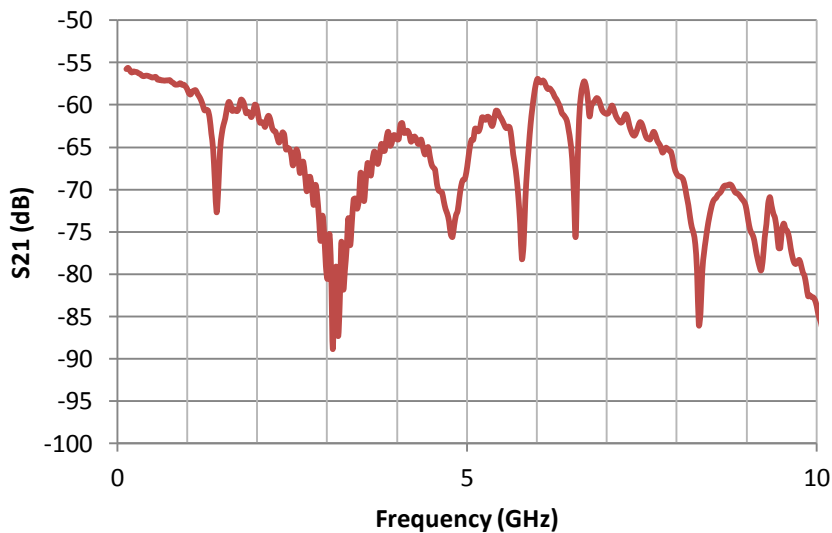
Figure 22 Optical Fiber S21 parameter measurement using a 1.55 um VCSEL.

From this measurement, recalling Equation (92), it is concluded that the Henry factor of the VCSEL is,

$$\alpha_H = 3.5$$

2.3 VCSEL Relative Intensity Noise (RIN)

The Relative Intensity Noise (RIN) of the VCSEL relates the photon density fluctuation to the mean photon square density. The (RIN) is expressed in dB/Hz. The RIN can be expressed as Equation (93). Graphically this could be defined as shown in Figure 23.
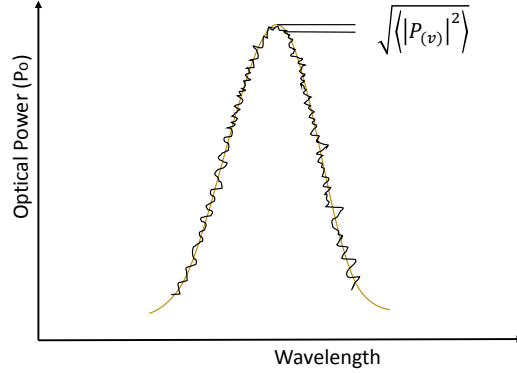
Figure 23 Relative intensity noise graphical explanation.

$$RIN = 2\frac{\langle|\Delta\tilde{S}(v)|^2\rangle}{\langle S\rangle^2} = 2\frac{\langle|\Delta\tilde{P}(v)|^2\rangle}{\langle P\rangle^2} = 2\frac{\langle|\Delta\tilde{I}_{PD}(v)|^2\rangle}{\langle I_{PD}\rangle^2} \tag{93}$$

Where the angular bracket terms correspond to averaged terms measured in an specific period of time. The term $\Delta\tilde{S}(v)$ corresponds to the photon density, $\Delta\tilde{P}(v)$ is the output power and $\Delta\tilde{I}_{PD}(v)$ is the photodetected current. Their mean values are $\langle S\rangle$, $\langle P\rangle$, and $\langle I_{PD}\rangle$. The photon density modulations come from the spontaneous emission process, from this, the current density variations are neglected. The RIN can be expressed in linear way as follows:

$$RIN(v) = \frac{4B_{sp}\Gamma\eta_{w0}}{\tau_{sp,w}\langle S\rangle}\frac{4\pi^2v^2 + \gamma^{*2}}{16\pi^4(v_r^2 - v^2)^2 + 4\pi^2\gamma^2v^2} \tag{94}$$

Where the modified damping factor (γ) is given by,

$$\gamma^* = \gamma - \frac{\varepsilon\langle S\rangle}{\tau_p(1 + \varepsilon\langle S\rangle)} \approx \frac{1}{\chi\tau_{sp,w}} + 4\pi^2v_t^2\tau^2 \tag{95}$$

The term B_{sp} represents the spontaneous emission factor, Γ is the confinement factor, v_r is the resonance frequency, χ is the transport factor, η_w is the quantum well efficiency, and $\tau_{sp,}$ spontaneous emission time constant.

To observe experimentally the behavior of the RIN for 1.3 and 1.5 µm VCSELs, the RIN measure was performed by constructing the setup shown in Figure 24. The VCSEL is biased at different currents and temperatures in order to evaluate the RIN under each condition. The photodetected current is measured at the bias monitoring port of the photodetector and the RF power is acquired from the Electrical Spectrum Analyzer (ESA).
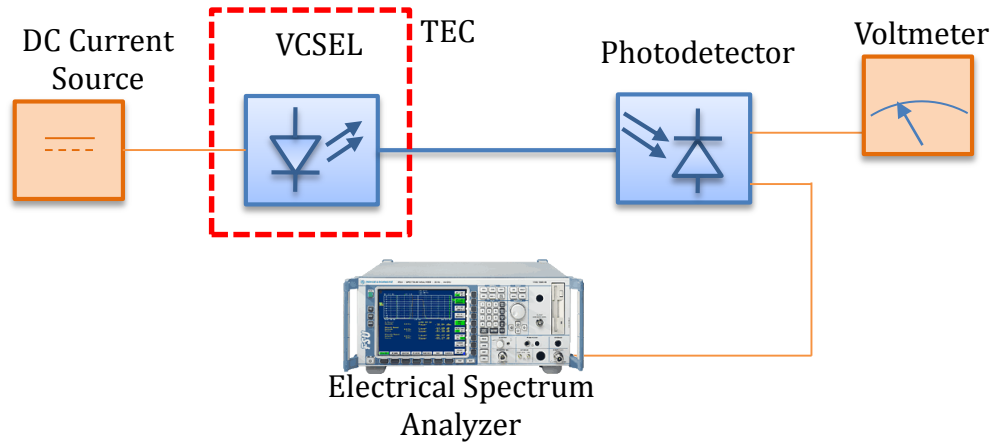
Figure 24 RIN measure setup.

2.3.1   RIN in 1.3 μm VCSEL

The RIN curves for a 1.3 μm VCSEL at 20°C are shown in Figure 25. From this it is seen an evident RIN reduction when the bias current increases. At low bias current, the output power linked to the stimulated emission is relatively low in regard to the spontaneous emission power, for this reason, the RIN is higher at low bias current. When the bias current increases, this trend reverses and the stimulated emission is much greater than the spontaneous emission power, leading to a RIN reduction and curve flattening. The RIN floor is -150 dB/Hz at low frequencies. At 7 mA the resonance peak of the RIN curve is -140 dB/Hz.

It is important to remark from Figure 25 the resonance frequency peak displacement towards higher frequencies. This is explained by the fact that the resonant frequency of a VCSEL can be expressed as,

$$v_r = \frac{1}{2\pi} \sqrt{\frac{\eta_i v_{gr} \Gamma a}{q V_p}} \sqrt{I - I_{th}} \tag{96}$$

Where, η_i is the VCSEL efficiency, v_{gr} is the group velocity, a is differential gain factor, q is the electron charge, V_p is the photon volume, I_{th} is the threshold current, and I is the biasing current. From Equation (24) it is possible to conclude that $v_r \propto I$.
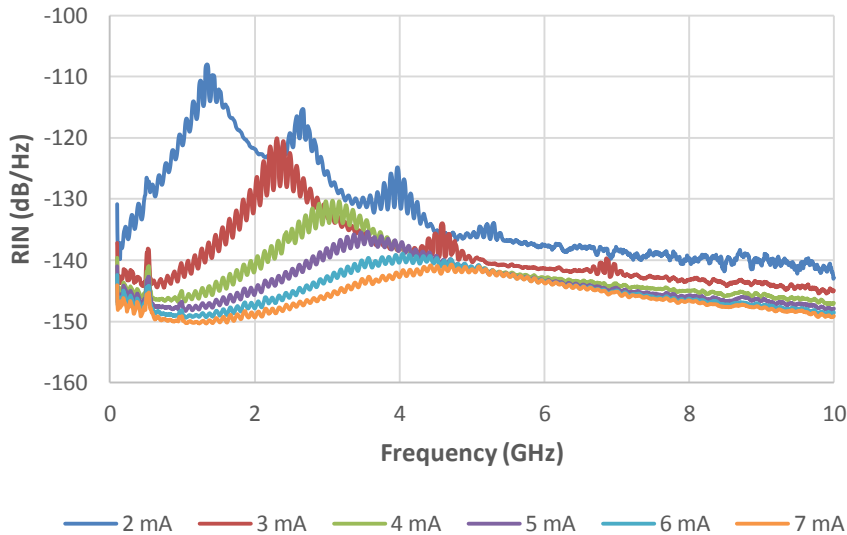
Figure 25 RIN measure results at 20°C.

The resonance frequency of the VCSEL as a function of the bias current is presented in Figure 26. Here it is observed the proportional relation between the bias current and the VCSEL resonance frequency. The slope of the linearization for this measure is 659 MHz/mA. It is important for direct modulation purpose to know the RIN of a VCSEL and its resonance peak have taking into account its influence on the oscillator noise when the VCSEL is under modulation.

$$fr = 0,659I + 0,247$$
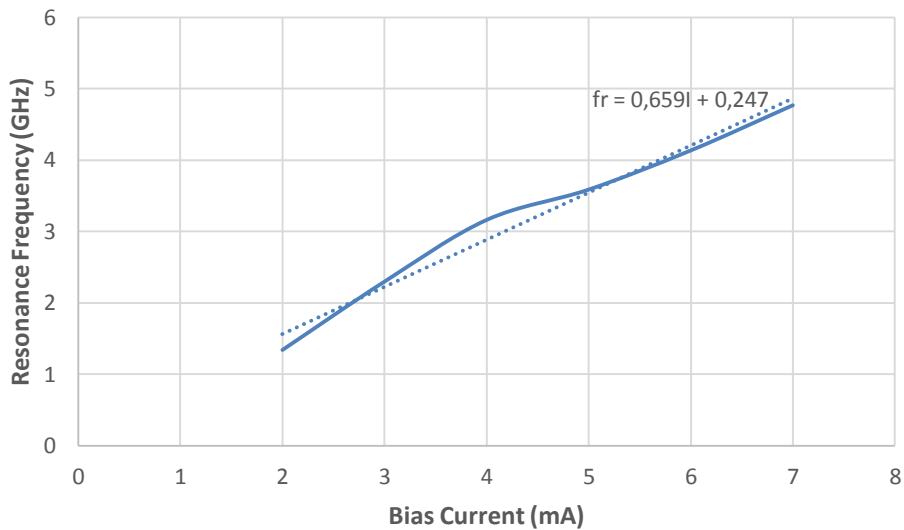
Figure 26 VCSEL RIN resonance frequency vs bias current.

Regarding to the temperature effects over the RIN, it was performed a test varying the VCSEL temperature from 15°C to 35°C at different currents. These results are presented in Figure 27.
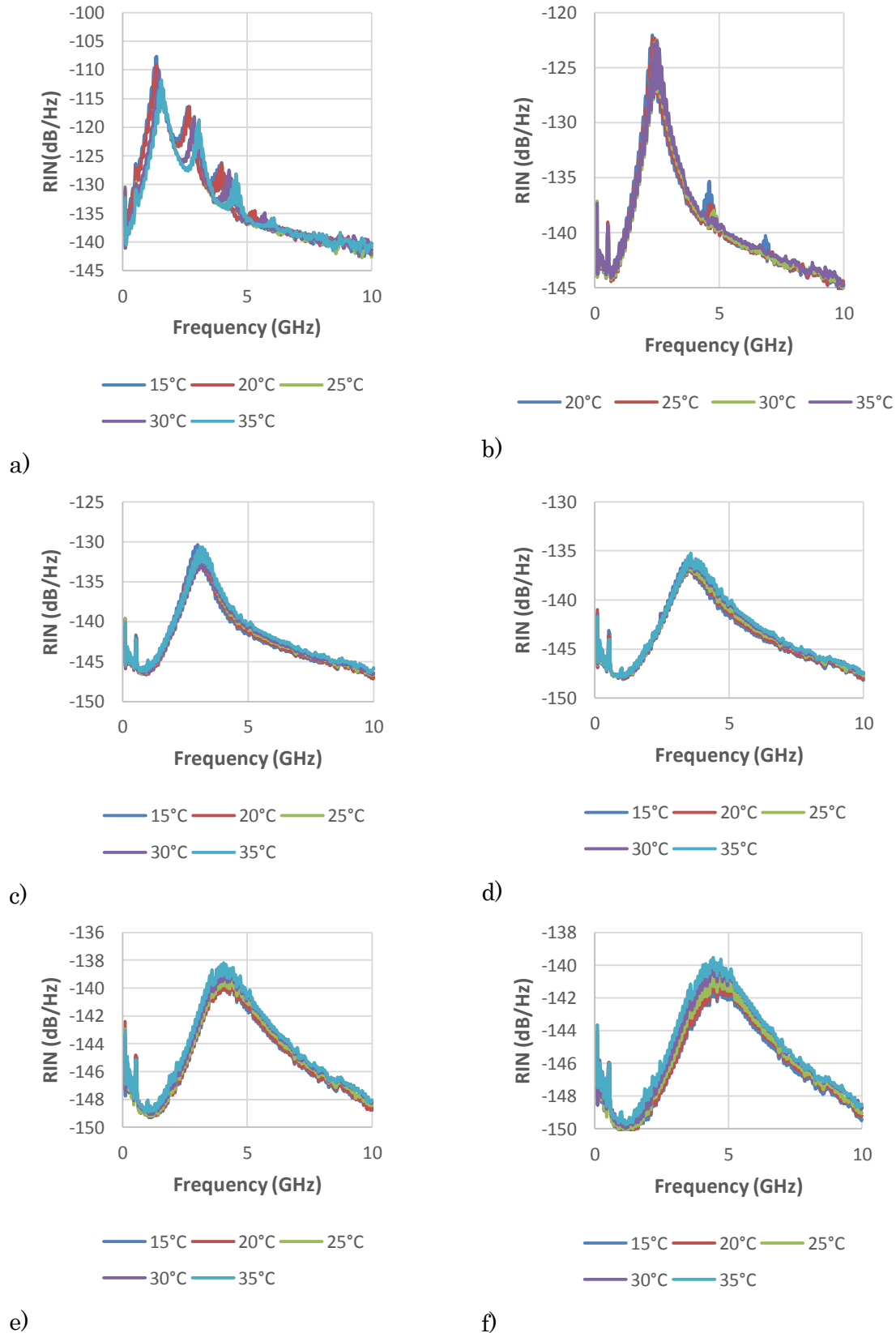
Figure 27 RIN curves for 1.3 um VCSEL at several temperatures biased at : a) 2mA b) 3 mA c) 4 mA d) 5 mA e) 6 mA f) 7 mA

From Figure 27, it is possible to conclude that the RIN of the VCSEL does not drift dramatically due to the temperature variation, at least for the measurements performed in this frequency range. The resonance frequency does not seem to drift with the temperature variation. For the Figure 27a, it is observed a strong influence of temperature

in the RIN, this is attributed to the mode competition inside the VCSEL cavity and the thermal expansion of the cavity. Analyzing these curves at an specific frequency and bias point, the RIN value is very stable, for instance, at 2.49 GHz measuring the RIN for bias current from 2 to 7 mA is plotted in Figure 28. Table 6 presents the RIN drift value for each bias current extracted from Figure 28. The higher magnitude slope value corresponds to those at lower bias currents; the slope becomes negative of some tenths of dB.
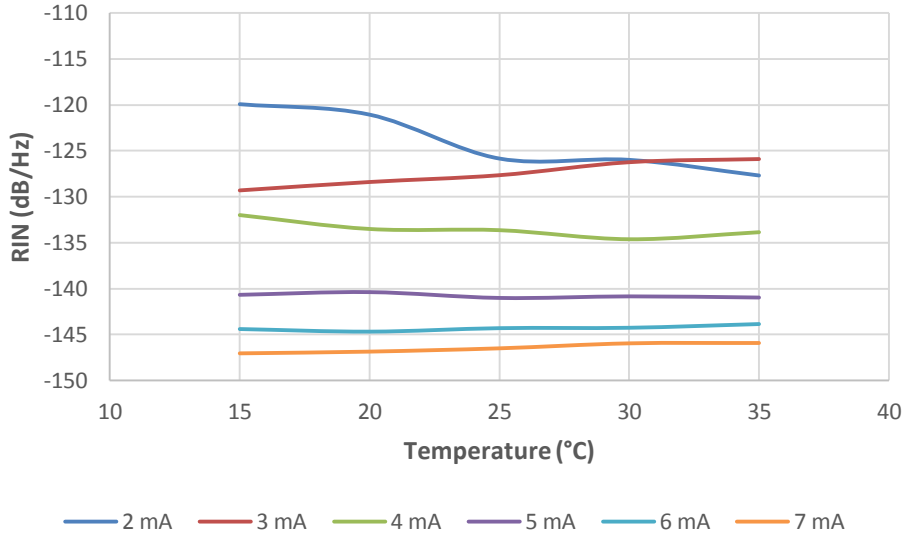
Figure 28 RIN at 2.49 GHz at several bias current for different operation temperature.

Bias Current	Slope (dB/Hz)/°C
2 mA	-0.409
3 mA	0.180
4 mA	-0.097
5 mA	-0.021
6 mA	-0.030
7 mA	-0.063

Table 6 RIN slope at 2.49 GHz for different bias currents.

2.3.2 RIN in 1.5 µm VCSEL

The 1.5 µm VCSEL RIN measure was performed in same temperature range (15 to 35°C). The RIN measure results at 20°C are shown in Figure 29. In this figure it is possible to observe the same trend as the 1.3 µm VCSEL. The higher the bias current, lower the RIN.
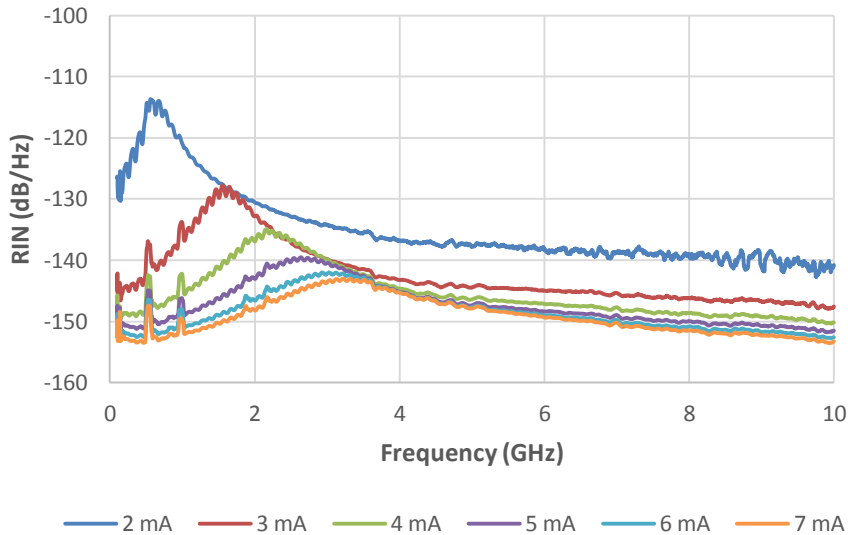
Figure 29 1.5 um VCSEL RIN at 20°C for several bias currents.

The resonance peak presents a frequency shift as the bias current increases. Figure 30 presents this trend for the 1.5 µm VCSEL. The resonance peak varies from 0.62 GHz up to 3.45 GHz.
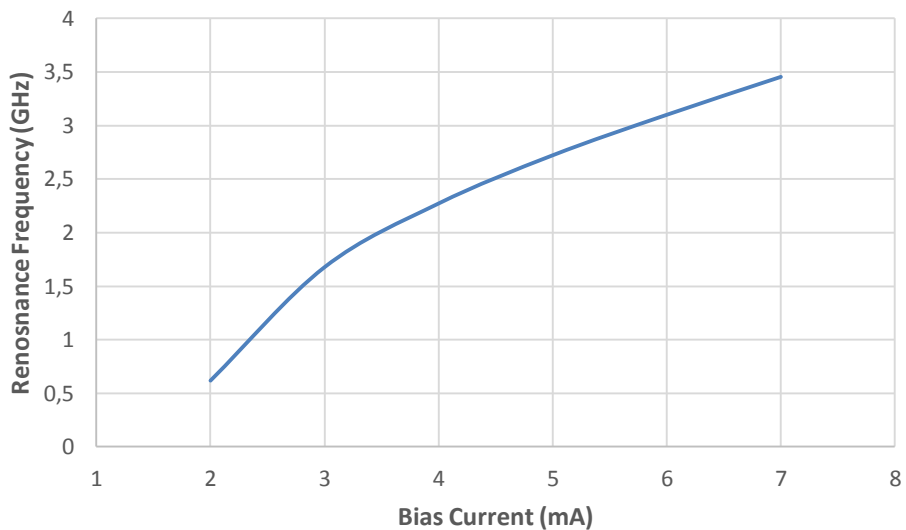
Figure 30 RIN resonance peak vs bias current for 1.5 µm VCSEL.

To observe the thermal stability of the RIN, it was performed a RIN measurement for a fixed bias current and several temperatures, the results are shown in Figure 31.
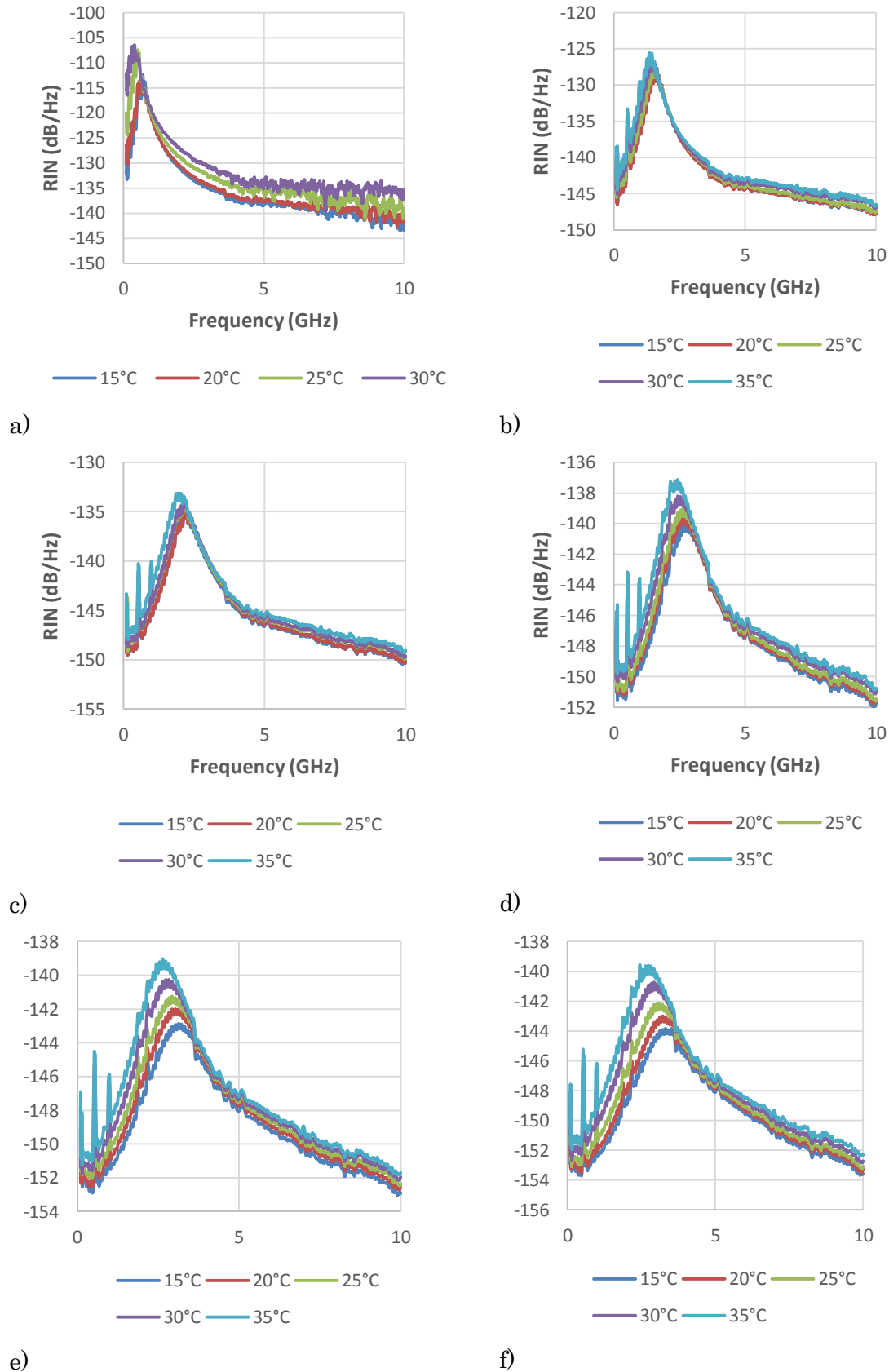
Figure 31 1.5 µm VCSEL RIN for different temperatures. a) 2 mA b) 3 mA c) 4 mA d) 5 mA e) 6 mA f) 7 mA.

From Figure 31 it is inferred that the RIN is enhanced when the bias current is increased. This behavior is explained through the definition of a strong dominant mode at higher bias current that reduces the carrier availability for spontaneous emission of the laser. To

analyze this in more detail, it is presented the RIN value at 2.49 GHz at different currents and temperatures in order to compute the slope of each condition. This is shown in Figure 32. For low current, the RIN is more sensitive to temperature variations, with a drift of 1.339 dB/Hz/°C, this because of the relatively low stimulated emission in comparison to the spontaneous emission, there is a mode competition inside the laser cavity at this bias current that makes the laser optically noisy. For higher currents the increase in RIN is also observed but the slope is smaller than in the low bias current case. Those values are shown in Table 7.
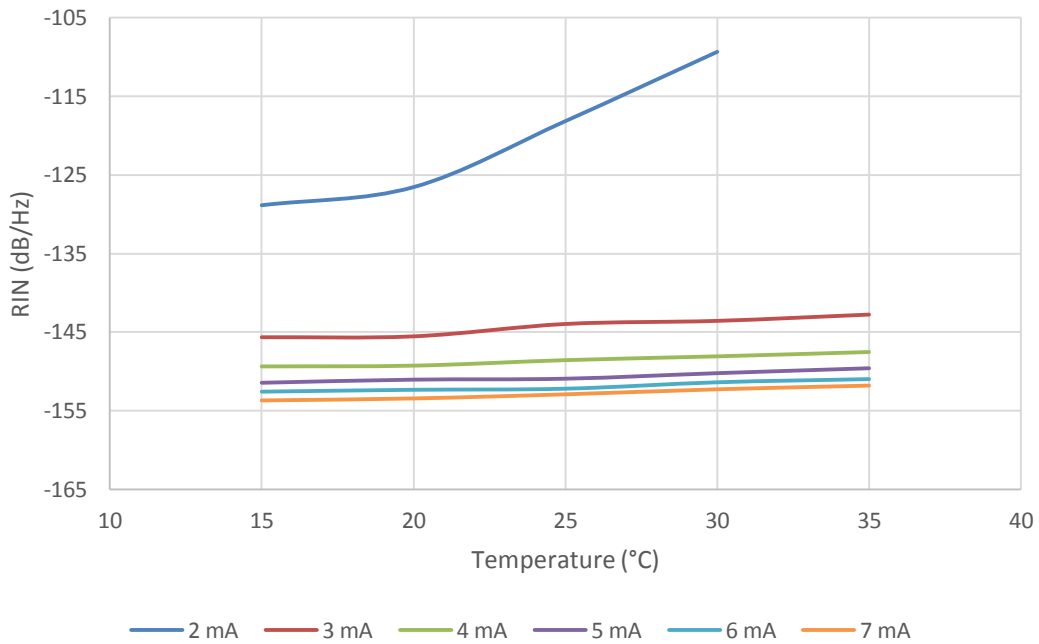
Figure 32 1.5 µm VCSEL RIN at 2.49 GHz for different bias current and temperature.

Bias Current	Slope (dB/Hz)/°C
2 mA	1.339
3 mA	0.155
4 mA	0.097
5 mA	0.090
6 mA	0.083
7 mA	0.099

Table 7 1.5 µm VCSEL RIN slope for different currents varying the temperature.

2.3.3   RIN and Optical Fiber Influence

With the aim to implement the VBO, a characterization of the RIN and its variation when the VCSEL is connected to different optical fiber lengths is performed. This is described in Figure 33. The VCSEL is biased at 7 mA and the optical fiber length is varied from 100 m to 25 km.

The results of this measure are presented in Figure 34. From this Figure it can be inferred that the RIN measured at the end of the optical fiber is degraded with respect to the non-fibered VCSEL due to the existence of other noise phenomena linked to the optical fiber (connector reflections, thermal lensing, fiber bending, etc) that are added to the measurement and not for a Change in the RIN characteristic of the VCSEL. The VCSEL RIN remains the same independently of the optical fiber length.
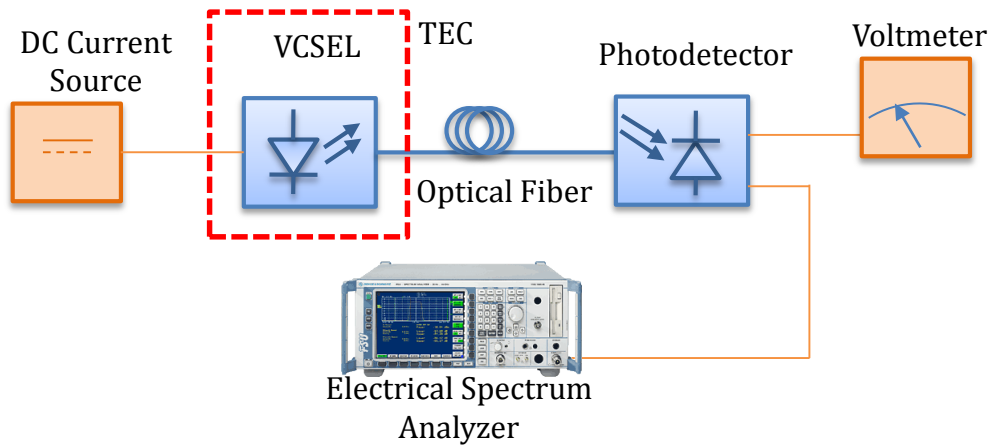
Figure 33 1.5 µm VCSEL RIN measurement varying the optical fiber length.
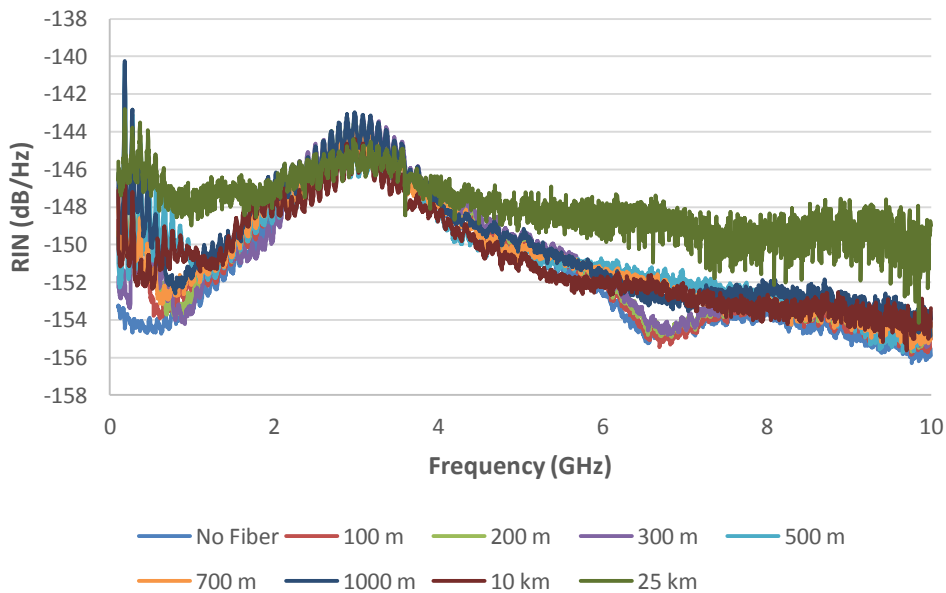
Figure 34 1.5 µm VCSEL RIN while varying the optical fiber length measure results.

2.3.4   RIN comparison between 1.3 and 1.5 µm VCSEL

Comparing the RIN measurements between the two VCSELs, it is observed that in both cases the RIN is reduced and the curve is flattened as the bias current is increased. Figure 35 presents the RIN curves for both laser wavelengths at several bias points.
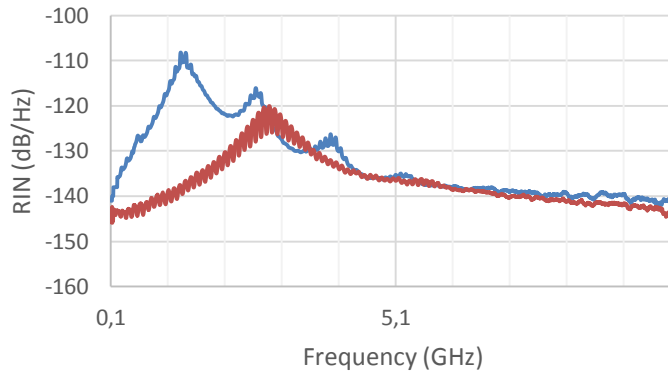
a)
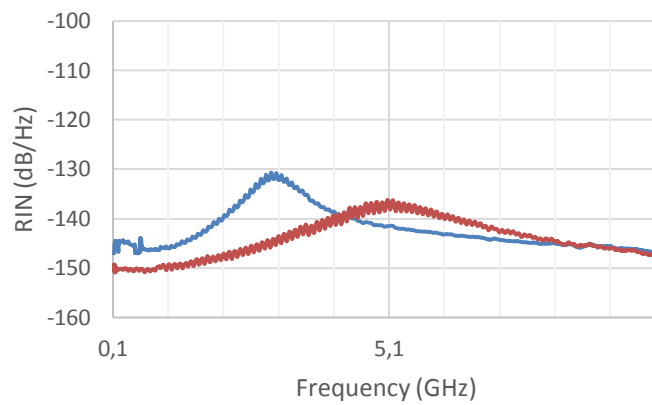
b)
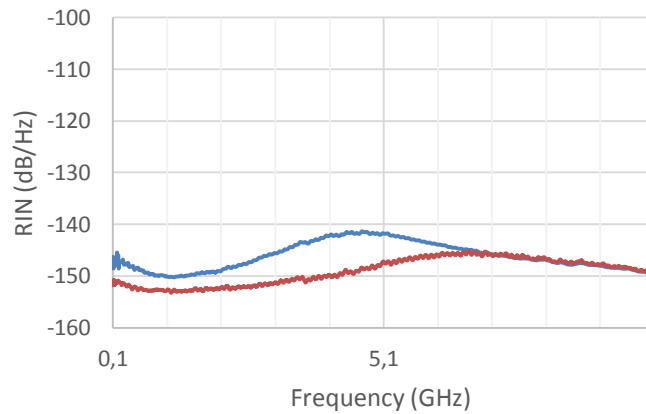
c)

Figure 35 RIN measurements for 1300 and 1500 nm VCSELs at a) 2Ith b) 4 Ith c) 7 Ith.

The relaxation frequency peak moves towards higher frequencies as the bias current is increased. The relaxation frequency peak is defined as follows [33],

$$f_r = \frac{1}{2\pi}\sqrt{\frac{\eta_I v_{gr}\Gamma_r \bar{a}}{qV_p}}\sqrt{I - I_{th}} = M_r\sqrt{I - I_{th}}$$

Where, η_I is the injection efficiency, v_{gr} is the group velocity, Γ_r is the confinement factor, q is the electron charge, V_P is the cavity volume and M_r is known as the modulation response of the laser.

As figure-of-merit, the modulation current efficiency factor (MCEF) is given to specify the increase of 3 dB corner frequency of VCSEL transfer function. This is expressed as follows,

$$MCEF = \frac{f_{r3dB}}{\sqrt{I - I_{th}}}$$

Where f_{r3dB} is the frequency 3 dB below the RIN peak. According to Iga [33], the factors M_r and $MCEF$ are related as,

$$MCEF \approx 1.55 M_r$$

Generally, the $MCEF$ value is used instead of M_r due to the ease of measure the f_{r3dB} directly from the RIN curve. These values are shown in Figure 36. The MCEF enhances as the current increases.
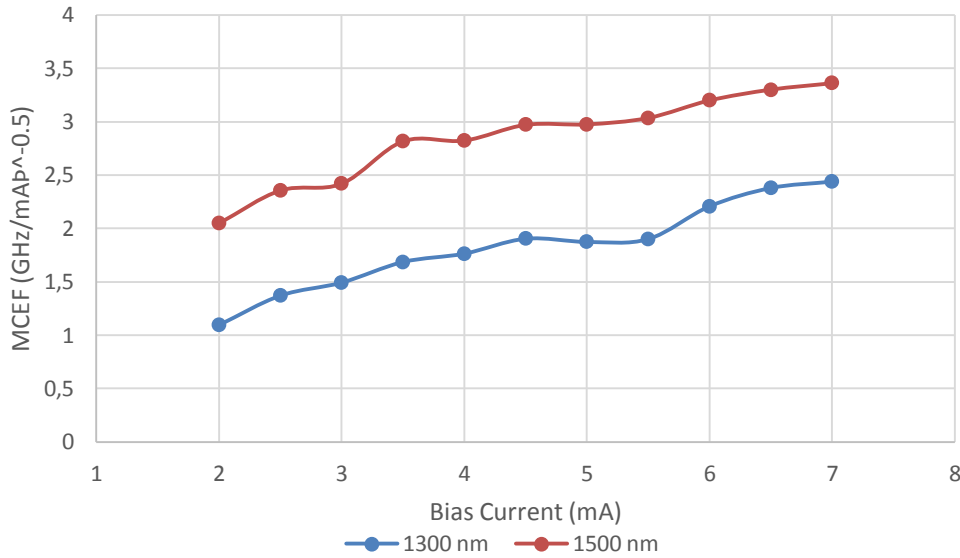
Figure 36 MCEF for 1300 and 1500 nm VCSELs.

The relaxation frequency of the RIN VCSEL measurement for each bias current is shown in Figure 37.
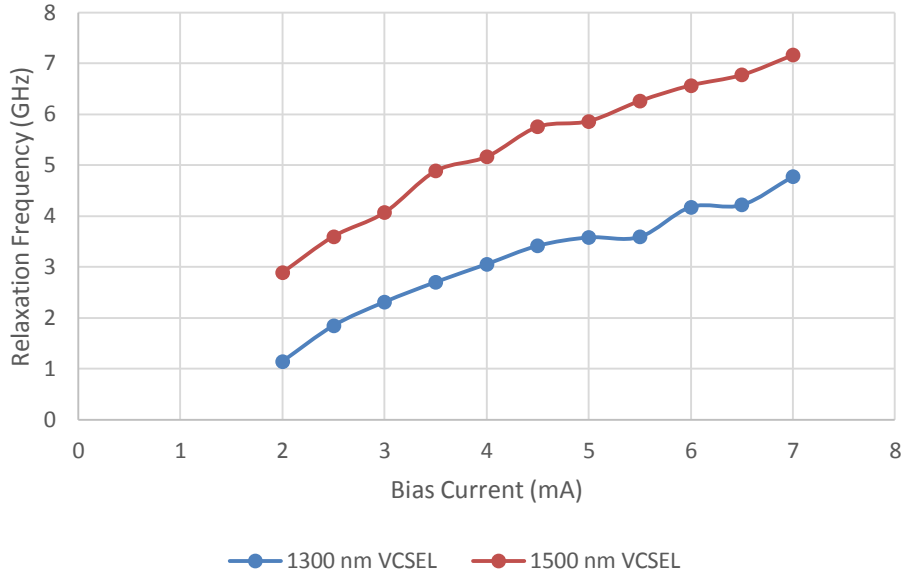
Figure 37 RIN frequency peak for 1300 and 1500 nm VCSELs.

With the purpose to implement the 2.49 GHz VBO, it is important to focus on the RIN at this frequency in order compare the performance of the two VCSELs and their contribution to the oscillator phase noise. Figure 38 presents this characteristic. The RIN of the 1500 nm VCSEL is lower than the 1300 nm one. At 2.49 GHz the RIN is enhanced in 27 dB for the 1300 nm VCSEL when the bias current is augmented from 2 to 7 mA. For the 1500 nm VCSEL the RIN is enhanced in 25 dB at the end of the bias current sweep. The hypothesis here is that a reduction in the RIN will be reflected in the enhancement of the optoelectronic oscillator frequency stability as a reduction of the phase noise. From this, it is expected to have lower phase noise using the 1500 nm VCSEL in the VBO.
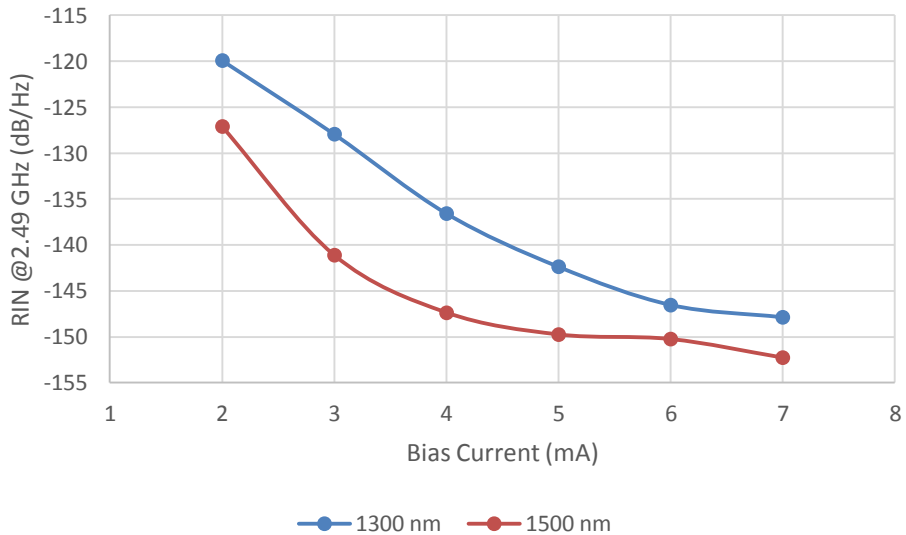
Figure 38 RIN of the 1300 and 1500 nm VCSELs at 2.49 GHz.

2.4 RayCan VCSEL Frequency Response [60]

The direct modulation frequency response of the VCSEL is a very important performance parameter for the purpose of this thesis. In fact, the VBO results presented throughout this thesis will be obtained by the direct current intensity modulation of the VCSEL by using a bias tee. From the frequency response curve is possible to find the effective bandwidth of a specific VCSEL in order to be used in the VBO.

To express the optical power output of the VCSEL, P_{VCSEL}, it is important to take into account the VCSEL cut-off frequency, this means, the highest frequency at which the VCSEL can be modulated. This can be modelled as the VCSEL transfer function, H_{VCSEL}, that is expressed as:

$$H_{VCSEL} = \frac{\omega_R^2}{\omega_R^2 - \omega^2 + j\omega\gamma}$$ (97)

Where, ω^2 is the resonance frequency and γ is the damping factor.
Additionally, it is possible to express the VCSEL power, P_{VCSEL} at the optical fiber input as follows,

$$P_{VCSEL} = P_o + P_{RF}$$ (98)

Where P_o is given by,

$$P_o = \eta_d * h * v * (I_{bias} - I_{threshold}) + \eta_d * \eta_{spontaneous} * \beta * h * v * I_{Threshold}$$ (99)

P_{RF} is obtained from,

$$\frac{P_{RF}}{i_{RF}} = \eta_d * h * v * H_{VCSEL}(\omega)$$ (100)

Where, η_d represents the quantum efficiency, $\eta_{spontaneous}$ represents the spontaneous emission efficiency, β is the spontaneous emission factor, h is the Planck's constant and v is the emission frequency of the laser. The RF current is linked to the oscillating signal as follows,

$$I_{RF} = \frac{V_{RF}(\omega)}{R_d}$$ (101)

Where, R_d is the dynamic resistance of the VCSEL.

To measure the frequency response of the VCSEL (transfer function), $H_{VCSEL}(\omega)$, a VNA and a high speed photodetector are used. The implemented setup description is shown in Figure 39. The VCSEL is directly modulated through a bias tee and the laser output is received by the high-speed photodetector.
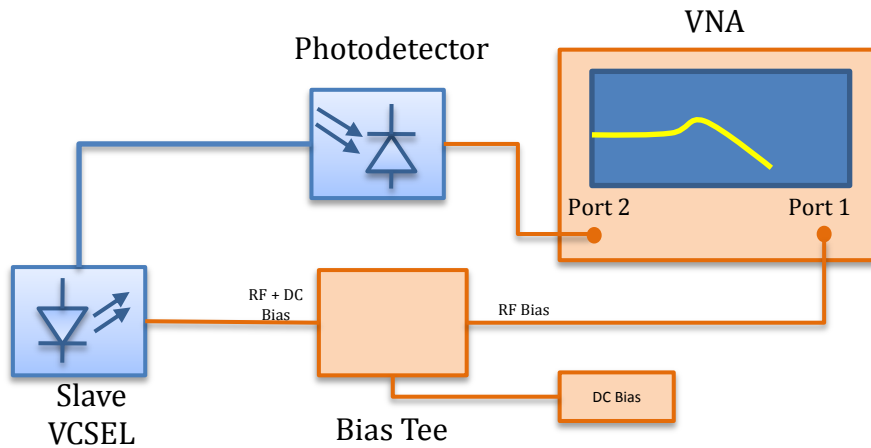
Figure 39 VCSEL frequency response measurement setup.

The extraction of the frequency response was performed by applying the technique described by Hayat [5]. This consists in the measurement of the S_{21} parameter well above the threshold current and from this measurement it is subtracted the measurement of the S_{21} parameter just above the threshold current. Using this method, most of the parasitic of the measurement linked to the input electrical connection are removed.

To model the VCSEL frequency response, a circuit-based model of the VCSEL is simulated inspired in that one proposed by Rissons [61]. This model translates the physical phenomena inside the VCSEL into electrical scheme, as shown in Figure 40. The electrical model of the active zone of the VCSEL is defined as R_j corresponding to the junction resistance and C_j corresponding to the junction capacitance. The photons reservoir and resonance damping are modelled through C_o and L_o, respectively. The circuit parameters are found by iteration and comparison with the actual measurement. The circuit parameters for the first iteration are computed for a second order Tchebycheff low pass microwave filter.
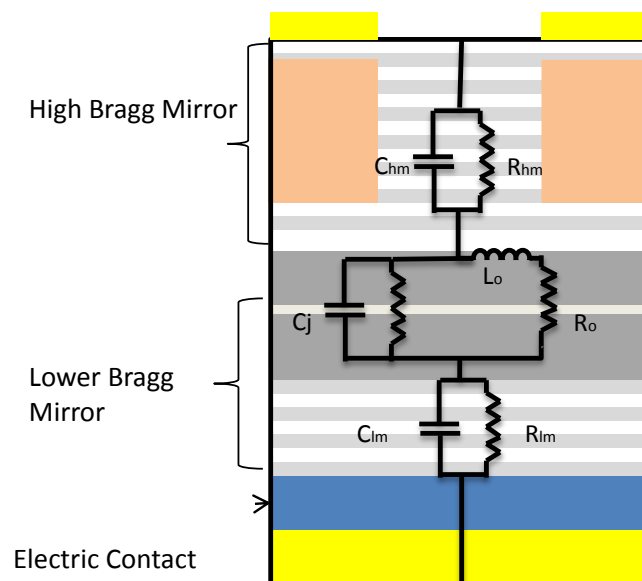
Figure 40 Electrical equivalent scheme of VCSEL.

The circuit model of the VCSEL has been implemented in the simulation software Advanced Design Systems (ADS), the circuit model implementation is presented in Figure 41.
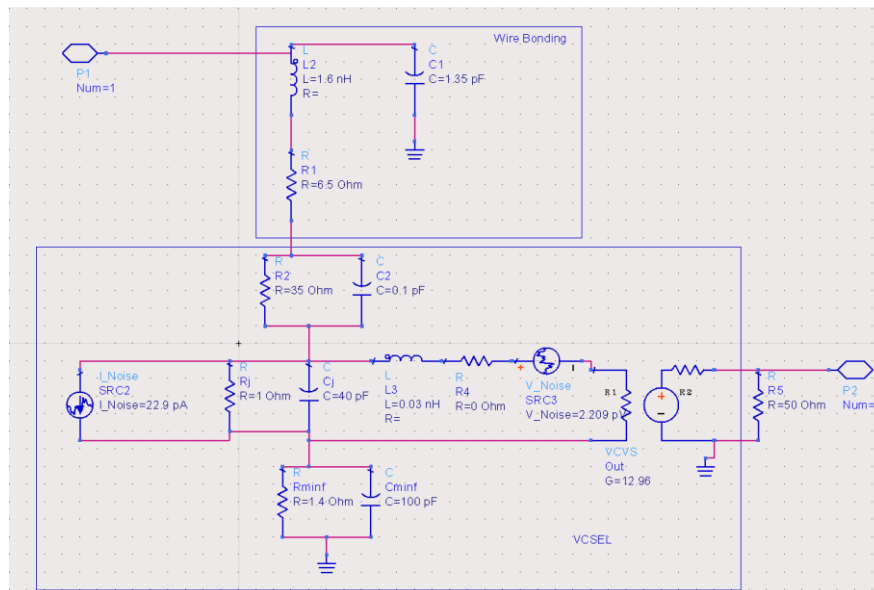
Figure 41 VCSEL circuit model

The VCSEL measured and simulated frequency are shown in Figure 42. For this characterization, the measurements and simulations were performed at 3, 5 and 7 mA. Table 8 summarizes the circuit parameters for each current.

Bias Current (mA)	R_{hm} (Ω)	C_{hm} (pF)	R_{lm} (Ω)	C_{lm} (pF)	R_j (Ω)	C_j (pF)	R_o (Ω)	C_o (pF)
3	35	0.1	1.4	100	1	145	0.03	0
5	35	0.1	1.4	100	1	40	0.03	0
7	35	0.1	1.4	100	1	30	0.03	0

Table 8 VCSEL equivalent circuit model parameters.

The VCSEL frequency response measured and simulated are plotted in Figure 42. The VCSEL direct modulation bandwidth increases as the bias current does, at 3 mA bias the VCSEL direct modulation bandwidth is 3.5 GHz and for 7 mA it is 4.8 GHz. For this reason, the frequency response of the VCSEL is not good enough to be modulated inside an optoelectronic oscillator taking into account that the Barkhausen gain condition must be satisfied at frequencies higher than 5 GHz. From this Figure, it is inferred that the VCSEL circuit model agrees well with the measurements carried out. In the same way, the damping slopes correspond to 20 dB/decade of the Tchebycheff second order low pass filter. The dips in the frequency response of the VCSEL are caused by the impedance mismatching between the connection pins and the laser package, these dips occurs always at the same frequency for all measures. The impedance mismatching that is present in Figure 16 is undesired. A non-packaged VCSEL frequency response exhibits a curve behavior similar to the simulated lines. Figure 43 presents a VCSEL frequency response curve measured by Bacou [38].

BW=3,5 GHz

Simulation   Measurement

a)

BW= 4,4 GHz

Simulated   Measured

b)

BW=4,8 GHz
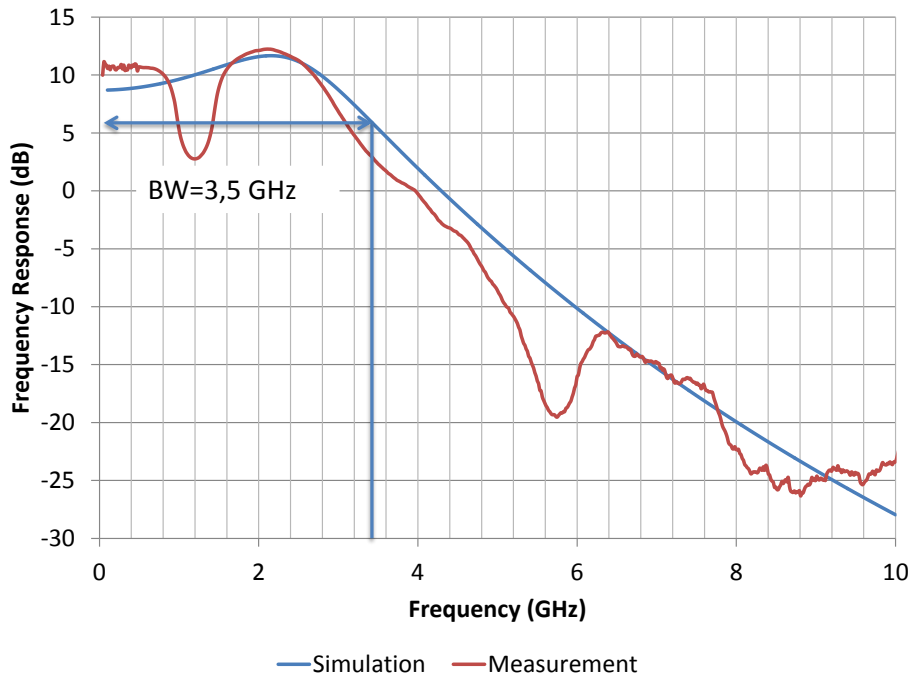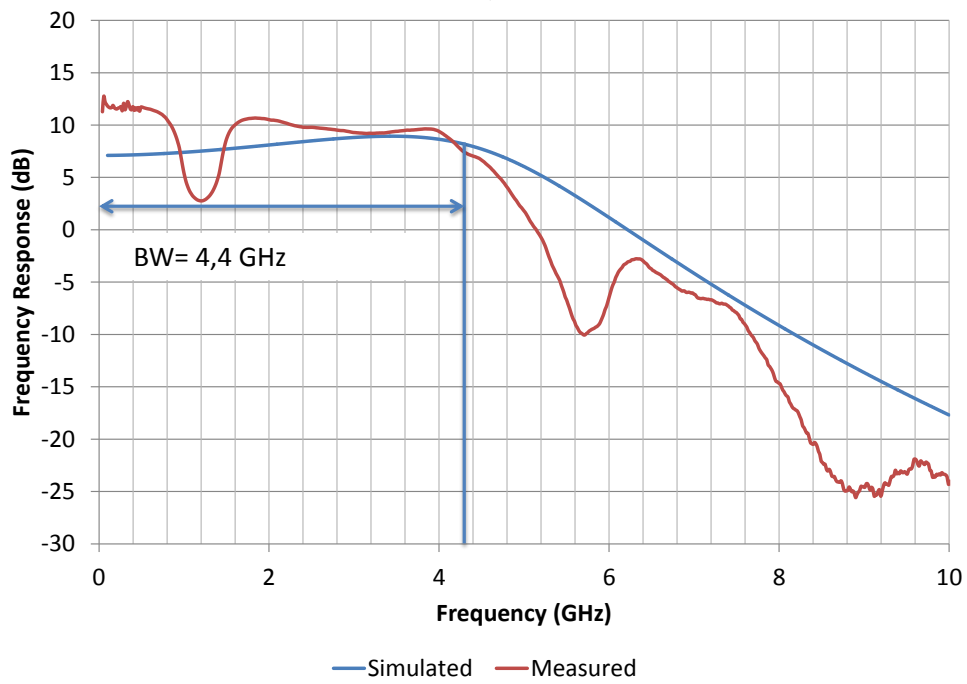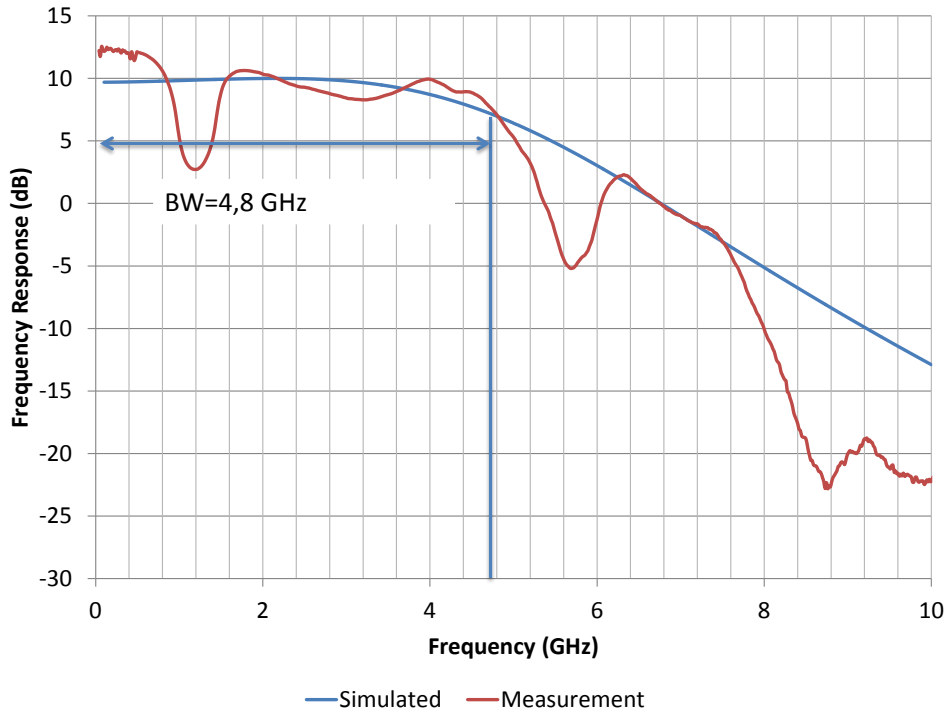
c)

Figure 42 RayCan VCSEL free running frequency response and VCSEL circuit model simulated in ADS at a) 3 mA b) 5 mA c) 7 mA.
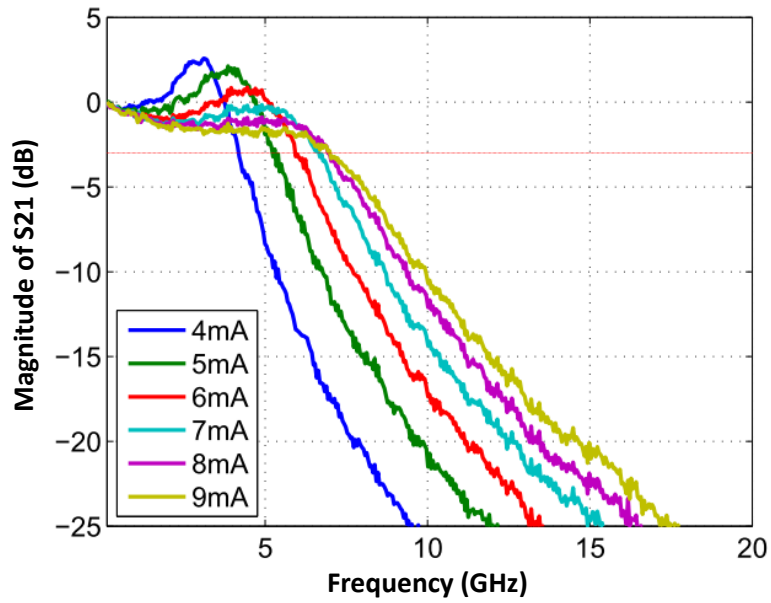
Figure 43 On chip VCSEL frequency response curve, taken from [38]*.*

Conclusion

Two single mode Vertical Cavity Surface Emitting Lasers (VCSELs) are characterized in terms of the optical spectrum, DC performance, direct modulation bandwidth and Relative Intensity Noise.

From the optical spectrum of the VCSEL, it is observed a single mode performance with a high Side Mode Suppression Ratio (SMSR) that is higher than 30 dB. The power versus current characteristic have shown the low power emission of the VCSELs (<1mW) for biasing current lower than 9 mA. The purpose of the use of VCSELs is to implement a low power consumption light source in the optoelectronic oscillator, this has been confirmed through these measurements.

The Relative Intensity Noise of the VCSELs measure is performed in order to characterize the noise properties of the optical source. Results show that VCSEL operating at a current higher that 5 mA (in the laser diode linear zone) exhibits low RIN values. The RIN resonance peak curve varies proportionally according to the bias current. It is necessary to find a trade-off between the RIN curve resonance peak and the bias point in order to modulate the VCSEL in a low RIN point of the curve. The 1.5 µm VCSEL exhibits lower RIN than the 1.3 µm laser. From the performed analysis in this work, this is explained by manufacturing process differences that are beyond the scope of this document.

The frequency response of the VCSELs is characterized in order to assure a good performance of the VCSEL when it is directly modulated. The VCSELs used have a low cut-off frequency, up to 6 GHz in the best of the measurements; this is explained by the fact that the laser carriers cannot follow the modulating signal due to its high frequency. The VCSEL frequency response is modeled by using an electrical circuit model implemented in ADS. It is evidenced that the VCSEL package used in these measurements presents impedance mismatching than introduces perturbations in the frequency response curves, anyway, these perturbations are not located at frequencies at which the VBO is going to be implemented. The RIN curves are not affected by the package neither the DC performance is affected.

Chapter 3

Long Wavelength VCSEL Based Optoelectronic Oscillator

Introduction

The VCSEL Based Optoelectronic Oscillator (VBO) was presented in 2008 [3], [62], [63] as a modification of the Optoelectronic Oscillator (OEO) presented by Yao and Maleki [2] in the middle 90's. The VBO is an OEO using a directly modulated VCSEL. A theoretical and experimental approach of the VBO will be presented in this chapter taking into account the effects in the frequency response, optical fiber length and the temperature. The use of last generation VCSELs used in the VBO leads to an enhancement in frequency stability of the system.

3.1   VCSEL Based Optoelectronic Oscillator (VBO)

The VCSEL Based Optoelectronic Oscillator (VBO) is a closed loop oscillator topology using a VCSEL as an optical source. The advantage of using a VCSEL is linked to its reduced power consumption and lower cost compared to other laser sources, especially when board systems are foreseen.

For this oscillator, the VCSEL will be directly modulated instead of being modulated with an external Mach-Zender modulator (MZM). The direct modulation permits the size and cost reduction of the system as well as the power consumption.

The oscillator loop is composed by a VCSEL, an optical fiber that acts as a delay line, a photodetector to transform the optical signal into electrical domain, a band pass filter tuned at the oscillator carrier frequency and a microwave amplifier. The operation principle of the VBO is the conversion of an optical wave into electrical microwave, then, this signal is filtered, amplified and fed back to the electrical access of the VCSEL to create a self-kept oscillation. The VBO scheme is shown in Figure 44.
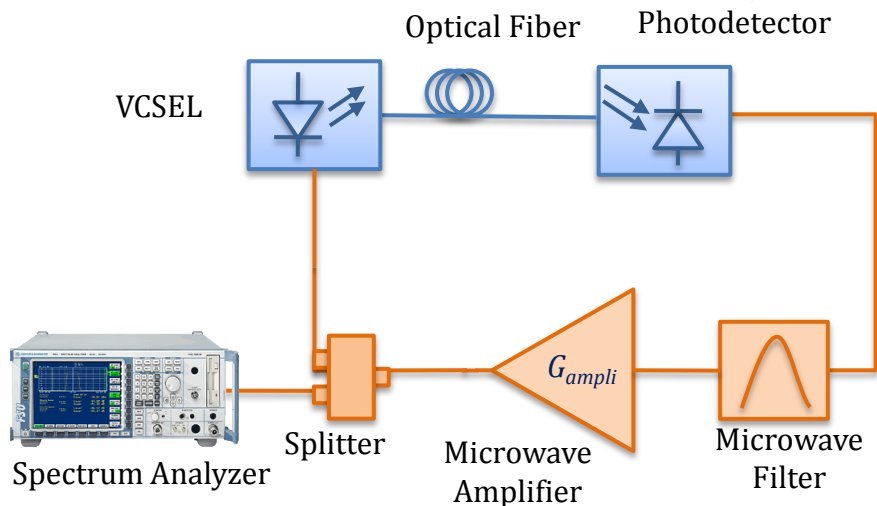
Figure 44 VCSEL Based Optoelectronic Oscillator.

3.1.1   VCSEL Based Optoelectronic Oscillator Open Loop Analysis

To analyze the VBO in open loop, it is going to be considered the link between the laser and the photodetector. After this, an expression for the microwave filter and amplifier will be shown. The VBO open loop schematic is shown in Figure 45.
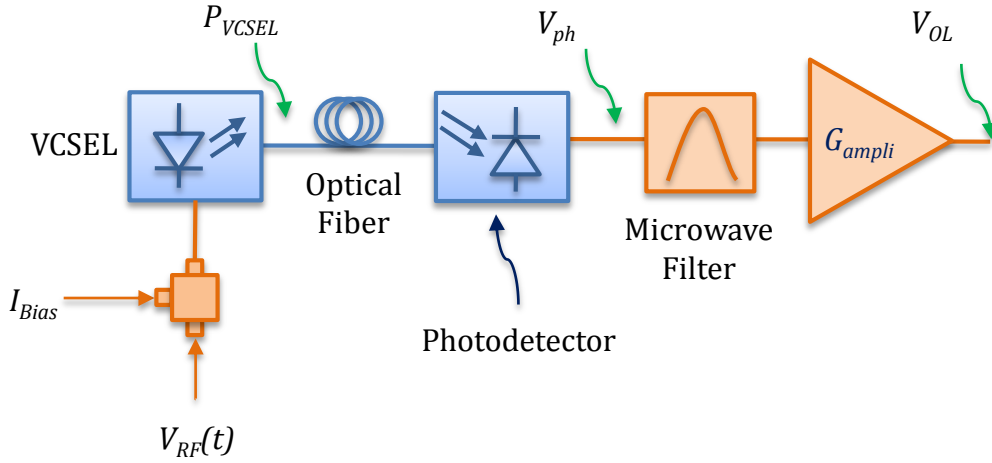
Figure 45 Open loop VBO.

Optical Signal Detection and Filtering

Assuming a VCSEL with a sinusoidal waveform, of the form,

$$V_{RF}(t) = V_A \sin(\omega_O t + \phi) \qquad (102)$$

It is possible to compute the photodetected current $\tilde{V}_{ph}$,

$$\tilde{V}_{ph} = \tilde{\alpha}_o P_{VCSEL} |H_{VCSEL}(\omega_o)| \tilde{S} R_{ph} \qquad (103)$$

$$\tilde{V}_{ph} = \tilde{\alpha}_o \tilde{S} R_{ph} \left(P_o + \eta_d h \nu \frac{V_A \sin(\omega_O t + \phi)}{R_d} |H_{VCSEL}(\omega_o)| \right) \qquad (104)$$

Where,

- R_d is the dynamic resistance of the VCSEL
- R_{ph} is the photodetector load resistance
- $\tilde{\alpha}_o$ represents the optical losses inside the loop ($\tilde{\alpha}_o = \alpha_o e^{-j\omega\tau_d}$) where τ_d is the optical delay time.
- $\tilde{S} = S e^{-j\omega\phi_s}$ that represents the photodetector responsivity.

Once the electrical signal is recovered by the photodetector, this signal is filtered and amplified, so the signal V_{OL} at the open loop output is given by:

$$V_{OL} = \tilde{\alpha}_E \tilde{G}_{ampli} \tilde{\alpha}_o \tilde{S} R_{ph} \tilde{F} \quad h\nu \frac{V_A \sin(\omega_O t + \phi)}{R_d} |H_{VCSEL}(\omega_o)| \qquad (105)$$

Where,
- $\tilde{\alpha}_E = \alpha_E e^{j\phi_E}$ represents the electrical losses inside the system.
- $\tilde{G}_{ampli} = G_{ampli} e^{j\phi_G}$ represents the voltage gain of the amplifier taking into account its phase shift.
- $\tilde{F} = F e^{j\phi_F}$ represents the voltage gain of the microwave filter.

From this it is possible to define the open loop gain as,

$$\tilde{V}_{OL} = \tilde{G}_{OL} V_{RF}(t) \qquad (106)$$

And $\tilde{G}_{OL}$ is given by,

$$G_{OL}(\omega_o) = \tilde{\alpha}_E \tilde{G}_{ampli} \tilde{\alpha}_o \check{S} R_{ph} \tilde{F} h\nu \frac{1}{R_d} |H_{VCSEL}(\omega_o)| \tag{107}$$

VCSEL Based Optoelectronic Oscillator Open Loop Frequency Response

The VBO open loop frequency response is simulated to assure the compliance to the Barkhausen gain condition ($G_{open\ loop} = 1$). To implement this simulation, each element of the optoelectronic oscillator is modelled in ADS according to their specifications. The VCSEL circuit model shown previously is used for this simulation. The ADS sketch is shown in Figure 46.
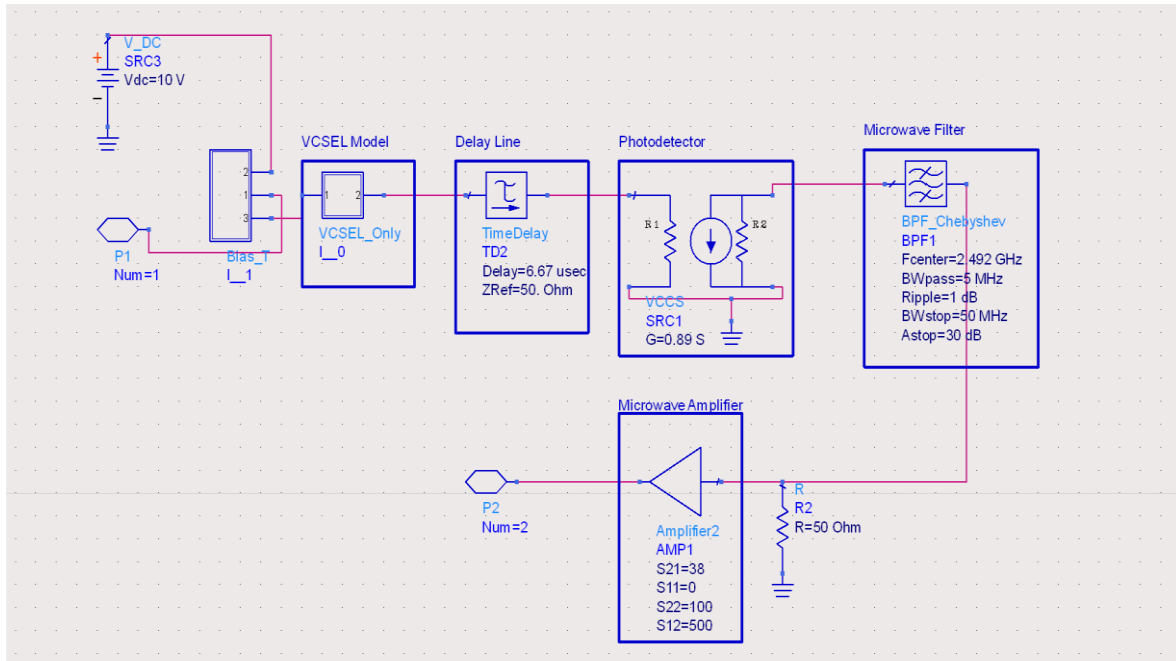
Figure 46 VCSEL based optoelectronic oscillator open loop sketch in ADS.

The open loop frequency response of the VBO at 2.49 GHz in shown in Figure 47. The gain curve confirms that the Barkhausen gain condition is accomplished (G=0 dB). The Oscilation side modes in the gain curve correspond to the free spectral range (FSR) of the oscillator caused by the traveling wave inside the optical fiber, those are spaced by a frequency that corresponds to the inverse of the travel time of the light inside the optical fiber. For this simulation, a 2000 m optical fiber is modelled as a time delay block (6.67 µs).
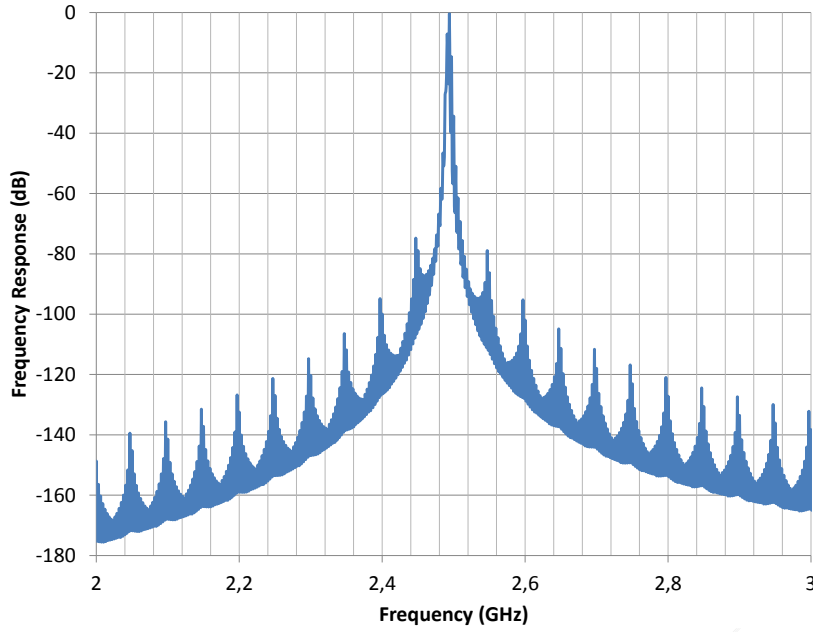
Figure 47 Open loop frequency response for the 2.49 GHz VBO.

3.1.2 VCSEL Based Optoelectronic Oscillator Closed Loop Analysis

The closed loop analysis presented in Chapter 1 is still valid for the VBO. For this reason it is recalled.

$$\left|\frac{V_{RF}}{V_{noise}}\right|^2 = \frac{G_{ampli}^2}{1 - |G_{OL}|^2 - 2|G_{OL}| * \cos(\omega_e\tau + \pi)} \tag{108}$$

Power and Frequency of the Oscillation

From the gain oscillation condition, the gain condition for the VBO is given by Equation (107).

$$\left|\tilde{\alpha}_E\tilde{G}_{ampli}\tilde{\alpha}_o\tilde{S}R_{ph}\tilde{F}h\nu\frac{1}{R_d}|H_{VCSEL}(\omega_o)|\right| = 1 \tag{109}$$

For the phase oscillation condition, the oscillation frequency is given by:

$$f_{osc} = \frac{k}{\tau} - \frac{\phi_o}{2\pi\tau_F} \tag{110}$$

The oscillation modes are linked to the electrical and optical fiber length time delay. These modes are spaced by the Free Spectral Range (FSR) that is given by:

$$FSR = \frac{1}{\tau} = \frac{1}{\tau_F + \tau_C} = \frac{1}{\frac{n_F L}{c} + \tau_C}$$

$$FSR_{Electrical} = \frac{1}{\tau_C}$$

$$FSR_{optical} = \frac{1}{\tau_F} = \frac{c}{n_F L}$$

(111)

Where τ_F is the optical fiber delay, τ_C is the delay related to electronic components, n_F is the optical fiber core refractive index, L is the optical fiber length, c is the speed of ligth.

The FSR and the microwave filter bandwidth define the mode selection in the oscillator.

3.1.3   Noise Processes inside the Oscillator

The oscillation energy starters for the optoelectronic oscillator are the noise sources inside the loop. Each component introduces certain noise signal inside the system. From the feedback, this signal is filtered and amplified up to satisfy the oscillation conditions. The noise sources inside the VBO can be divided into two categories as follows:

- External noise: These are mechanical, acoustic, or electromagnetic interferences linked to the VBO operating environment of the VBO. These noise sources are beyond the scope of this thesis and they will not be discussed.
- Internal noise sources: These sources are linked to the electronic intrinsic properties of the materials and their discrete behavior (quantum phenomena). They will be discussed in the upcoming sections.

Thermal Perturbations
The phase of the optical wave inside an optical fiber can vary because of the thermal influence in the optical fiber. This phase is defined as:

$$\phi = \beta L$$

(112)

Where β is the optical fiber line phase constant (wave number) and L is the optical fiber length.

The optical fiber is vulnerable to refractive index variations caused by the fiber bending. This bending changes the optical fiber diameter D and the effective refractive index of the fiber core n.

The optical phase shift can be expressed as,
$$\Delta\phi = \beta L + L\Delta\beta$$

(113)

The first term in Equation (112) corresponds to the optical fiber lengthen and the second term corresponds to diameter and refractive index variations, this is given by,

$$L\Delta\beta = L\frac{d\beta}{dn}\Delta n + L\frac{d\beta}{dD}\Delta D \tag{114}$$

However, the diameter variation term can be neglected if a not isolated fiber is considered. So,

$$\frac{\Delta\phi}{L} = \beta\frac{\Delta L}{L} + \frac{d\beta}{dn}\Delta n \tag{115}$$

The modulated optical signal (at f_{osc}) will be detected by a photodiode. The phase variation in optical domain will be converted into electrical domain. By this, it is possible to use the electrical wave number, β_e, given by:

$$\beta_e = \frac{2\pi f_{osc}n}{c} \tag{116}$$

And,

$$\frac{d\beta_e}{dn} = \frac{\beta_e}{n} \tag{117}$$

So, the electrical phase shift can be described as,

$$\frac{\Delta\phi}{L} = \beta_e\left(\frac{\Delta L}{L} + \frac{\Delta n}{n}\right) \tag{118}$$

It is possible to express the phase shift as a function of the temperature effects as follows,

$$\frac{\Delta\phi}{\Delta T\, L} = \beta_e\left(\frac{1}{L}\frac{dL}{dT} + \frac{1}{n}\frac{dn}{dT}\right) \tag{119}$$

And the phase variation related to temperature variation is given by,

$$\frac{\Delta\phi}{\phi\Delta T} = \frac{1}{L}\frac{dL}{dT} + \frac{1}{n}\frac{dn}{dT} \tag{120}$$

From Equation (117), it is possible to analyze the effect of the temperature in the oscillation frequency. The delay in an optical fiber spool is given by τ, from this, it is possible to obtain the optical phase shift as a function of the temperature. This relation is as follows,

$$\frac{\Delta f_{osc}}{\Delta\tau} = \frac{k}{\tau^2} = \frac{f_{osc}}{\tau} \tag{121}$$

And the frequency variation due to temperature variation is given by,

$$\frac{\Delta f_{osc}}{\Delta T} = \frac{c}{2\pi Ln}\frac{\Delta\phi}{\Delta T} \tag{122}$$

Replacing Equation (117) into (119), this leads to,

$$\frac{\Delta f_{osc}}{\Delta T} = f_{osc}\beta_e\left(\frac{1}{L}\frac{dL}{dT} + \frac{1}{n}\frac{dn}{dT}\right)$$

(123)

This expression is valid, as mentioned before, for an optical fiber without coat. However, the sensibility of a coated optical fiber will be higher that his case because of the thermal expansion of the coat material and its mechanical influence on the optical fiber.

Internal Perturbations

Shot Noise [64]

This noise comes from the photodetector. This is due to quantum nature of the electronic phenomena that governs photodetector operation. Each electron-hole pair produces an individual pulse of electric current. When the laser beam arrives at the photodetector, there will be a constructive phenomenon that will lead to the noise-generated photodetected current. The random behavior of photon contribution creates a fluctuating intensity given by,

$$I_{ph}(t) = I_o + i_{shot}(t)$$

(124)

Where $I_o = S * P_{optical}$ (as mentioned before, S is the photodetector responsivity and is the incident optical power in the photodetector) and corresponds to the shot noise current. The power spectral density of the shot noise is expressed as,

$$S_{shot} = 2qI_o$$

(125)

Where q is the electron charge.

The squared mean shot noisecurrent in a Δf bandwidth is given by,

$$\langle I_{shot}{}^2\rangle = 2qI_o\Delta f$$

(126)

Thermal Noise

At any temperature, the electrons move in a random way in conductor surface. For this reason, in all electrical systems, there is always a varying current even when the system is not biased. If the case of the photodetector in the optoelectronic oscillator is observed, there is a load resistor at the output of its amplifier. For this reason, a thermal noise component is added into the system. According to this, the total current in the system is defined as,

$$I(t) = I_o + I_{shot}(t) + I_{Thermal}(t)$$

(127)

Where, $I_{Thermal}$ represents the thermal noise current contribution. $I_{Thermal}$ is modeled as a stationary Gaussian random process with a power spectral density $S_T(f)$ given by,

$$S_T(f) = \frac{k_B T}{R_L}$$
(128)

Where, k_B is the Boltzman constant, T is the absolute temperature, and R_L is the photodetector amplifier load resistance.

From the spectral density of thermal noise, it is possible to obtain the thermal noise variance, defined as,

$$\sigma_T^2 = \langle i_T^2(t) \rangle = \frac{4k_B T}{R_L} \Delta f$$
(129)

Where, Δf is the effective noise bandwidth. To take into account effects linked to the amplifier topology and components, the quantity F_n is included, this is called, *amplifier noise figure*, and Equation (35) presents the new noise variance expression as follows,

$$\sigma_T^2 = \langle i_T^2(t) \rangle = \frac{4k_B T}{R_L} F_n \Delta f$$
(130)

The total variance current noise added by shot and thermal noise is expressed as,

$$\sigma^2 = \langle (\Delta I)^2 \rangle = 2q(I_o + I_{shot})\Delta f + \frac{4k_B T}{R_L} F_n \Delta f$$
(131)

3.1.4   Conversion of the Optical Phase Noise into Intensity Noise in the Optical Fiber

Inside the optical fiber of the oscillator the light transmission is attenuated and reflected due to its non-ideal material nature. Consequently, there are some phenomena that must be taken into account for the oscillator design. This is described by two phenomena, the Raman diffusion (optical) and Brillouin diffusion (acoustic).

Stimulated Brillouin Diffusion (SBD)

This diffusion phenomenon appears when the incident optical wave front creates an acoustic wave. This perturbation creates a refractive index variation that leads to a Bragg grating. The frequency shift is linked to the Doppler Effect associated to the grating displacement in this medium. This becomes negligible beyond certain injected power. This power is known as *Critical Power* P_{cr}, and it is defined as the point where the input frequency is reduced to its half and converted into new frequency waves. This is given by,

$$P_{cr} L_{eff} \cong 21 \left(1 + \frac{\Delta v}{\Delta v_B} \right) \frac{A_{eff}}{g_B}$$
(132)

Where, g_B is the stimulated Brillouin diffusion $\left(5.1 * 10^{-11} \frac{m}{W} \, for \, silica \, optical \, fibers \right)$, $A_{eff} = \pi \omega^2$ is the effective area of the fiber core and ω is the spot size (typical $A_{eff} \approx 70 \mu m^2$), Δv_B is the Brillouin spectral linewidth (typical value around 10 to 100 MHz), Δv is the laser spectral linewidth and L_{eff} is the interaction effective length given by:

$$L_{eff} = \frac{1 - e^{-\alpha L}}{\alpha} \tag{133}$$

Where, α represents the optical fiber losses ($\approx 0.2\ dB/km$) and L is the actual length of the optical fiber. To observe this effect Figure 48 is presented. It is seenthat for lengths among 100 m to 10 km (300 mW to 3.3 mW, respectively), the optical power injected by the laser can produce a important Brillouin perturbation. Fortunately, the VCSEL optical power is not high enough to produce a wave reflection that could make a round tour inside the optical fiber and for this reason, it is highly reduced but it still remains in the fiber.
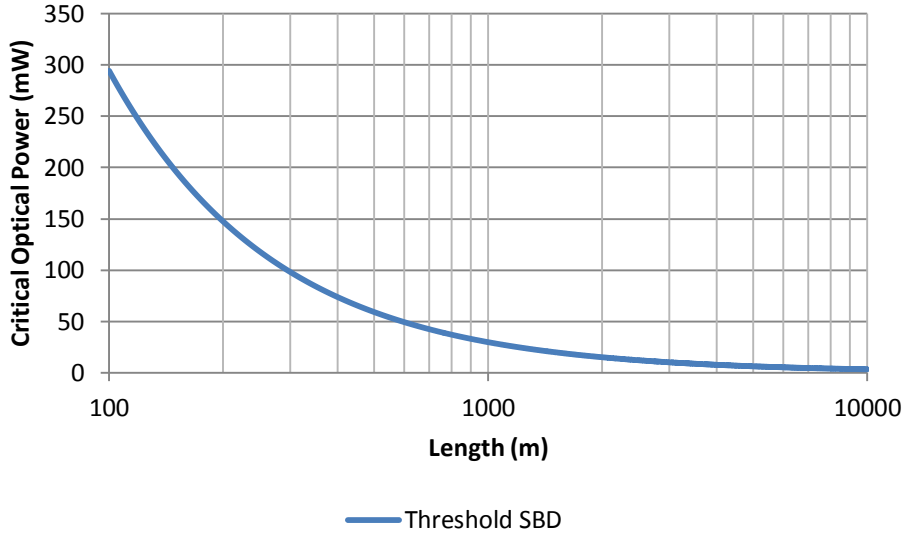
Figure 48 Stimulated Brillouin difussion threshold power.

Stimulated Raman Difussion (SRD)

This noise source is related to the optical injected power inside the optical fiber. The energy of the incident photons is converted into phonons that create lower energy photons. It is possible to compute the threshold Raman power, P_{cr} as,

$$P_{cr}L_{eff} \cong 16\frac{A_{eff}}{g_R} \tag{134}$$

Where g_R is the Stimulated Raman Diffusion (SRD) ($\approx 6.5 * 10^4 m/W$ for 1.55 μm). A_{eff} is defined as in the Brillouin diffusion. The theoretical threshold values for the SRD are shown in Figure 49. This noise source can be neglected for our purposes taking into account the reduced power emission of the VCSELs used in this project.
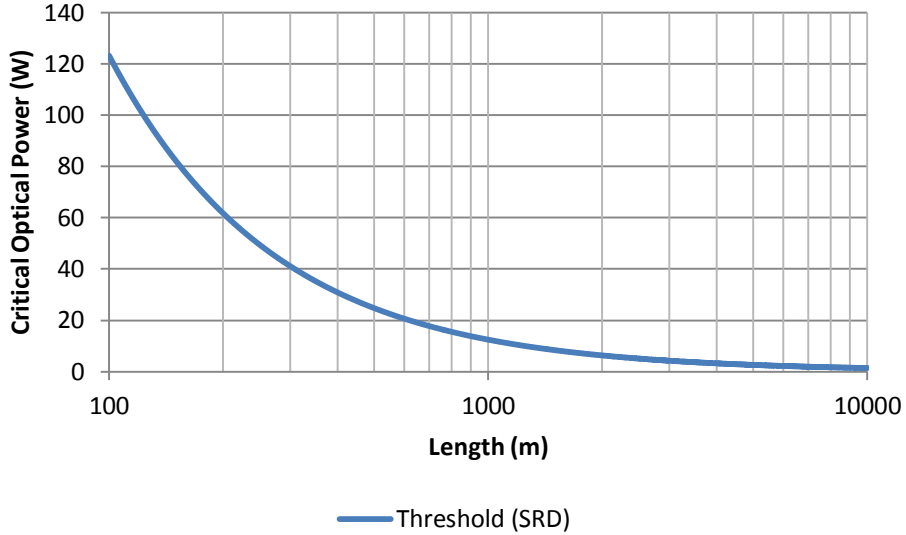
Figure 49 Stimulated Raman diffusion threshold power.

Rayleigh Diffusion [65]

The Rayleigh diffusion is caused by the microscopic variations of the optical fiber refractive index. Figure 50 presents the Rayleigh diffusion approach.
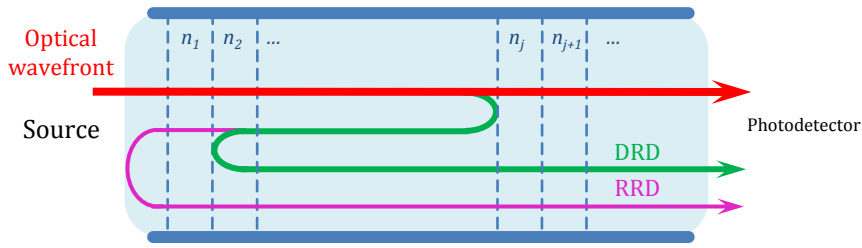
Figure 50 Rayleigh diffusion noise principle.

This noise can be divided into two categories:

- Double Rayleigh Diffusion:

This noise is characterized by reflections of a small part of the optical power in backward and forward propagation sense. This creates an additive noise that can be seen as relative intensity noise (RIN_{DRD}) in the fiber output. This RIN can be expressed as,

$$RIN_{DRD} \cong \frac{4S_{Diff}^2 \alpha_s L_{effDRD}}{\pi \Delta v} \frac{1}{1 + \left(\frac{f}{\Delta v}\right)^2} \qquad (135)$$

Where, for a monomode optical fiber at 1550 nm, $S_{diff} = 10^{-3}$ is the light part that is diffused and received by the photodetector, $\alpha_s = 3.2 * 10^{-2} km^{-1}$ is the Rayleigh coefficient, the effective length is expressed as

$$L_{eff} = \frac{1 - e^{-\alpha L}}{2\alpha} \qquad (136)$$

And Δv is the laser linedwidth and f is the Fourier frequency.

Reflected Rayleigh Diffusion

This noise process is similar to the previous one. The difference is that the second diffusion is replaced by a reflection at the optical fiber input. This is seen as relative intensity noise (RIN_{RRD}) at the optical fiber output. This noise can be expressed as:

$$RIN_{RRD} \cong \frac{4R_p S_{Diff}^2 \alpha_s L_{effRRD}}{\pi \Delta v} \frac{1}{1 + \left(\frac{f}{\Delta v}\right)^2} \tag{137}$$

Where R_p corresponds to the reflection coefficient at the fiber input, L_{effRRD} is defined as in Equation (135).

3.1.5 Leeson Model in the VCSEL Based Optoelectronic Oscillator [17]

The closed-loop oscillator is composed by the amplifier and the reactive chain. From the Leeson's model it is possible to predict the phase spectral power density S_φ at the oscillator output from the phase spectral density fluctuations at the oscillator input, $S_{\Delta\theta}$. To find this, the relation presented in Equation (138) is presented [12].

$$S_\varphi(f) = S_{\Delta\theta}\left[1 + \left(\frac{f_o}{2Qf}\right)^2\right] \tag{138}$$

From this expression the phase noise is computed once the noise sources are known. As mentioned in the previous section the noise sources due to thermal effect, electronic and optical fiber are taken into account. Those sources are assumed as current sources in a parallel circuit. These are:

- i_{Fiber} due to optical fiber RIN
- i_{Laser} due to laser RIN
- i_{shot} due to photodetector shot noise
- $i_{thermal}$ due to thermal noise inside the system

Figure 51 presents the noise sources and their loads (Z_{ph} for the photodetector output impedance and Z_A for the amplifier output impedance).
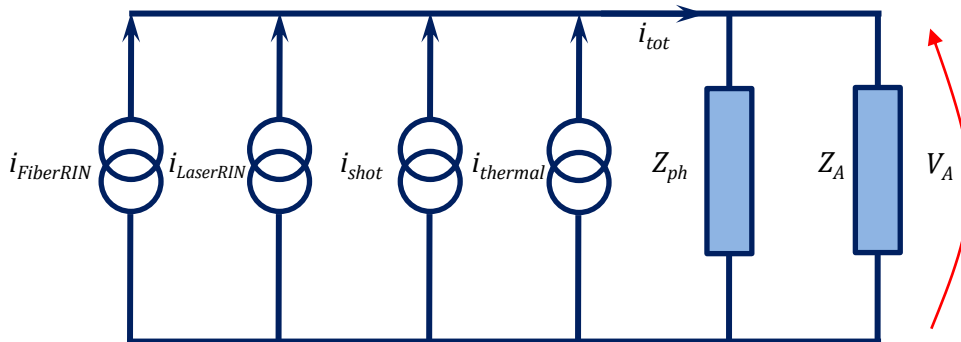
Figure 51 VBO noise sources circuit model.

From Figure 51 it is possible to find the total current linked to noise sources. This current, i_{tot} as,

$$i_{tot} = i_{FiberRIN} + i_{LaserRIN} + i_{shot} + i_{thermal} \tag{139}$$

In Figure 51, the output voltage, V_A, is given by,

$$V_A = i_{tot} \frac{Z_{ph} Z_A}{Z_{ph} + Z_A} \tag{140}$$

The input power at the amplifier, is expressed as,

$$P_A = P_{noise} = \frac{V_A^2}{Z_A} = \langle i_{tot}^2 \rangle Z_A \left(\frac{Z_{ph}}{Z_{ph} + Z_A} \right)^2 \tag{141}$$

To compute the power spectral noise density at amplifier input, the following expression is useful.

$$P_{noise} = S_{noise} \Delta f \tag{142}$$

From Equation (142) and including Equations $(127 - 132)$; the noise power spectral density is found.

$$S_{noise}(f) = \left[(RIN_{Laser} + RIN_{DRD} + RIN_{RRD}) i_{ph}^2 + 2q I_{ph} + 4k_B T F \right] Z_{eq} \tag{143}$$

Where, the equivalent impedance is given as:

$$Z_{eq} = Z_A \left(\frac{Z_{ph}}{Z_{ph} + Z_A} \right)^2 \tag{144}$$

And I_{ph} is the photodetected current.
Then, the power spectral density of the phase noise is expressed as [12]:

$$S_{\Delta\theta} = \frac{G_{ampli}^2 * S_{noise}}{P_{oscilltion}} \left(1 + \frac{f_c}{f} \right) \tag{145}$$

Finally, the power spectral density of the phase noise at the oscillator output is given by,

$$S_{\varphi}(f) = \frac{G_{ampli}^2 * S_{noise}}{P_{oscillation}} \left(1 + \frac{f_c}{f} \right) \left[1 + \left(\frac{f_o}{2Qf} \right)^2 \right] \tag{146}$$

From the power spectral density of the phase noise equation, it can be inferred that higher the quality factor of the resonant element of the optoelectronic oscillator lower the phase noise is going to be. For this reason it is mandatory the use of a high quality resonator to assure a high performing optoelectronic oscillator.

3.1.6 VCSEL Based Optoelectronic Oscillator State-of-the-Art

Previous VCSEL based optoelectronic oscillator implementations had been reported. These VBOs use different wavelength VCSELs (850, 1100 nm). With the appearance of the long wavelength VCSELs, new possibilities of experimentation are foreseen. For this reason, Varon [3] implemented a VBO at 2.5 GHz using 850 nm and 1500 nm lasers. Hasegawa and Koizumi had implemented VBOs at higher frequency, as shown in Table 9.

Author	Frequency (GHz)	VCSEL Wavelength (nm)	Optical Fiber Length (m)	Phase Noise at 10 kHz offset (dBc/Hz)	Year
Hasegawa[66]	10	850	200	-80	2007
Varón [3]	2.49	850	120	-100	2008
Varón [3]	2.49	1500	100	-95	2008
Koizumi [67]	10	1100	1000	-70	2010
Belkin	3	1500	65	-106	2012

Table 9 Directly-modulated VCSEL based optoelectronic oscillator performance.

3.2 VCSEL Based Optoelectronic Oscillator Experimental Approach

The VCSEL based optoelectronic oscillator is implemented according to the setup presented in Figure 52. Several component configurations are built in order to evaluate the VBO stability when the delay line length is varied for different VCSEL wavelengths (1.3 and 1.5 μm). The VBOs implemented in this project are tuned at S-band.
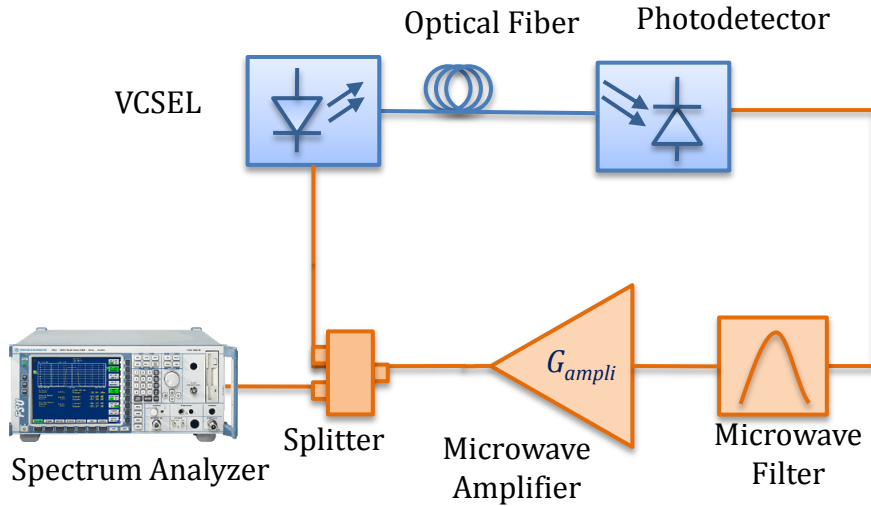
Figure 52 VCSEL based optoelectronic oscillator.

3.2.1 Study of the VCSEL Based Optoelectronic Oscillator at 2.49 GHz Stability under Optical Fiber Length Variation

The VBO test bench is shown in Figure 53. Two VBO configurations were built using different laser wavelength and optical fiber lengths. The goal of this measurement is to observe the frequency stability taking into account the effects of the laser wavelength (RIN and optical fiber dispersion) and the resonance element quality factor (filter and optical fiber length) on the frequency stability of the VBO (phase noise). The VCSELs used in this project were manufactured by RayCan. The VCSEL temperature is controlled at 20°C.
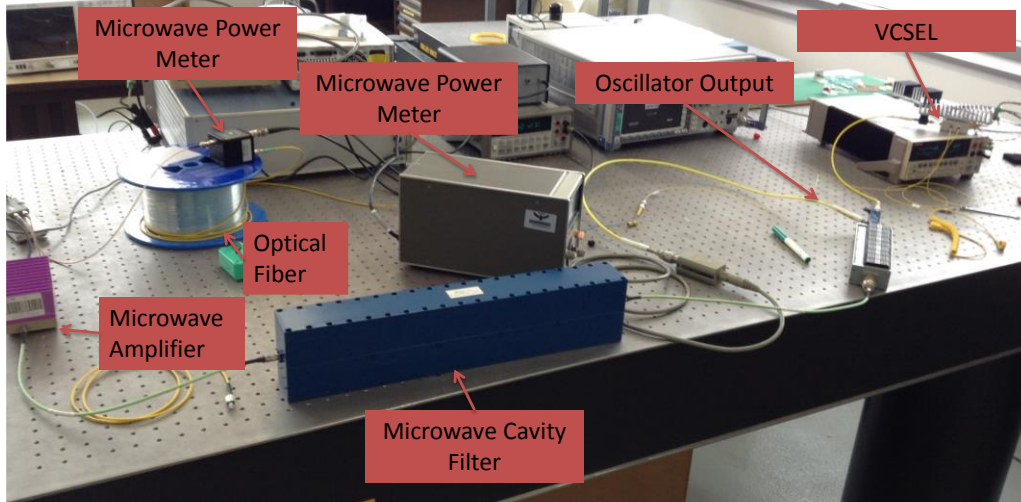
Figure 53 VBO test bench.

The first VBO configuration is a 1.3 µm VCSEL and the wavelength is varied by using different optical fiber spools of 200, 300, 700, 1000, 2000 and 10000 m. The second VBO uses a 1.5 µm VCSEL with the same optical fiber lengths.

3.2.1.1   1.3 µm VCSEL Based Optoelectronic Oscillator at 2.49 GHz

The 2.49 GHz VBO output spectrum is shown in Figure 54.
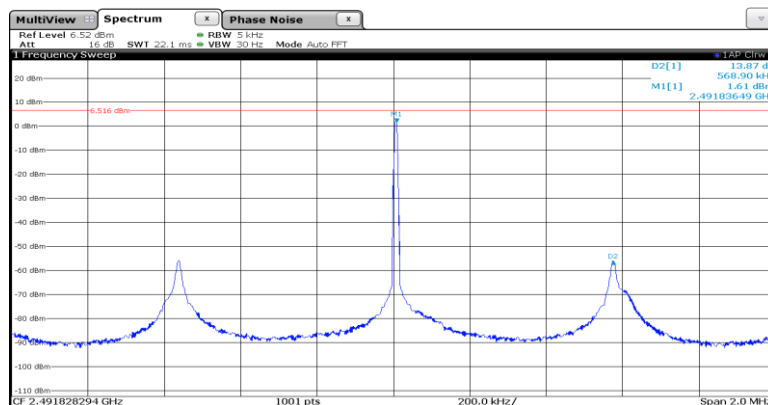
Figure 54 Output spectrum for a 2.49 GHz VBO using 1.3 um VCSEL .

For the delay line optoelectronic oscillators, the increase of the optical fiber length reduces the free spectral range of the carrier. These modes, that look similar to a Fabry-Perot cavity, are spaced according to the following relation:

$$FSR = \frac{1}{\tau_{Fiber}}$$

(147)

Where, τ_{Fiber} is the optical fiber time delay. This is defined as follows:

$$\tau_{Fiber} = \frac{\eta_i L}{c}$$

(148)

Where, η_i is the refractive index of the optical fiber. From this set of equations, the FSR and Q_{fiber} are found for each optical fiber length, as shown in Table 10. $Q_{fiber} = 2\pi f \tau_d$.

Optical Fiber Length (m)	FSR (MHz)	Q_{fiber}
100	2,069	$3.78 * 10^3$
200	1,035	$7.56 * 10^3$
300	0,690	$1.13 * 10^4$
500	0,414	$1.89 * 10^4$
700	0,296	$2.65 * 10^4$
1000	0,207	$3.78 * 10^4$
2000	0,103	$7.56 * 10^4$
10000	0,021	$3.78 * 10^5$

Table 10 FSR and Q for several fiber lengths.

VCSEL Based Optoelectronic Oscillator Frequency Stability

The 2.49 GHz VBO phase noise was measured for several optical fiber lengths. The effect of the phase noise reduction due to the optical fiber length increase (due to the increase of the resonant element quality factor) is observed. Figure 55 presents the phase noise measurement of the VBO. The phase noise value at 10 kHz offset is enhanced from -101 dBc/Hz for 200 m long optical fiber spool to -125.41 dBc/Hz for 10 km long optical fiber spool. The side modes approach when the optical fiber is longer enough to be selected by the microwave bandpass filer is observed for the 10 km optical fiber. The phase noise reduction for each fiber length at 10 kHz offset is presented in Figure 56.
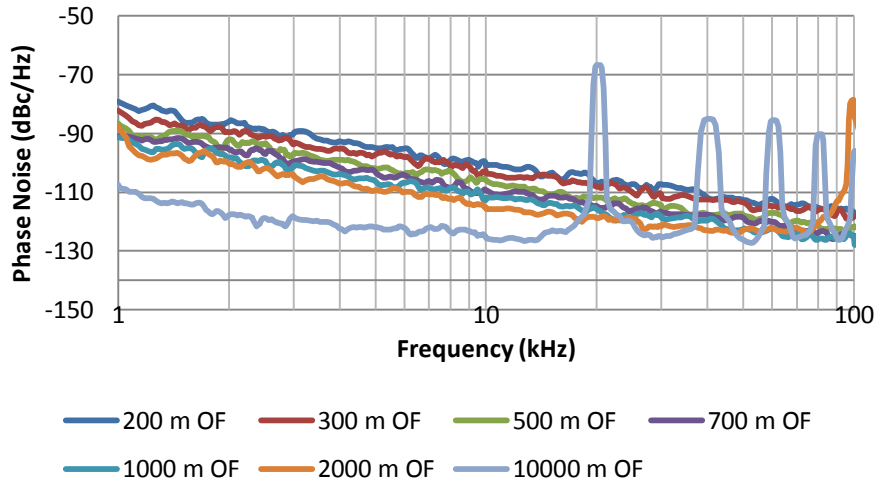
Figure 55 Phase noise for a 2.49 GHz VBO with 1.3 um VCSEL and different optical fiber lengths.
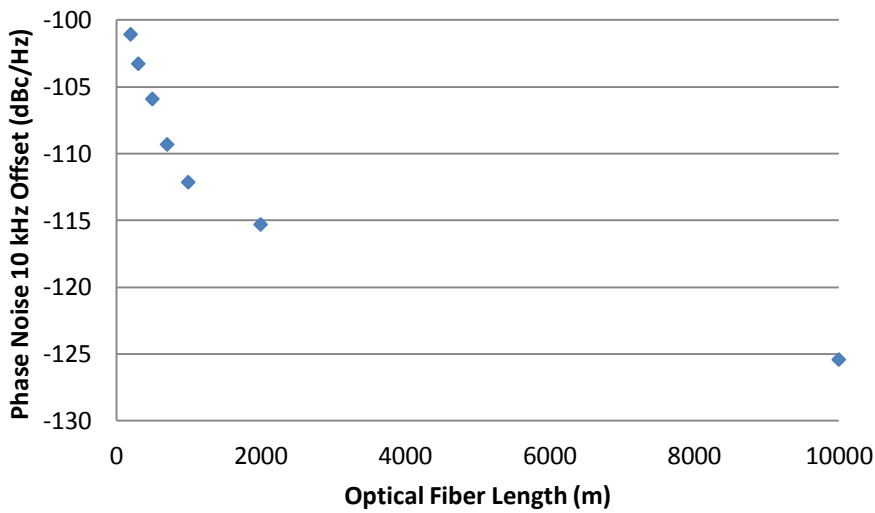
Figure 56 Phase noise at 10 kHz offset for 2.49 GHz VBO with1.3 um VCSEL.

To summarize the results of the 2.49 GHz VBO performance using 1.3 μm VCSEL, Table 11 is presented. From this table it is possible to interpret that:

- The frequency stability is enhanced by enlarging the optical fiber because of the increase in the resonant element quality factor.

- When the length of the optical fiber is increased, the secondary modes are closer and they cannot be filtered by the bandpass microwave filter whose bandwidth is 4 MHz.

Optical Fiber Length (m)	Phase Noise at 10 kHz offset (dBc/Hz)
200	-101.0
300	-103.3
500	-105.9
700	-109.3
1000	-112.5
2000	-115.3
10000	-125.41

Table 11 2.49 GHz VBO performance paramenters using 1.3um VCSEL and different optical fiber lengths.

2.1.1.1   1.5 μm VCSEL Based Optoelectronic Oscillator at 2.49 GHz

The VBO configuration using a 1.5 μm VCSEL was implemented. The optical fiber length is varied from 200 m to 2000 m optical fiber. Figure 57 presents the phase noise measure for different optical fiber lengths.
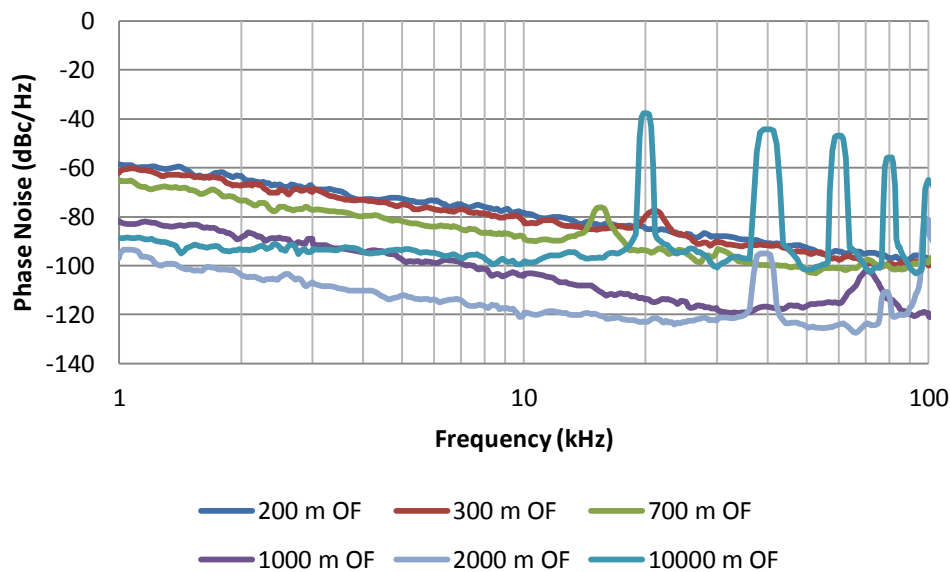
Figure 57 Phase noise for a 2.49 GHz VBO using 1.5 um VCSEL and different wavelengths.

Table 12 summarizes the phase noise measurements at 10 kHz offset that are presented in Figure 58. The reduction of the phase noise is evidenced for the optical fiber lengthen. It is important to remark that the phase noise for the 10 km VBO is degraded because of the high attenuation of the optical fiber, this reduces the stimulated mission detected in the photodetector. Lower photodetected current makes the oscillator susceptible to noise perturbations.

Optical Fiber Length (m)	Phase Noise at 10 kHz offset (dBc/Hz)
200	-78.5
300	-82.0
700	-88.6
1000	-103.7
2000	-119.5
10000	-98

Table 12 The 2.49 GHz VBO performance parameters with 1.5 um VCSEL and different optical fiber lengths.
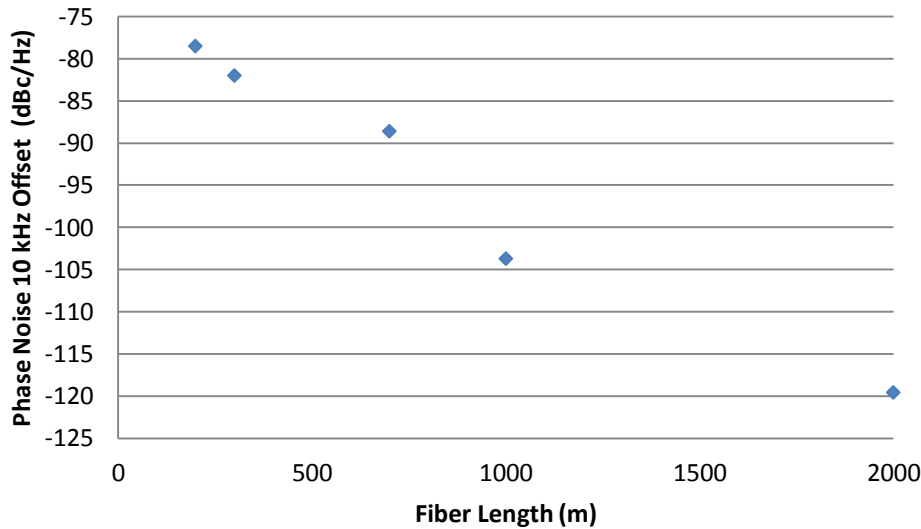
Figure 58 Phase noise at 10 kHz offset for 2.49 GHz VBO with 1.5 um VCSEL.

3.2.2   VCSEL Based Optoelectronic Oscillator Phase Noise Analysis with the Leeson Model Approach

The VCSEL Based Optoelectronic oscillator frequency stability performance is analyzed according to the Leeson model for the phase noise. The oscillator resonator phase noise frequency response is simulated according to the expression presented by Rubiola and Brendel [68] for the delay line optoelectronic oscillator. The additive noise definition of the Leeson model is used to predict the VBO phase noise. The phase noise transfer function of the phase noise for the delay line and the microwave amplifier are modelled using the parameters shown in Table 13. The computed phase noise values for the resonator (optical fiber delay line) and the microwave amplifier are added to predict the VBO phase noise. The phase noise curves for the VBO using 1.3 and 1.5 µm VCSEL are shown in Figure 59.

Parameter	1.3 µm VBO	1.5 µm VBO
RIN @ 2.49 GHz	-147 dB/Hz	-151 dB/Hz
RIN DRR	-190 dB/Hz	-190 dB/Hz
RIN DDR	-190 dB/Hz	-190 dB/Hz
Photodetected current	0.157 mA	0.354 mA
Amplifier noise figure	3.5	3.5
b_0	-125 dB/Hz	-125 dB/Hz
b_{-1} (assumed from literature)	-120	-120
$Q_{delay\ line}$	$7.57 * 10^4$	$7.57 * 10^4$
Optical fiber time delay	9.67 µs	9.67 µs

Table 13 Parameters used to predict the VBO phase noise.

For the 1.3 µm VBO (Figure 59 a) the phase noise spectrum is characterized by a f^{-1} (red line) trend that agress well with the phase noise of the optical fiber delay line. At the left side of the Leeson frequency ($f_L = 16.5\ kHz$), the microwave amplifier f^{-2} phase noise is dominant in the VBO phase noise curve.

The 1.5 µm VBO (Figure 59 b) phase noise spectrum presents an electronic noise dominated by the resonator phase noise (f^{-1}) after the Leeson frequency at the right side of the Figure 59 b) at the left of the Leeson frequency, the Leeson effect takes place with a f^{-2} phase noise trend linked to the microwave amplifier phase noise.

In both VBOs, the presence of the Leeson effect is evidenced for the direct modulated lasers. Indeed, the phase noise profiles measured in this test agree with the Type 1 phase noise curve profile presented by Rubiola and Brendel [68]. The additive phase noise contribution of the VBO elements is confirmed in the direct modulated VCSEL based optoelectronic oscillators implemented in this project.

a)
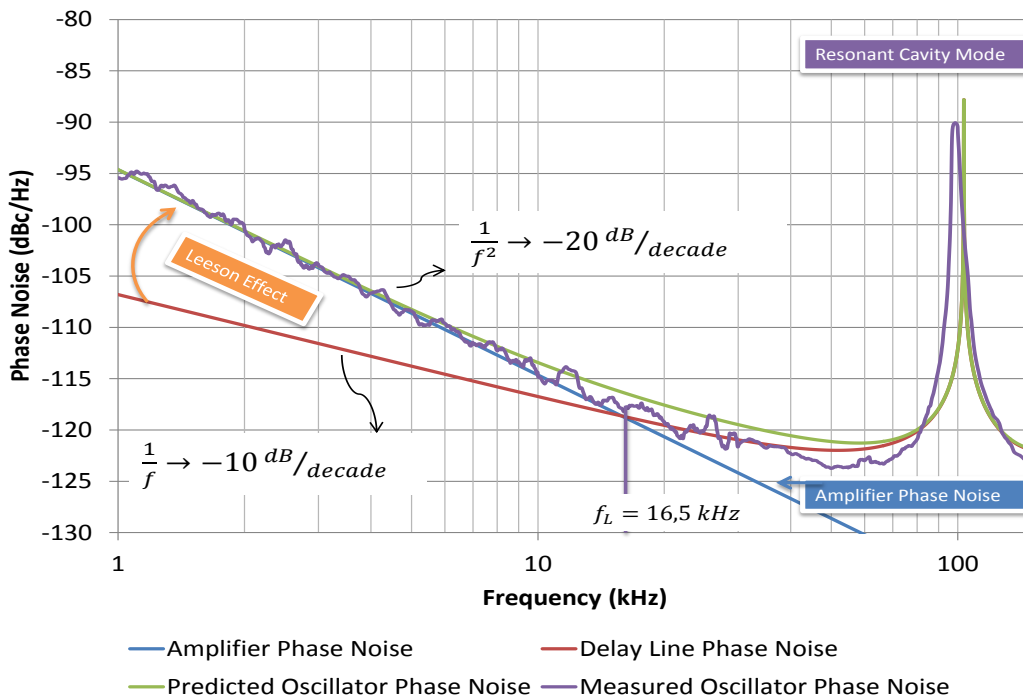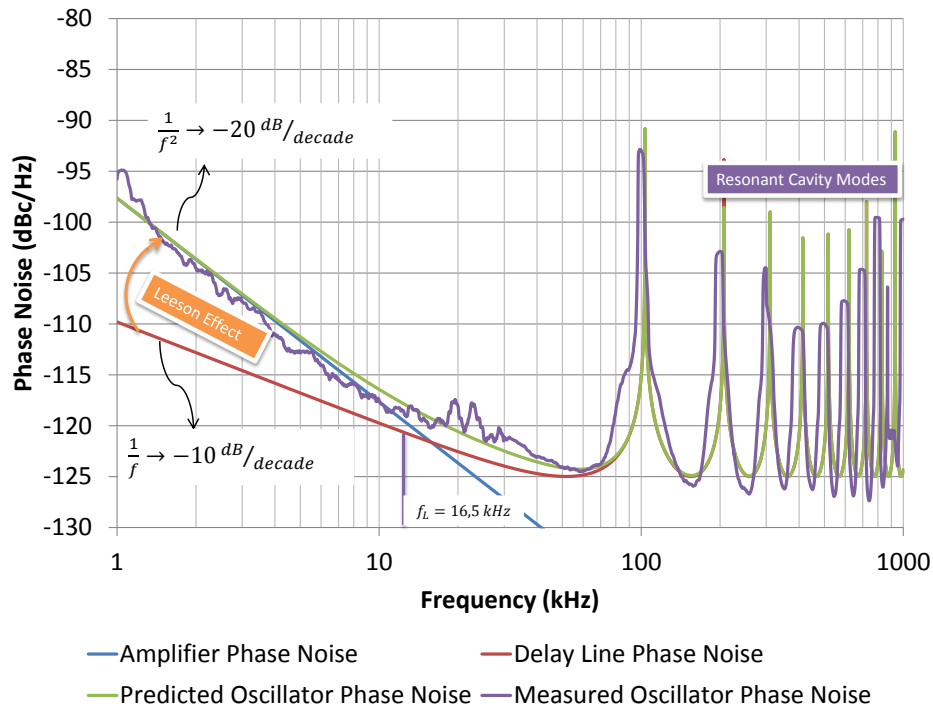
Figure 59 VCSEL based optoelectronic oscillator phase noise analysis according to the Leeson model.

3.2.3 Thermal Effects in the VCSEL Based Optoelectronic Oscillator

The VBO performance, as mentioned before, is the result of the performance of all loop components. For this reason, it was performed a temperature test over the oscillator optical fiber in order to evaluate the impact on the VBO frequency stability linked to the optical fiber heating. The test schematic setup is seen in Figure 60. The optical fiber spool is introduced into a thermal enclosure (Climats Spiral) with temperature control, as seen in Figure 61.

The VBO built for this test is a 1.3 µm VCSEL based oscillator with 1000 m optical fiber length tuned at 2.492 GHz (nominal center frequency of the microwave band pass filter) with an InP high speed photodetector and a low noise microwave amplifier.
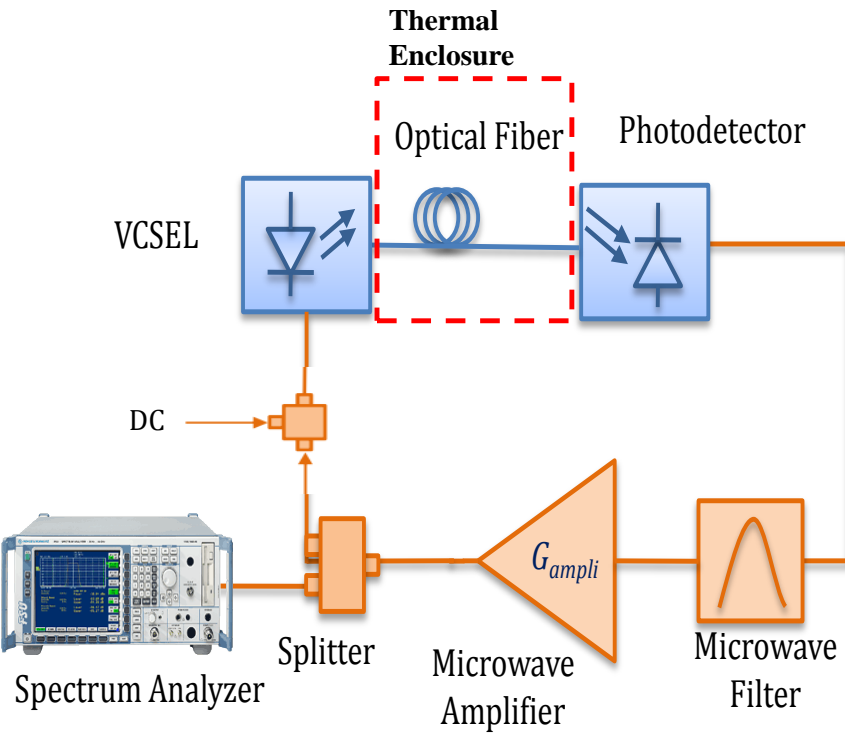
Figure 60 VBO thermal test setup.
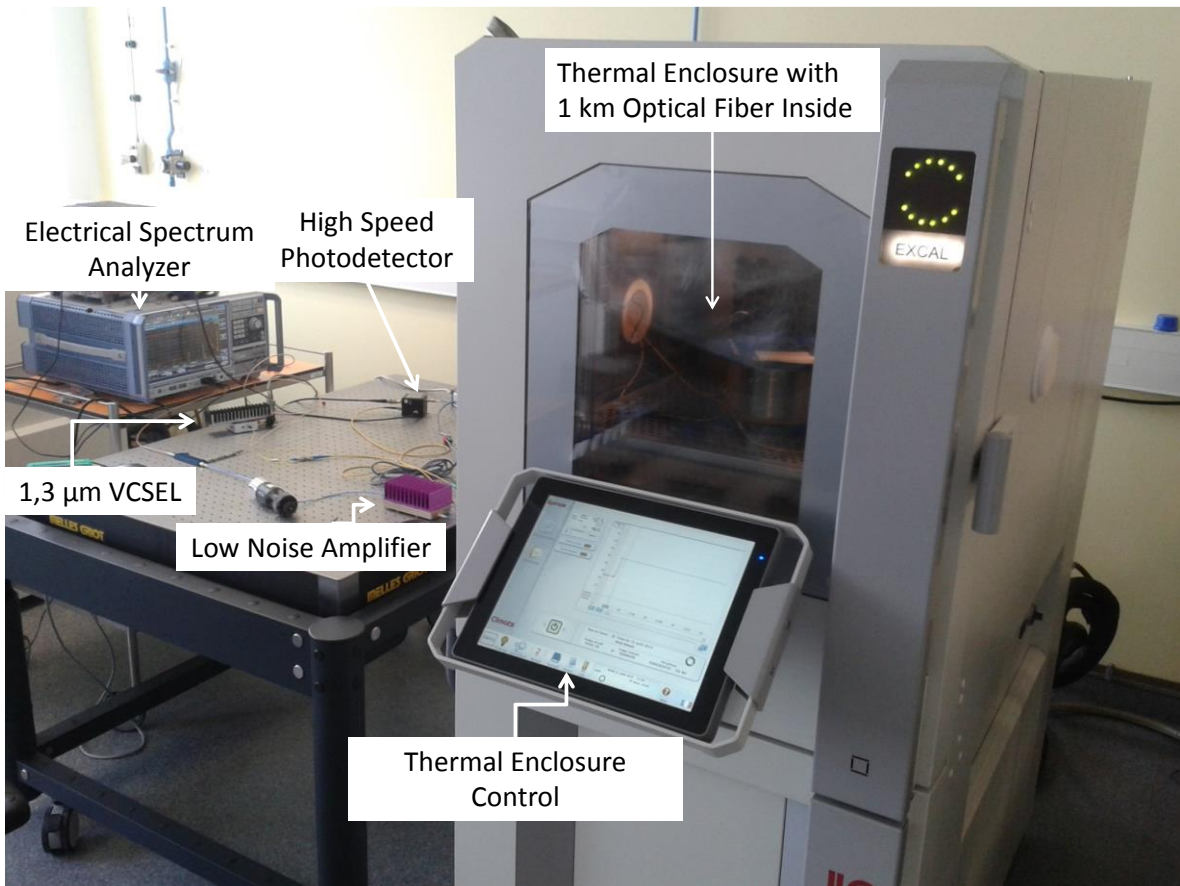
Figure 61 VBO thermal testbench.

To analyze the thermal stability of the VBO, the measure of the frequency stability of the oscillator in a temperature sweep from 5 to 35 °C, as well as the carrier frequency to analyze its drift by heating the optical fiber spool.

The VBO frequency drift is evidenced in Figure 62. The total frequency drift for the extreme values of this test was 611.4 kHz for a 30ºC temperature range. To compare this result with other optoelectronic oscillator technology, Saleh [30] reports a frequency shift of 2.5 MHz using a fiber ring resonator for a 35ºK temperature range.

The average frequency drift for each temperature step was 101.9 kHz. This frequency reduction is due to the length variation due to temperature change that is expressed as follows [30].

$$\Delta L = 0.5 * 10^{-6} * L * \Delta T \qquad (149)$$

Where, ΔL is the optical fiber length variation, L is the ambient optical fiber length and ΔT is the temperature variation.
The optical fiber refractive index variation behaves as temperature function following the relation,

$$\Delta n = 9.2 * 10^{-6} * \Delta T \qquad (150)$$

All these factors affect the time delay in the optical fiber leading to a frequency drift in the carrier.
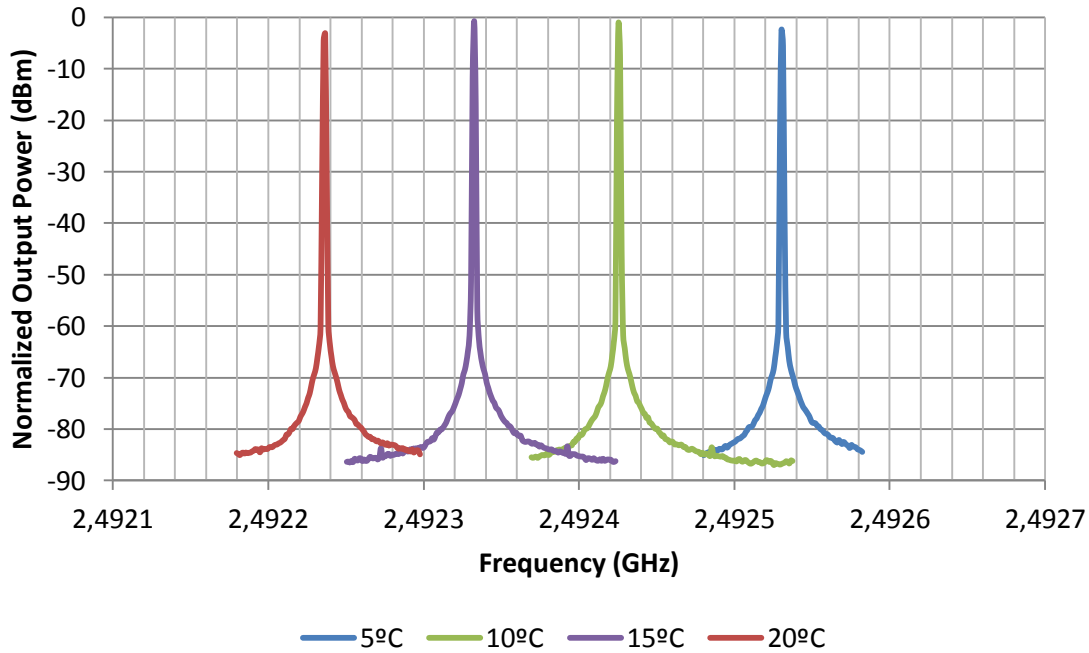
Figure 62 VBO with optical fiber under thermal heating spectrum.

The carrier frequency shift follows a linear trend in the temperature test range, as presented in Figure 63. As the temperature of the thermal enclosure rises, the carrier frequency decreases in 20.4 kHz/ºC.
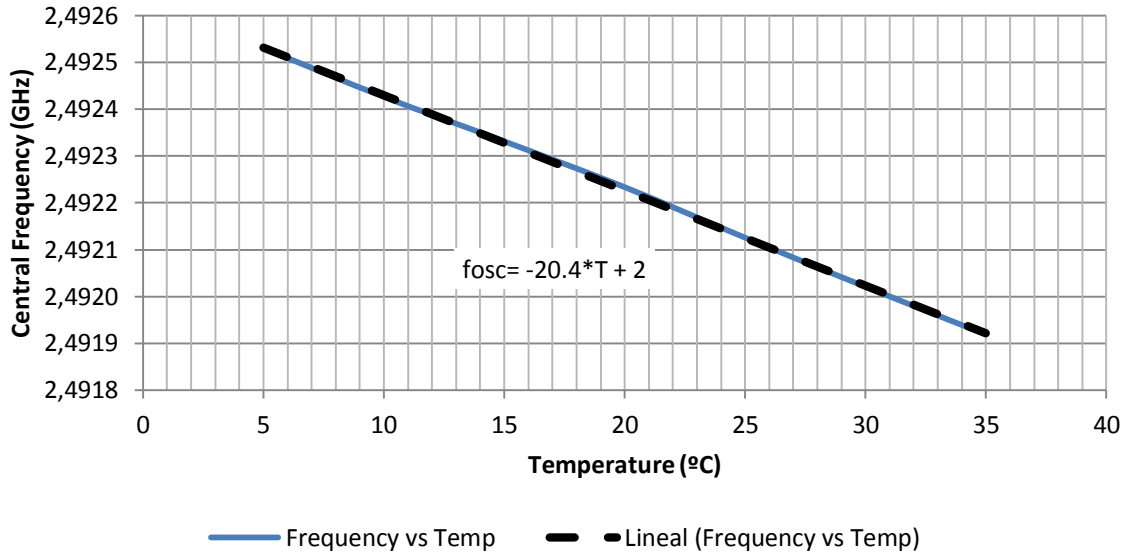
Figure 63 Carrier frequency as a function of optical fiber temperature.

Using a thermal stability analysis [30], [69], it is possible to define the relationship between the frequency shift of the carrier and the free spectral range of the oscillator, as follows,

$$\frac{\Delta f_{RF}}{f_{RF}} = \frac{\Delta FSR}{FSR} \tag{151}$$

According to the performed measurements, the thermal stability of the oscillator carrier for a $\Delta T = 30°C$ is,

$$\frac{\Delta f_{RF}}{f_{RF}} = -8.18 \ ppm/ºC \tag{152}$$

This VBO presents a good thermal stability if compared with other oscillator technologies [70]. From this result, it is possible to mention that the optical fiber temperature has a strong influence in the oscillator performance, taking into account the fact that the thermal stability of a fiber ring resonator is $6.8 \ ppm/ºC$ [30]. Comparing this result to other oscillator technologies, Table 14 presents the thermal stability values that places the VBO in a high performing place.

Oscillator technology [30], [70]	Thermal stability (ppm/°C)
Quartz	0.1
Coaxial cable	100
Metallic cavity	100
Dielectric resonant oscillator	$0.1 - 10$
Fiber ring optoelectronic oscillator	6.8
VCSEL based optoelectronic oscillator (VBO)	8.18

Table 14 Thermal stability comparison of the VBO with respect to other oscillator topologies.

Additionally, the frequency stability of the VBO is also analyzed in this test. The phase noise of the VBO was measured for each temperature step, as presented in Figure 64. From this figure, it is possible to conclude that, despite the slight carrier frequency drift

of the VBO, the carrier quality is not degraded. Table 15 presents the phase noise value at 10 kHz offset for each temperature step.
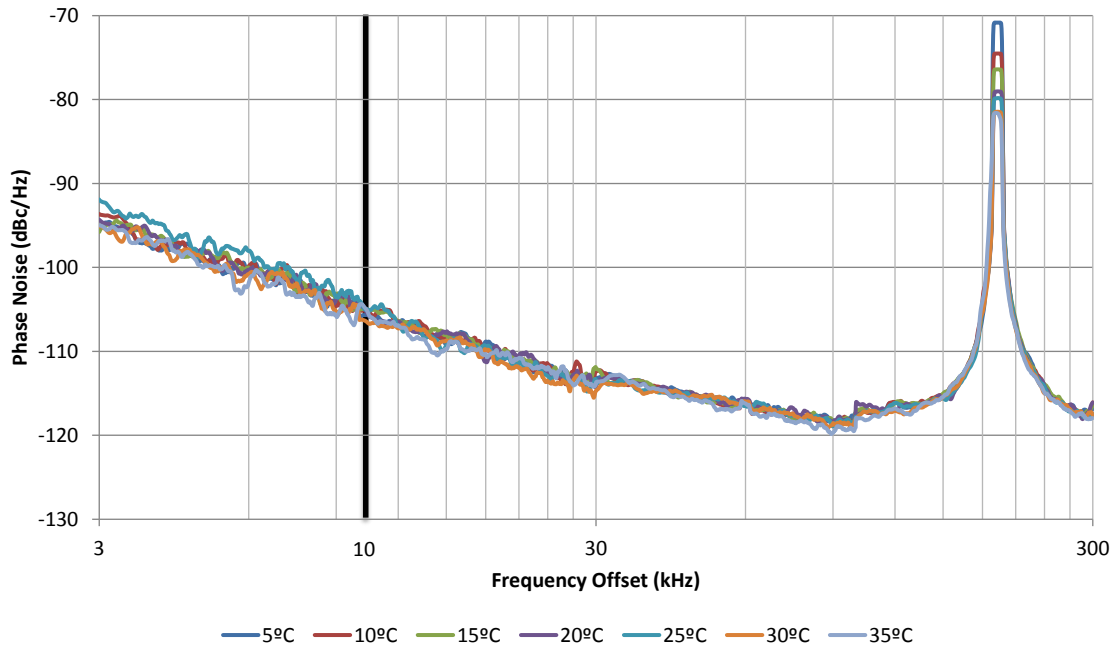
Figure 64 Phase noise curves of the 2.49 GHz VBO for several temperatures.

Temperature (ºC)	Phase Noise at 10 kHz Offset (dBc/Hz)
5	-105,01
10	-105,15
15	-105,37
20	-105,64
25	-105,45
30	-106,42
35	-106,45

Table 15 Phase noise values at 10 kHz offset for the 2.49 GHz VBO at different temperatures.

Conclusion

The experimental approach for the VCSEL Based Oscillator (VBO) is presented in this Chapter. A performance comparison of two VBO's operating at the same frequency using 1.3 and 1.5 µm was carried out. The optical fiber length was varied for both oscillators. From these tests, it is shown that the optical fiber length varies the quality factor of the resonant cavity for long wavelength VBO's and allow to reduce the phase noise of the carrier. Under the same operating conditions, the 1.5 µm VBO presents lower phase noise than the 1.3 µm case. In terms of RIN, the 1.3 µm VCSEL is noisier than the 1.5 µm one. This confirms the hypothesis of the RIN direct relation with the frequency stability. The enhancement of the VCSEL manufacturing techniques had led to an important enhancement in the VCSEL RIN reduction. When comparing the VBO results of Varón [63] using long wavelength VCSELs with higher RIN and these results, the RIN is dramatically reduced.

The Leeson model to describe the VBO phase noise behavior is taken in order to determine the noise sources in the oscillator. By analyzing the phase noise slopes, it is possible to define the phase noise processes inside the oscillator. The carrier phase noise behaves well according to that predicted by the Leeson model.

A thermal stability test of the VBO has been performed. From this test it is important to remark that the VBO presents a good thermal stability compared to other OEO topologies. There is a slight frequency drift of the carrier frequency due to the optical fiber heating. The thermal effects are observed in the carrier frequency but not in the phase noise measurement that remains almost invariable.

From these set of test it is concluded that the VCSEL Based Optoelectronic oscillator is a feasible technology to build a stable oscillator. The only drawback of this oscillator topology is the relatively low direct modulation bandwidth of the VCSEL. In the next chapter, the optical injection locking technique will be addressed in order to enhance this weakness of the VCSEL.

Chapter 4

Optical Injection Locking of VCSEL Experiments

Introduction

The basics of the Optical Injection Locking Technique (OIL) are described in this Chapter. It has been shown by several authors that the OIL enhance the microwave performance and relative intensity noise (RIN) of a laser [71]–[73]. In this Chapter, a characterization of the OIL VCSEL is presented. This characterization covers to scopes of the OIL VCSEL: the first one corresponds to the optical noise of the injection locked VCSEL (RIN) and the second one covers the microwave performance direct modulated VCSEL.

The goal of this chapter is to show the suitability of the OIL VCSEL to be directly modulated and integrated into the optoelectronic oscillator.

4.1 Optical Injection Locking

The Optical Injection Locking (OIL) technique is shown in Figure 65. In this Figure, there are two lasers connected through an optical circulator. The beam emitted by the master laser is injected through the optical circulator into the slave laser. Then the injection-locked output beam (Figure 66) is emitted through the third port of the optical circulator.

The Optical Injection Locking technique (OIL) was first suggested by Pantell in 1965 [74]. In 1972 the optical injection locking technique was demonstrated using to CO_2 lasers [75]. With the arrival of the semiconductor lasers in the 80's, the OIL recovered interest for the researchers. Kobayashi and Kimura made the OIL using two AlGaAs 840 nm lasers [76].

In the middle 80's, the OIL technique was explored to enhance the semiconductor laser linewidth to obtain chirp-free transmissions [77]. At this decade, there was a milestone progress in the theoretical approach, when Lang proposed a modified set of rate equations modelling the semiconductor laser behavior under OIL [78]. These rate equations will be presented in the coming sections.

In the 90's, Meng and Simpson [79], [80] demonstrated the increase of the modulation bandwidth of the semiconductor lasers under OIL. Anyway, the external modulation technologies and EDFA's took the interest for long haul communications. Nowadays, due to the fast spreading of optical networks, it is necessary to develop reliable, low cost and efficient communication devices. This made the OIL a suitable technique to be applied in communications, especially when direct modulation is used.
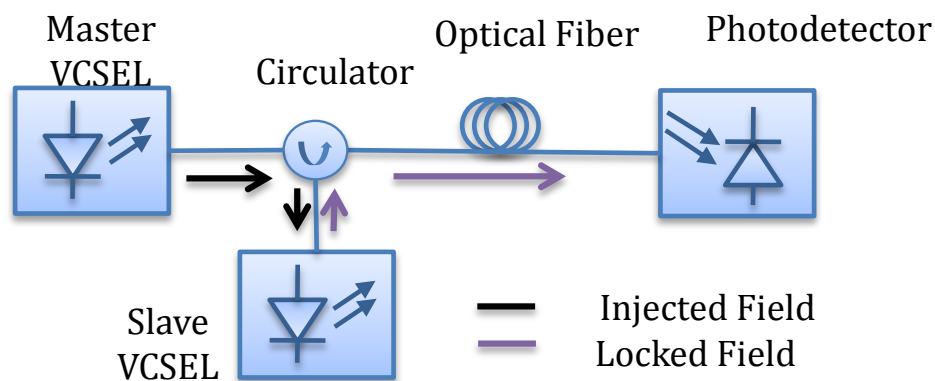
Figure 65 Optical Injection Locking configuration.
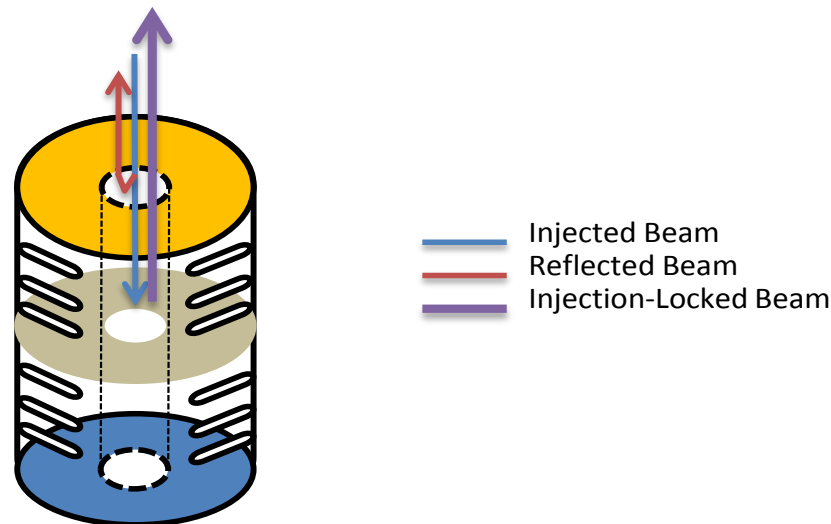
Figure 66 Optical Injection Locked VCSEL general structure.

4.1.1   Definition of the Locking Phenomena

When applying injection locking, there is a unidirectional coupling of one laser (master laser) to another laser (slave laser). When the light of a master laser is injected into the slave laser, the wavelength of the slave laser will be shifted to that of the master laser. In other words, the slave laser will be "referenced" to the master one.

4.1.2   Advantages of the Optical Injection Locking Technique [81]

The OIL technique results in several advantages for the OIL semiconductor laser operation. When a laser is injection locked, is stated that:

- The first effect over the slave laser is the noise reduction in the emission due to the light combination inside the laser cavity that will lead to an increase in the carrier number in the dominant mode instead of being available for the secondary modes.

- Due to the locking phenomena, the slave laser wavelength will not drift as it would do in free running condition because of the non-perfect clamping between the carriers to its threshold density.

- The modulation bandwidth of the laser will be enhanced due to the combination of several phenomena inside the laser cavity. The threshold of the locked mode is reduced respect to the free running case, the increase of the differential gain because of the threshold reduction and the photon density is higher for the locked mode that will suppress the spontaneous emission. All these factors contribute to increase the resonance frequency of the laser and, by that way, the modulation bandwidth.

- The optical injection locking reduces the linewidth of the slave laser by reducing the side mode suppression ratio (SMSR) or suppressing completely the lateral modes.

4.1.3 Optically Injection Locked VCSEL Rate Equations [5], [81], [82]

The semiconductor laser cavity can be defined as resonator where the electrons at the input and the photons at the output are related according to the cavity parameters. During the optical injection locking, the parameters of the cavity are changed by photon concentration inside it. The behavior of the injection locking condition can be changed by the photon injection and the phase detuning between the two lasers.

The equations defined by Pantell for the semiconductor lasers are as follows:

$$\frac{dN(t)}{dt} = \frac{\eta I}{q V_{act}} - (A + B N(t) + C N(t)^2) - v_g G S(t) \tag{154}$$

$$\frac{dS(t)}{dt} = \Gamma v_g G S(t) - \frac{S(t)}{\tau_p} + \Gamma B \beta N(t)^2 \tag{155}$$

$$\frac{d\phi(t)}{dt} = \frac{\alpha_H \Gamma v_g a_o}{2} (N(t) - N_{tr})) \tag{156}$$

The Equation (154) is known as the carrier number equation, the Equation (155) is the photon number equation and the Equation (156) is the phase equation. The terms of this set of equations are described in Table 16.

Parameter	Description	Expression
$N(t)$	Electron density	-
$S(t)$	Photon density	-
V_{act}	Active region volume	-
v_g	Group velocity	-
β	Spontaneous emission coefficient	-
Γ	Confinement factor	-
τ_p	Photon lifetime	-
R_{sp}	Spontaneous emission rate	-
A	Shockly-Read-Hall non-radiative recombination coefficient	-
B	Bimolecular recombination coefficient	-
C	Auger non-radiative recombination coefficient	-
G	Gain	$G = a_o \dfrac{N(t) - N_{tr}}{1 + \varepsilon S(t)}$
a_o	Differential gain coefficient	-
N_{tr}	Transparency carrier density	-
ε	Gain compression factor	-
α_H	Henry Factor	-
L	Cavity Length	-

Table 16 VCSEL rate equation terms.

This set of equations was modified by Lang [78] to model the effects of the optical injection locking. These are redefined as follows,

$$\frac{dN(t)}{dt} = \frac{\eta I}{qV_{act}} - (A + BN(t) + CN(t)^2) - v_g GS(t) \qquad (157)$$

$$\frac{dS(t)}{dt} = \Gamma v_g GS(t) - \frac{S(t)}{\tau_p} + \frac{v_g}{L}\sqrt{S(t)S_{inj}}\cos(\theta) + \Gamma B\beta N(t)^2 \qquad (158)$$

$$\frac{d\phi(t)}{dt} = \frac{\alpha_H \Gamma v_g a_o}{2}(N(t) - N_{tr}) - \Delta\omega - \frac{v_g}{2L}\sqrt{\frac{S_{inj}}{S(t)}}\sin(\theta) \qquad (159)$$

The injection locking terms are defined in Table 17. From this set of equations it is possible to infer the following:

- The injected light into the cavity, represented as the photon number change the slave VCSEL behavior.

- The wavelength and phase detuning between the master and slave laser has influence inside the cavity properties due to the photons of both lasers using the same number of carriers inside the cavity.

Parameter	Descrition	Expression
S_{inj}	Photon density injected inside the follower VCSEL	-
θ	Phase difference between the master and follower optical fields	$\theta = \phi_{inj} - \phi(t)$
$\Delta\omega$	Frequency detuning	$\Delta\omega = \omega_{master} - \omega_{follower}$
κ_c	Coupling coefficient	$\kappa_c = \frac{v_g}{2L}$

Table 17 Injection Locked VCSEL rate equation terms.

4.1.4   Locking Range Calculations[5], [83]

By setting Equations (158) and (159) equal to zero, the steady state VCSEL locking range can be calculated. Solving Equations them for $\Delta\omega$, leads to:

$$\Delta\omega = \kappa_c \sqrt{\frac{S_{inj}}{S}}[\sin(\theta) - \alpha_H\cos(\theta)] \qquad (160)$$

The Equation (160) defines the frequency detuning between the master and slave laser. For manipulation ease, it can be arranged follows [5],

$$\Delta\omega = \kappa_c \sqrt{\frac{S_{inj}}{S}}\left[\sqrt{1 + \alpha_H^2}\right]\sin(\theta - tan^{-1}\alpha_H) \qquad (161)$$

This equation is useful to calculate de effective locking bandwidth of the system. Due to the sine function inside, the possible solution of this expression is limited by:

$$|\Delta\omega| \leq \kappa_c \sqrt{\frac{S_{inj}}{S}} \left[\sqrt{1 + \alpha_H^2} \right] \qquad (162)$$

According to [84], [85], the value of θ is limited between $-\frac{\pi}{2} < \theta < \frac{\pi}{2}$, and for this reason the boundaries of $\Delta\omega$ are given by:

$$-\kappa_c \sqrt{\frac{S_{inj}}{S}} \left[\sqrt{1 + \alpha_H^2} \right] \leq \Delta\omega \leq \kappa_c \sqrt{\frac{S_{inj}}{S}} \qquad (163)$$

Figure 67 presents the calculation of $\Delta\omega$ for $\alpha_H = 3.5$. From this calculation it is possible to conclude that the higher the injected power, the higher wavelength detuning between the two lasers.
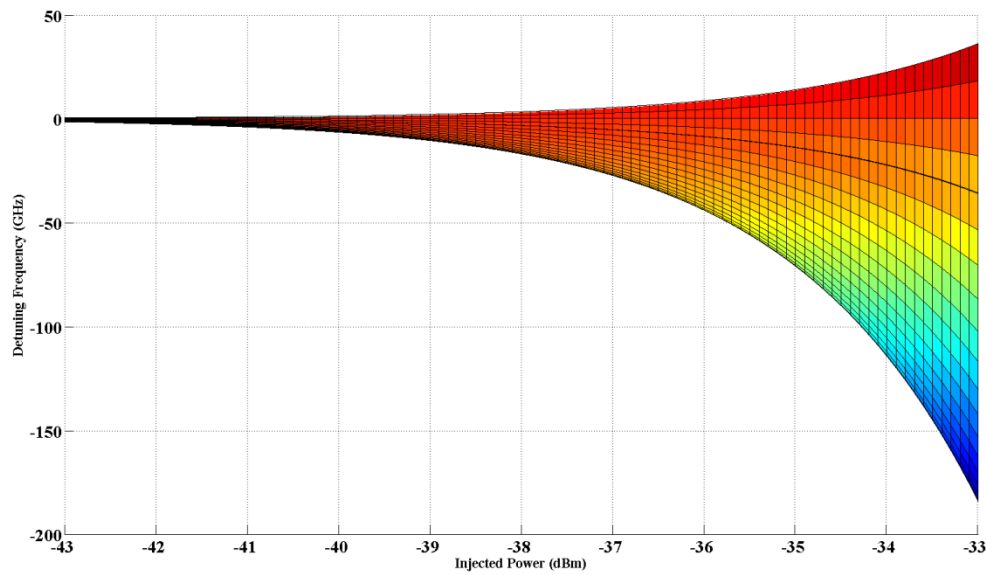
Figure 67 Calculated Locking range for α_H= 3.5.

4.1.5   Small Signal Analysis

The small signal analysis of the injection locked VCSEL allows to simplify the computation of the VCSEL response by assuming a single tone and small signal modulation. Using this analysis, it is no necessary to solve the set of differential equations which is time consuming and let us understand in a better way the complex dynamics of the injection locked laser. From this analysis, the frequency response of the OIL VCSEL is obtained. It is important to remark that for the small signal analysis, the modulating current magnitude is smaller than the DC bias current ($\Delta I \ll I_{bias}$), and the bias point is considered in the linear operation zone of the VCSEL P-I curve.

Recalling Equations $(157 - 159)$, we have the set of rate equations.

$$\frac{dN(t)}{dt} = \frac{\eta I}{qV_{act}} - (A + BN(t) + CN(t)^2) - v_g GS(t) \qquad (164)$$

$$\frac{dS(t)}{dt} = \Gamma v_g G S(t) - \frac{S(t)}{\tau_p} + \frac{v_g}{L}\sqrt{S(t)S_{inj}}\cos(\theta) + \Gamma B \beta N(t)^2 \tag{165}$$

$$\frac{d\phi(t)}{dt} = \frac{\alpha_H \Gamma v_g a_o}{2}(N(t) - N_{tr}) - \Delta\omega - \frac{v_g}{2L}\sqrt{\frac{S_{inj}}{S(t)}}\sin(\theta) \tag{166}$$

First, we consider that the laser is modulated by a current signal $\Delta I e^{j\omega t}$ that is biased at $\bar{I}$. The same assumption is made for the photon, carrier and phase variations. These variables are expressed as,

$$I(t) = \bar{I} + \Delta I e^{j\omega t} \tag{167}$$

$$N(t) = \bar{N} + \Delta N e^{j\omega t} \tag{168}$$

$$S(t) = \bar{S} + \Delta S e^{j\omega t} \tag{169}$$

$$\phi(t) = \bar{\phi} + \Delta\phi e^{j\omega t} \tag{170}$$

Then, the differential terms of the equations can be written as:

$$\dot{N} = \frac{dN}{dt} \tag{171}$$

$$\dot{S} = \frac{dS}{dt} \tag{172}$$

$$\dot{\phi} = \frac{d\phi}{dt} \tag{173}$$

Replacing Equations (167-170) into (171-173), we have,

$$\Delta\dot{N}(I, N, S) = \frac{\partial \dot{N}}{\partial I}\Delta I + \frac{\partial \dot{N}}{\partial N}\Delta N + \frac{\partial \dot{N}}{\partial S}\Delta S \tag{174}$$

$$\Delta\dot{S}(N, S, \phi) = \frac{\partial \dot{S}}{\partial N}\Delta N + \frac{\partial \dot{S}}{\partial S}\Delta S + \frac{\partial \dot{N}}{\partial \phi}\Delta\phi \tag{175}$$

$$\Delta\dot{\phi}(N, S, \phi) = \frac{\partial \dot{\phi}}{\partial N}\Delta N + \frac{\partial \dot{\phi}}{\partial S}\Delta S + \frac{\partial \dot{\phi}}{\partial \phi}\Delta\phi \tag{176}$$

The gain was defined in Table 16, when it is derived respect to N and S, it is necessary to use two variables of interest, they are defined as follows,

$$G_N = \frac{\partial G}{\partial N} = \frac{a_o}{1 + \epsilon S} \tag{178}$$

$$G_N = \frac{\partial G}{\partial N} = \frac{a_o \epsilon (N - N_{tr})}{(1 + \epsilon S)^2} \tag{179}$$

Differentiating Equation (157) with respect to N, S, ϕ results in the following equations,

$$\frac{\partial \dot{N}}{\partial N} \Delta N = \left(-(A + 2BN + 3CN^2) - v_g G_N S\right) \Delta N \tag{180}$$

$$\frac{\partial \dot{N}}{\partial S} \Delta S = \left(-v_g G + v_g GS\right) \Delta S \tag{181}$$

$$\frac{\partial \dot{N}}{\partial I} \Delta I = \frac{\eta_i}{q V_{act}} \Delta I \tag{182}$$

Here, a new variable ρ is defined as:

$$\rho = \frac{v_g}{2L} \sqrt{\frac{S_{inj}}{S}} \tag{183}$$

Differentiating Equation (158) with respect to results in the following equations,

$$\frac{\partial \dot{S}}{\partial N} \Delta N = \left(\Gamma v_g G_N S - 2\beta BN\right) \Delta N \tag{184}$$

$$\frac{\partial \dot{S}}{\partial S} \Delta S = \left(-\Gamma v_g G_S S + \rho \cos \theta\right) \Delta S \tag{185}$$

$$\frac{\partial \dot{S}}{\partial \phi} \Delta \phi = \left(-2\rho S \sin \phi\right) \Delta \phi \tag{186}$$

The differentiation of the Equation (159) with respect to N, S, ϕ results in the following equations,

$$\frac{\partial \dot{\phi}}{\partial N} \Delta N = \frac{\alpha_H \Gamma v_g a_o}{2} \Delta N \tag{187}$$

$$\frac{\partial \dot{\phi}}{\partial S} \Delta S = \frac{\rho \sin \theta}{2S} \Delta S \tag{188}$$

$$\frac{\partial \dot{\phi}}{\partial \phi} \Delta \phi = \left(-\rho \cos \phi\right) \Delta \phi \tag{189}$$

Linearizing the rate equations, we have:

$$\Delta \dot{N} = \frac{\eta I}{q V_{act}} \Delta I - \left(A + BN + CN^2 + v_g GS(t)\right) \Delta N - \left(v_g G - v_g GS\right) \Delta S \tag{190}$$

$$\Delta \dot{S} = \left(\Gamma v_g G_N S - 2\beta BN\right) \Delta N - \left(-\Gamma v_g G_S S + \rho \cos \theta\right) \Delta S - \left(2\rho S \sin \phi\right) \Delta \phi \tag{191}$$

$$\Delta\dot{\phi} = \left(\frac{\alpha_H \Gamma v_g a_o}{2}\right)\Delta N + \left(\frac{\rho \sin\theta}{2S}\right)\Delta S - (\rho \cos\phi)\Delta\phi \tag{192}$$

Replacing these partial derivatives by variables to facilitate the manipulation, we have:

$$\Delta\dot{N} = \frac{\eta_i}{qV_{act}}\Delta I - \gamma_{NN}\Delta N - \gamma_{NS}\Delta S \tag{193}$$

$$\Delta\dot{S} = \gamma_{SN}\Delta N - \gamma_{SS}\Delta S - \gamma_{S\Phi}\Delta\phi \tag{194}$$

$$\Delta\dot{\phi} = \gamma_{\phi N}\Delta N + \gamma_{\phi S}\Delta S - \gamma_{\phi\phi}\Delta\phi \tag{195}$$

Now, it is possible to arrange the terms in the following equation system,

$$\frac{d}{dt}\begin{bmatrix}\Delta S\\\Delta N\\\Delta\phi\end{bmatrix} = \begin{bmatrix}-\gamma_{SS} & \gamma_{SN} & \gamma_{S\Phi}\\-\gamma_{NS} & -\gamma_{NN} & -\gamma_{N\phi}\\\gamma_{\phi N} & \gamma_{\phi S} & \gamma_{\phi\phi}\end{bmatrix}\begin{bmatrix}\Delta S\\\Delta N\\\Delta\phi\end{bmatrix} + \frac{\eta_i I}{qV_{act}}\begin{bmatrix}0\\\Delta I\\0\end{bmatrix} \tag{196}$$

To transform this equation from time domain to frequency domain, we apply the Laplace transformation, giving the following equation:

$$\begin{bmatrix}-\gamma_{SS} + j\omega & -\gamma_{SN} & \gamma_{S\Phi}\\\gamma_{NS} & \gamma_{NN} + j\omega & 0\\-\gamma_{\phi N} & -\gamma_{\phi S} & \gamma_{\phi\phi} + j\omega\end{bmatrix}\begin{bmatrix}\Delta\tilde{S}\\\Delta\tilde{N}\\\Delta\tilde{\phi}\end{bmatrix} + \frac{\eta_i \tilde{I}}{qV_{act}}\begin{bmatrix}0\\1\\0\end{bmatrix} \tag{197}$$

To solve Equation (197), it is necessary to calculate the determinant of the matrix for the γ terms, as follows.

$$\Lambda = \begin{vmatrix}\gamma_{SS} + j\omega & -\gamma_{SN} & \gamma_{S\Phi}\\\gamma_{NS} & \gamma_{NN} + j\omega & 0\\-\gamma_{\phi N} & -\gamma_{\phi S} & \gamma_{\phi\phi} + j\omega\end{vmatrix} \tag{198}$$

Then, using the rule of Kramer, it is possible to solve the system for $\Delta\tilde{S}$, as follows,

$$\Delta\tilde{S} = \frac{\eta_i \tilde{I}}{qV_{act}}\frac{\begin{vmatrix}0 & -\gamma_{SN} & \gamma_{S\Phi}\\1 & \gamma_{NN} + j\omega & 0\\0 & -\gamma_{\phi S} & \gamma_{\phi\phi} + j\omega\end{vmatrix}}{\Lambda} \tag{199}$$

By simplifying the Equation (199)

$$\Delta\tilde{S} = \frac{\eta_i \tilde{I}}{qV_{act}}\frac{(\gamma_{SN}\gamma_{\phi\phi} - \gamma_{\phi N}\gamma_{N\phi}) + j\omega\gamma_{SN}}{\Lambda} \tag{200}$$

Equation (197) can be solved to find $\Delta\tilde{I}$. Once $\Delta\tilde{I}$ is found, is it possible to define the transfer function of the OIL VCSEL. The transfer function is defined by Equation (201).

$$H(j\omega) = \frac{\Delta\tilde{S}}{\Delta\tilde{I}} \tag{201}$$

4.1.6 Physical Interpretation of the Optical Injection Locking

The Optical Injection Locking allows to enhance the direct modulation bandwidth of the VCSEL. This enhancement is due to the higher photon number inside the VCSEL cavity. The properties of the cavity are only changed by varying the bias current of the VCSEL or varying the injection conditions. The injection conditions can be changed in two ways:

- By varying the injected optical power that will lead to a photon number variation inside the cavity of the slave VCSEL. The photon number increase inside the cavity will compete for a fixed number of available carriers, this modifies the cavity parameters.

- By varying the frequency (wavelength) frequency between the master and slave lasers, this is known as the "frequency detuning", it is expressed as:

$$\Delta\omega = \omega_{Master} - \omega_{Slave} \tag{202}$$

When the slave VCSEL is under locking condition, the slave laser emits at the master frequency. The Figure 68 summarizes the optical injection locking principles.
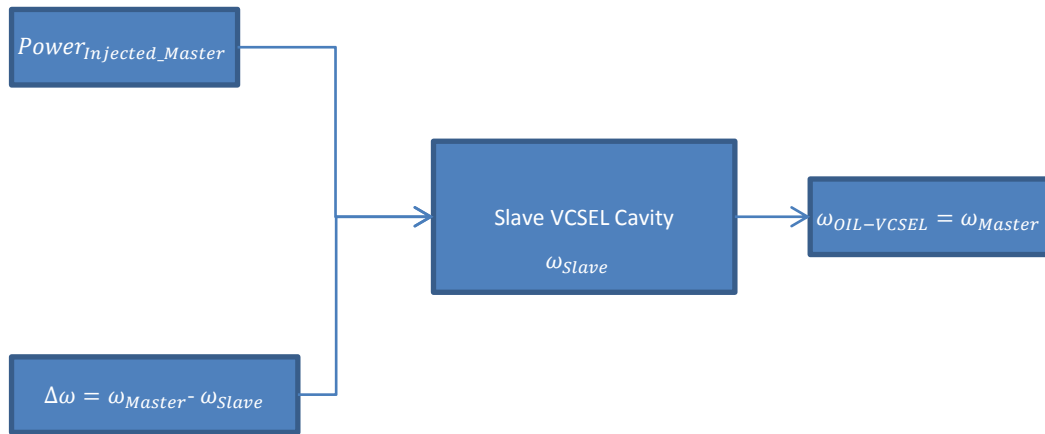
Figure 68 Optical Injection Lockingof VCSEL (OIL) variables.

The resonance frequency increase of the injection locked laser is caused by the cavity mode shift to a lower resonance frequency ($\omega_{downshifted}$) under optical injection locking. The difference from the master laser frequency ω_{Master} and the downshifted frequency ($\omega_{downshifted}$) defines the enhanced resonance frequency, expressed as follows.

$$\omega_{Enhanced\_Resonance\_Freq} = \omega_{Master} - \omega_{Donshifted} \tag{203}$$

4.2 Frequency Response of the Optically Injection Locked VCSEL

The optical injection locking experiments performed in this work were performed using packaged and pigtailed VCSELs from the Korean manufacturer RayCan. The frequency response is obtained using the extraction process described by Hayat [5].

4.2.1 External Cavity Laser by 1.5 µm VCSEL Optical Injection Locking

The first experimental setup built to test the optical injection locking technique is shown in Figure 69. A 1.5 µm single mode VCSEL is locked to an external cavity tunable laser in the 1.5 µm band. To observe the spectrum of the optically injection-locked VCSEL an Optical Spectrum Analyzer (OSA) is used. In Figure 70 the optically injection-locked VCSEL spectrum is shown when biased at 7 mA in free running condition with a frequency detuning of 10 GHz and 3 mW of power injection into the slave laser cavity.
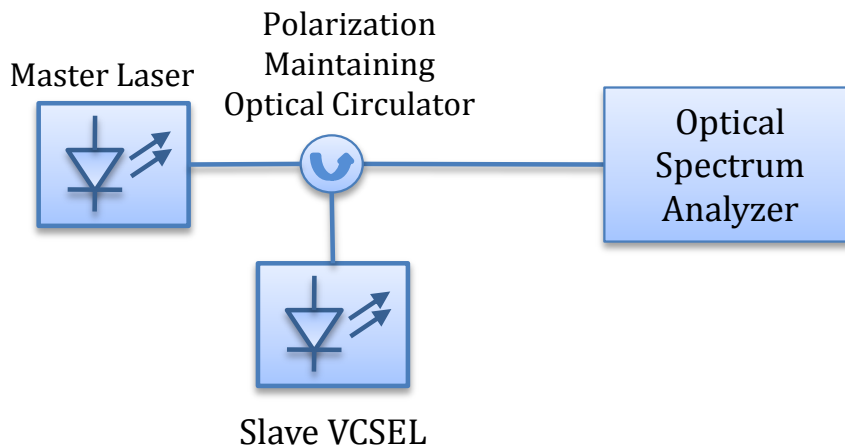
Figure 69 Optical injection locking testbench.
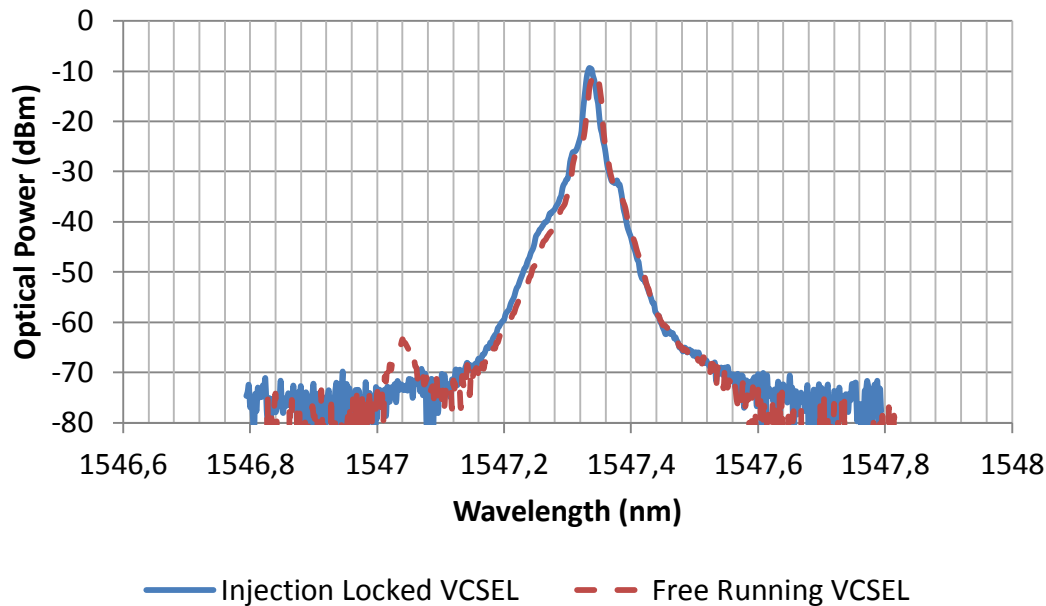
Figure 70 Optical spectrum for a VCSEL in free-running and injection-locked conditions.

To achieve the optical injection-locked state it is relatively simple using an OSA to confirm the locked state. The slave VCSEL is optically injection-locked when the dominant mode towards that one of the master laser, in this case, the lateral mode of the free-running VCSEL disappears completely, and the lasing mode is reinforced.

Once the VCSEL is under injection-locked state, the frequency response test is performed following the setup described in Figure 71. The injection-locked VCSEL is directly modulated through a bias tee with a signal injected from the RF port of the Vector Network Analyzer (VNA). From the output/input relation computed in a frequency sweep by the VNA. The bandwidth of the direct modulated VCSEL is defined according to the -3 dB criteria, a decrease of 3 dB on the frequency response magnitude defines the cut-off frequency of the laser.
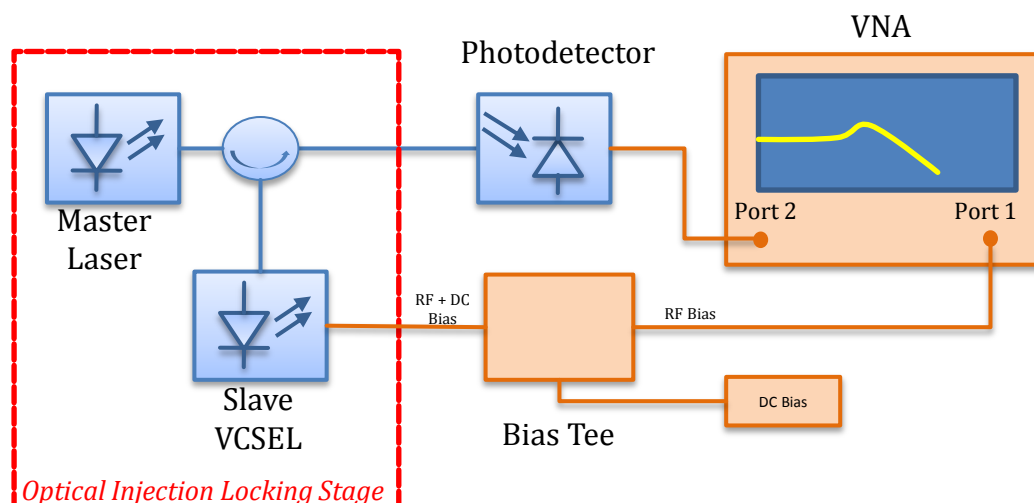
Figure 71 Optical injection-locked VCSEL frequency response test bench setup.

The frequency response of the external cavity laser by VCSEL OIL is presented in Figure 72. The direct modulation frequency response of the OIL laser is enhanced with respect to the free running frequency response of the VCSEL in 6 GHz. The

conditions for this measurement were a fixed optical injection of 7.5 dB with a frequency detuning of 5 GHz. The slave VCSEL bias current is swept from 3 to 8 mA.

To validate these results, a comparison with OIL VCSEL circuit model is implemented in ADS (Advanced Design Systems) software and the rate equations small signal model implemented using Matlab. The predictive models approaches to the measured frequency response of the laser. A frequency peak disparity is observed in the rate equation based curve, this can be attributed to the non modelling of the impedance matching in the Matlab model. The circuit model of the OIL VCSEL is based in the design of a low pass microwave filter of third order, it is shown in Figure 73. Each model parameters are summarized in Table 18 and 19.
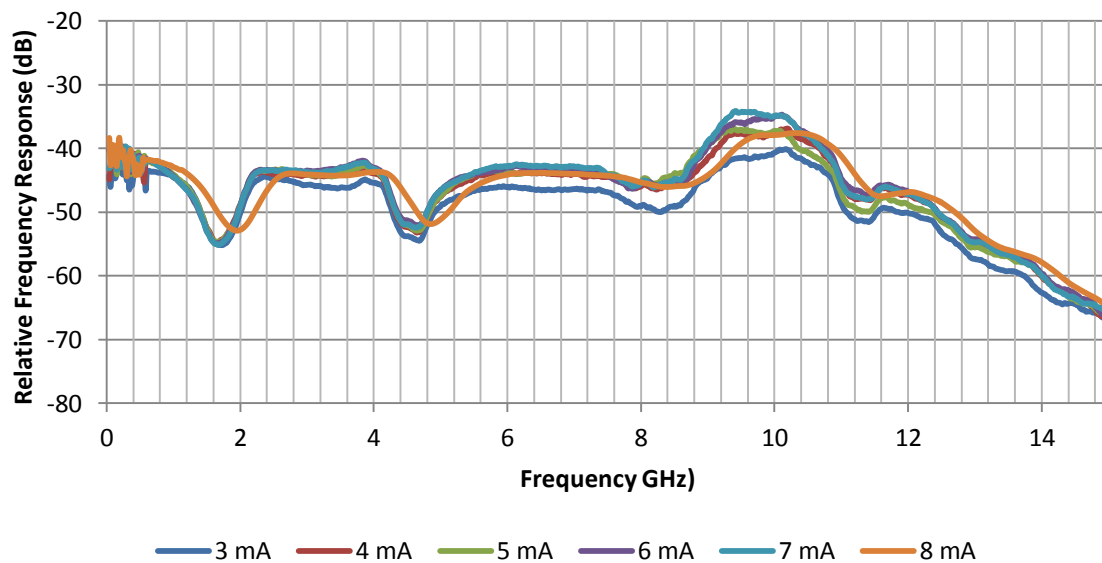
a)
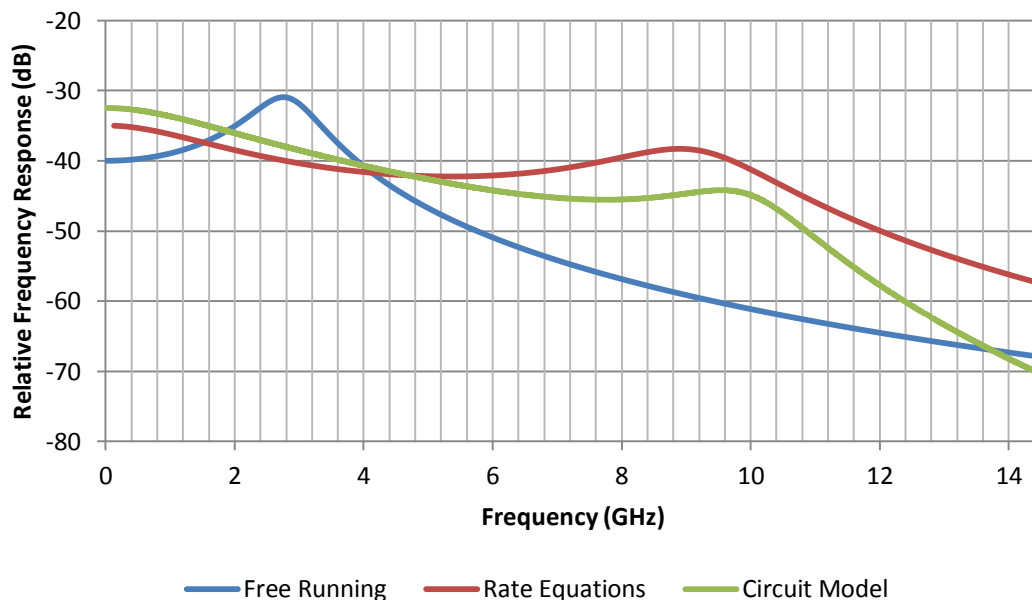
b)

Figure 72 External cavity laser by VCSEL 1.5 um optical injection locking frequency response a) measured b) simulated.

Figure 73 Optical injection locked VCSEL circuit based model.

4.2.2   DFB and 1.3 µm VCSEL Optical Injection Locking

The direct modulation frequency response for a 1.3 µm Raycan VCSEL under optical injection locking is characterized. A 1.3 µm DFB is used as a master laser, the optical injection locking conditions are set as follows: the VCSEL was biased at 3, 5 and 7 mA with a constant injection locking of 10 dB. The frequency detuning between the master and slave lasers is 6 GHz. The direct modulation bandwidth measurement setup is as in Figure 71. The frequency response of the DFB by VCSEL OIL is shown in Figure 74. The injection locked VCSEL bandwidth is enlarged respect to the free running VCSEL frequency response presented in Chapter 2 in 5 GHz. The measured frequency responses are compared with the rate equations and circuit model. These parameters are summarized in Table 18 and 19.

a)

b)

Figure 74 DFB by VCSEL optically injection locked laser frequency response a) Measure b) Simulated.

4.2.3   1.3 µm VCSEL by VCSEL Optical Injection Locking

The OIL technique was implemented using 1.3 µm VCSELs as master and slave. These are both manufactured by Raycan in pigtailed TO package configuration. To lock the slave VCSEL, it is necessary to use a semiconductor optical amplifier (SOA)

to boost the power injection, this is presented in Figure 75. The use of the SOA is required to locate the injection locked slave VCSEL inside the locking area, as presented in Figure 67.
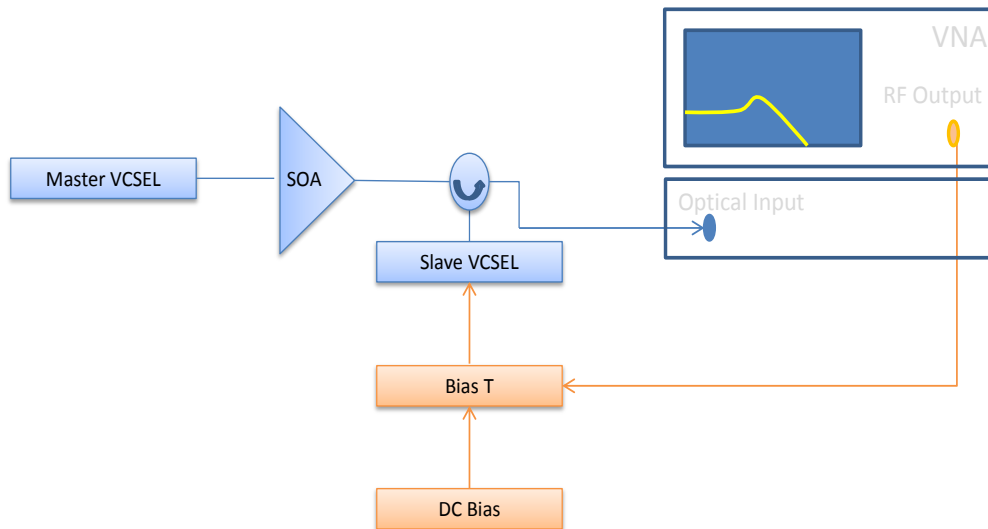
Figure 75 VCSEL by VCSEL OIL with SOA schematic configuration.

The VCSEL by VCSEL OIL is implemented by tuning the VCSELs at closed wavelengths. This is done by varying the bias current of the VCSELs. In this test, the slave VCSEL is biased at 7.7 mA and the injected power from the master laser is 0.7 dBm. The frequency response is presented in Figure 76. At this bias current, the cut-off frequency of the free running VCSEL is 4.4 GHz and for the OIL VCSEL is 10.1 GHz, with a negative frequency detuning between the lasers of 0.6 GHz. It is important to remark that when using the SOA, the optical spectrum profile of the master VCSEL is distorted due to the nonlinear effect of the SOA gain medium (Fabry-Perot structure inside), Figure 77 presents the VCSEL by VCSEL OIL spectrum.
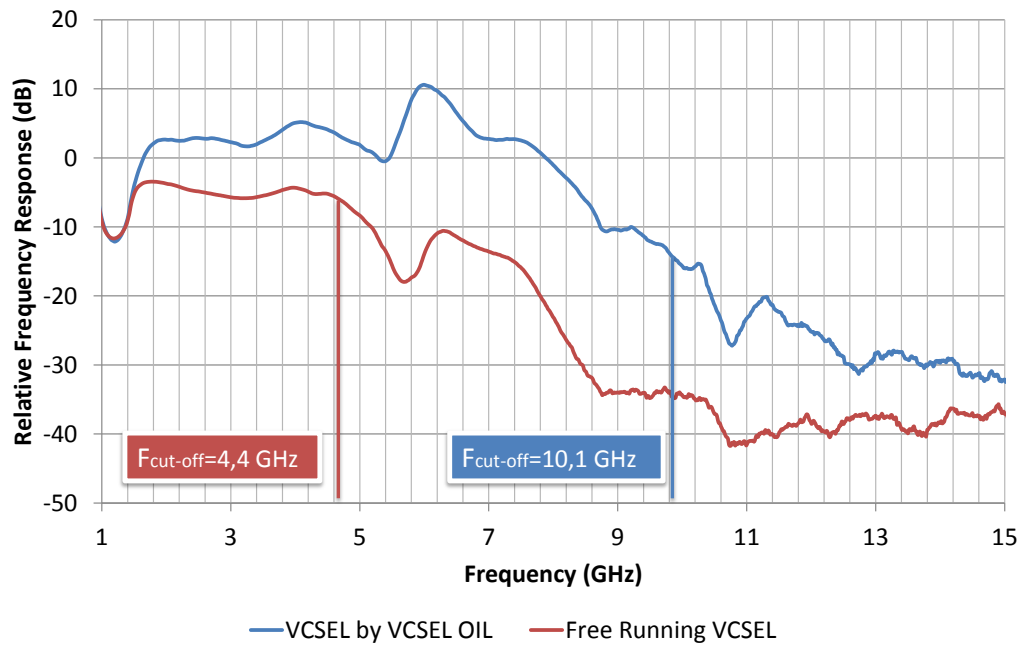
a)
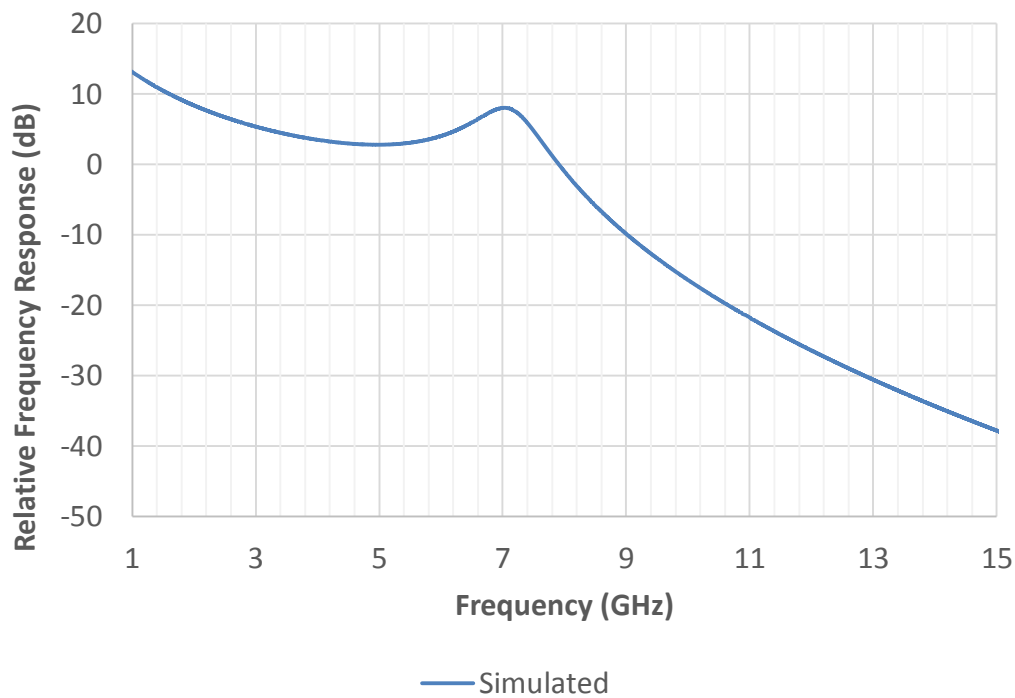
b)

Figure 76 VCSEL by VCSEL OIL frequency response without SOA.
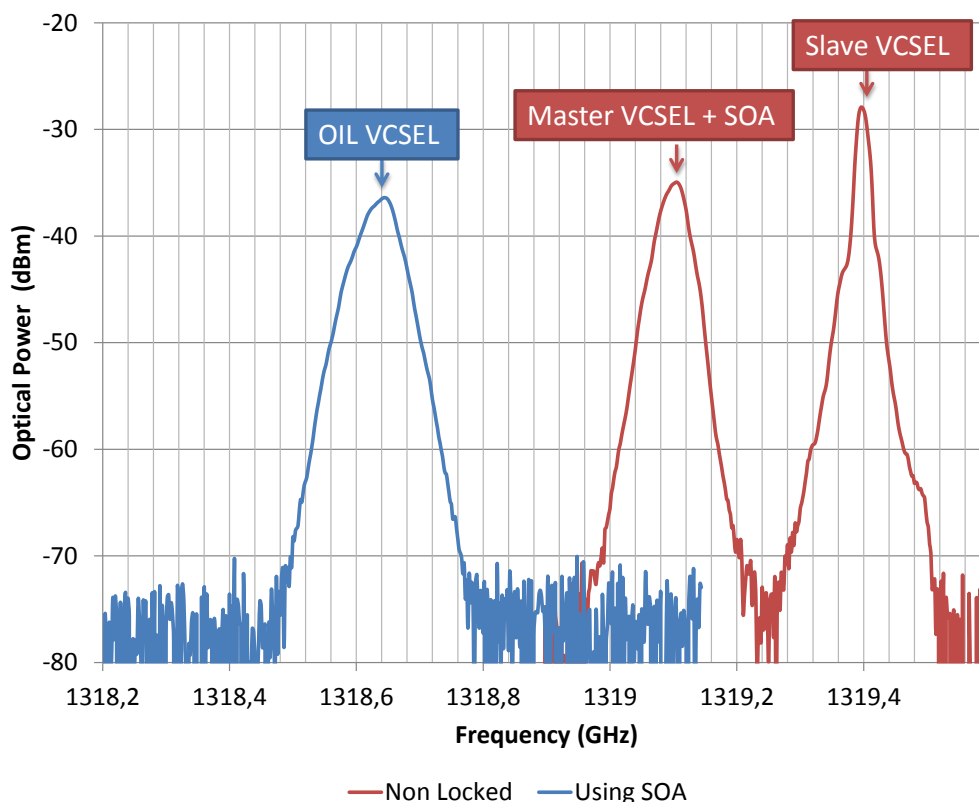
Figure 77 Optical spectrum of a 1.3 μm injection locked VCSEL using SOA and VCSEL as master laser.

4.2.4   Predictive model parameter summary

The circuit model parameters of the OIL VCSEL are presented in Table 18. For the OIL VCSEL small signal model, Table 19 summarizes its variables.

OIL Master/Slave Configuration	C_1	L_2	C_2	L_2
External cavity – 1.5 μm VCSEL	1.094 pF	0.595 nH	1.3837 pF	0.4711 nH
DFB – 1.3 μm VCSEL	0.8460 pF	1.4545 nH	0.8460 pF	-
VCSEL – 1.3 μm VCSEL	0.7817 pF	1.3427 nH	0.7810 nH	-

Table 18 OIL VCSEL circuit model parameters.

Parameter	Units	Value
η_i	-	0.8
τ_e	Ns	0.61
N_{th}	cm^{-3}	$5.33 * 10^{18}$
N_{tr}	cm^{-3}	$1.8 * 10^{18}$
A	s^{-1}	$7 * 10^7$
B	$cm^3/_S$	$0.8 * 10^{10}$
C	$cm^6/_S$	$3.5 * 10^{-29}$
a_o	cm^2	$2 * 10^{-16}$
v_g	$cm/_S$	$0.8 * 10^{10}$
ε	cm^3	$0.7 * 10^{-17}$
τ_p	ps	4
S	cm^{-3}	$7.93 * 10^{14}$
Γ	-	0.04
β	-	$1 * 10^{-4}$
V_{act}	cm^3	$1 * 10^{-12}$
τ_e	s^{-1}	$0.67 * 10^{-9}$

Table 19 OIL small signal model simulation intrinsic VCSEL parameters.

4.3 Relative Intensity Noise in Long Wavelength Optically Injection-Locked VCSELs

The Relative Intensity Noise (RIN) basics are presented in Chapter 2. In this section, the RIN of OIL VCSELs is measured at different locking conditions. In this section the OIL VCSELs RIN is measured for the following Master Laser / Slave Laser configuration:

- External cavity tunable laser (master) – 1.5 µm VCSEL (slave)
- DFB Laser (master) – 1.3 µm VCSEL (slave)
- 1.3 µm VCSEL (master) – 1.3 µm VCSEL (slave)

The RIN measurement setup schematic is presented in Figure 78. This consists in the OIL VCSEL module connected to a high speed photodetector to measure the photodetected current and the RF power. Using the RIN definition described in Chapter 2 the RIN is found.
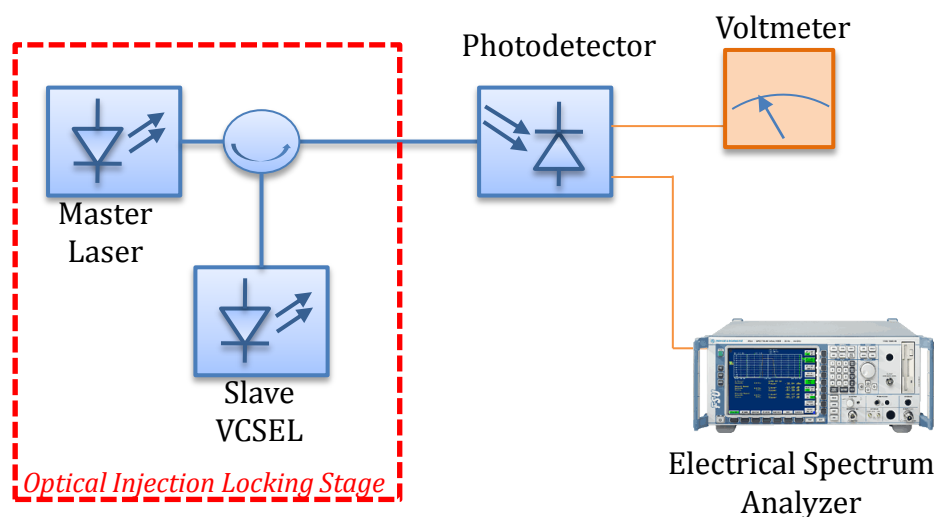
Figure 78 OIL VCSEL RIN measurement setup.

4.3.1 Relative Intensity Noise of the Optical Injection Locking using External Cavity Tunable Laser by 1.5 µm VCSEL

A RIN measurement comparison is performed between a free running 1.5 µm VCSEL and an OIL 1.5 µm VCSEL. It is important to remark the resonance peak of the RIN is shifted due to the injection into the VCSEL cavity. This is explained from the fact that when the OIL is applied, most of the carriers are available for the stimulated emission, leaving less for the spontaneous process and reducing by this way the laser noise. The OIL VCSEL RIN for a 1.5 µm VCSEL is presented in Figure 79.

When OIL is applied, it is said that the RIN is reduced, but saying this in a more detailed way, it is important to take into account that the resonance peak is just moved forward other frequency, this mechanism permits the reduction of the VCSEL

RIN at an specific frequency range that is useful when the RIN peak is placed at the modulating frequency.

In this measure, the injected power into the slave VCSEL is 3.6 mW and the frequency detuning is -3GHz. The resonance peak is moved from 3.86 GHz in free running (RIN=-139.40 dB/Hz) condition to 5.57 GHz under OIL (RIN=148.84 dB/Hz). If the free running resonance peak is considered, the enhancement of the RIN using OIL is 9.44 dB.
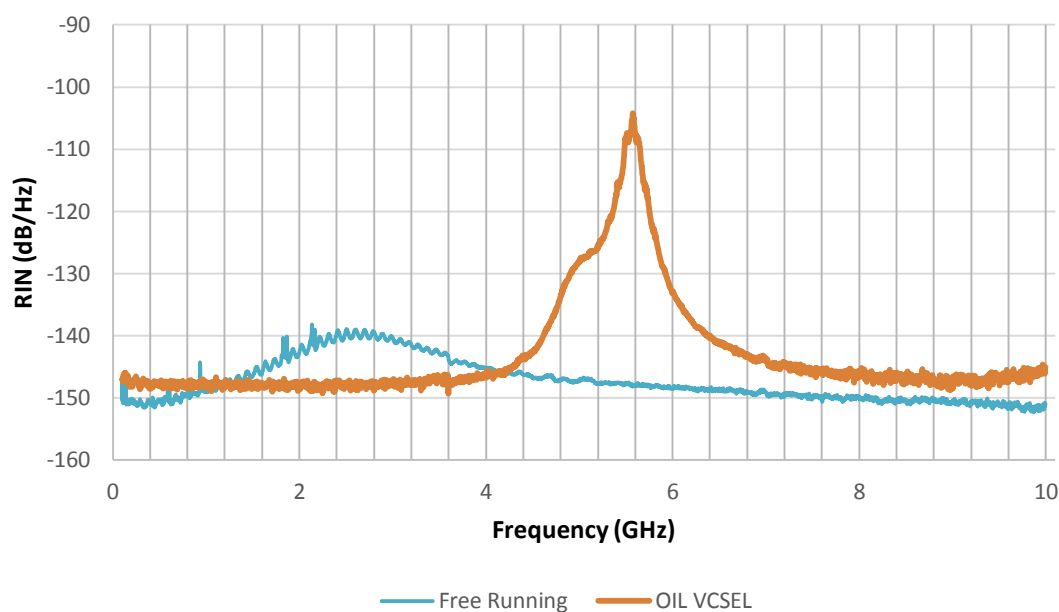
Figure 79 RIN measurement for free running and OIL 1.5 μm VCSEL.

4.3.2 Relative Intensity Noise of the Optical Injection Locking using DFB and 1.3 μm VCSEL

A 1.3 μm OIL VCSEL RIN is measured using a DFB laser as master. This configuration measurement is performed by biasing the VCSEL at three different currents in the linear operation regime of the semiconductor laser (3, 5 and 7 mA). The RIN is measured for two injected power values, 5 and 12 mW. These results are shown in Figure 80. For these set of measurements, it is interesting to observe the RIN trends. In the first case, for the OIL VCSEL biased a 3 mA, there is an evident RIN enhancement of 10 dB of RIN respect to the free running VCSEL resonance peak, the resonance peak is moved to 4.95 GHz and 6 GHz for the injection power at 5 and 12 mW, respectively. The trend is not the same for the OIL of VCSEL when biasing at 5 and 7 mA, in these cases to lock the VCSEL it is necessary to increase the temperature of the DFB master laser to match the VCSEL wavelength – taking into account that the VCSEL wavelength increases when increasing the bias current – The heating of the DFB derives out a RIN degradation and by the way, degrading the OIL VCSEL RIN, see Figures 80 b and c. When increasing the injected power, the resonance peak is moved toward higher frequencies, this keeps the same trend than in the 1.5 μm case. These results are summarized in Table 20.
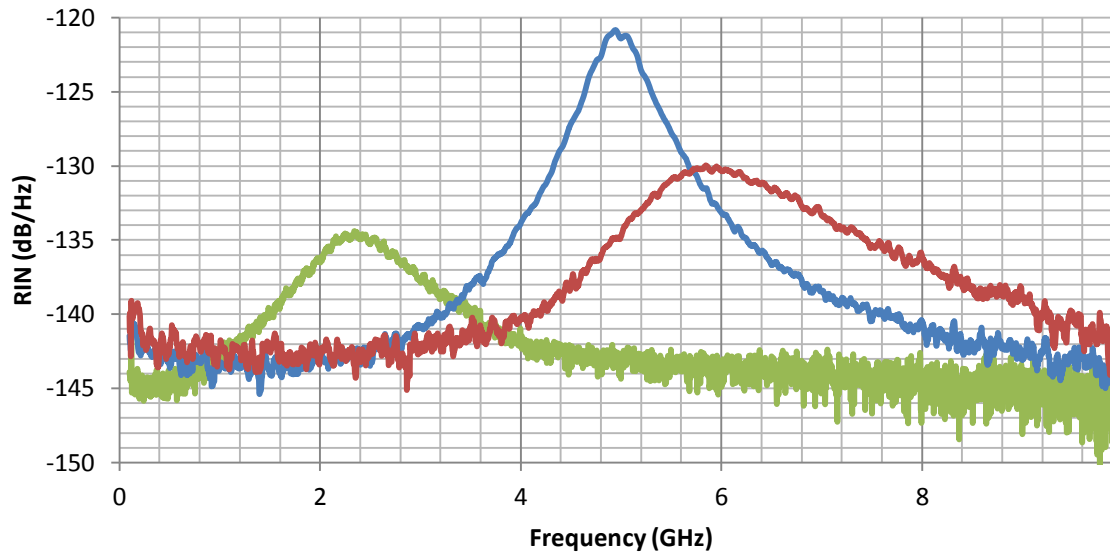
a)

b)

c)
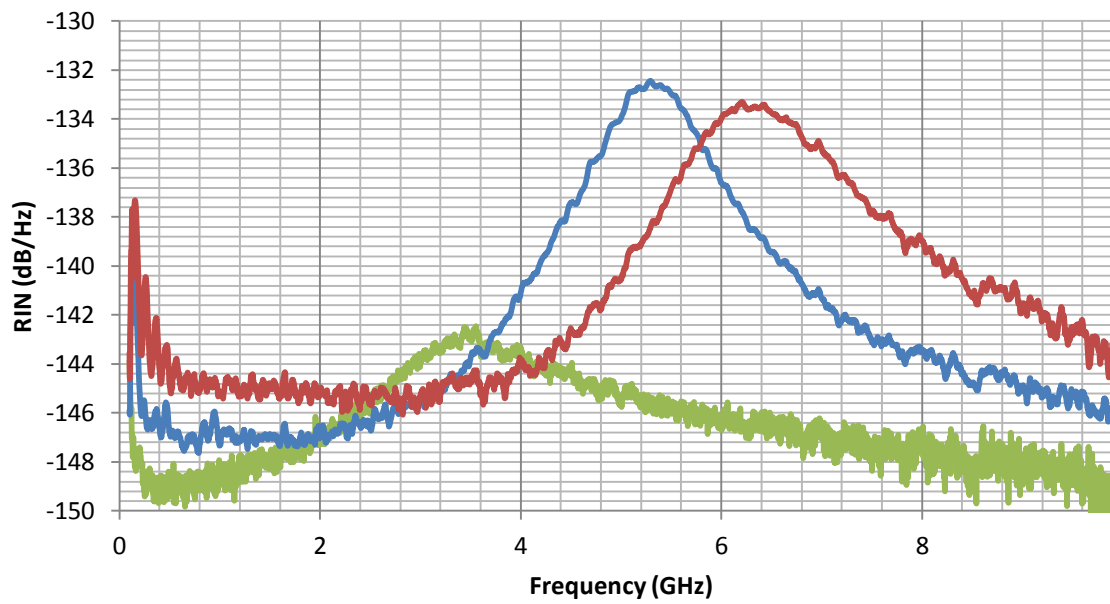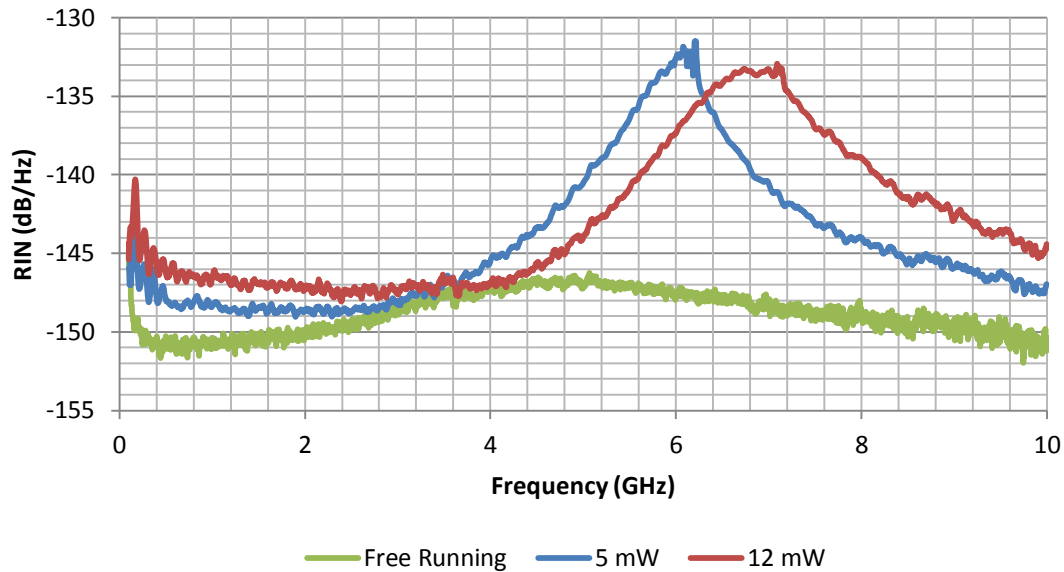
Figure 80 OIL 1.3 µm VCSEL RIN measurement with the VCSEL biased at a) 3 mA b) 5 mA c) 7 mA.

The relevant RIN values for the purpose of this project are summarized in Table 20. The resonance frequency increase for the rising of the bias current has been already shown for free running VCSELs, the resonance frequency of the RIN increases as $\sqrt{I_{threshold} - I_{bias}}$ does. Furthermore, the resonance frequency increase of the OIL VCSEL RIN is observed for each bias step, they are higher than the free running VCSEL RIN. We take advantage of this phenomenon by shifting the RIN peak towards higher frequencies when it is necessary to apply direct modulation to the laser at frequencies that are usually perturbed by high RIN values. Regarding to the application goal where the OIL VCSELs are going to be used, the RIN value of the VCSELs at 2.49 and 10 GHz are shown in this Table. There is an evident reduction of RIN at those frequencies when the OIL technique is applied. These values will be use for the phase noise predictive model in Chapter 5.

Configuration	VCSEL bias current (mA)	Injected power (mW)	RIN resonance peak (GHz)	RIN at peak (dB/Hz)	RIN at 2.49 GHz (dB/Hz)	RIN at 10 GHz (dB/Hz)
Free running VCSEL	3	-	2.25	-134.6	-134.9	-143.7
	5	-	3.53	-142.5	-135.3	-148.8
	7	-	4.83	-146.5	-149.8	-151.2
OIL VCSEL (DFB/VCSEL)	3	5	4.91	-120.9	-143.4	-142.6
		12	5.92	-130.4	-142.3	-142.0
	5	5	5.31	-132.5	-146.5	-145.7
		12	6.32	-133.5	-145.7	-143.6
	7	5	6.06	-132.4	-148.8	-146.9
		12	6.78	-133.4	-147.7	-144.4

Table 20 RIN summary for the 1.3 um DFB by VCSEL optical injection locked laser.

4.3.3 Relative Intensity Noise of the 1.3 μm VCSEL by VCSEL Optical Injection Locking

The VCSEL by VCSEL OIL RIN measurement is carried out using 1.3 μm wavelength lasers. Both lasers are pigtailed and TO packaged. Due to the non-tunable nature of these VCSELs, to get to the OIL condition, the master VCSEL wavelength is locked to the slave one by setting the master VCSEL bias current and temperature in the right values to make the master VCSEL emission shift to the slave VCSEL, this is done by monitoring the optical spectrum with the OSA. The measurements are taken with the slave VCSEL biased at 3, 5 and 7 mA. To boost the master VCSEL power, a semiconductor optical amplifier is placed at the master output, as shown in Figure 81. The use of the SOA assures the locking condition of the slave laser.
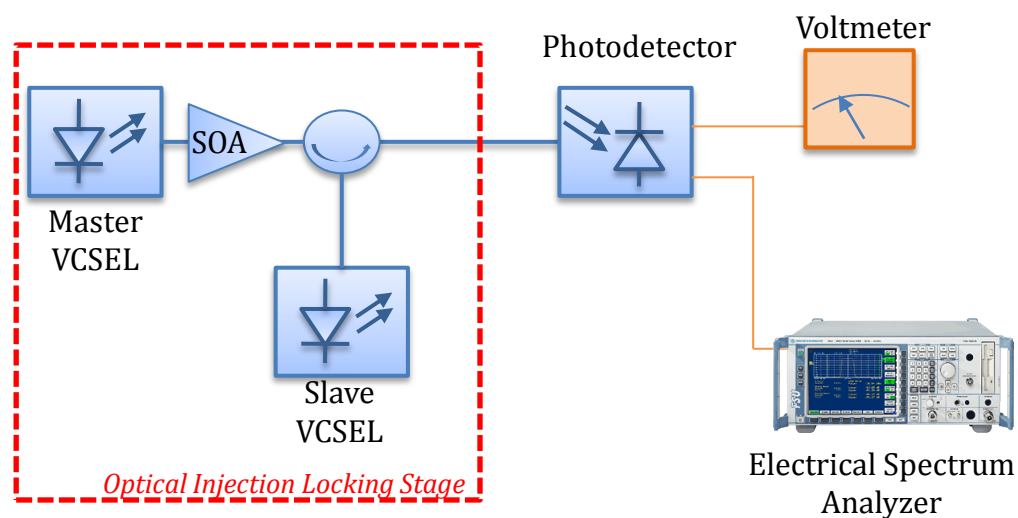
Figure 81 VCSEL by VCSEL OIL RIN measurement schematic using SOA.

The RIN curves obtained from these measurements are shown in Figure 82. The optical injected power into the slave VCSEL cavity is 1.25 mW. It is observed from this figure that RIN suffers a dramatic degradation when the VCSEL by VCSEL OIL technique is implemented (average of 30 dB in the frequency range). This is explained by the noise introduction from the semiconductor optical amplifier (SOA), the SOA is susceptible to high frequency noise, a carrier life time of 1 ns permits a good frequency response up to 1 GHz from the pump source, beyond this frequency it becomes nonlinear and noisier [86], [87]. The RIN measurement is performed from 100 MHz to 10 GHz. The RIN curves for the VCSEL by VCSEL OIL at 3 and 5 mA show the resonance peak shift with respect to the free running case. For the 7 mA VCSEL by VCSEL OIL curve, this trend is not follow due to the SOA low saturation power. These results are summarized in Table 21.

a)

b)

c)
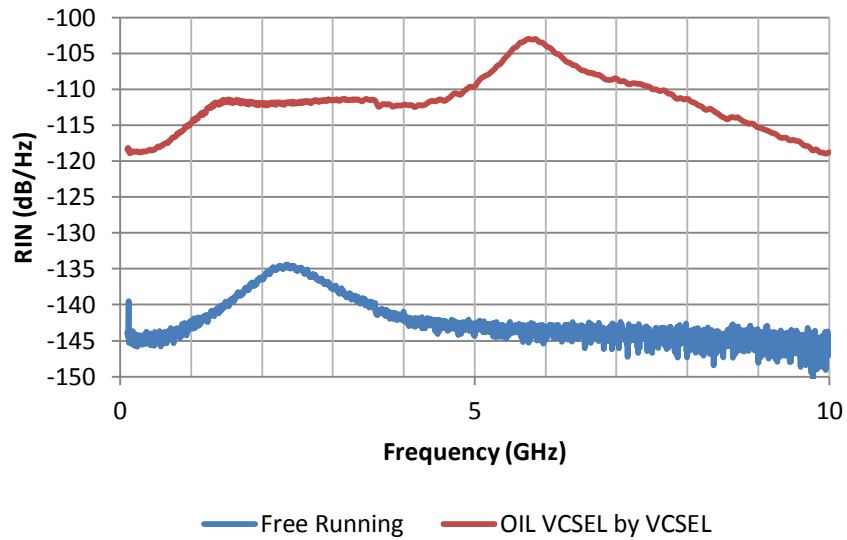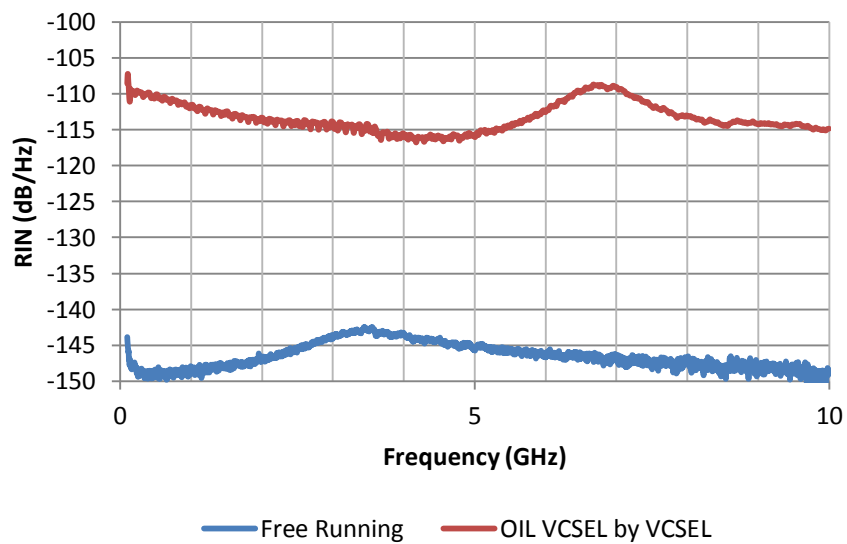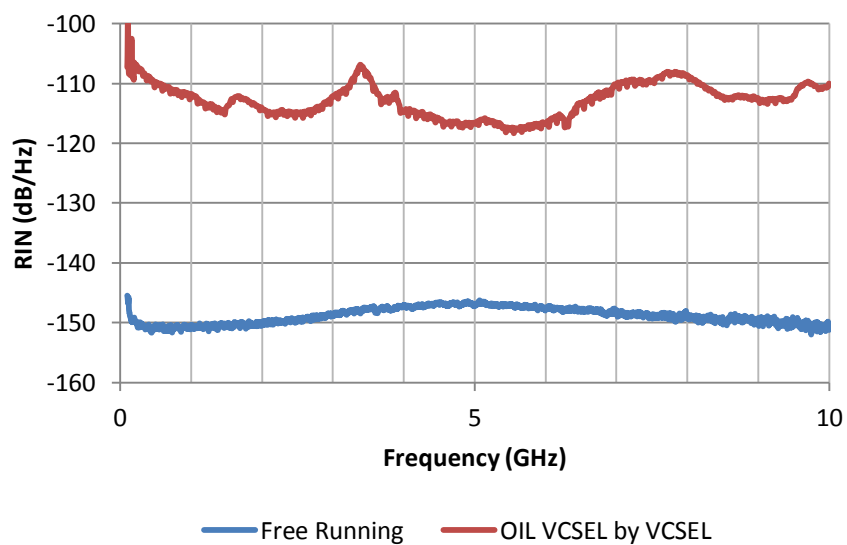
Figure 82 1.3 µm VCSEL by VCSEL OIL RIN curves a) 3 mA b) 5 mA c) 7 mA.

Configuration	VCSEL bias current (mA)	Injected power (mW)	RIN resonance peak (GHz)	RIN at peak (dB/Hz)	RIN at 2.49 GHz (dB/Hz)	RIN at 10 GHz (dB/Hz)
Free running VCSEL	3	-	2.25	-134.4	-135.2	-146.1
	5	-	3.53	-142.8	-145.6	-148.8
	7	-	4.88	-146.8	-149.6	-151.2
OIL VCSEL (VCSEL/VCSEL)	3	1.25	5.82	-103.1	-111.9	-118.8
	5	1.25	6.81	-108.7	-113.7	-114.8
	7	1.25	-	-	-114.8	-110.0

Table 21 RIN summary for the 1.3 um VCSEL by VCSEL optical injection locked laser.

Conclusion

Along this Chapter, the OIL technique has been applied to long wavelength VCSELs. From the experiences performed it is seen that the OIL enhances the bandwidth of the VCSELs. From the frequency response curves of the OIL VCSEL, it is observed that parasitic effects of the VCSEL TO package dwindles the microwave performance of the laser, especially at the VCSEL input impedance mismatch. For this reason, when the injection locked VCSEL rate equations are modeled, they do not track the same values than the actual measurement, anyway, the OIL TO packaged VCSEL frequency response follows well the rate equations trend. A circuit based model of the OIL VCSEL frequency response is proposed inspired in the low pass filter characteristic behavior of the VCSEL dynamic response.

The RIN measurements performed along this chapter permit to conclude that if an OIL VCSEL RIN enhancement is desired, the master laser must have lower RIN than the slave laser. If the previous condition is not satisfied, there will be a degradation of the OIL VCSEL RIN compared to that one of the VCSEL in free running condition.

When the VCSEL by VCSEL OIL is implemented, it is necessary to assure the VCSEL wavelengths proximity and power in pursuance of the OIL state. From the experiments performed for the RIN measurement of the VCSEL by VCSEL OIL it is observed that is necessary to boost the master laser beam to arrive at the OIL VCSEL locking range. The drawback under this configuration is that, due to the high RIN nature of the SOA, the VCSEL by VCSEL OIL output RIN is highly degraded.

Chapter 5

Optically Injection Locked VCSEL Based Optoelectronic Oscillator Experiments

Introduction

This Chapter presents the experimental results of the Optically Injection Locked VCSEL application into the optoelectronic oscillator. Several Master/Slave laser configuration of the Optical Injection Locking technique are introduced into the optoelectronic oscillator.

These experiments are carried out using long wavelength VCSELs at 1.3 and 1.5 µm. The implemented Optically Injection Locked VCSEL Based Optoelectronic (OILVBO) oscillator configurations are as follows:

- 1.5 µm external cavity tunable laser/VCSEL 2.49 GHz OILVBO
- 1.5 µm external cavity tunable laser/VCSEL 10 GHz OILVBO
- 1.3 µm DFB/VCSEL 10 GHz OILVBO.
- 1.3 µm VCSEL/VCSEL 10 GHz OILVBO.
- 1.3 µm OEO with external modulation at 2.49, 10 and 12 GHz.

The implemented VCSEL based optoelectronic oscillators are characterized in terms of frequency stability in order to study the spectral purity of the oscillator when the optical injection locking technique is applied. The performance of the OILVBO is compared to that one of an optoelectronic oscillator using external modulation.

5.1 Optically Injection Locked VCSEL Based Optoelectronic Oscillators

5.1.1 External Cavity Tunable Laser-by-VCSEL Optically Injection Locked 1.5 µm VCSEL Based Optoelectronic Oscillator at 2.49 GHz

A 2.49 GHz OILVBO is implemented according to the setup described in Figure 83. For the optical injection locking stage it is used a 1.5 µm external cavity tunable laser, and a Raycan pigtailed and TO packaged VCSEL at the same wavelength. A 2000 m optical fiber spool is used as delay line connected to a high-speed photodetector. A microwave bandpass cavity filter tuned at 2.49 GHz is used. A low noise microwave amplifier is used to assure the loop threshold gain.

It is important to remark that for this measurement, the OIL conditions (bias point in linear zone, injected power and frequency detuning) to assure the VCSEL locking are set to be those ones of Chapter 4 bandwidth measurement in order to assure a good microwave performance of the OIL under direct modulation. For this test the OIL conditions are as described in Table 22.

Parameter	Value
VCSEL bias current	3 mA
Frequency detuning (Δf)	6 GHz
OIL VCSEL Wavelength	1536.33 nm
VCSEL temperature	20 ºC

Table 22 OIL conditions for the 2.49 GHz OILVBO.

The OIL is under dynamic conditions when implemented in the OLVBO due to the fact that it is being directly modulated when the oscillator is operating. Figure 84 presents the optical spectrum for the 1.5 µm VCSEL in steady state (Figure 84a) and the spectrum when the oscillator is operating (Figure 84b). In steady state condition, the cavity mode suppression ratio (CMSR) is 40 dB, as shown in Figure 84a. For the modulated optical spectrum, the CMSR is 7 dB. Despite the modulation, the slave VCSEL does not go to unlocked condition. It is important to keep an adequate modulation power in the oscillator loop in order to not move the locking condition to an unstable state.
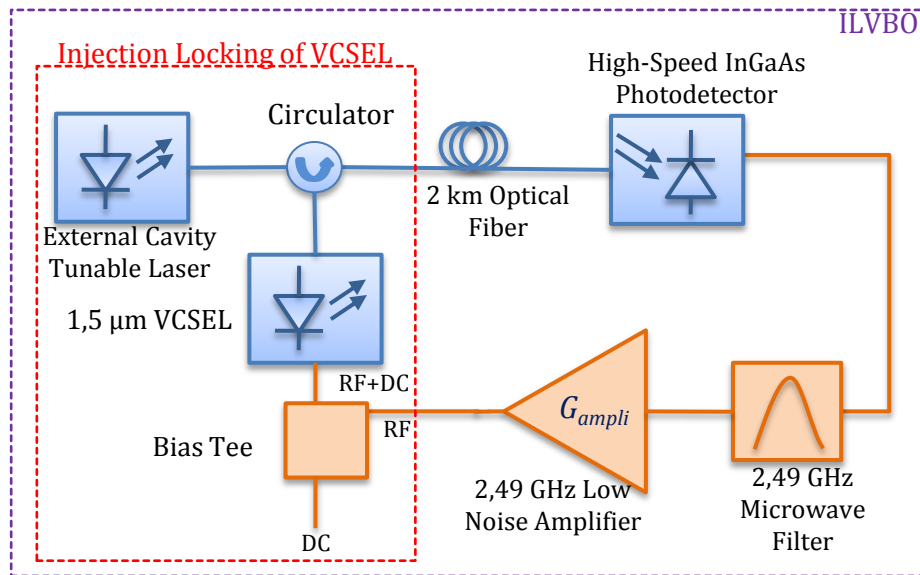
Figure 83 OIVBO using 1.5 μm VCSEL at 2.49 GHz scheme.

a)   b)
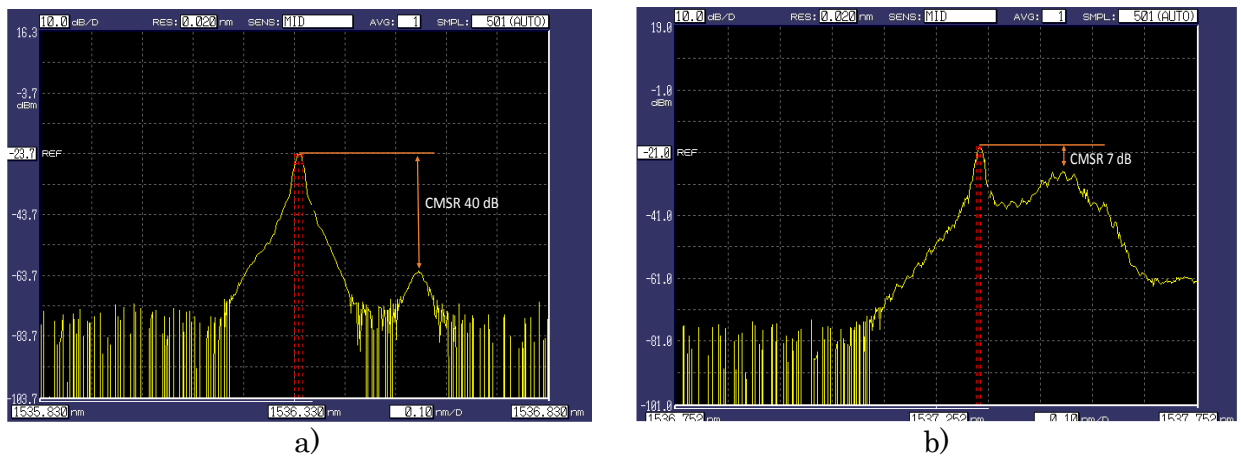
Figure 84 OIL VCSEL optical spectrum a) steady state b) under modulation.

The output signal spectrum is seen in Figure 85.
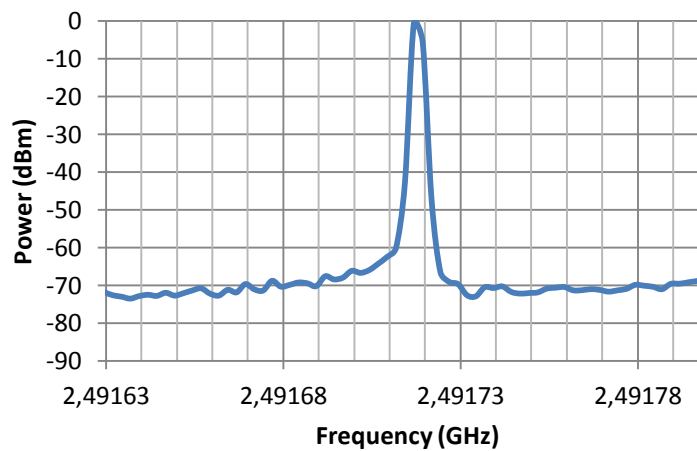
Figure 85 OILVBO using 1.5 μm VCSEL at 2.49 GHz output spectrum.

The phase noise measurement is performed using direct measurement method. Figure 86 presents the phase noise measurement for this oscillator. From this figure, it is possible to infer the following conclusions taking into account the Leeson model for a better understanding of this measurement:

- A -50 dB/decade slope up to 6 kHz offset. This slope is due to the optical interferometric noise conversion into close-in RF phase noise, which is caused by several factors in the photonics system such as the reflections in the optical fiber, connectors, optical circulator and the optical interference between the two beams of the master and slave lasers. The close-in phase noise due to optical interference in RF systems is described by Shieh and Maleki [69]. In this test the main close-in phase noise contribution is the beam interference between the slave and master laser.
- A -4.5 dB/decade slope due to flicker and white phase noise up to 12 kHz offset.
- Beyond 12 kHz offset, 0 dB/decade, it is the white phase noise that dominates the measurement.
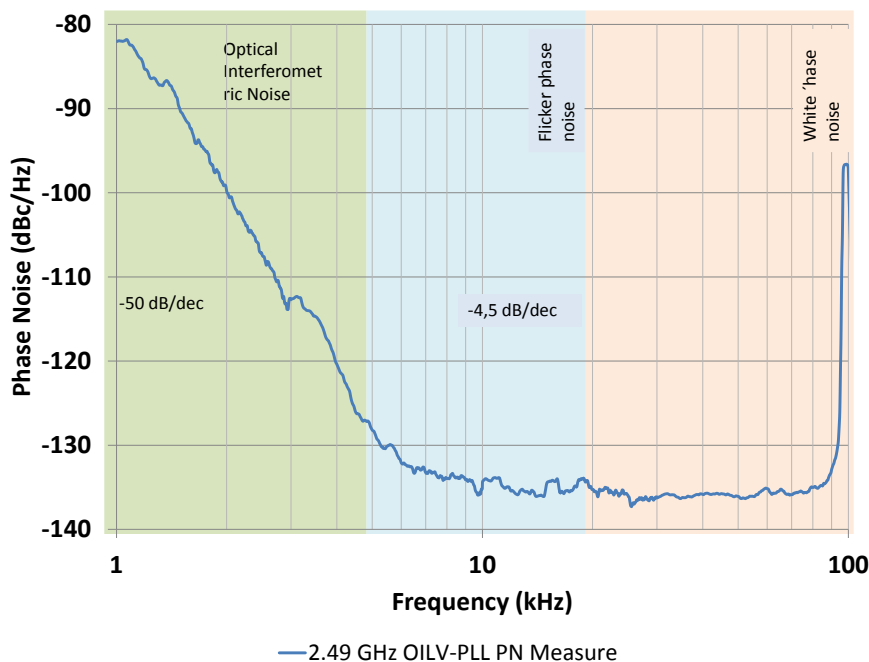
—2.49 GHz OILV-PLL PN Measure
Figure 86 Phase noise measurement result for a 1.5 µm OILVBO at 2.49 GHz.

The phase noise measured at 10 kHz offset is -135.58 dBc/Hz. This phase noise value is the lowest obtained in the laboratory for a 2.49 GHz VCSEL based optoelectronic oscillator. This is the lowest reported value according to the state-of-the-art for VCSEL based oscillators for the 2.5 GHz band.

The optical power injected into the OIL VCSEL does not reduce the phase noise of the oscillator beyond the previous value as long as the VCSEL is injection-locked. The injected power from the master laser is increased while the phase noise of the oscillator is measured. Table 23 presents the phase noise value measured at 10 kHz offset for several injected power values. This can be explained by the fact that the power injected into the slave VCSEL cavity increases the bandwidth of the laser but it does not increases the frequency response amplitude of the laser with respect to another OIL VCSEL at different power injection. This is supported as well by the fact that the RIN is the same for different injected power values as long as the VCSEL is injection locked, the RIN changes when the frequency detuning between

the lasers is varied. Figure 87 presents the phase noise measurement for each case. It is observed from Figure 87 that all the phase noise curve slopes are kept, there is an increase of the phase noise value in the optical interferometric noise area, this is supported on the fact that the injection ratio is increased for each measurement and the optical interferometric phenomenon becomes more important at higher injection rates (4, 6, 8.4 and 11.6 times the VCSEL emission power).

Injected Power (mW)	Phase Noise at 10 kHz Offset (dBc/Hz)
2.00	-134.98
3.00	-134.23
4.23	-134.01
5.85	-133.94

Table 23 2.49 GHz OILVBO phase noise values for several injected power values.
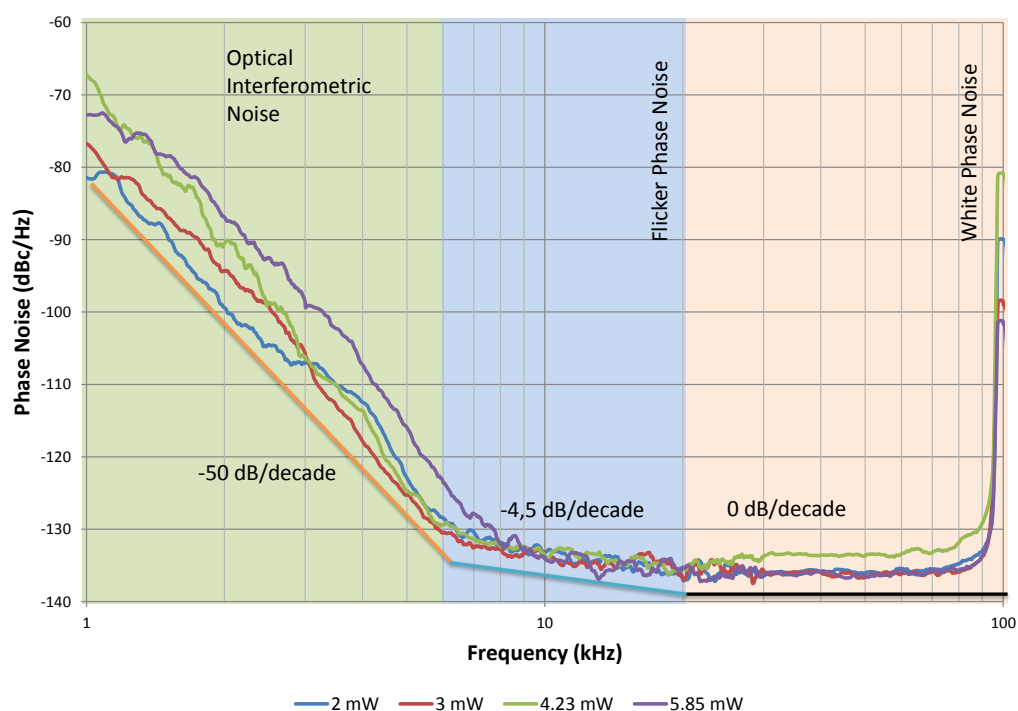
Figure 87 Phase noise curves for a 1.5 μm OILVBO at 2.49 GHz for several injected power values.

5.1.2 External Cavity Tunable Laser-by-VCSEL Optically Injection Locked 1.5 μm VCSEL Based Optoelectronic Oscillator at 10 GHz

A 10 GHz OILVBO is implemented. As shown in Chapter 4, the OIL technique permits the enhancement of the VCSEL direct modulation bandwidth. The OIL VCSEL is modulated at 10 GHz taking into account that this frequency is part of the enhanced bandwidth range. The OIL is implemented according to the scheme presented in Figure 88. With respect to the previous implementation, it is changed the microwave bandpass filter and amplifier (reference MPA 90501050) for those at the right frequency for this case.
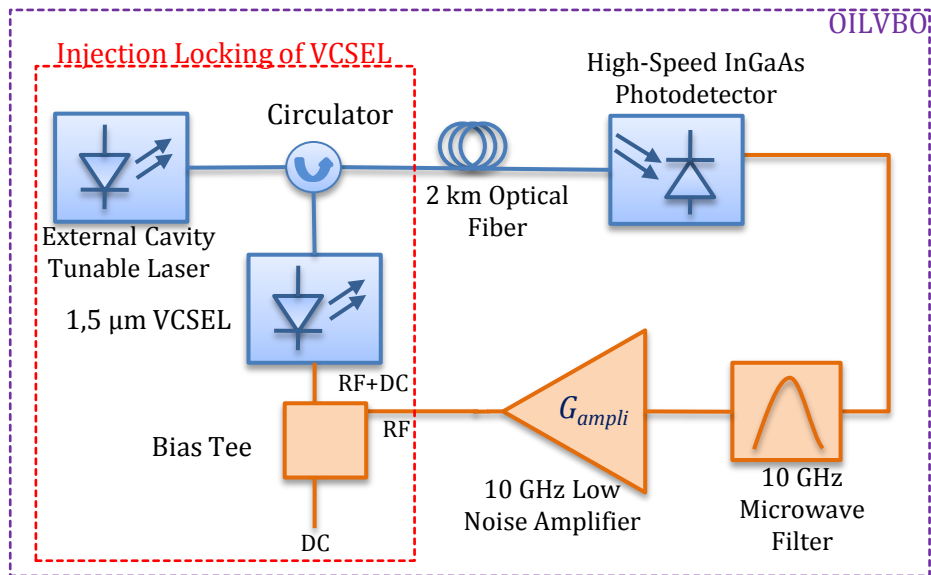
Figure 88 OILVBO using 1.5 μm VCSEL at 10 GHz setup scheme.

The OIL conditions are the same as described in Table 22. The oscillator output spectrum at 10 GHz is shown in figure 89.
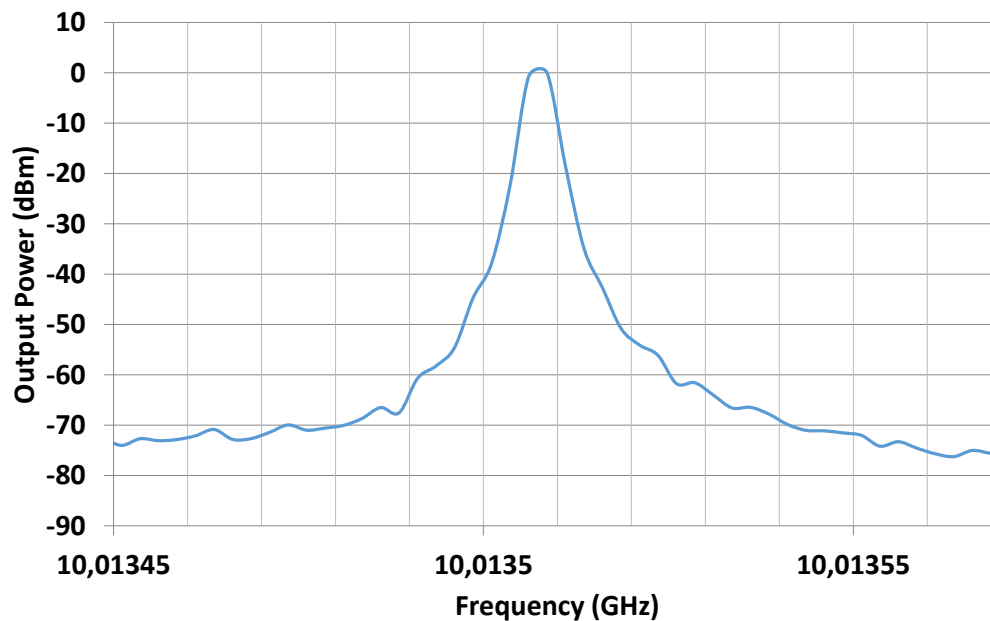
Figure 89 Output spectrum for the 1.5 μm OILVBO at 10 GHz.

The phase noise measurement is carried out through the direct measurement method. Figure 90 presents the phase noise curve. The phase noise is computed using the Leeson model equations for a delay line oscillator presented in Chapter 3, the computation parameters are summarized in Table 24. Analyzing the slopes along the curve, it is possible to infer that:

- A -57.3 dB/decade slope up to 10 kHz offset is due to the optical interferometric noise result of the OIL of VCSEL as explained before. This

noise source is not modelled by the Leeson model. This noise component is caused by the linewidth of the external cavity tunable laser used to lock the VCSEL.

- A -29 dB/decade slope that correspond to the contribution of the microwave amplifier frequency noise to the oscillator phase noise.
- A 0 dB/decade slope that correspond to the system white phase noise.

The phase noise value measured at 10 kHz offset is -93.07 dBc/Hz and the predicted value is -92.08 dBc/Hz.
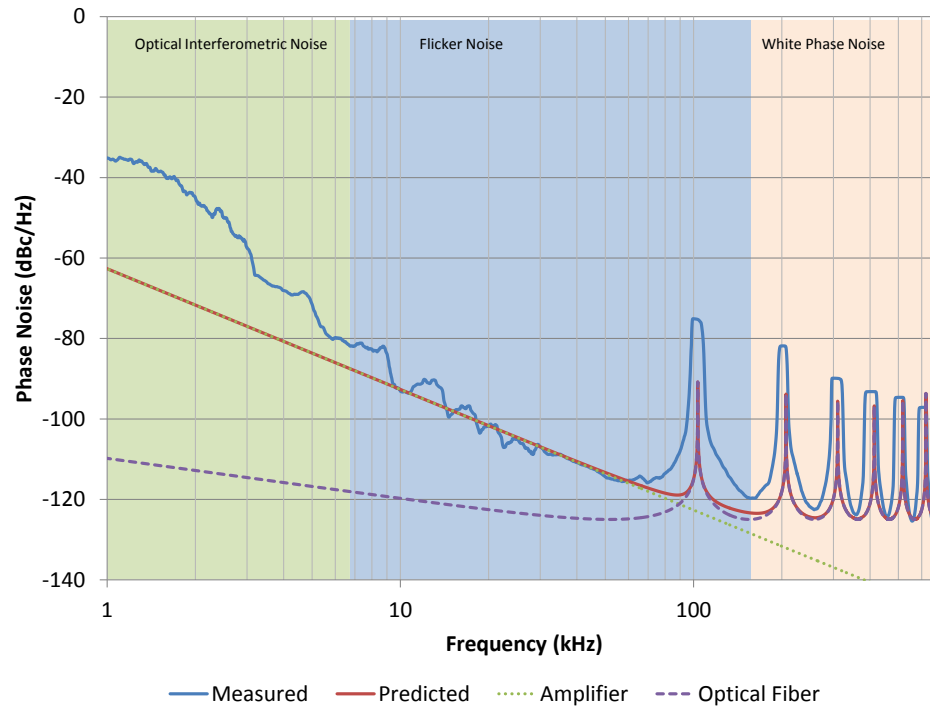
Figure 90 Phase noise measurement result for a 1.5 µm OILVBO at 10 GHz.

5.1.3   DFB-by-VCSEL Optically Injection Locked 1.3 µm VCSEL Based Optoelectronic Oscillator at 10 GHz

A DFB-by-VCSEL OILVBO at 10 GHz is implemented. This oscillator is built using 1.3 µm lasers. The oscillator configuration is the same as shown in Figure 88. The frequency detuning between the lasers is 25 GHz with a power injection of 14 mW. For this oscillator the frequency and long term stability are measured. The long term stability is measured through the Allan standard deviation [88]. The output spectrum is shown in Figure 91.
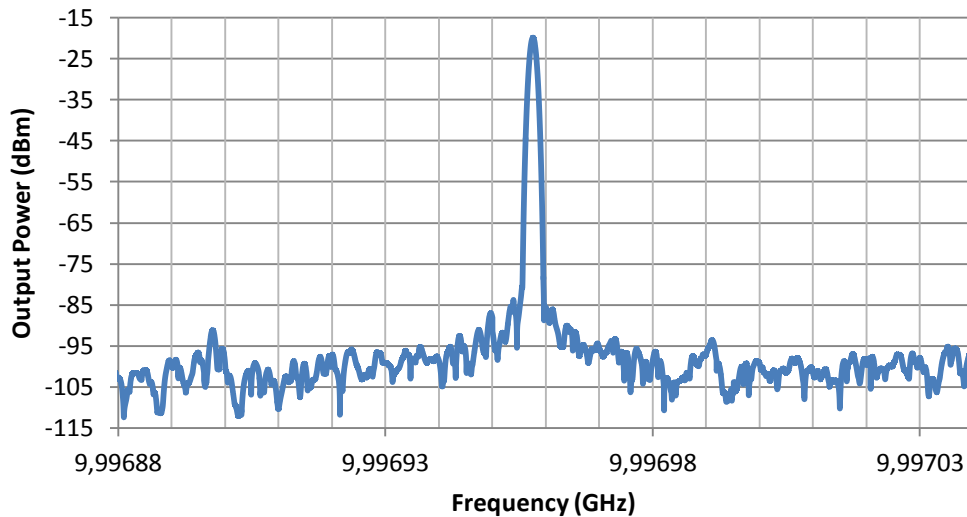
Figure 91 DFB-by-VCSEL 1.3 µm OILVBO at 10 GHz spectrum.

The phase noise curve for the 10 GHz OILVBO is shown in Figure 92. The phase noise value at 10 kHz offset is -105.7 dBc/Hz and its prediction is -105.72 dBc/Hz. Looking at this Figure, from left to right side, it is possible to infer that from 1 kHz to 8 kHz offset the phase noise curve has -30 dB/decade slope due to flicker frequency noise of the microwave amplifier; from 8 kHz to 22 kHz offset, the phase noise curve is dominated by the flicker phase noise due to the microwave amplifier topology (several stages) with a slope of -10 dB/decade; from 22 kHz offset, the phase noise curve presents a 0 dB/decade slope linked to white noise in the oscillator loop.
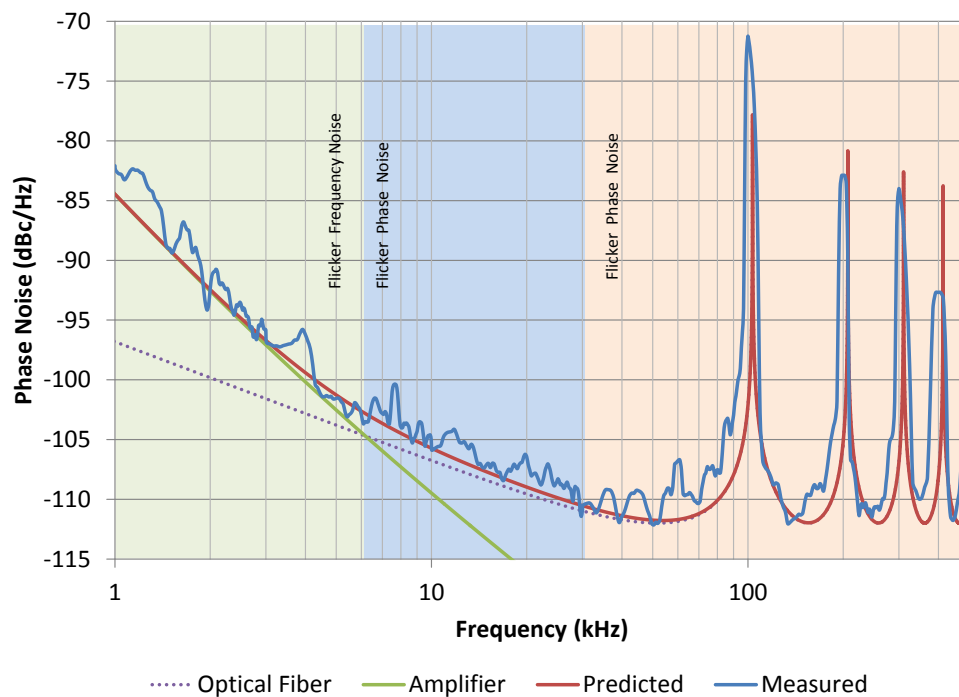
Figure 92 Phase noise measurement for a 1.3 µm DFB-VCSEL OILVBO at 10 GHz.

The time domain stability measurement of the oscillator is performed. The Allan standard deviation is measured for a 500 s time interval. This curve is shown in

Figure 93. From the five noise processes described in the Leeson model of the oscillator [17], three of them are observed in the measurement, from left to right:

- The white frequency noise curve that is proportional to $\tau^{-0.5}$ slope. This noise process is observed in the phase noise measurement as the -10 dB/decade slope area.
- The flicker frequency noise area correspond to that with slope proportional to τ^0. This process is seen as well in the phase noise curve, corresponding to that area with -30 dB/decade.
- The random walk frequency noise process is observed in the right side of the curve. This area of the curve has a slope proportional to $\tau^{0.5}$. The random walk frequency noise process is not seen in the phase noise curve, this appears at an offset frequency closed to the carrier in frequency domain. The phase noise measurement is performed from 1000 Hz and this process appears at lower frequencies.
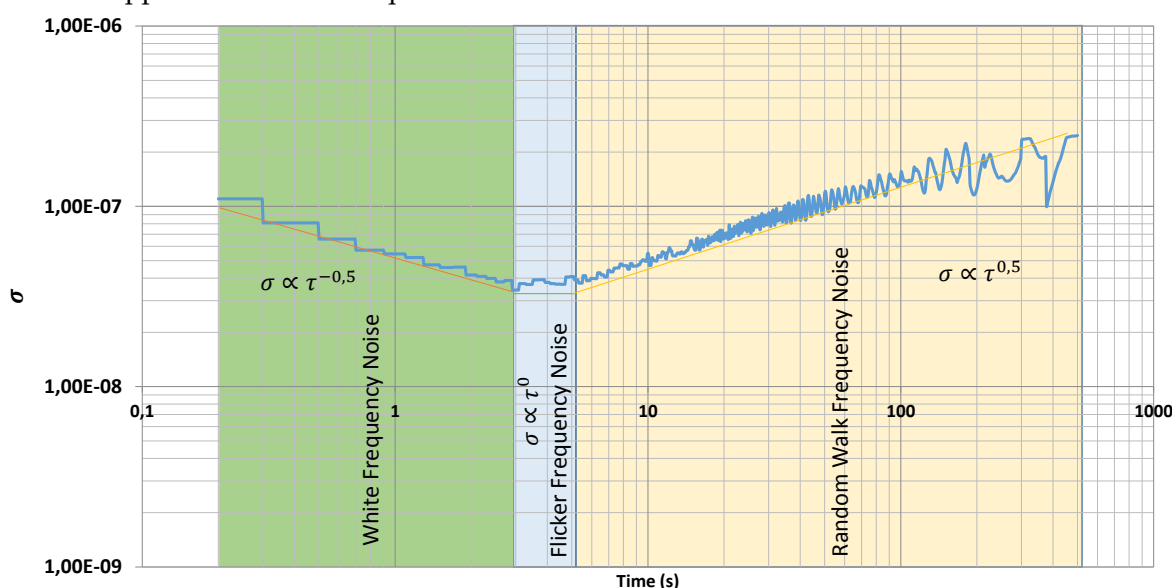
Figure 93 Allan standard deviation for the 10 GHz 1.3um OILVBO.

It is important to remark that the Optical interferometric noise observed (can be considered as random walk frequency noise) is not observed in the phase noise curve for the 1.3 µm OILVBO this can be explained by the lower linewidth of the 1.3 µm DFB master laser compared to the linewidth of the 1.5 µm of the tunable laser.

5.1.4 DFB-by-VCSEL Optically Injection Locked 1.3 µm VCSEL Based Optoelectronic Oscillator at 12 GHz

A DFB-by-VCSEL OILVBO at 12 GHz is implemented. The oscillator configuration is the same as shown in Figure 88. The frequency detuning between the lasers is 25 GHz with a power injection of 14 mW. For this oscillator the frequency and long term stability are measured. The long term stability is measured through the Allan standard deviation [88]. The output spectrum is shown in Figure 94.
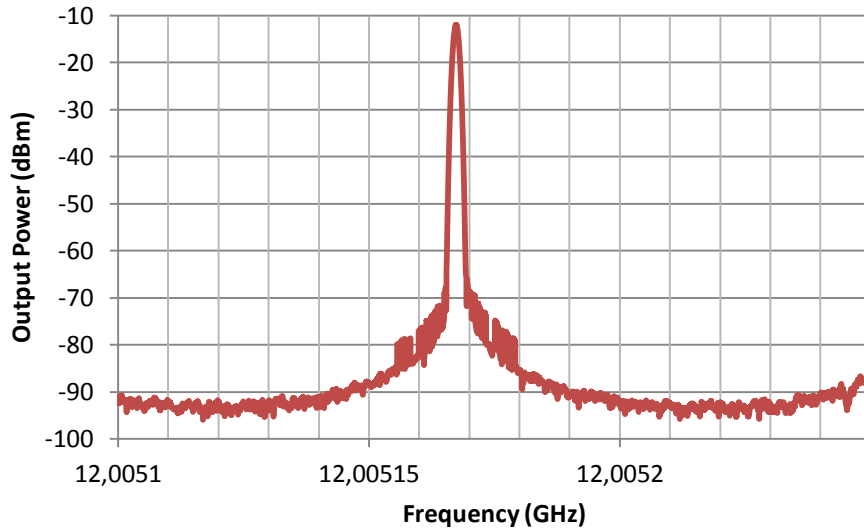
Figure 94 DFB-by-VCSEL 1.3 µm OILVBO at 12 GHz spectrum.

The phase noise curve is shown in Figure 13. The phase noise at 10 kHz offset is -96.5 dBc/Hz and the predicted value -97.93 dB/Hz. The phase noise contribution of the delay line and microwave amplifier are shown in Figure 95. The phase noise curve is led by the white frequency noise process with a characteristic slope of -20 dB/decade, typical from the Leeson effect in the oscillator. With respect to the previous implemented OILVBO at 10 GHz, it is seen that using a 12 GHz amplifier, the flicker phase noise process is not identified in this curve neither the optical interferometric noise process.
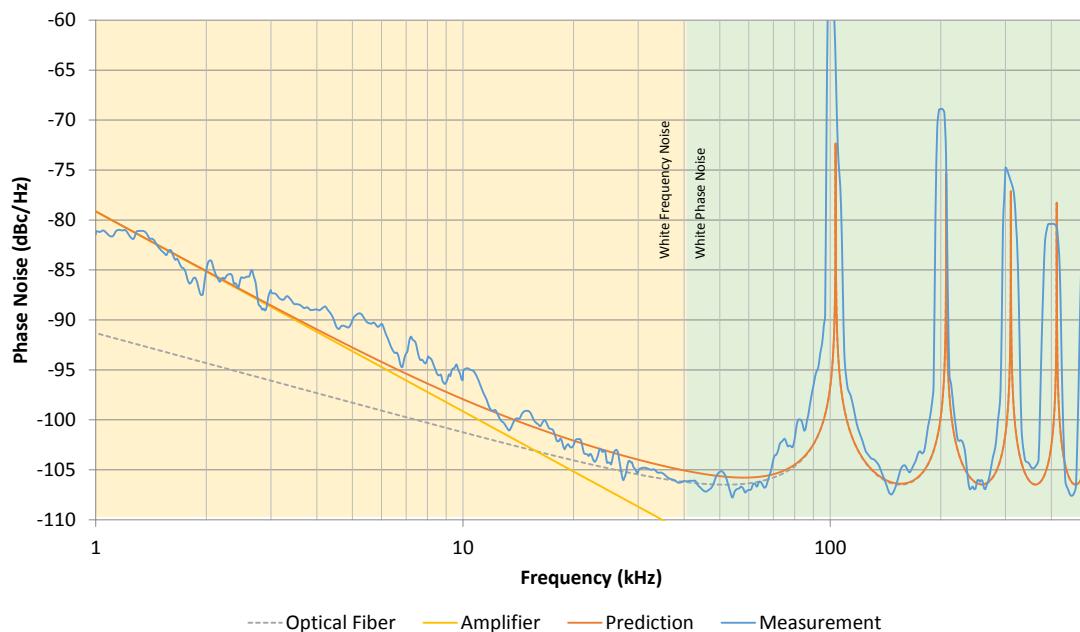
Figure 95 Phase noise measurement for a 1.3 µm DFB-VCSEL OILVBO at 12 GHz.

The Allan standard deviation is measured for this oscillator. The Figure 96 presents the measurement curve. Three areas are defined in this measurement, from them it is possible to infer that:

- There is a white frequency noise process in the oscillator from 0.2 to 10 s, this is observed in the phase noise measurement curve in the -20 dB/decade area.
- The flicker frequency noise process in the oscillator is not observed in the phase noise curve, but it is clearly evidenced in the time domain stability measurement. This means that the flicker frequency noise process occurs closer to carrier in frequency domain. This is a natural phenomenon in all oscillator due to the electronic nature of the amplifier transistors.
- From 20 to 500 s, the Allan standard deviation trend describes a random walk frequency noise process in the oscillator. This noise process is not observed in the phase noise curve due to the frequency range used for the measurement (1 kHz to 1 MHz).
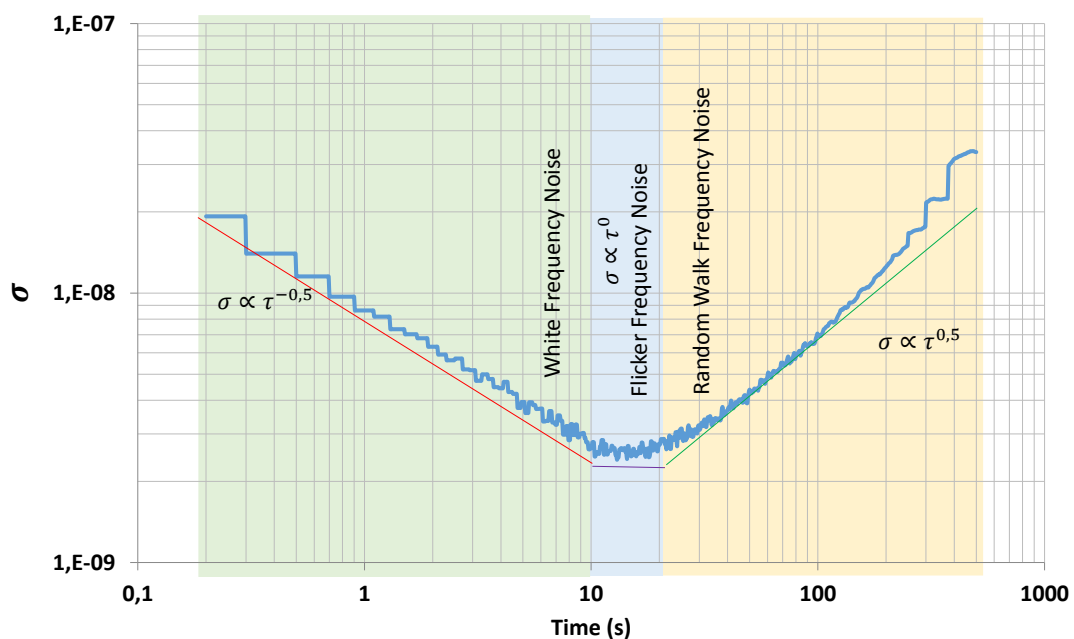
Figure 96 Allan standard deviation for the 12 GHz 1.3um OILVBO.

5.1.5   VCSEL-by-VCSEL Optically Injection Locked 1.3 μm VCSEL Based Optoelectronic Oscillator at 10 GHz

The VCSEL-by-VCSEL OIL technique is implemented in the VCSEL based optoelectronic oscillator. Two 1.3 μm VCSELs are used in master/slave configuration. The oscillator frequency choice is made based on the VCSEL-by-VCSEL OIL direct modulation bandwidth tests performed in Chapter 4. The experimental setup for the VCSEL-by-VCSEL OILVBO is presented in Figure 97. The OIL is implemented using a temperature controlled slave VCSEL at 18ºC and biased at 7.7 mA. The master laser is not directly temperature controlled but the implementation is performed inside a clean room with temperature stabilized at 22 ºC and biased at 6.82 mA. To boost the master laser emission, a Semiconductor Optical Amplifier is used to increase the injection ratio into the slave laser cavity. The injected power into the slave laser cavity is 10 mW with a frequency detuning of 12 GHz between the VCSELs.
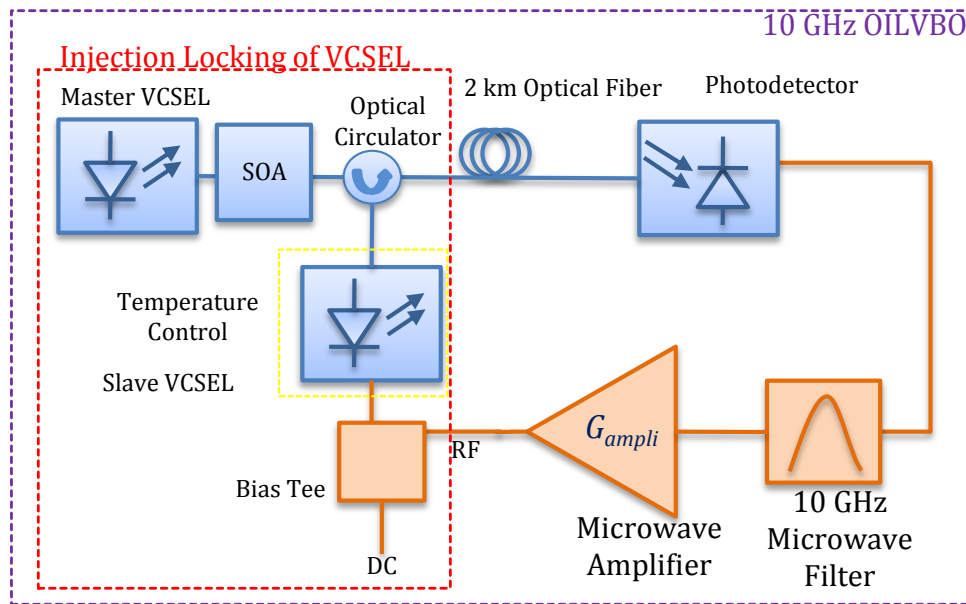
Figure 97 1.3 μm VCSEL-by-VCSEL 10 GHz OILVBO scheme.

The spectrum for this oscillator is shown in Figure 98. The oscillation power is 14 dBm. The frequency stability of the oscillator is measured, the phase noise value at 10 kHz offset is -92 dBc/Hz and the prediction is -92.91 dBc/Hz. The phase noise curve noise floor is higher than in the precedent oscillators due to the RIN increase of the OIL VCSEL due to the integration of the SOA into the system, as shown in Chapter 4, this increases the oscillation noise.
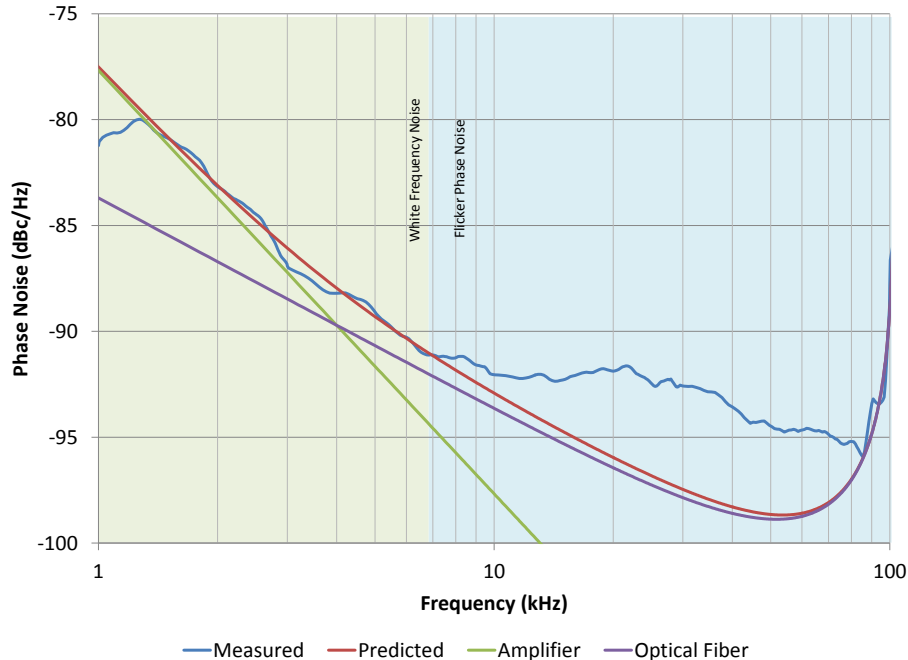
Figure 98 1.3 μm VCSEL-by-VCSEL 10 GHz OILVBO phase noise curve.

The Allan standard deviation is measured for this oscillator. The time domain stability curve is shown in Figure 99. From this curve it is evident that the noise process that most affects the oscillator stability in long term is the random walk frequency noise (from 1.4 to 500 s). This noise process is linked to the optical interferometric noise that is enforced by the use of a SOA to boost the master laser power.
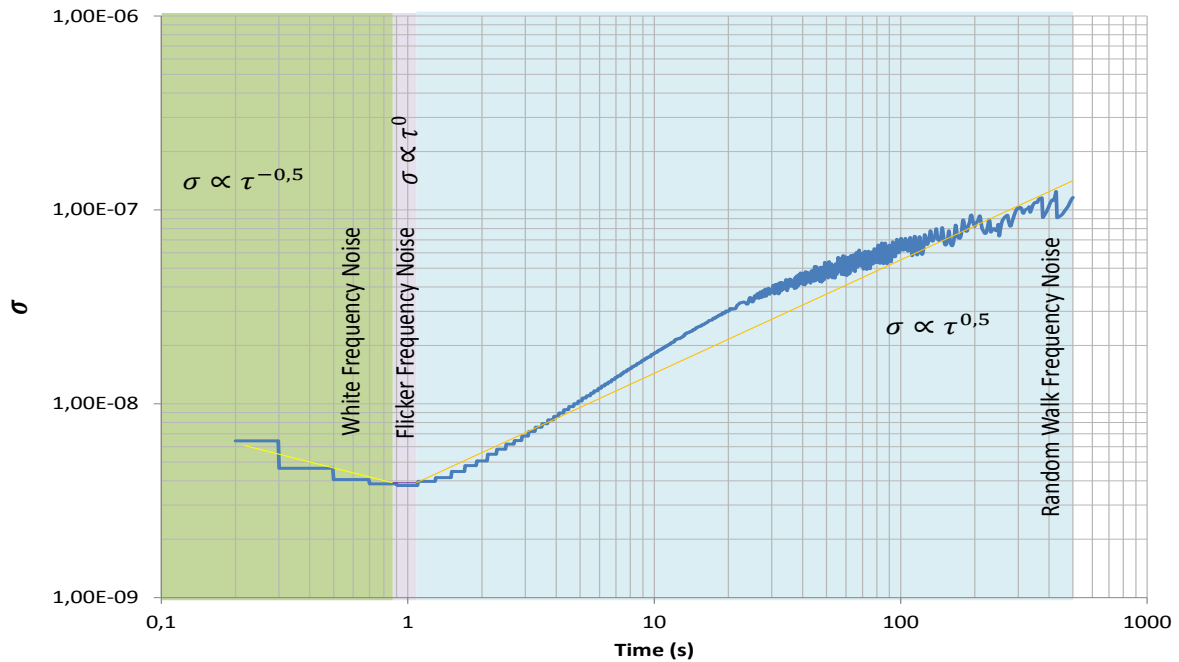
Figure 99 Allan standard deviation for the 10 GHz 1.3um VCSEL-by-VCSEL OILVBO.

5.1.6 Optically Injection Locked VCSEL Based Optoelectronic Oscillator Parameter Summary

From the previous results, the phase noise power spectral density is computed according to the Leeson model prediction [17], [68] and taking into account the equations for the delay line optoelectronic oscillator. As input values for the model are summarized in Table 24, the measured and predicted phase noise values for each optoelectronic oscillator are shown in Table 25.

OILVBO Configuration	Oscillation Frequency (GHz)	Optical Fiber Time Delay (µs)	RIN OIL VCSEL at Oscillation Frequency (dB/Hz)	Amplifier Gain	b_o	b_1
1.5 µm external cavity laser/VCSEL OILVBO	10	9.67	-145	35	$1.58 * 10^{-13}$	$1.99 * 10^{-6}$
1.3 µm DFB/VCSEL OILVBO	10	9.67	-142.6	50	$3.16 * 10^{-12}$	$1 * 10^{-8}$
1.3 µm DFB/VCSEL OILVBO	12	9.67	-143.5	50	$3.16 * 10^{-12}$	$1.2 * 10^{-7}$
1.3 µm VCSEL/VCSEL OILVBO	10	9.67	-110	40	$6.3 * 10^{-11}$	$1.7 * 10^{-8}$

Table 24 Phase noise model computation parameters input.

OILVBO Configuration	Phase Noise Measured at 10 kHz offset (dBc/Hz)	Phase Noise Predicted at 10 kHz offset (dBc/Hz)	Allan's Standard Deviation (σ)
1.5 µm external cavity laser/VCSEL OILVBO at 10 GHz	-93.2	-92.7	-
1.3 µm DFB/VCSEL OILVBO at 10 GHz	-105.7	-105.7	$10^{-8} < \sigma < 10^{-7}$
1.3 µm DFB/VCSEL OILVBO at 12 GHz	-95.4	-97.9	$10^{-9} < \sigma < 10^{-7}$
1.3 µm VCSEL/VCSEL OILVBO at 10 GHz	-92.0	-92.9	$10^{-8} < \sigma < 10^{-7}$

Table 25 Phase noise and Allan standard deviation values measured and simulated for the implemented optically injection locked VCSEL based optoelectronic oscillators.

5.2   Optoelectronic Oscillators Using External Modulation

Three optoelectronic oscillators using external modulation are implemented at different frequencies in order to make a comparison with respect the OILVBOs implemented along this research. For these OEOs, the external modulation is done through a LiNbO₃ Mach-Zender modulator. The setup for these tests is shown in Figure 100. The laser source is a 1.3 m DFB laser, see datasheet in Annex 6. An optical fiber spool of 2 km is used as delay line and the microwave filters and amplifiers are the same used in the OILVBOs for each frequency.
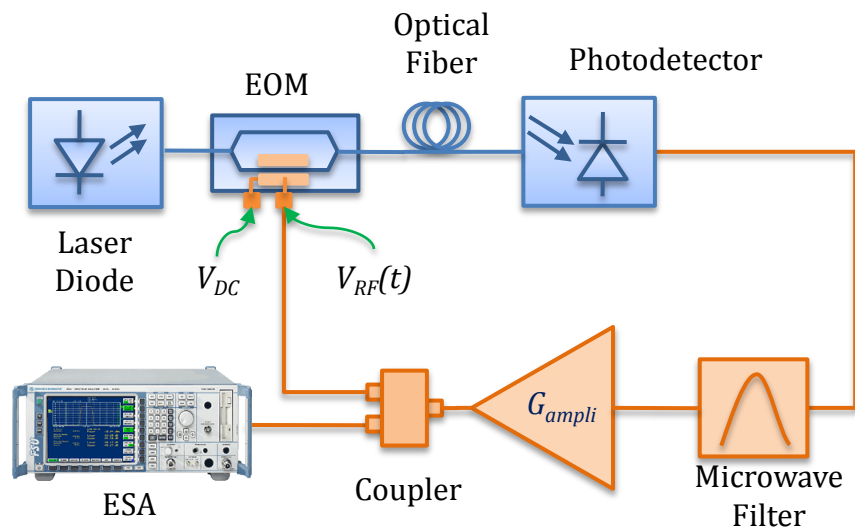
Figure 100 OEO with external modulation schematic setup.

5.2.1   2.49 GHz Optoelectronic Oscillator

The output spectrum of this OEO is shown in Figure 101. The output power of the oscillator is 10.9 dBm. The phase noise curve is shown in Figure 102. The phase noise value at 10 kHz offset is -124.9 dBc/Hz. In this phase noise curve there is evidence of three noise processes inside the oscillator: Random walk frequency noise at frequencies less than 1 kHz, the white frequency noise due to the amplifier transistors and the white phase noise inside the oscillator between 2 and 20 kHz. The Allan standard deviation curve is shown in Figure 102.
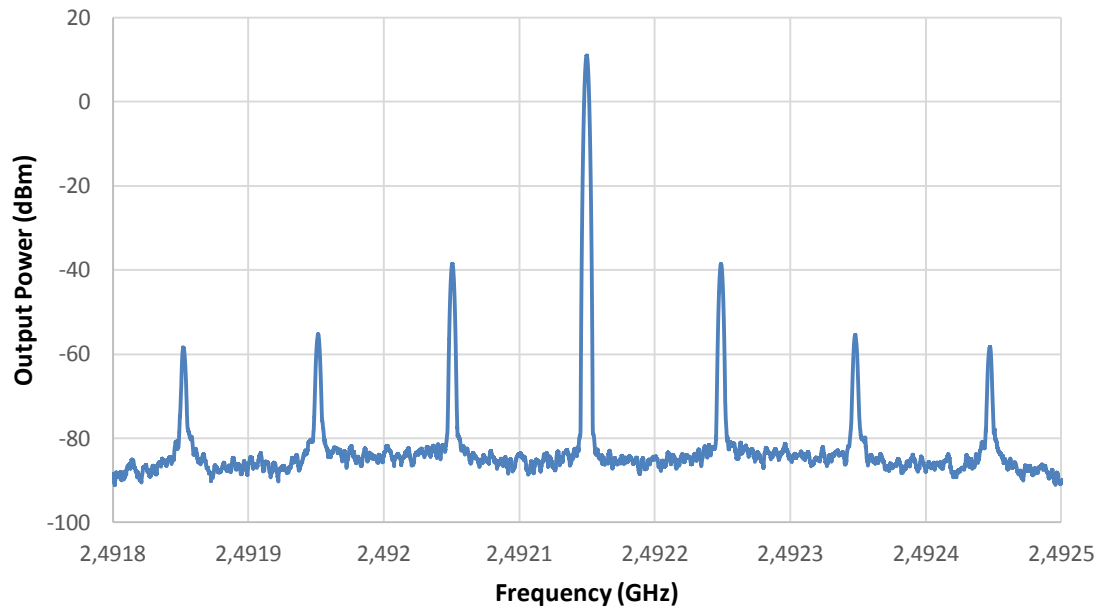
Figure 101 2.49 GHz OEO spectrum.
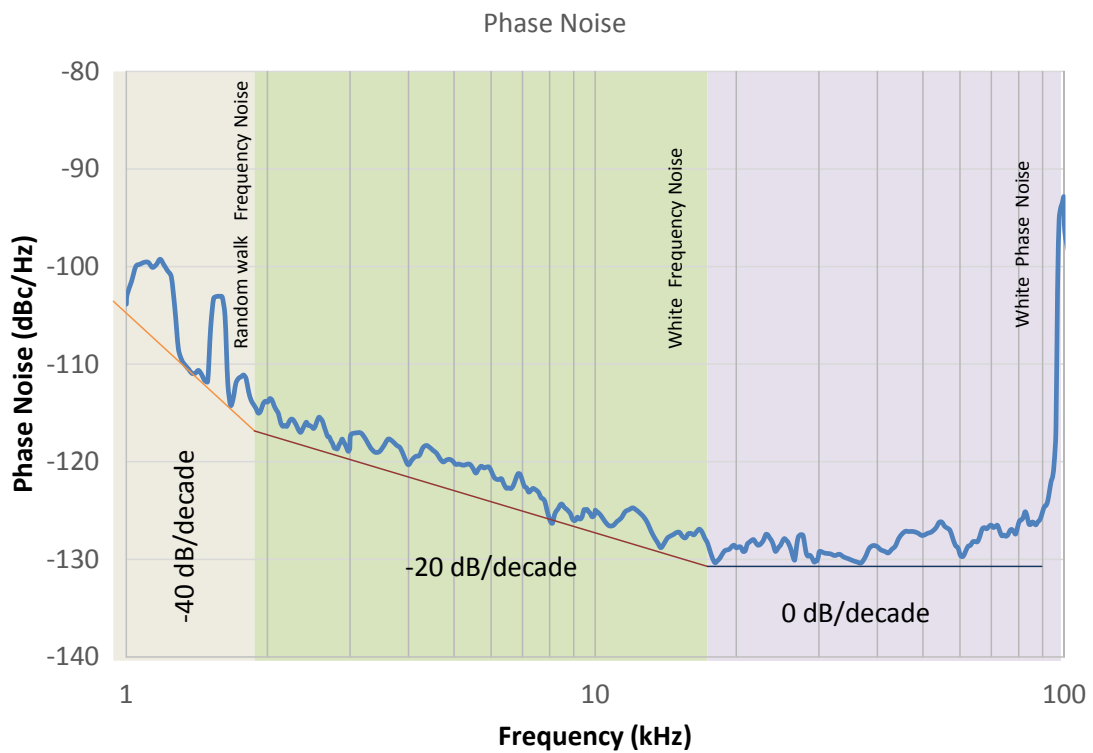
Figure 102 2.49 GHz phase noise curve.
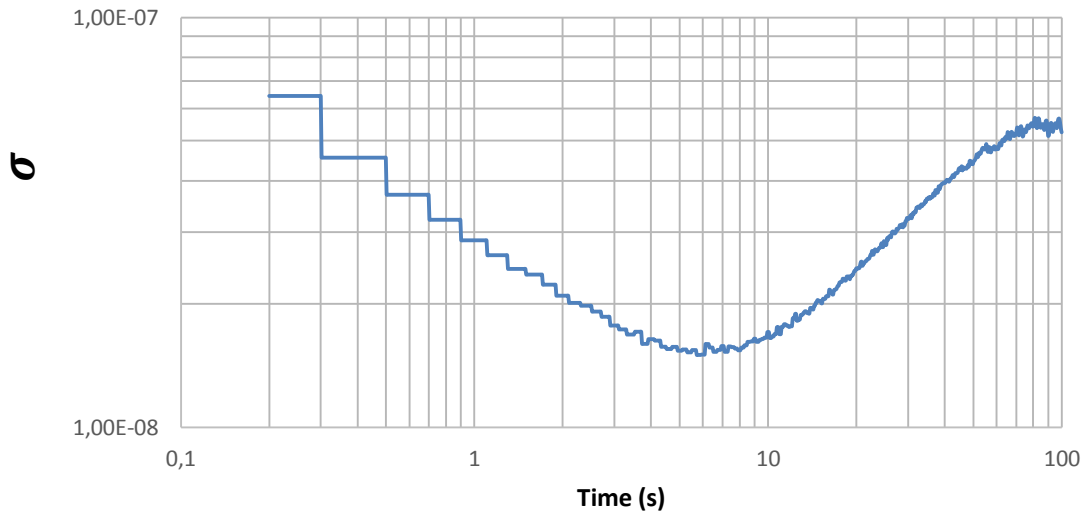
Figure 103 Allan standard deviation for the 2.49 GHz OEO.

5.2.2   10 GHz Optoelectronic Oscillator

The spectrum of this oscillator is shown in Figure 104. The output power of this oscillator is 8.5 dBm. The phase noise of this oscillator at 10 kHz offset is -110.5 dBc/Hz. The phase noise curve is shown in Figure 104, in this Figure it is possible to define the flicker frequency noise process area from 1 kHz to 10.8 kHz offset. The Allan standard deviation is measured and shown in Figure 105.
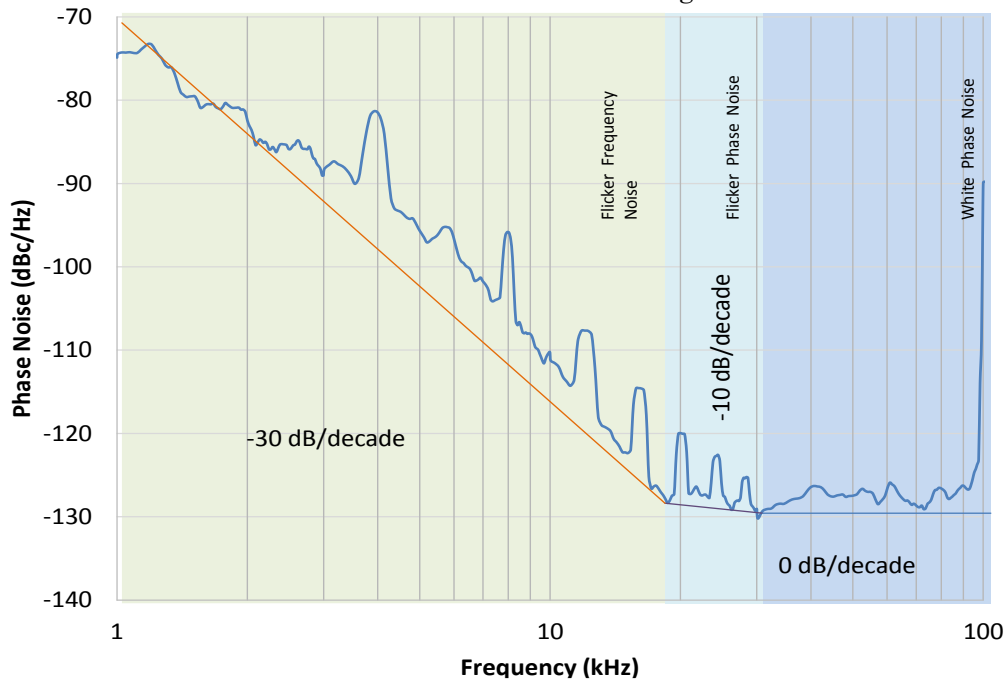
Figure 104 10 GHz phase noise curve.
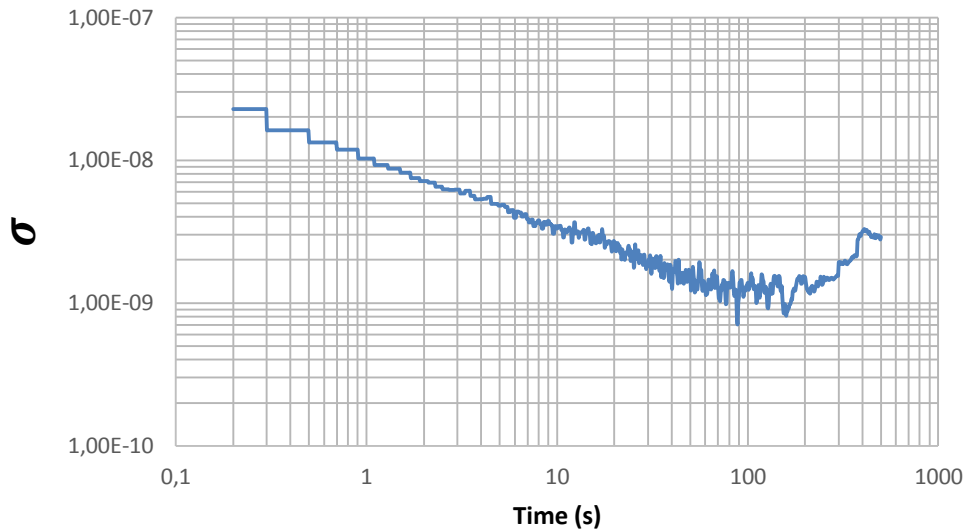
Figure 105 10 GHz OEO Allan standard deviation curve.

5.2.3 12 GHz externally modulated OEO

The 12 GHz OEO output spectrum is shown in Figure 106. The output power of this oscillator is 12 dBm. The phase noise value at 10 kHz offset is -123.72 dBc/Hz. The phase noise curve is shown in Figure 107. The Allan standard deviation curve is shown in Figure 108.
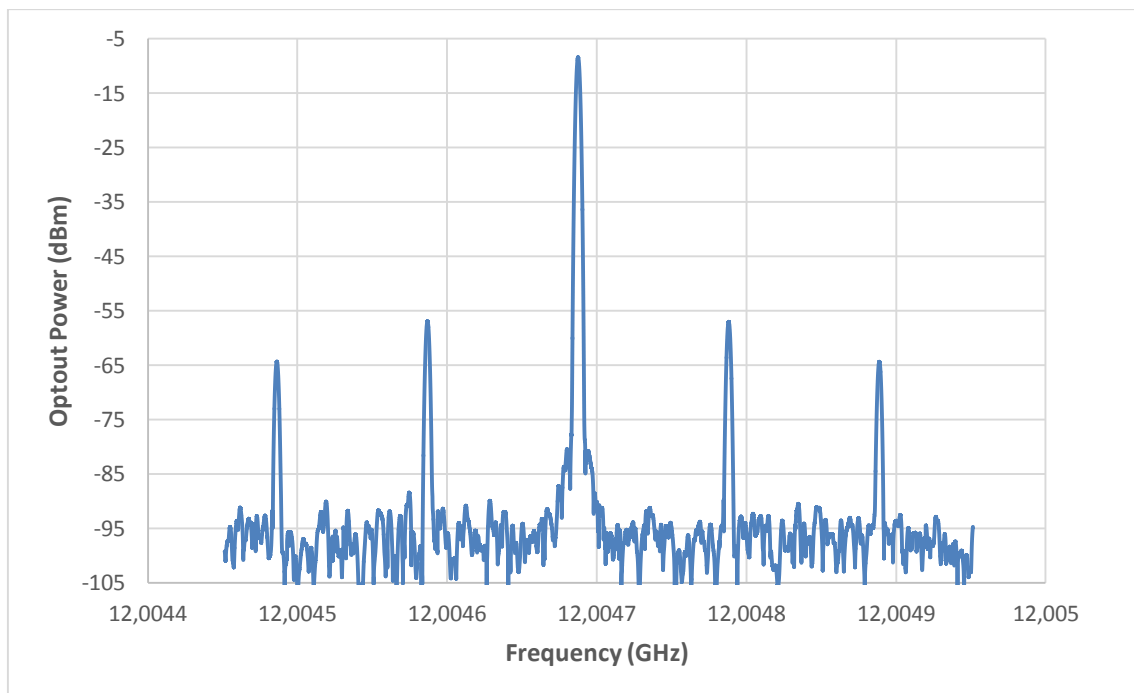
Figure 106 12 GHz OEO spectrum.
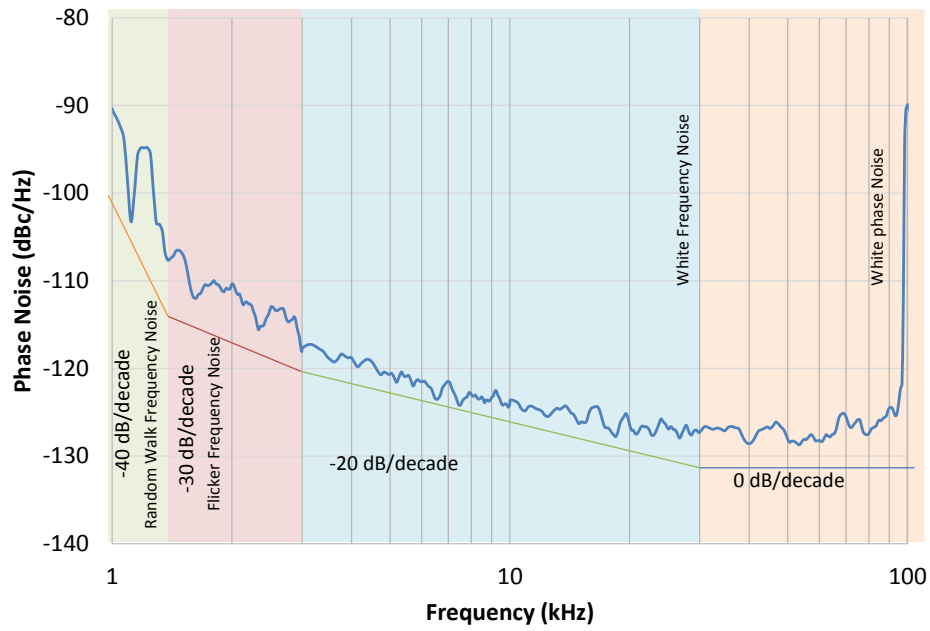
Figure 107 12 GHz OEO phase noise curve.
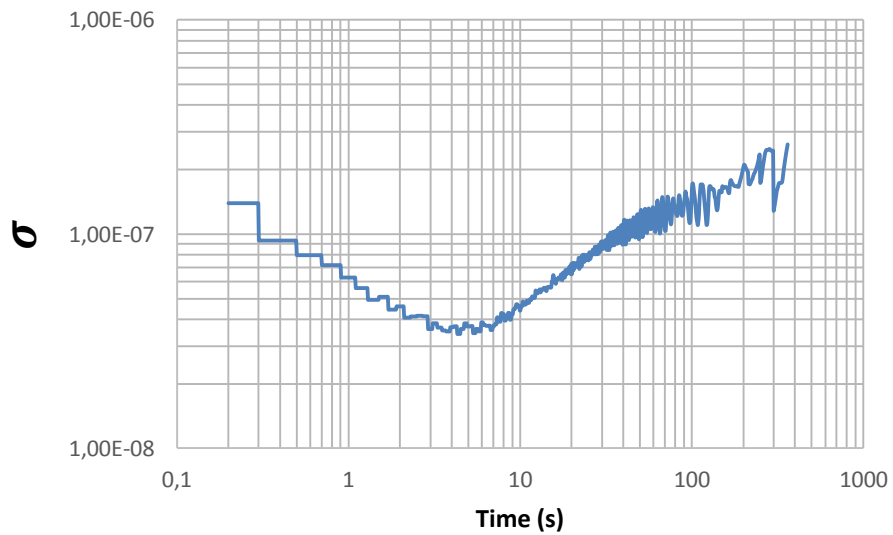
Figure 108 12 GHz OEO Allan standard deviation curve.

5.3   Performance Analysis of the OEOs and OILVBOs

From the measurements performed for OEOs with external modulation and OILVBOs at different frequencies, it is possible to provide a performance comparison between them. These oscillators are implemented by keeping the same experimental conditions for each frequency. The goal of this section is to balance the benefits and constraints of each topology. Table 26 presents the main performance parameter for each oscillator at 2.49 GHz.

Parameter	1.5 µm Tunable Laser-VCSEL OILVBO at 2.49 GHz	1.3 µm OEO with External Modulation at 2.49 GHz
Laser Optical Power (dBm)	7.8	11.5
Laser RIN (dB/Hz)	-146.9	-145.2
Phase Noise at 10 kHz offset (dBc/Hz)	-133.9	-124.9
Oscillation Power (dBm)	-6	10.9
Optical Fiber Length (km)	2	2
Master Laser Bias Current (mA)	100	35
Slave Laser Bias Current (mA)	5	5

Table 26 Performance comparison of the 2.49 GHz OEO and OILVBO.

From these parameters it is possible to infer that the OILVBO requires less optical power that the OEO using external modulation. The OIL VCSEL exhibits lower RIN value than the laser used for the OEO with external modulation. Regarding to the frequency stability, the phase noise value at 10 kHz offset for the OILVBO is 9 dB lower than the OEO using external modulation. Despite the lower phase noise of the OILVBO, it is important to remark that the OEO oscillation power is 17 dB higher than the OILVBO. The higher oscillation power of the OEO is explained from the fact that the laser source of the OEO (DFB Laser, Datasheet in Annex 5) has higher power than the slave VCSEL, for this reason the photodetected current is higher for the OEO. The lower phase noise value of the OILVBO can be explained from the RIN reduction of the VCSEL when is under OIL and the lower power of the carrier that leads to lower difference between the frequency peak and the noise floor of the measurement.

For the 10 GHz oscillators, this comparison is presented. Table 27 presents the performance parameters comparing the following oscillators:

- 1.3 µm DFB-by-VCSEL OILVBO at 10 GHz
- 1.3 µm VCSEL-by-VCSEL OILVBO at 10 GHz
- 1.5 µm external cavity tunable laser-by-VCSEL OILVBO at 10 GHz
- 1.3 µm DFB OEO with external modulation at 10 GHz

Parameter	1.3 µm DFB-by-VCSEL OILVBO at 10 GHz	1.3 µm VCSEL-by-VCSEL OILVBO at 10 GHz	1.5 µm Tunable laser-by-VCSEL OILVBO at 10 GHz	1.3 µm OEO with External Modulation at 10 GHz
Optical Power (dBm)	11.4	10	7.8	11.4
Laser RIN (dB/Hz)	-143.5	-118.5	-145	-142.6
Phase Noise at 10 kHz offset (dBc/Hz)	-105.7	-92	-93.2	-110.5
Oscillation Power (dBm)	18	14	10	8.5
Optical Fiber Length (km)	2	2	2	2
Master Laser Bias Current (mA)	35	6.82	100	35
Slave Laser Bias Current (mA)	5	7.7	5	-

Table 27 Performance comparison of the 10 GHz OEO and OILVBO.

The highest oscillation power is achieved when the 1.3 µm DFB is used directly modulated and as master laser to lock the slave VCSEL. This is explained because of the high power of this laser that leads to a higher photodetected current. In terms of RIN, the 1.3 µm DFB has the lowest RIN value of all lasers used in these tests.

From these tests it is possible to infer that the highest oscillation power is achieved when the DFB-by-VCSEL OILVBO at 10 GHz is implemented. This supports the hypothesis of the direct modulation bandwidth enhancement of the VCSEL when is under OIL condition. The enhanced frequency response of the OIL VCSEL leads to a higher optical power that arrives at the oscillator photodetector and, by the way, delivers a higher photodetected current.

The lowest phase noise value for the 10 GHz oscillators is measured for the OEO with external modulation. For the OILVBOs it is seen that a low RIN master laser is essential to get an injection-locked slave laser with low RIN. Regarding to the DFB-by-VCSEL and the VCSEL-by-VCSEL RIN, it is remarked that the RIN of the VCSEL-by-VCSEL is 26.7 dB worst that the DFB-by-VCSEL OIL laser. From measurements performed in Chapter 4, the use of a SOA is required to boost the master VCSEL power. The optical noisy behavior of the SOA degrades the RIN of the slave laser. In consequence, the high RIN value of the directly modulated VCSEL-by-VCSEL laser deteriorates the phase noise of the VCSEL-by-VCSEL OILVBO.

The phase noise process inside the OILVBO is governed by the white frequency noise and flicker frequency noise, this depending on the amplifier used in the oscillator. The presence of the optical interferometric noise in the OILVBO phase noise for the

OILVBOs using 1.5 µm lasers seems to be linked to a high linewidth of the master tunable laser used for these oscillators at 2.49 and 10 GHz using this wavelength.

For the 12 GHz frequency, the implemented OILVBO and OEO with external modulation are:

Parameter	1.3 µm DFB-by-VCSEL OILVBO at 12 GHz	1.3 µm OEO with External Modulation at 12 GHz
Laser Optical Power (dBm)	11.4	11.4
Laser RIN (dB/Hz)	-143.5	-147
Phase Noise at 10 kHz offset (dBc/Hz)	-95.4	-123.72
Oscillation Power (dBm)	10	12
Optical Fiber Length (km)	2	2
Master Laser Bias Current (mA)	35	35
Slave Laser Bias Current (mA)	5	-

Table 28 Performance comparison of the 12 GHz OEO and OILVBO.

The optical power for both 12 GHz oscillators is the same. Both of them use the same 1.3 µm DFB laser. The frequency response of the OIL VCSEL reach its limit at this frequency, for this reason there is a 27.2 dB degradation of the phase noise compared with the external modulated OEO.

The VCSEL-by-VCSEL OILVBO is not implemented at this frequency because the master VCSEL power injection is not high enough to satisfy the OIL condition at this frequency.

Conclusion

The OILVBOs are implemented along this Chapter. From the evidence of the direct modulation bandwidth enhancement shown in Chapter 4, the OILVBOs are implemented close to the OIL VCSEL cut-off frequency (10 and 12 GHz) and 2.49 GHz as well to evidence the frequency stabilization for a frequency inside the free running direct modulation bandwidth.

From the tests performed along this Chapter it is concluded that the OIL technique applied to VCSELs is feasible to increase the oscillator frequency. Nevertheless, to assure a low RIN, the RIN of the master laser must be lower than that one of the free running VCSEL. If this condition is not satisfied, the oscillation is going to be reached but with lower frequency stability.

The optical fiber length phase noise reduction has been already shown by previous results [3], [10], [12]. It is necessary to explore the noise reduction in RF components in order to enhance the electronic components performance as well. The VCSEL TO package limits the direct modulation VCSEL bandwidth, for this reason it is suggested to explore the implementation of the OILVBO using on-chip VCSEL and VCSEL matrix OIL.

The RIN of the laser has a direct influence in the oscillator phase noise, for this reason a complete modeling of RIN is required to predict the phase noise behavior of the oscillator.

The time domain oscillator stability measurement is performed, from this, it is concluded that OILVBO presents in long term a random walk frequency process linked quantic nature of lasers and a flickering noise process coming from the microwave amplifier and optical model competition inside the slave laser cavity.

Conclusions and Future Work

The results presented in this Thesis Report are the fruit of the research effort inside the international academic framework between the **Universidad Nacional de Colombia** and The **Institut Supérieur de l'Aéronautique et de l'Espace**, specially from the research groups *Grupo de Investigacion en Telecomunicaciones y Electrónica de Alta Frecuencia (CMUN)* and *Micro-ondes et Optronique pour Systèmes Embarqués (MOSE)*.

Along this research work, the optical generation of microwave signal technique is explored. At the beginning of this document, the basic concepts of the optoelectronic oscillator theory and their figures-of-merit as the phase noise and the Allan standard deviation were recalled.

The VCSEL Based Optoelectronic Oscillator (VBO) was implemented at 2.49 GHz using 1.3 and 1.5 µm VCSELs. For these VCSELs, the Relative Intensity Noise (RIN) was measured, from thischaracterization, it is concluded that manufacturing techniques for VCSELs had improved taking into account that the RIN of these VCSELs is lower than those ones used for the VCSEL Based Optoelectronic Oscillator proposed by Varón in 2008 [3].

The implemented VCSEL Based Optoelectronic Oscillators at 2.49 GHz exhibited a phase noise of -115.3 and -119.5 dBc/Hz at 10 kHz offset for 1.3 and 1.5 µm VCSELs, respectively. It was shown that the drawback of the VCSEL Based Optoelectronic Oscillator is the relative low modulation bandwidth of the laser source, but despite of this, the spectral purity of the VCSEL Based Optoelectronic Oscillator is as good as that one of electronic oscillators at the same operation frequency.

The Optical Injection Locking of VCSEL was implemented for 1.3 and 1.5 µm VCSELs. Several Master/Slave VCSEL configurations were characterized. The direct modulation frequency response of the VCSEL is dramatically enhanced up to 10.1 GHz for the 1.3 µm Optically Injection Locked VCSEL (VCSEL by VCSEL OIL configuration) and 12 GHz for the 1.5 µm Optically Injection Locked VCSEL (Tunable Laser/VCSEL configuration).

The direct modulation bandwidth of the VCSELs used in this work in free running and Optical Injection Locking condition is limited due to the TO package that is not designed for high frequency operation. Anyway, the modulation frequency applied to the VCSELs in the oscillator loop was always chosen to be inside the VCSEL direct modulation bandwidth. It is necessary to work in the design of a high frequency packaging for the laser.

The Relative Intensity Noise (RIN) of the Optically Injection Locked VCSEL is measured and it is observed that it is possible to reduce the slave laser RIN thanks to the RIN resonance peak shift toward higher frequencies. It is concluded that the Optically Injection Locked VCSEL RIN is reduced just if the Master Laser RIN is lower than that one of the slave VCSEL.

The Optically Injection Locked VCSEL Based Optoelectronic Oscillator (OILVBO) is implemented with 1.3 and 1.5 µm VCSELs using as Master Laser a tunable laser, a Distributed Feedback laser (DFB) and a VCSEL. The OILVBO was implemented at

2.5, 10 and 12 GHz. For the 1.5 μm OILVBO at 2.5 GHz a phase noise record value of -134 dBc/Hz at 10 kHz offset is measured. 1.3 μm OILVBO at 10 and 12 GHz using DFB/VCSEL OIL are built and the phase noise values measured at 10 kHz offset were -105.7 dBc/Hz and -95.4 dBc/Hz, respectively. It was implemented for first time a 1.3 μm VCSEL by VCSEL Optically Injection Locked Optoelectronic Oscillator at 10 GHz with a phase noise value of -92 dBc/Hz at 10 kHz offset. The phase noise of these oscillators is modelled according to the additive noise model of Leeson taking into account the considerations for a delay line optoelectronic oscillator. It has been found a good agreement between the measurements and simulations.

The time domain stability of the OILVBO is studied through the Allan's standard deviation (σ). From this characterization it is that the time domain stability of the implemented OILVBOs is lower than 10^{-7} in a time window of 500 s. The OILVBO with better time stability was DFB/VCSEL 12 GHz configuration with $\sigma < 10^{-8}$. When comparing the OILVBO time domain stability to that one of the externally modulated OEO using a Mach-Zender intensity modulator, it is observed that the magnitude order of σ is the same for both topologies.

The use of the optical signal generation techniques for space applications has been considered to be implemented by industrials and researchers thanks to the low power consumption of optical sources. The use of VCSEL for aerospace applications is a feasible option thanks to its low power consumption (10 mW) when compared to other laser technologies. The VCSEL connections are very simple and the direct modulation of the laser allows the suppression of the Mach-Zender intensity modulator from the oscillator chain.

To enhance the optoelectronic oscillator stability, it is concluded that a thermal control for the VCSEL and the optical fiber delay line is required to avoid the laser wavelength drift and the time delay variations of the optical fiber due to the thermal lensing effect.

From this work it is concluded that it is feasible to implement an Optical Injection Locked VCSEL Based Optoelectronic Oscillator thanks to the microwave performance enhancement of the VCSEL through the Optical Injection Locking technique.

As future considerations, a zero dispersion optical fiber delay line should be used in order to optimize the propagation of the laser beam. Regarding to electronics, it should be considered the use of a low noise microwave amplifier instead of using discrete components as it was done for this project. Additionally, the use of an optical filter should be considered as a strategy to enhance the resonator frequency selectivity.

Finally, a next step towards the integration of the Optically Injection Locked Optoelectronic Oscillator could be done if an on-chip VCSEL by VCSEL Optically Injection Locked source is developed.

References

[1]   L. Maleki, "Sources: The optoelectronic oscillator," *Nat. Photonics*, vol. 5, no. 12, pp. 728–730, Dec. 2011.

[2]   X. S. Yao and L. Maleki, "Optoelectronic oscillator for photonic systems," *Quantum Electron. IEEE J.*, vol. 32, no. 7, pp. 1141–1149, 1996.

[3]   M. Varón, "Étude et réalisation d'un oscillateur opto-microonde à base de VCSEL pour la génération harmonique de signaux microondes," Université de Toulouse, 2008.

[4]   L. Chrostowski, "Optical Injection Locking of Vertical Cavity Surface Emitting Lasers," University of California, 2003.

[5]   A. Hayat, "Optical Injection-Locking of 1.3µm and 1.5µm VCSELs: Experiments and Modeling," Institu Supérieur de l'Aéronautique et l'Espace, 2009.

[6]   X. S. Yao and L. Maleki, "Opto-electronic oscillator and its applications," in *Microwave Photonics, 1996. MWP '96.*, 1996, pp. 265–268.

[7]   A. Neyer and E. Voges, "High Frequency Electro-Optic Oscillator using an integrated interferometer," *Appl. Phys. Lett.*, vol. 40, no. 1, 1982.

[8]   X. S. Yao, L. Maleki, and D. Eliyahu, "Progress in the opto-electronic oscillator - a ten year anniversary review," in *Microwave Symposium Digest, 2004 IEEE MTT-S International*, 2004, pp. 287–290.

[9]   C. Moorlas, "Etude et realisation d'un oscillateur hybride microonde et optique fibrée monomode pour l'application à la dettection hétérodyne à 1.55 um," Ecole Nationale Superieure de l'Aeronautique et de l'Espace, 2000.

[10]   A. Le Kernec, "Étude et réalisation d'une source opto-microonde basée sur une architecture en anneau : potentialités de miniaturisation par l'utilisation de microrésonateurs optiques," Institut Supérieur de l'Aéroautique et de l'Espace, 2007.

[11]   M. Abramowitz and I. Stegun, *Handbook of Mathematical Functions*. Dover Publications, 1965.

[12]   M. Kaba, "Etude Approfondie et Realisation d'un Oscillateur Opto-Microondes por Applications Fibreés à 1550 nm," Ecole Nationale Superieure de l'Aeronautique et de l'Espace, 2003.

[13]   D. Pozar, *Microwave Engineering*, 3rd ed. Wiley, 2005.

[14]   O. Llopis, "Approche théorique et expérimentale du bruit de phase des oscillateurs microondes," Laboratoire d'Analyse et d'Architecture des Systèmes, Toulouse, 2000.

[15]   J. Rutman and F. L. Walls, "Characterization of frequency stability in precision frequency sources," *Proc. IEEE*, vol. 79, no. 7, pp. 952–960, Jul. 1991.

[16]   Y. Le Guennec, G. Maury, and B. Cabon, "Performance of Interferometric Systems for Optical Processing of Microwave Signals: Influence of Laser- and Microwave-Phase Noises," *IEEE Photonics Technol. Lett.*, vol. 16, no. 9, pp. 2120–2122, Sep. 2004.

[17]   D. Leeson, "Simple Model of Feedback Oscillator Noise Spectrum," *Proc. IEEE*, vol. 54, no. 2, pp. 329–330, 1966.

[18]   J. A. Barnes, A. R. Chi, L. S. Cutler, D. J. Healey, D. B. Leeson, T. E. McGunigal, J. A. Mullen, W. L. Smith, R. L. Sydnor, R. F. C. Vessot, and G. M. R. Winkler, "Characterization of Frequency Stability," *IEEE Trans. Instrum. Meas.*, vol. IM–20, no. 2, pp. 105–120, May 1971.

[19]   J. Gagnepain, "Phase and frequency noises in oscillators, Noise in physical systems and 1/f noise," 1983.

[20]   L. Zhou, W. Yin, J. Wang, and L. Wu, "Dielectric Resonators With High Q Factor for Tunable Low Phase Noise Oscillators," *IEEE Trans. Components, Packag. Manuf. Technol.*, vol. 3, no. 6, pp. 1008–1015, Jun. 2013.

[21]   E. N. Ivanov and M. E. Tobar, "Low phase-noise sapphire crystal microwave oscillators: Current status," *IEEE Trans. Ultrason. Ferroelectr. Freq. Control*, vol. 56, no. 2, pp. 263–269, 2009.

[22]   M. M. Mosso, V. P. R. Magri, C. L. Barucke, J. A. M. Souza, O. D. Aguiar, and S. R. Furtado, "A low phase noise oscillator prototype at 10GHz using Sapphire cavity for the Brazilian gravitational wave detector Mario Schenberg," in *2013 SBMO/IEEE MTT-S International Microwave & Optoelectronics Conference (IMOC)*, 2013, no. 2, pp. 1–5.

[23]   H. El Aabbaoui, J. David, E. de Foucauld, and P. Vincent, "Ultra low phase noise 2.1 GHz Colpitts oscillators using BAW resonator," in *2009 IEEE MTT-S International Microwave Symposium Digest*, 2009, pp. 1285–1288.

[24]   G. De Giovanni and M. Chomiki, "New phase noise measurement techniques ultra-low noise SAW oscillators," in *2010 IEEE International Frequency Control Symposium*, 2010, pp. 116–118.

[25]   M. Regis, O. Llopis, B. Van Haaren, R. Plana, A. Gruhle, J. Rayssac, and J. Graffeuil, "Ultra low phase noise C and X band bipolar transistors dielectric resonator oscillators," in *Proceedings of the 1998 IEEE International Frequency Control Symposium (Cat. No.98CH36165)*, 1998, pp. 507–511.

[26]   Hao Wang, Xiaole Cui, Chung Len Lee, and Zuolin Cheng, "A 2.34 - 3.29GHz CMOS LC VCO with low phase noise and low power," in *2014 IEEE International Conference on Electron Devices and Solid-State Circuits*, 2014, pp. 1–2.

[27]   Wen-Chieh Wang and Chung-Yu Wu, "The 1-V 24-GHz low-voltage low-power current- mode transmitter in 130-nm CMOS technology," in *2007 Ph.D Research in Microelectronics and Electronics Conference*, 2007, pp. 49–52.

[28]   J. Tsai, C. Chao, and H. Shih, "A X-band fully integrated CMOS frequency synthesizer," in *2012 Asia Pacific Microwave Conference Proceedings*, 2012, pp. 1226–1228.

[29]   P.-H. Merrer, K. Saleh, O. Llopis, S. Berneschi, F. Cosi, and G. Nunzi Conti, "Characterization technique of optical whispering gallery mode resonators in the microwave frequency domain for optoelectronic oscillators," *Appl. Opt.*, vol. 51, no. 20, p. 4742, Jul. 2012.

[30]   K. Saleh, "High Spectral Purity Microwave Sources Based on optical resonators," University of Toulouse, 2012.

[31]   L. Maleki and A. B. Matsko, "Optical generation of microwave reference frequencies," in *2011 XXXth URSI General Assembly and Scientific Symposium*, 2011, pp. 1–4.

[32]   K. Iga, "Surface-emitting laser-its birth and generation of new optoelectronics field," *IEEE J. Sel. Top. Quantum Electron.*, vol. 6, no. 6, pp. 1201–1215, Nov. 2000.

[33]   K. Iga, *Vertical Cavity Surface Emitting Laser Devices*. Springer Berlin Heidelberg, 2002.

[34]   F. Koyama, S. Kinoshita, and K. Iga, "Room-temperature continuous wave lasing characteristics of a GaAs vertical cavity surface-emitting laser," *Appl. Phys. Lett.*, vol. 55, no. 3, pp. 221–222, 1989.

[35]   J. L. Jewell, S. L. McCall, A. Scherer, H. H. Houh, N. A. Whitaker, A. C. Gossard, and J. H. English, "Transverse modes, waveguide dispersion, and 30 ps recovery in submicron GaAs/AlAs microresonators," *Appl. Phys. Lett.*, vol. 55, no. 1, pp. 22–24, 1989.

[36]   H. Shimizu, C. Setiagung, M. Ariga, Y. Ikenaga, K. Kumada, T. Hama, N. Ueda, N. Iwai, and A. Kasukawa, "1.3 um-Range GaInNAsSb-GaAs VCSELs," *IEEE J. Sel. Top. Quantum Electron.*, vol. 9, no. 5, pp. 1214–1219, 2003.

[37]   G. Boehm, M. Ortsiefer, R. Shau, J. Rosskopf, C. Lauer, M. Maute, F. Köhler, F. Mederer, R. Meyer, and M.-C. Amann, "InP-based VCSEL technology covering the wavelength range from 1.3 to 2.0μm," *J. Cryst. Growth*, vol. 251, no. 1–4, pp. 748–753, Apr. 2003.

[38]   A. Bacou, "Caractérisation et modélisation optoélectronique de VCSELs à grande longueur d'onde pour sous-ensembles optiques intégrés," Institut Superieur de l'Aeronautiqye et de l'Espace, 2008.

[39]   A. Mereuta, V. Iakovlev, A. Caliman, A. Syrbu, P. Royo, A. Rudra, and E. Kapon, "In(Al)GaAs-AlGaAs wafer fused VCSELs emitting at 2um wavelength," *IEEE Photonics Technol. Lett.*, vol. 20, no. 1, pp. 24–26, 2008.

[40]   H. Soda, K. Iga, C. Kitahara, and Y. Suematsu, "GaInAsP/InP Surface Emitting Injection Lasers," *Japanese Journal of Applied Physics*, vol. 18, no. 12. pp. 2329–2330, 1979.

[41]   P. Salet, F. Gaborit, P. Pagnod-Rossiaux, A. Plais, E. Derouin, J. Pasquier, and J. Jacquet, "Room-temperature pulsed operation of 1.3 [micro sign]m vertical-cavity lasers including bottom InGaAsP/InP multilayer Bragg mirrors," *Electron. Lett.*, vol. 33, no. 24, p. 2048, 1997.

[42]   J. Boucart, C. Starck, F. Gaborit, A. Plais, N. Bouche, E. Derouin, L. Goldstein, C. Fortin, D. Carpentier, P. Salet, F. Brillouet, and J. Jacquet, "1-mW CW-RT

monolithic VCSEL at 1.55 um," *IEEE Photonics Technol. Lett.*, vol. 11, no. 6, pp. 629–631, Jun. 1999.

[43] A. Black, A. R. Hawkins, N. M. Margalit, D. I. Babic, A. L. Holmes, Y.-L. Chang, P. Abraham, J. E. Bowers, and E. L. Hu, "Wafer fusion: materials issues and device results," *IEEE J. Sel. Top. Quantum Electron.*, vol. 3, no. 3, pp. 943–951, Jun. 1997.

[44] T. Baba, Y. Yogo, K. Suzuki, F. Koyama, and K. Iga, "Near room temperature continuous wave lasing characteristics of GaInAsP/InP surface emitting laser," *Electron. Lett.*, vol. 29, no. 10, p. 913, 1993.

[45] M. C. Larson, M. Kondow, T. Kitatani, K. Nakahara, K. Tamura, H. Inoue, and K. Uomi, "GaInNAs-GaAs long-wavelength vertical-cavity surface-emitting laser diodes," *IEEE Photonics Technol. Lett.*, vol. 10, no. 2, pp. 188–190, 1998.

[46] N. M. Margalit, K. A. Black, Y. J. Chiu, E. R. Hegblom, K. Streubel, P. Abraham, M. Anzlowar, J. E. Bowers, and E. L. Hu, "Top-emitting double-fused 1.5 um vertical cavity lasers," *Electron. Lett.*, vol. 34, no. 3, p. 285, 1998.

[47] S. Rapp, F. Salomonsson, J. Bentell, I. Sagnes, H. Moussa, C. Mériadec, R. Raj, K. Streubel, and M. Hammar, "Near room-temperature continuous-wave operation of electrically pumped 1.55 um vertical cavity lasers with InGaAsP/InP bottom mirror," *Electron. Lett.*, vol. 35, no. 1, p. 49, 1999.

[48] C. Kazmierski, J. P. Debray, R. Madani, I. Sagnes, A. Ougazzaden, N. Bouadma, J. Etrillard, F. Alexandre, and M. Quillec, "+55°C pulse lasing at 1.56 um of all-monolithic InGaAlAs/InP vertical cavity lasers," *Electron. Lett.*, vol. 35, no. 10, p. 811, 1999.

[49] J. K. Kim, E. Hall, O. Sjolund, and L. A. Coldren, "Room-temperature, electrically-pumped, multiple-active-region VCSELs with high differential efficiency at 1.55 um," *1999 IEEE LEOS Annu. Meet. Conf. Proceedings. LEOS'99. 12th Annu. Meet. IEEE Lasers Electro-Optics Soc. 1999 Annu. Meet. (Cat. No.99CH37009)*, 1999.

[50] E. Hall, G. Almuneau, J. K. Kim, O. Sjolund, H. Kroemer, and L. A. Coldren, "Design considerations in electrically-pumped, single-epitaxial VCSELs at 1.55 um with Sb-based mirrors," in *1999 IEEE LEOS Annual Meeting Conference Proceedings. LEOS'99. 12th Annual Meeting. IEEE Lasers and Electro-Optics Society 1999 Annual Meeting (Cat. No.99CH37009)*, 1999.

[51] M. Yamada, T. Anan, K. Kurihara, K. Nishi, K. Tokutome, A. Kamei, and S. Sugou, "Room temperature low-threshold CW operation of 1.23 um GaAsSb VCSELs on GaAs substrates," *Electron. Lett.*, vol. 36, no. 7, p. 637, 2000.

[52] S. Makino, T. Miyamoto, T. Kageyarna, Y. Ikenaga, N. Nishiyama, A. Matsutani, F. Koyama, and K. Iga, "Room temperature continuous-wave operation of GaInNAs/GaAs VCSELs grown by chemical beam epitaxy with output power exceeding 1 mW," *Tech. Dig. CLEO/Pacific Rim 2001. 4th Pacific Rim Conf. Lasers Electro-Optics (Cat. No.01TH8557)*, vol. 2, 2001.

[53] E. Hall, S. Nakagawa, G. Almuneau, J. K. Kim, and L. A. Coldren, "Selectively etched undercut apertures in AIAsSb-based VCSELs," *IEEE Photonics*

Technol. Lett., vol. 13, no. 2, pp. 97–99, 2001.

[54] M. Muller and M. C. Amann, "State-of-the-art and perspectives for long-wavelength high speed VCSELs," in *2011 13th International Conference on Transparent Optical Networks*, 2011, pp. 1–4.

[55] L. Coldren, S. Corzine, and M. Mashanovitch, *Diode lasers and photonic integrated circuits*. Wiley, 2002.

[56] C. Henry, "Theory of the linewidth of semiconductor lasers," *IEEE J. Quantum Electron.*, vol. 18, no. 2, pp. 259–264, Feb. 1982.

[57] G. P. Agrawal, "Intensity dependence of the linewidth enhancement factor and its implications for semiconductor lasers," *IEEE Photonics Technol. Lett.*, vol. 1, no. 8, pp. 212–214, Aug. 1989.

[58] F. Devaux, Y. Sorel, and J. F. Kerdiles, "Simple measurement of fiber dispersion and of chirp parameter of intensity modulated light emitter," *J. Light. Technol.*, vol. 11, no. 12, pp. 1937–1940, 1993.

[59] D. Derickson, *Fiber Optic Test and Measurements*. Hewlett-Packard, 1997.

[60] K. Petermann, *Laser Diode Modulation and Noise*. Dordrecht: Springer Netherlands, 1988.

[61] A. Rissons, "Caracterisation et Modélisation Optoelectronique de Diode Laser à Cavité Verticale Émettant par la Surface (VCSEL)," Ecole Nationale Supérieure de l'Aéronautique et de l'Espace, 2003.

[62] A. Hayat, M. Varon, A. Bacou, A. Rissons, and J. C. Mollier, "2.49 GHz low phase-noise optoelectronic oscillator using 1.55 um VCSEL for avionics and aerospace applications," in *Microwave photonics, 2008. jointly held with the 2008 asia-pacific microwave photonics conference. mwp/apmp 2008. international topical meeting on*, 2008, pp. 98–101.

[63] M. Varon, A. LeKernec, and M. Jean-Claude, "Opto-microwave source using harmonic frequency generator driven by a VCSEL-based ring oscillator," in *Proceedings of the European Microwave Association*, 2007, p. 248.

[64] G. Agrawal, *Fiber Optic Communication Systems*. Wiley, 2014.

[65] A. Yariv, H. Blauvelt, and S.-W. Wu, "A reduction of interferometric phase-to-intensity conversion noise in fiber links by large index phase modulation of the optical beam," *J. Light. Technol.*, vol. 10, no. 7, pp. 978–981, Jul. 1992.

[66] H. Hasegawa, Y. Oikawa, and M. Nakazawa, "A 10-GHz Optoelectronic Oscillator at 850 nm Using a Single-Mode VCSEL and a Photonic Crystal Fiber," *Photonics Technol. Lett. IEEE*, vol. 19, no. 19, pp. 1451–1453, 2007.

[67] K. Koizumi, M. Yoshida, and M. Nakazawa, "A 10-GHz Optoelectronic Oscillator at 1.1 um Using a Single-Mode VCSEL and a Photonic Crystal Fiber," *Photonics Technol. Lett. IEEE*, vol. 22, no. 5, pp. 293–295, 2010.

[68] E. Rubiola, *A generalization of the Leeson effect*. FEMTO-ST Institute, 2010.

[69] C. Y. Chang, S., Hsu, C. C., Huang, T. H., Chuang, W. C., Tsai, Y. S., Shieh, J.

Y., & Leung, "Heterodyne interferometric measurement of the thermo-optic coefficient of single mode fiber.," *Chinese J. Phys.*, vol. 38, pp. 437 – 442, 2000.

[70]   M. Kaba, H. Li, and A. Daryoush, "Improving thermal stability of opto-electronic oscillators," *IEEE Microw. Mag.*, vol. 7, no. 4, pp. 38–47, 2006.

[71]   L. Chrostowsky, X. Zhao, and C. J. Chang-Hasnain, "Microwave Performance of Optically Injection-Locked VCSELs," *IEEE Trans. Microw. Theory Tech.*, vol. 54, no. 2, pp. 788–796, 2006.

[72]   A. Hayat, A. Bacou, A. Rissons, J. Mollier, V. Iakovlev, A. Syrbu, and E. Kapon, "1.3 um single-mode VCSEL-by-VCSEL optical injection-locking for enhanced microwave performance," in *IEEE Lasers and Electro-Optics Society, 2008. LEOS 2008. 21st Annual Meeting of the*, 2008, pp. 224–225.

[73]   A. Hayat, A. Bacou, A. Rissons, J. Mollier, V. Iakovlev, A. Sirbu, and E. Kapon, "Long Wavelength VCSEL-by-VCSEL Optical Injection Locking," *Microw. Theory Tech. IEEE Trans.*, vol. 57, no. 7, pp. 1850–1858, 2009.

[74]   R. H. Pantell, "The laser oscillator with an external signal," *Proc. IEEE*, vol. 53, no. 5, pp. 474–477, 1965.

[75]   C. Buczek and R. Freiberg, "Hybrid injection locking of higher power CO2 lasers," *IEEE J. Quantum Electron.*, vol. 8, no. 7, pp. 641–650, Jul. 1972.

[76]   S. Kobayashi and T. Kimura, "Coherence of injection phase-locked AlGaAs semiconductor laser," *Electron. Lett.*, vol. 16, no. 17, p. 668, 1980.

[77]   C. Lin and F. Mengel, "Reduction of frequency chirping and dynamic linewidth in high-speed directly modulated semiconductor lasers by injection locking," *Electron. Lett.*, vol. 20, no. 25–26, p. 1073, 1984.

[78]   R. Lang, "Injection locking properties of a semiconductor laser," *Quantum Electron. IEEE J.*, vol. 18, no. 6, pp. 976–983, 1982.

[79]   T. Jung and M. C. Wu, "Gain and bandwidth enhancement of directly modulated analog fiber optic links using injection-locked gain-coupled DFB lasers," in *International Topical Meeting on Microwave Photonics. MWP'99. Technical Digest (Cat. No.99EX301)*, pp. 141–144.

[80]   T. B. Simpson, J. M. Liu, and A. Gavrielides, "Bandwidth enhancement and broadband noise reduction in injection-locked semiconductor lasers," *IEEE Photonics Technol. Lett.*, vol. 7, no. 7, pp. 709–711, Jul. 1995.

[81]   C.-H. Chang, "High Speed Vertical Cavity Surface Emitting Lasers with Injection Locking," UNIVERSITY of CALIFORNIA at BERKELEY, 2002.

[82]   D. Parekh, "Optical Injection Locking of Vertical Cavity Surface- Emitting Lasers ：Digital and Analog Applications," University of California, 2012.

[83]   A. Hayat, A. Bacou, A. Rissons, and J.-C. Mollier, "Optical Injection-Locking of VCSELs," in *Advances in Optical and Photonic Devices*, K. Y. Kim, Ed. InTech, 2010, pp. 67–100.

[84]   I. Petitbon, P. Gallion, G. Debarge, and C. Chabran, "Locking bandwidth and relaxation oscillations of an injection-locked semiconductor laser," *IEEE J.*

Quantum Electron., vol. 24, no. 2, pp. 148–154, Feb. 1988.

[85] C. Henry, N. Olsson, and N. Dutta, "Locking range and stability of injection locked 1.54 µm InGaAsp semiconductor lasers," *IEEE J. Quantum Electron.*, vol. 21, no. 8, pp. 1152–1156, Aug. 1985.

[86] C. Rumelhard, C. Algani, and A.-L. Billabert, *Composants et circuits pour liaisons photoniques en micro-ondes*. Lavoisier, 2010.

[87] J. Liu, "Semiconductor Lasers and Light Emitting Diodes," in *Photonic Devices*, Cambridge University Press, 2005.

[88] F. Ramian, "Time Domain Oscillator Stability Measurement Allan variance," *Rohde Schwarz Appl. Note*, pp. 1–16, 2012.

[89] H. Packard, "Phase Noise measurement Seminar," 1988.

[90] L. S. Cutler and C. L. Searle, "Some aspects of the theory and measurement of frequency fluctuations in frequency standards," *Proc. IEEE*, vol. 54, no. 2, pp. 136–154, 1966.

[91] I. T. Decker and B. Temple, "Choosing a Phase Noise Measurement Technique Concepts and Implementation RF & Microwave Measurement Symposium and Exhibition," 2000.

[92] H. Brahimi, "Etude en bruit de systèmes optiques hyperfréquences Modelisation, caractérisation et application a la métrologie en bruit de phase et à la géneration de fréquence," Université de Toulouse, 2010.

[93] A. Karim, S. Björlin, J. Piprek, and J. E. Bowers, "Long-wavelength vertical-cavity lasers and amplifiers," *IEEE J. Sel. Top. Quantum Electron.*, vol. 6, no. 6, pp. 1244–1253, 2000.

[94] "All-Epitaxial, Long-Wavelength, Vertical-Cavity Surface-Emitting Lasers using Bipolar Cascaded Active Region for High Differential Quantum Efficiency," University of California at Santa Barbara, 2005.

[95] P. Julien, "Caractérisation et modélisation du bruit d'intensité de VCSELs (AlGaAs) et de son influence sur le bruit de phase des liasons opto-hyperfréquences," Ecole Nationale de l'Aeronautique et de l'Espace.

[96] T. S. Kim, A. J. Danner, D. M. Grasso, E. W. Young, and K. D. Choquette, "Single fundamental mode photonic crystal vertical cavity surface emitting laser with 9 GHz bandwidth," *Electron. Lett.*, vol. 40, no. 21, p. 1340, 2004.

[97] S. F. Yu, *Analysis and Design of Vertical Cavity Surface Emitting Lasers*. Hoboken, NJ, USA: John Wiley & Sons, Inc., 2003.

[98] K. D. Choquette, D. F. Siriani, A. M. Kasten, M. P. Tan, J. D. Sulkin, P. O. Leisher, J. J. Raftery, and A. J. Danner, "Single Mode Photonic Crystal Vertical Cavity Surface Emitting Lasers," *Adv. Opt. Technol.*, vol. 2012, pp. 1–8, 2012.

[99] J. K. Kim, E. Hall, S. Nakagawa, A. Huntington, and L. A. Coldren, "Bipolar cascade 1.55 µm VCSELs with >1 differential quantum efficiency and CW operation," in *Conference Digest. 2000 IEEE 17th International*

Semiconductor Laser Conference. (Cat. No.00CH37092), 2000, pp. 155–156.

[100]   F. L. Walls, E. S. Ferre-Pikal, and S. R. Jefferts, "Origin of 1/f PM and AM noise in bipolar junction transistor amplifiers," *IEEE Trans. Ultrason. Ferroelectr. Freq. Control*, vol. 44, no. 2, pp. 326–334, Mar. 1997.

[101]   D. Halford, A. E. Wainwright, and J. A. Barnes, "Flicker Noise of Phase in RF Amplifiers and Frequency Multipliers: Characterization, Cause, and Cure," in *22nd Annual Symposium on Frequency Control*, 1968, pp. 340–341.

[102]   A. Hati, D. A. Howe, F. L. Walls, and D. Walker, "Noise figure vs. PM noise measurements: a study at microwave frequencies," in *IEEE International Frequency Control Sympposium and PDA Exhibition Jointly with the 17th European Frequency and Time Forum, 2003.*, 2003, pp. 516–520.

[103]   E. Rubiola, "The Leeson effect - Phase noise in quasilinear oscillators," Université Henri Poincaré, Feb. 2005.

Annex 1

Phase Noise Meaurement Techniques

1. Phase Noise Measurement Techniques [89]–[92]

To measure the phase noise it is possible to use several techniques. The direct measurement using an electrical spectrum analyzer (ESA), the source comparison mehod, and the frequency discriminator method. To select a measurement method it is necessary to take into account the sensibility of the measurement device and the oscillator's stability as well.

2. Direct Measurement

This technique is the easiest to implement. The oscillator is directly connected to the electrical spectrum analyzer. The RF display of the ESA permits to read the carrier power (P_{osc}) and the power offset (P_{offset}), from this the phase noise power spectral density is given by:

$$\mathcal{L}(f) = 10\log(P_{osc}) - 10\log\bigl(P_{offset}\bigr) - 10\log(C) + k \ [\text{dBc/Hz}]$$

(204)

There are two correction coefficients:

- The Resolution Bandwith Filter (RBW) of the ESA is not squared but loretzian shaped ant it must be corrected as C=1.2RBW.

- The detection circuit consists of a logarithmic amplifier followed by a peak detector. Generally, k is 2.5 dB.

Using this method, it is important to take into account some factors that may reduce the coherence of the results. For this, it is necessary to follow these rules:

1. The source under test must have an amplitude modulation lower than the phase modulation.

2. The local oscillator of the ESA must has a noise level at least ten times lower that the measured source.

3. The phase noise measurements for offset lower than some kHz are not possible to be measured due to the source frequency drift.

3. Method Using Source Comparison

With this method it is possible to convert the phase difference between the source under test and a reference source at the same frequency. The two sources at same frequency and in quadrature are injected inside a mixer that acts as a phase detector,

as seen in Figure 109. At the mixer output there is one signal with frequency equal to the difference of the two signals and another one that corresponds to the double of the frequency, this one is filtered by a low pass filter.
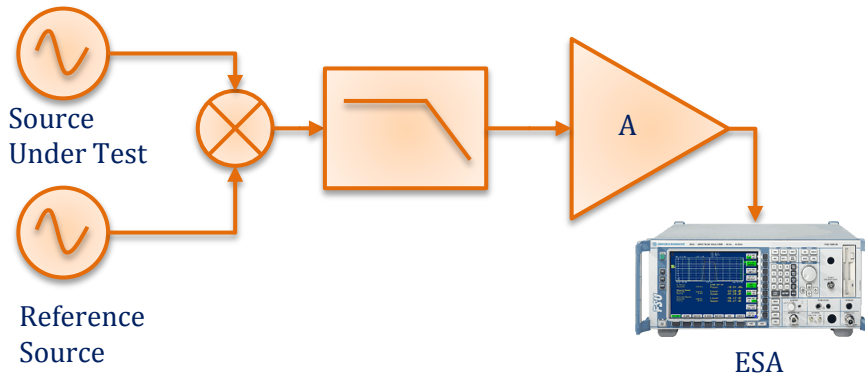
Figure 109 Phase noise measurement using two sources method.

Over signal at frequency equal to the difference of both (with zero average value) there is a signal that overlaps whose amplitude is proportional to the phase noise of both signals. This signal is then amplified and measured with an ESA at base band. Using the transfer function of the detector it is possible to obtain the phase noise by subtracting the frequency response from the measurement.

4. Residual Modulation Method (Frequency Discriminator)

This technique proposes the use of a frequency discriminator followed by a filter, see Figure 110. The bandwidth is fixed at a specific value, usually between 300 Hz to 3 kHz. The output voltage of the filter is proportional to the frequency fluctuation in Hz.
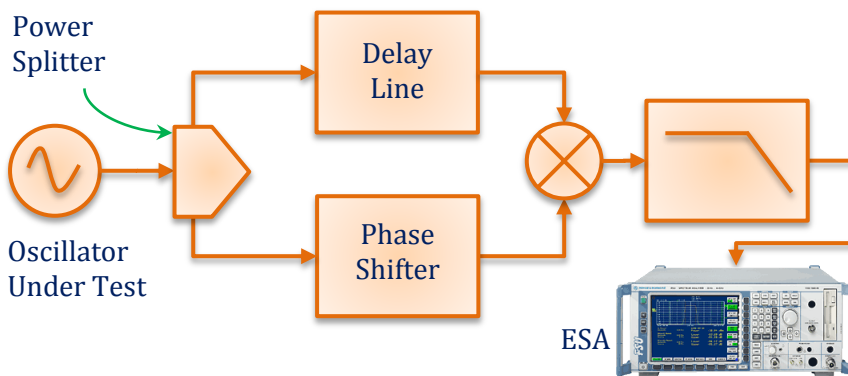
Figure 110 Frequency discriminator phase noise measurement method.

The operation principle of this method is the use of a delay line and a phase detector. The delay line transforms the frequency variations (Δf) in phase fluctuations ($\Delta \phi$) between the two inputs mixer, by this the relation $S_\phi(f) = 2\pi\tau S_{\Delta f}(f)$, where τ represents the delay of the line. The sensibility of the discriminator is given by, $D = 2\pi k\tau$ which is expressed in [V/Hz].

Annex 2

VCSEL Structure

1. Vertical Cavity Surface Emitting Laser (VCSEL) Description [32]

The Vertical Cavity Surface Emitting Laser (VCSEL) differs from other laser structures due to the fact that this is a surface emitting device instead of an edge emitting device. Usually common semiconductor lasers, known as Edge Emitting Lasers (EELs), emit their energy in a transverse direction compared with the junction, as seen in Figure 111. VCSELs emit their energy perpendicular to semiconductor layers, as seen in Figure 112.
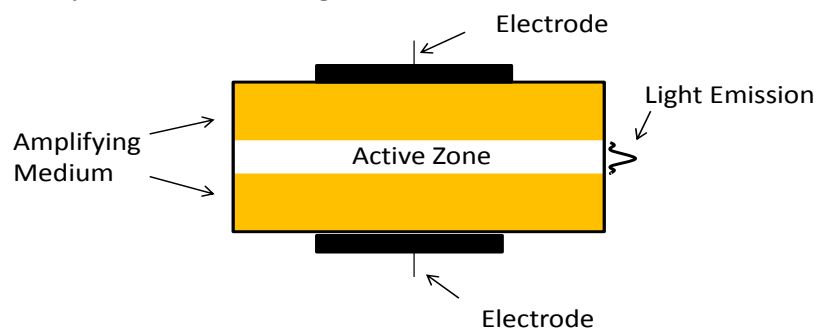
Figure 111 Edge Emitting Laser Structure [33].
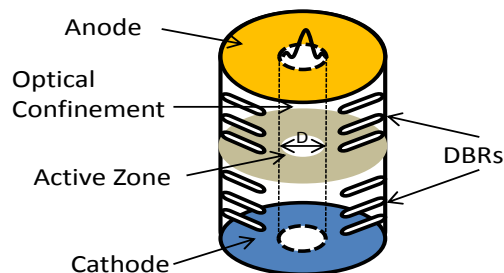
Figure 112 VCSEL Structure [52].

The first VCSEL was implemented in 1979 [33] as the need to design a laser that could emit its energy perpendicular to semiconductor junction. It was not until the end of 80's decade when Koyama [34] and Jewell [35] developed techniques that led to wide spread VCSELs use.

2. Distributed Bragg Reflectors (DRBs)

The Distributed Bragg Reflectors (DBR's) play an important role inside VCSELs. This is due to the fact that they are in charge of electron circulation inside the cavity. It is important to mention that DBRs reflects the generated wave inside the cavity in order to create an oscillation. Due to the VCSEL reduced cavity size, it is mandatory for DBRs to have high reflectivity in order to achieve oscillation condition in such cavity [93].

The principle that makes DBR work is a series of layers arranged one over the other, the key resides in the fact that their refractive index is slightly different each other. This make possible to guide and reflect light achieving with not too much layer high reflectivity close to 99%. The thickness of each layer is quarter of desired wavelength. The wave phase that goes through a DBR pair is given by:

$$\phi = \frac{2\pi}{\lambda} nd$$

(205)

Where n represents diffraction index of each layer. The thickness of each layer is related to the wavelength by the following expression:

$$d = \frac{\lambda}{4n}$$

(206)

Depending of the selected material the number of layer varies. For instance, Figure 113 presents the number of layers required to achieve high reflectivity according to selected material. Figure 114 presents a DBR detailed structure.
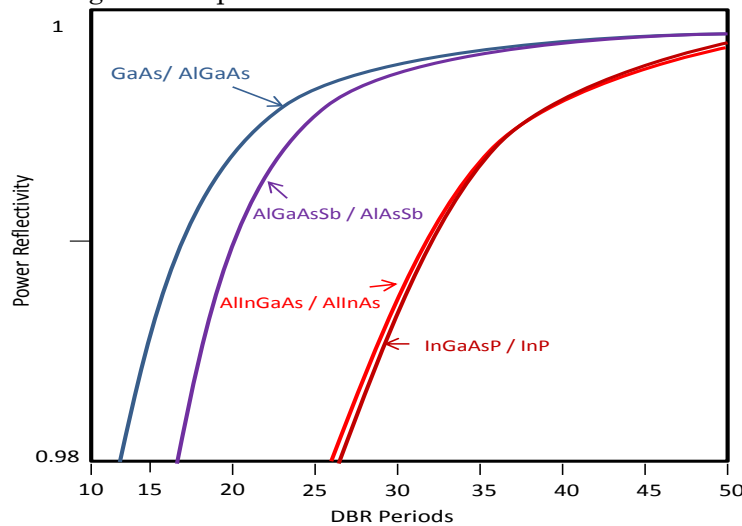
Figure 113 Maximun reflectivity vs DBR pair number for several 1.55 um VCSEL[60].
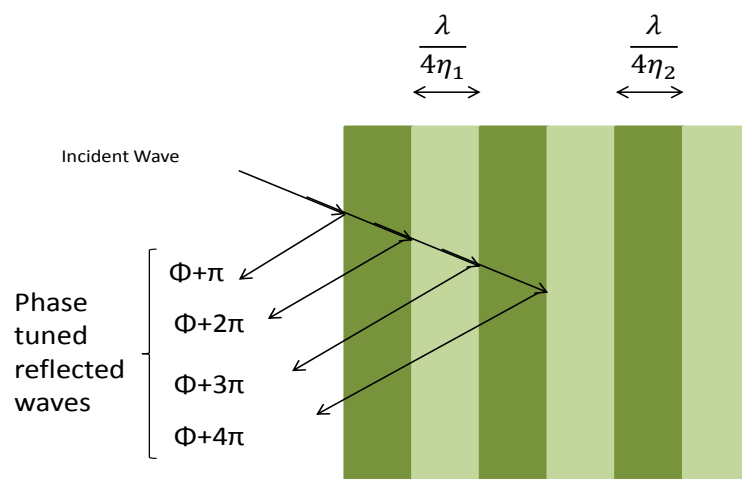
Figure 114 Bragg reflector operation principle.

3. Active Zone

The active zone is the place where lasing phenomena takes place. Basically this happens in the quantum wells [33]. In the quantum wells the electrons confinement

and material gain produces energy interchange among quantum levels as seen in Figure 115. In VCSELs the confinement is enhance due to the lasing configuration, the structures in active zone are known as SCH (Separate Confinement Heterostructure) which leads to reduced bias current and high carrier confinement.
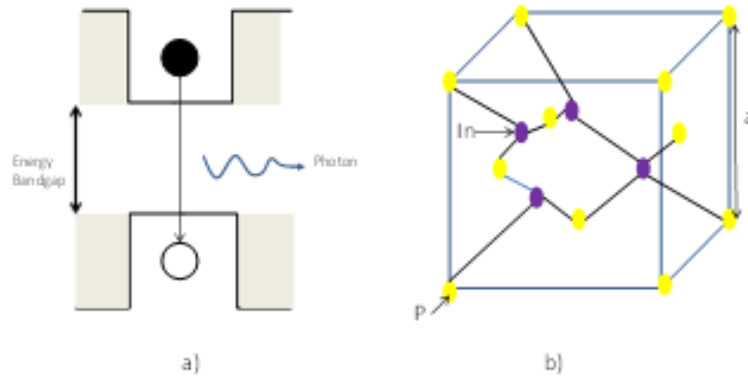
Figure 115 a)Quantum well b) Indium phoshide lattice.

Manufacturing process depends of material used. Each material has different lattice structure. Each one is characterized by its lattice constant a as seen in Figure 115b. To develop a device using a subtract with lattice constant a1, the semiconductor must be an a1 lattice constant as well. For instance, Indium Phosphide is widely used in VCSEL manufacturing as substrate.

4. VCSEL Structures [95]–[99]

Depending on the manufacturer, the wavelength and power of the VCSEL, different VCSEL structures have been proposed.

4.1 Photon Implantation

This technique is used to enhance carrier guidance through the active zone. This structure is presented in Figure 116.
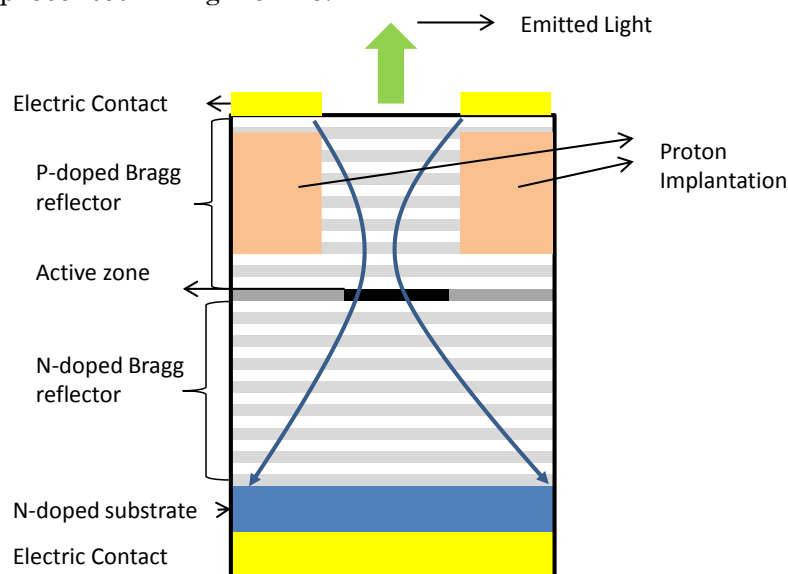
Figure 116 VCSEL with photon implantations.

4.2 Buried Structure

This structure has performed well in 850 nm band. It emits single mode with a reduced threshold current. This structure presents degradation due to thermal effects. Optic beam is guided and confined through a column. This "column" is buried in a lower conductivity and refractive index material.

Electric Contact

P-doped Bragg reflector

Blocking Layer

Active zone

N-doped Bragg reflector

N-doped substrate

Electric Contact

Emitted Light
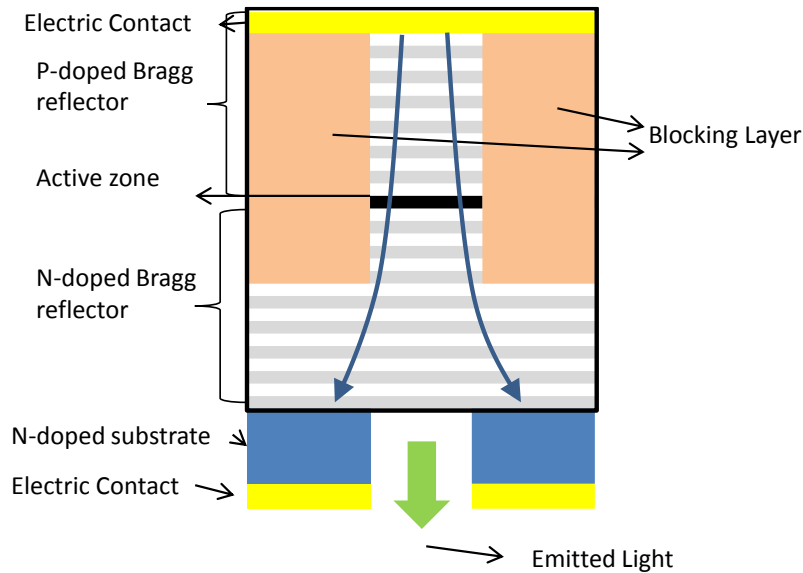
Figure 117 VCSEL buried structure.

4.3 VCSEL Oxide Diaphragm

A thin oxide layer (AlOx) is deposed over the circular area around the active zone in order to enhance carrier confinement. Some structures have oxide layer over the active zone in order to increase the confinement. This method has been successfully applied in commercial production. Figure 118 presents VCSEL oxide diaphragm structure.

Emitted Light

Electric Contact

P-doped Bragg reflector

Emitted Light

Active zone

N-doped Bragg reflector

N-doped substrate

Electric Contact
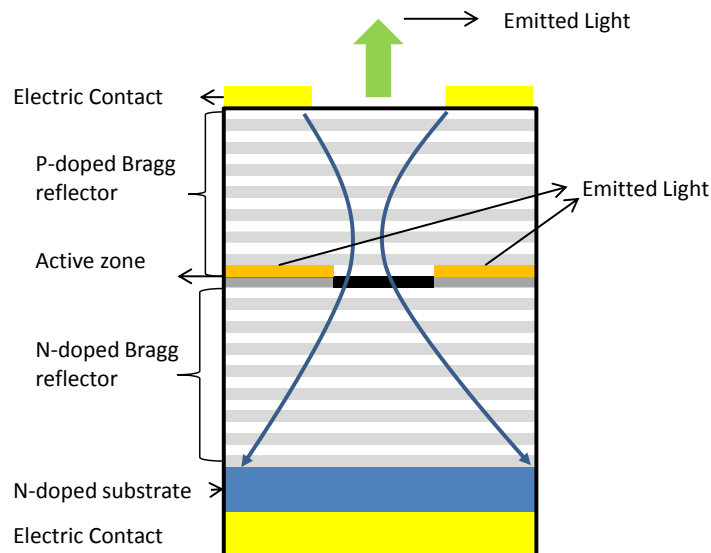
Figure 118 VCSEL oxide diaphragm structure.

In order to avoid undesired transversal modes due to refractive index guided it is necessary to reduce guide diameter, less than 5 μm, with this increases electrical

resistance of DBRs having as consequence thermal effects and by this, reducing VCSEL bandwidth.

4.4 Photonic Crystal VCSEL (PC-VCSEL)

This type of structure is designed to single mode VCSELs. Some "crystal holes" are located in semiconductor material, in the upper mirror, as shown in Figure 119.
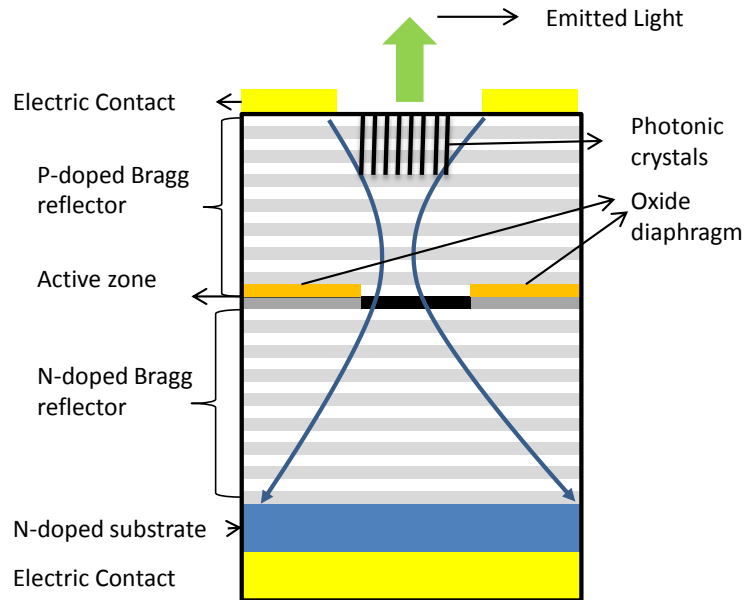
Figure 119 PC-VCSEL structure.

4.5 Multiple Active Region VCSELs (MAR-VCSELs) or Bipolar Cascade VCSELs (BC-VCSELs)

This kind of structures uses several active regions. The first active region produces a cascade effect to the second active region through a junction tunnel and so on. Figure 120 presents MAR VCSEL quantum well scheme. Figure 121 presents MAR VCSEL structure, in this two active region can be seen. This concept was proposed by K. Iga in 1984 and it was implemented by L. Coldren in 2000.

First Active Region

Injected current

Conduction band

3 photons

Tunnel effect

Second Active Region

Valence Band

3 photons
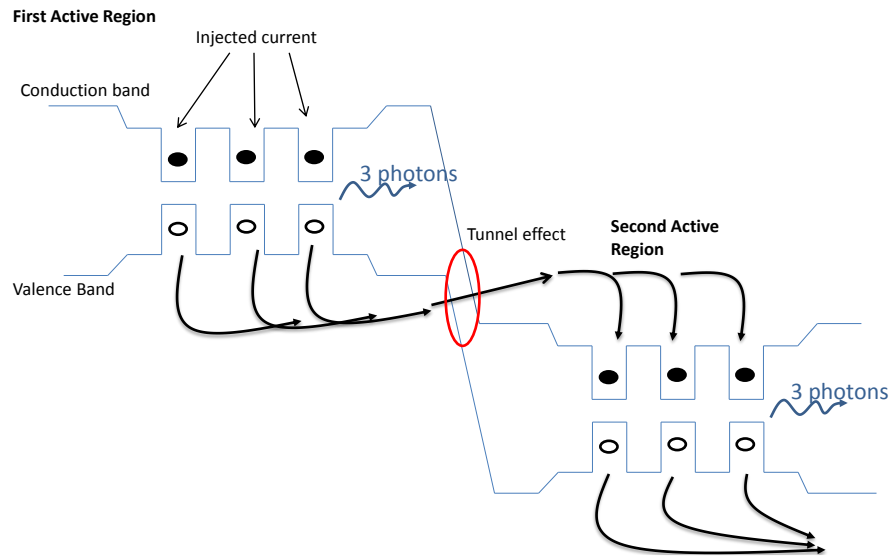
Figure 120 MAR-VCSEL quantum well structure.

Cathode

Upper DBR

Optical confinement

3 active regions

Anode

Lower DBR
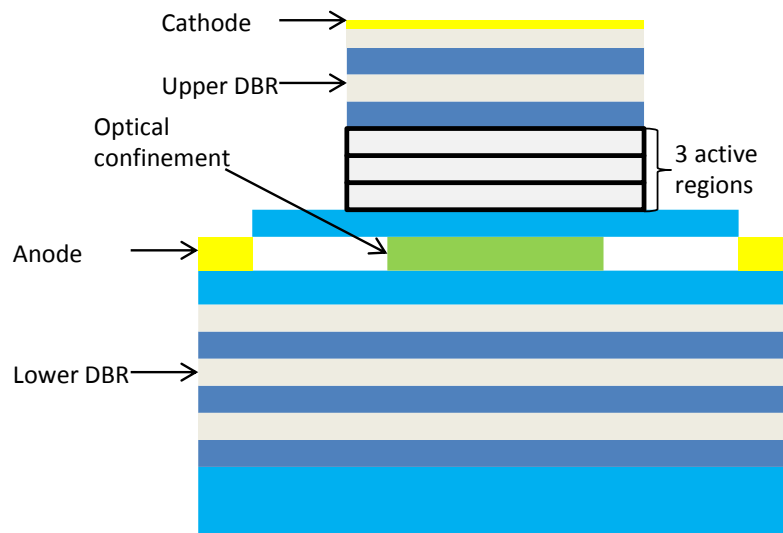
Figure 121 MAR-VCSEL structure.

Annex 3
RayCan VCSEL Datasheet

RayCan — *1550 nm Vertical-Cavity Surface-Emitting Laser*

RC33xxx1-F

Description
The RayCan 1550 nm single mode VCSEL is designed for high-speed, high-performance communication applications.

Features
- Low dependence of electrical and optical characteristics over temperature
- Data rates up to 4.25 Gbps
- Cylindrical TO package with single mode fiber pigtail

Applications
- Access network for long distance (>2 km)
- Metro area network
- Gigabit Ethernet

Electrical and optical characteristics
(T = 25°C unless otherwise stated)

Parameter	Symbol	Min.	Typ.	Max.	Unit	Notes
Threshold current	I_{th}		2	4	mA	
Forward voltage	V_f			3	V	
Series resistance	R_s		100	200	Ω	
Output power	P_o	0.4	0.5		mW	
Wavelength	λ	1530	1550	1570	nm	
Side mode suppression	SMSR	30	35		dB	
Rise and fall time	t_r t_f		~90 ~120		psec	(20%-80%)
Operating temperature	T_{op}		0~70		°C	

Absolute maximum ratings
(T = 25°C unless otherwise stated)

Parameter	Symbol	Rating	Unit	Notes
Forward current	I_f	15	mA	
Reverse voltage	V_r	5	V	
Operating temperature	T_{op}	70	°C	
Storage Temperature	T_{sg}	0~100	°C	
Reflow Temperature	T_{ref}	260	°C	10 sec. 2 mm from case

090115 Rev 4.0

RayCan

RayCan — *1550 nm Vertical-Cavity Surface-Emitting Laser*

RC33xxx1-F

Notice

Conditions exceeding those listed may cause permanent damage to the device. Devices subjected to conditions beyond the limits specified for extended periods of time may adversely affect reliability.

TO-56 pigtail VCSEL

Dimensions   unit : mm
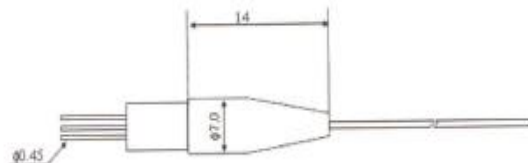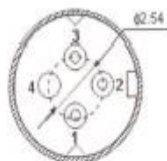
Bottom side view   **pin configuration**

Number	Function
1	VCSEL Anode
2	VCSEL Cathode
3	NA
4	Case

DANGER

Laser RADIATION AVOID DIRECT EXPOSURE TO BEAM

Class 3b or Class 2b Product

VISIBLE AND/OR INVISIBLE LASER DIODE — AVOID EXPOSURE Laser Radiation is emitted from this aperture

ATTENTION

OBSERVE PRECAUTIONS FOR HANDLING ELECTROSTATIC SENSITIVE DEVICES

Warning

The VCSEL is a class IIIb laser. Laser beams emitted from this product are hazardous to the naked eye. Avoid eye or skin exposure to direct or scattered radiation. Due to the size of the component, the applicable warning logotype, aperture label, and identification label can not be placed on the component.

Caution

This product is sensitive to the electrostatic discharge(ESD). To prevent ESD-induced damage and/or degradation to equipment, take normal ESD precautions when handling this product.

RayCan

Inspection table

P/N : RC33xxx1-FSA
VCSEL1

Description : 1550nm 4.25G VCSEL Pigtailed

Serial no : RC330221-FSA-05341206

Customer :

Test results

L-I-V (T = 25 ℃)

Spectrum (I = 7 mA)
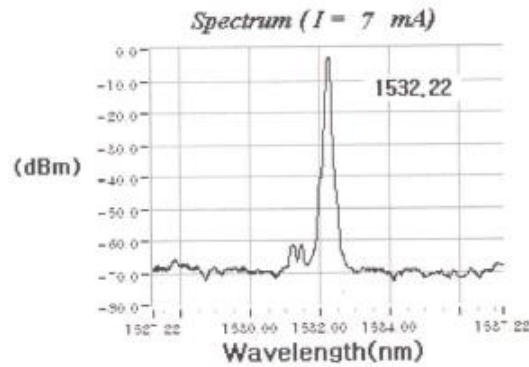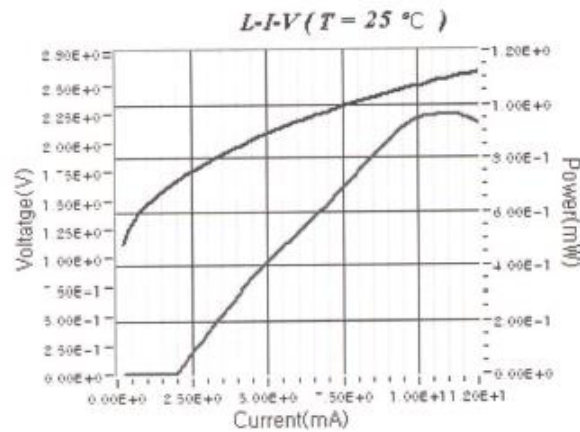
Date : 2013. 05. 22

Confirmed by : Y - S. JEON

Annex 4 Photodetector, Microwave Filter and Amplifier Information

New Focus 1544 B Photodetector

A New Focus 1544B InGaAs high speed photodetector is used in the VBO, see Figure 122. According to the datasheet, the manufacturer certifies that the photodetector works up to 12.5 GHz, this was verified in the laboratory by measuring its frequency response. According to our measurement, the bandwidth of the photodetector agrees to that described in the datasheet.
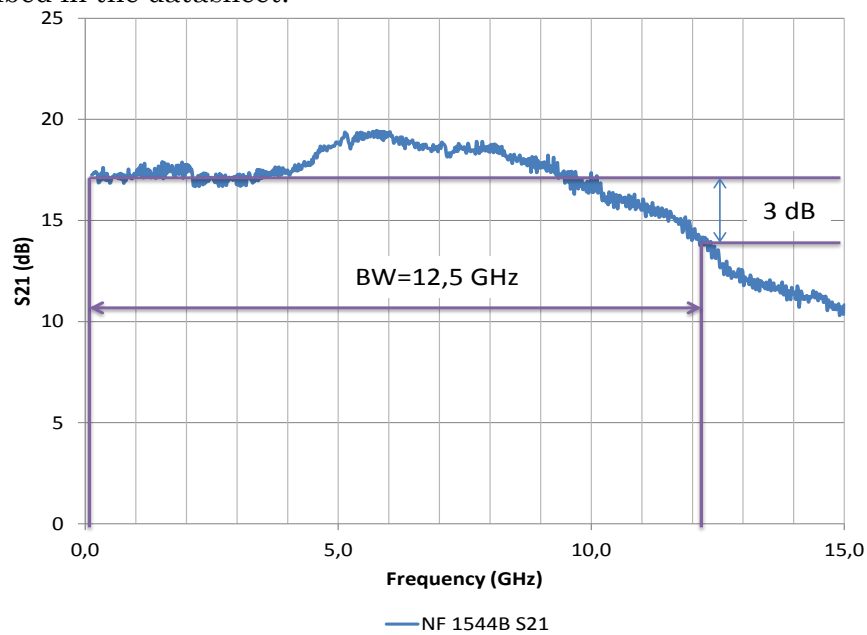
Figure 122 New Focus 1544B bandwidth measurement.

The Figure 123 presents the schematic schematic connection photodetector bandwidth measurement. This was performed using and electrical/optical HP8510C vector network analyzer. An optical laser is modulated using a frequency sweep at the photodetector input. The RF output of the photodetector is connected to the RF port of the HP8510C.
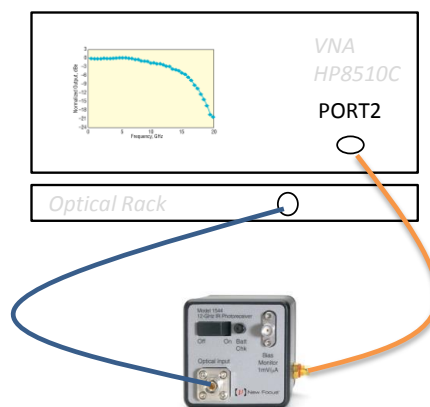
Figure 123 Photodector bandwidth measurement setup.

Photodetected Current

To characterize the photodetector performance, a 1300 and 1500 nm VCSELs are connected to the photodetector. A bias current sweep from 2 to 7 mA is carried out to verify the responsivity of the device. The responsivity values are these:

$$R_{@1300nm} = 0.649 \frac{A}{W}$$

$$R_{@1500nm} = 0.698 \frac{A}{W}$$

The detected optical power is plot in Figure 124.
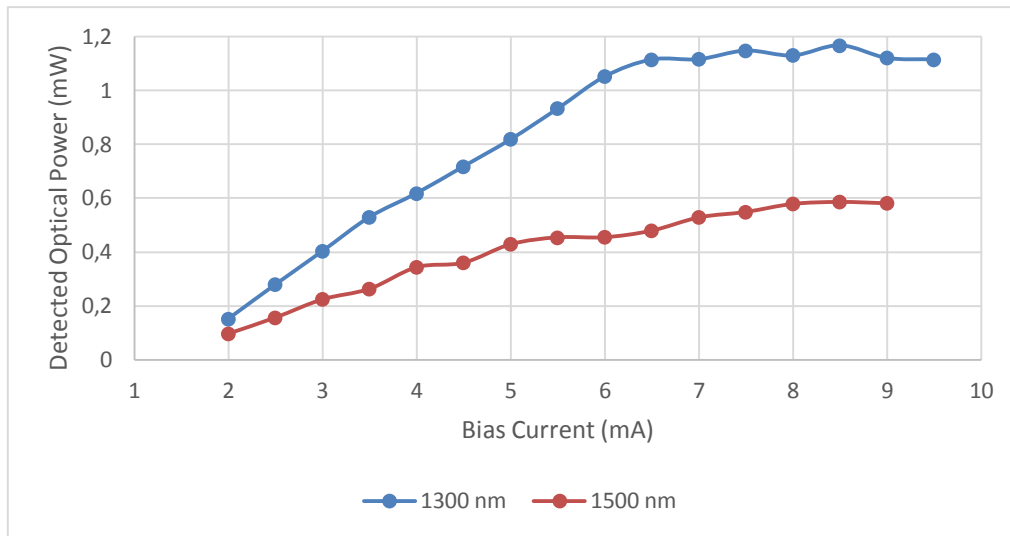
Figure 124 Detected optical power for 1300 and 1500 nm VCSELs.

2.49 GHz Microwave Filter (Reactel 4W8-2492-3)

For the 2.49 GHz VBO, a Reactel cavity filter was used, see Figure 125. This band pass filter has a bandwidth of 3 MHz. Its band pass profile can be seen in Figure 126.
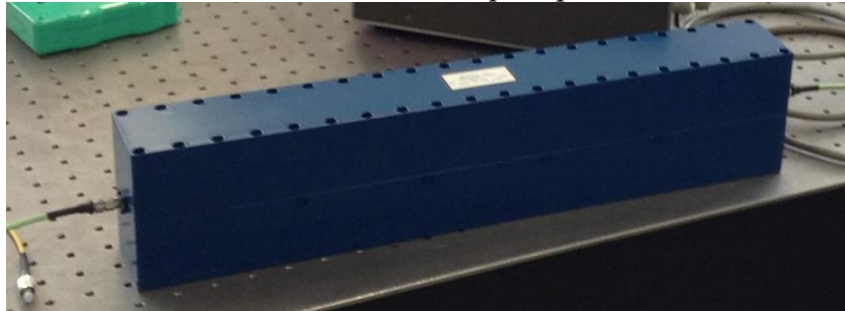
Figure 125 Band pass microwave cavity filter.
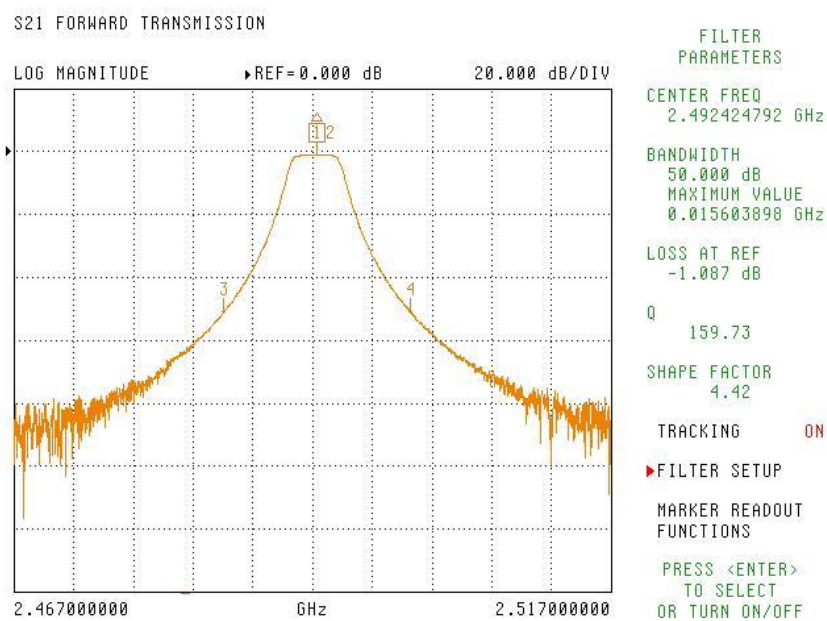
Figure 126 Microwave cavity filter bandwidth measurement.

10 GHz Microwave Filter (Reactel FTC-998109-BPS1-A)

p/n: FTC-998109-BPS1-A

	Test condition	min	typ	max	Unit
Center Frequency		9.995	10.000	10.005	GHz
Insert Loss				8	dB
Pass Band Ripple					dB
VSWR				1.5 : 1	dB
Rejection	@ 9.985 GHz @ 10.015 GHz	30 30			dB
Power Handling					Watts
Impedance			50		Ohms
Operating Temperature		-10		+50	℃
Connector (In/Out)			SMA-Female		

Outline drawing (Unit: mm)
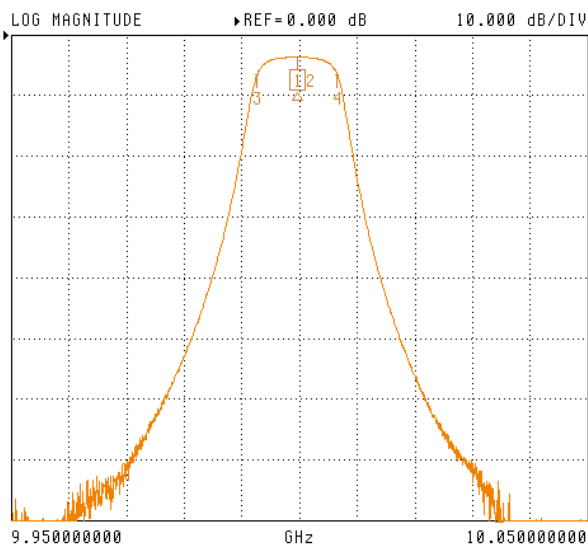

```
S21 FORWARD TRANSMISSION

LOG MAGNITUDE        ▶REF=0.000 dB      10.000 dB/DIV

9.950000000          GHz          10.050000000

SET MARKERS

▶MARKER 1  ΔREF  ON
   9.999625000 GHz

 MARKER 2        ON
   9.999677311 GHz

 MARKER 3        ON
   9.992725287 GHz

 MARKER 4        ON
  10.006629335 GHz

 MARKER 5        OFF

 MARKER 6        OFF

 DISPLAY         ON
 MARKERS

 ΔREF MODE       ON

 SELECT
 ΔREF MARKER

 MARKER READOUT
 FUNCTIONS
```

12 GHz Microwave Filter (Reactel FTC-1291-29-BPS1-A)

S21 FORWARD TRANSMISSION

LOG MAGNITUDE ▸REF=0.000 dB 10.000 dB/DIV

11.950000000	GHz	12.050000000
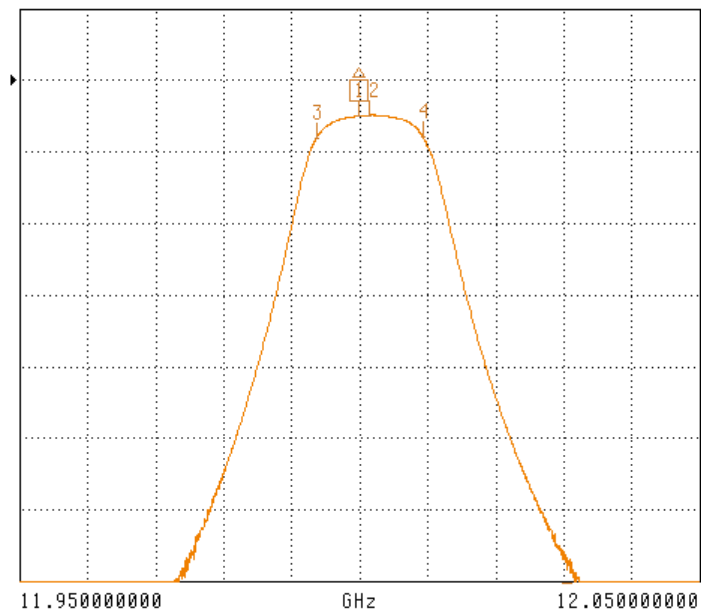
SET MARKERS

▸MARKER 1 ΔREF ON
12.000000000 GHz

MARKER 2 ON
12.001555356 GHz

MARKER 3 ON
11.993706221 GHz

MARKER 4 ON
12.009404491 GHz

MARKER 5 OFF

MARKER 6 OFF

DISPLAY ON
MARKERS

ΔREF MODE ON

SELECT
ΔREF MARKER

MARKER READOUT
FUNCTIONS

2.49 GHz Microwave Amplifier (Stealth Microwave SM2040-37H)

Parameter	Specification
Frequency Range	2.0 – 4.0 GHz
Pout (P1dB)	+37 dBm (min)
Output Third Order Intercept Point (OIP3)	+47 dBm (typ.)
Linear Gain	37 ± 1.0 dB
Gain Flatness (over full band)	± .75 dB
Input/Output Return Loss	-8 dB / -8 dB
DC Input Voltage	+12 Volts
DC Input Current	2.9 Amperes
Mechanical Dimensions (Without Heatsink)	5.0 x 2.5 x .563 inches
RF Connectors	SMA Female
Operating Temperature (Baseplate)	0ºC to +55ºC
Operating Humidity	95% Non-condensing
Operating Altitude	Up to 10,000 feet above Sea Level

Pin	Description	Values
RF IN	Input Connector (SMA Female)	+ 19 dBm (max.)
RF OUT	Output Connector (SMA Female)	+ 37 dBm @ P1dB
GND	Ground Turret	----
+12 VDC	DC Input Voltage	+ 12 Volts @ 2.9 Amps.
ON/OFF	TTL Logic On/Off	0 Volts = Off, +5 Volts = On

Specifications subject to change without notice.

7 to 10 GHz Microwave Amplifier (Liconn LNA700012000A)
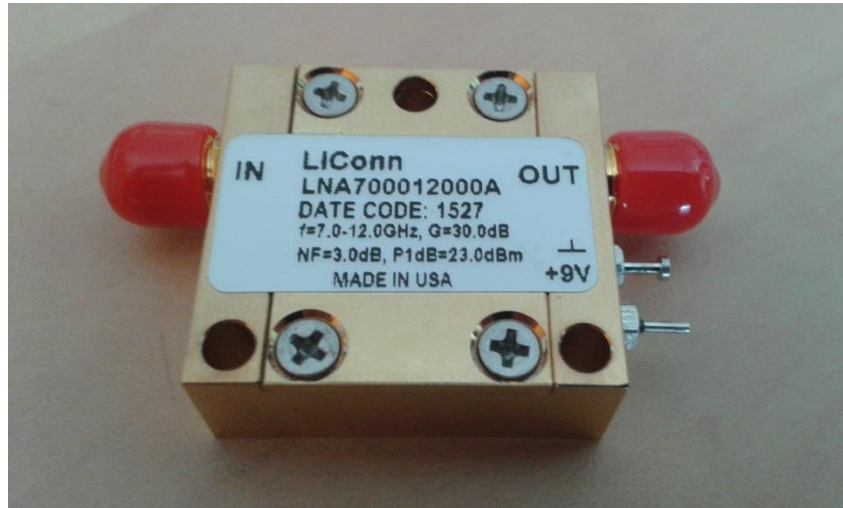
Symbol	Parameters/Conditions	Unit	Min	Typical	Max
G	Gain	dB	28		34
ΔG	Gain Flatness	dB			±2.5
I_d	Device Current (V_{dd}=+9V)	mA		220	
NF	Noise Figure (10M-30MHz)	dB	2.0		4.0
P_{1dB}	Output 1dB Gain Compression	dBm	22	24	
$VSWR_1$	Input VSWR	Ratio			2:1
$VSWR_2$	Output VSWR	Ratio			2:1
S_{12}	Reverse Isolation	dB	40		
V_{dd}	Positive Power Supply Voltage	V	+8.5	+9.0	+9.5
$P_{in, max}$	Maximum Average RF Input Power	dBm			20
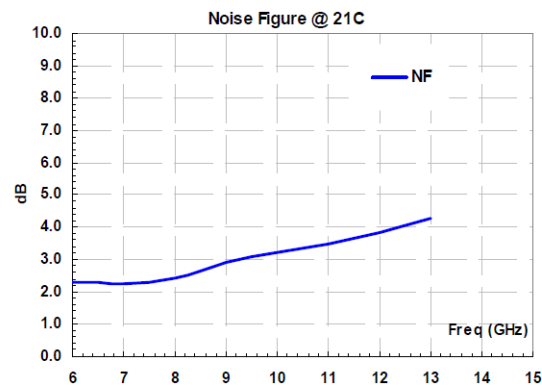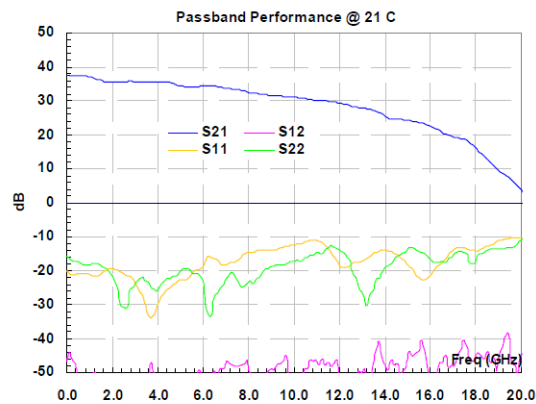
30 MHz to 10 GHz Microwave Amplifier (Liconn LNA003012000A)
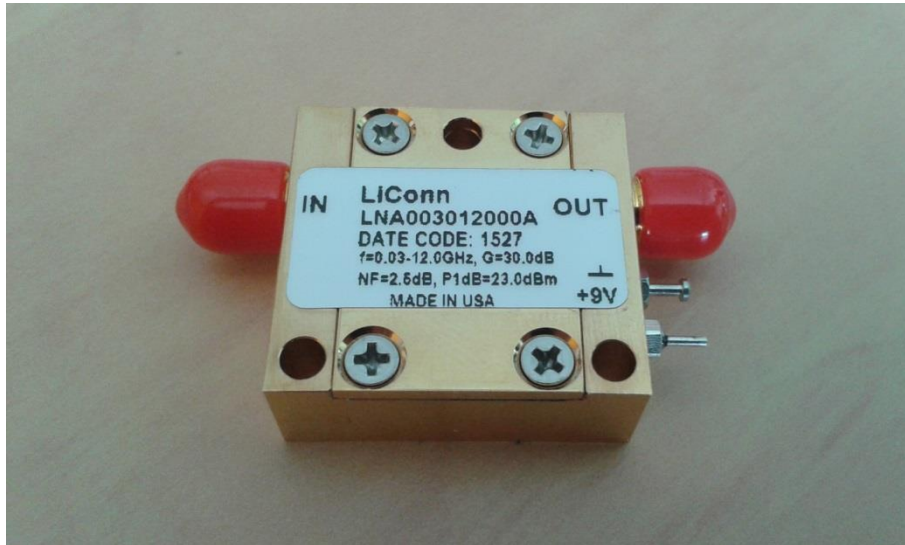
Symbol	Parameters/Conditions	Unit	Min	Typical	Max
G	Gain	dB	28		38
ΔG	Gain Flatness (Every 100 MHz)	dB			±0.2
I_d	Device Current (V_{dd}=+9V)	mA		220	
NF	Noise Figure (10M-30MHz)	dB	1.5		4.0
P_{1dB}	Output 1dB Gain Compression	dBm	22	24	
$VSWR_1$	Input VSWR	Ratio			2:1
$VSWR_2$	Output VSWR	Ratio			2:1
S_{12}	Reverse Isolation	dB	40		
V_{dd}	Positive Power Supply Voltage	V	+8.5	+9.0	+9.5
$P_{in,\,max}$	Maximum Average RF Input Power	dBm			20
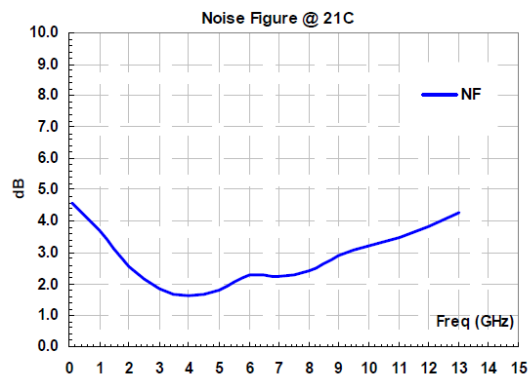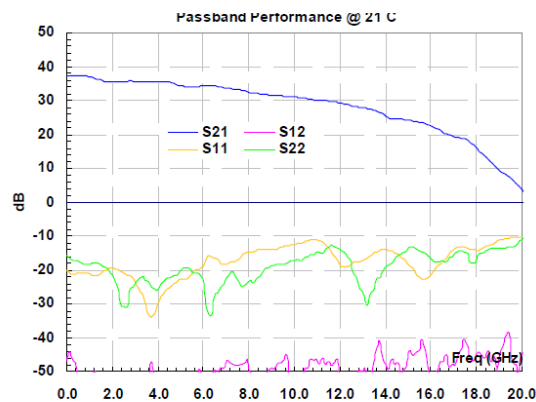
11.5 to 12.5 GHz Microwave Amplifier (PA2083P-25)

Model No.	PA2083P-25
Frequency	11.5 to 12.5 GHz
Gain	30 dB min
Flatness	±1.0 dB
Output P1dB	+33 dBm min
Noise Figure	3.5 dB @ 25°C
VSWR input	2.0:1
Output	2.5:1
DC Supply +12 ± .5V	@ 2.0A max
Operating Case Temperature	-30 to +65°C

9.5 to 10.5 GHz Microwave Amplifier (MPA-09501050-35-23)

★	Référence Amplificateur	:	SMP_MPA_09501050_35_23
★	Bande passante	:	9.5 à 10.5 GHz
★	Gain	:	35 dB min.
★	P1dB	:	$\geq$ 23 dBm
★	NF	:	$\leq$ 2 dB
★	TOS IN/OUT	:	2
★	Connecteur	:	SMA femelle
★	Alimentation	:	15 V – 350 mA max.

Annex 5 Microwave and Optical Measurement Equipment

Vector Network Analyzer Agilent HP8510C

The technical specifications of this device are available at http://cp.literature.agilent.com/litweb/pdf/5091-8484E.pdf

System capabilities[1]

Measurement

Number of display channels: Two display channels are available.

Number of display parameters: The four basic parameters, S11, S21, S12, S22, can be displayed for either selected channel in either a "four quadrant" or an "overlay" format.

Measurement parameters: S11, S21, S12, S22. Parameters may be redefined by the user for special applications. Conversion to Z1 (input impedance), Z2 (output impedance), Y1 (input admittance), Y2 (output admittance), and 1/S is also provided.

Domains available: Frequency, time (Option 010), pulse profile[2] (Option 008), auxiliary voltage (rear panel output acting as device stimulus, range is ±10 VDC), and power[3] (sweep power level at a CW frequency).

Formats

Cartesian: log/linear magnitude, phase, group delay, SWR, real part of complex parameter, imaginary part of complex parameter.

Smith chart: Marker format can be selected as log magnitude, linear magnitude, R + jX, or G + jB.

Polar: Marker format can be selected as log magnitude, linear magnitude, phase, or real and imaginary.

Data markers: Five independent data markers read out and display the value of the formatted parameter and stimulus (frequency, time, or auxiliary voltage).

Marker functions

Marker search: Specific trace values can be located, such as MAX, MIN, and target (for example–3.00 dB point)

Discrete/continuous: Markers can indicate data at actual data points or they can interpolate between data points to allow the setting of a marker at an exact stimulus value.

Delta marker: Marker readout shows difference between active marker and the reference marker (any marker can be used as the reference).

Group delay characteristics

Group delay is computed by measuring the phase change within a specified step (determined by the frequency span and the number of points per sweep).

Aperture: Determined by the frequency span, the number of steps per sweep, and the amount of smoothing applied.

Minimum aperture = (frequency span)/(# points –1)
Maximum aperture = 20% of the frequency span

Range: The maximum delay is limited to measuring no more than ±180 degrees of phase change within the minimum aperture.

Range = 1/(2 x minimum aperture)

For example, with a minimum aperture of 200 kHz, the maximum delay that can be measured is 2.5 μsec.

Accuracy: The following graph shows group delay accuracy at 20 GHz with an 8514B test set and an 83621A operating in stepped sweep mode. Insertion loss is assumed to be zero.

Typical Group Delay Accuracy
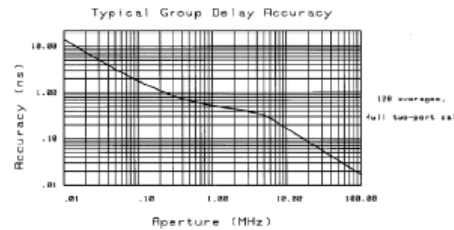
In general, the following formula can be used to determine the accuracy, in seconds, of a specific group delay measurement.

$$\frac{0.003 \times \text{Phase accuracy (deg)} + \text{delay (sec)} \times \text{linearity (Hz)}}{\text{Aperture (Hz)}}$$

Depending on the aperture and the device length, the phase accuracy used is either incremental phase accuracy or worst case phase accuracy. The above graph shows this transition.

Source control

All source control is provided from the 8510C front panel.

Compatible sources

8360 series synthesized sweeper
8340A/B synthesized sweeper[4]
8341A/B synthesized sweeper[4]
8350B sweep oscillator with 835xx RF plug-in[4] (ramp sweep mode only)

Sweep limits: Set start/stop or center/span of the stimulus parameter (frequency, time, or auxiliary voltage).

Measured # points per sweep: Selectable as 51, 101, 201, 401, or 801 points. In frequency list mode, the number of points can range from 1 to 792.

Sweep modes

Ramp sweep[5] (analog)

Stepped sweep (available with all sources except the Agilent 8350B): A faster version of step sweep, called "quick step", is selectable when using an 8360 series synthesized sweeper.

Frequency list sweep: Define up to 30 different arbitrary sub-sweep frequency ranges by specifying start/stop, center/span, or CW sweeps. Define the number of points or step size for each range. Display all segments or a single segment on-screen. All frequencies are synthesized if using the 8340/41 or 8360 series synthesized sweepers. Frequency domain only.

Single point (single frequency)

Fast CW mode (GPIB only): Raw data (real and imaginary) is sent immediately to GPIB as soon as it is taken. Display is blanked in this mode. The source is phase-locked once when entering this mode, but is not re-phase-locked at each point. Must be triggered externally (TTL). Data is available approximately 500 μsec after the trigger pulse is received.

---

1. The symbol ⁺ denotes a new feature or capability due to the 8510C firmware revision 7.0.
2. Pulse profile domain is not available in the 8510XF systems.
3. Power domain requires 8360 series sources. Sources with firmware revisions prior to 01 Oct 93 require updating.
4. The 8340, 8341 and 8350 series sources are not compatible with the 8510XF systems.
5. Ramp sweep mode is not available in the 8510XF systems.

Vector Network Analyzer Anritsu 37000D

The technical information about this device is available at http://www.testequipmentdatasheets.com/index_cards/A/Anritsu/37000D_Series.pdf

The Lightning D-Series Vector Network Analyzer (VNAs) are high performance test tools designed to satisfy the growing needs of defense, satellite, radar, broadband communication, and high speed component markets. The new 37000D VNAs improve upon performance while providing a wider set of standard application features to better suit the needs of R&D engineers working on next generation designs. These new features, when combined with the ease of programming through helpful software utilities and faster data transfer over Ethernet, make it an equally valuable tool for manufacturing as well.
The Lightning D-Series consists of two primary configurations built for R&D and Production applications:

Premium Models (37300D)
The Premium series are designed for active and passive device applications, where versatility is the main priority. These are high performance two-port VNAs that include step attenuators, internal bias tees, a gain compression application and wider power range as standard features. They are available in four different frequency ranges; 20 (37347D), 40 (37369D), 50 (37377D) and 65 (37397D) GHz. Each one of them can be configured as an ME7808B millimeter wave VNA by simply adding a broadband test set, two synthesizers and the desired millimeter wave modules. The 37397D is also directly upgradeable to an ME7808B Broadband VNA with single sweep coverage from 40 MHz to 110 GHz.

Economy Models (37200D)
The Economy series are basic two-port VNAs designed for passive applications. They are available in four different frequency ranges; 20 (37247D), 40 (37269D), 50 (37277D) and 65 (37297D) GHz. Each one of them can be configured as an Economy millimeter wave VNA by simply adding a broadband test set, two synthesizers and the desired mmW modules.

The 37300D Premium models include:
- Multiple Source Control and Frequency Offset
- E/O and O/E Application
- Gain Compression Application
- Internal Bias Tees
- Extended Power Range (Source Step Attenuator and Receiver Step Attenuator)
- Rear Panel IF Inputs (for upgrade to Millimeter Wave)
- NxN calibration Utility for Mixer Measurements
- Embed/De-Embed application
- High Stability Frequency Reference
- 1 Hz Frequency Resolution

The 37200D Economy models include:
- Multiple Source Control and Frequency Offset
- E/O and O/E Application
- Rear Panel IF Inputs (for upgrade to Millimeter Wave)
- NxN calibration Utility for Mixer Measurements
- Embed/De-Embed application
- High Stability Frequency Reference
- 1 Hz Frequency Resolution

Features

• High speed data transfer and control
For maximum efficiency, an Ethernet connection and dual GPIB ports are standard on every 37000D VNA. Ethernet connection provides high speed data transfers and remote data extraction from the VNA. The same can also be achieved via the standard GPIB interface. The second GPIB port is dedicated to control of peripheral devices such as plotters, power meters, and frequency synthesizers. The 37000D series maximize throughput by combining fast, error-corrected sweeps with high-speed data transfers.

• Time domain analysis (Option 2A)
Analyze impedance discontinuities as a function of time or distance with the 37000D's high-speed time domain. Isolate individual reflections in time and evaluate their effects in the frequency domain. Remove the effects of device packages and fixturing with time domain gating to see the actual performance of your designs. Use the independent display channels to view the response of your designs before, during, and after time domain processing.
The software provides four different windowing functions to optimize dynamic range and resolution. The exclusive phasor impulse mode will show you the true impedance characteristics of mismatches in waveguide, microstrip, and other band-limited media.

• Multiple source control and set-on receiver mode
The frequency of two sources and a receiver can be controlled without the need for an external controller using this function. Independently specify the sweep ranges and output powers of the sources and the sweep range of the receiver to accommodate mixer, swept IMD, TOI, and harmonic measurements. The 37000D's set-on receiver mode allows it to operate as a tuned receiver by phase locking all of its local oscillators to its internal crystal reference oscillator.

Rohde and Schwarz Electrical Spectrum Analyzer FSW50

Thetechnical specifications of this device are available at http://www.rohde-schwarz.de/file_20078/FSW_dat-sw_en_5214-5984-22_v0700.pdf

Version 07.00, June 2013

Specifications

Frequency

Frequency range	R&S®FSW8	
	DC coupled	2 Hz to 8 GHz
	AC coupled	10 MHz to 8 GHz
	R&S®FSW13	
	DC coupled	2 Hz to 13.6 GHz
	AC coupled	10 MHz to 13.6 GHz
	R&S®FSW26	
	DC coupled	2 Hz to 26.5 GHz
	AC coupled	10 MHz to 26.5 GHz
	R&S®FSW43	
	DC coupled	2 Hz to 43.5 GHz
	AC coupled	10 MHz to 43.5 GHz
	R&S®FSW50	
	DC coupled	2 Hz to 50 GHz
	AC coupled	10 MHz to 50 GHz
Frequency resolution		0.01 Hz

Reference frequency, internal		
Accuracy		±(time since last adjustment × aging rate + temperature drift + calibration accuracy)
Aging per year	standard	$\pm 1 \times 10^{-7}$
	with R&S®FSW-B4 OCXO precision frequency reference option	$\pm 3 \times 10^{-8}$
Temperature drift (0 °C to +50 °C)	standard	$\pm 1 \times 10^{-7}$
	with R&S®FSW-B4 OCXO precision frequency reference option	$\pm 1 \times 10^{-9}$
Achievable initial calibration accuracy	standard	$\pm 1 \times 10^{-6}$
	with R&S®FSW-B4 OCXO precision frequency reference option	$\pm 5 \times 10^{-9}$

Frequency readout		
Marker resolution		1 Hz
Uncertainty		±(marker frequency × reference accuracy + 10 % × resolution bandwidth + ½ (span/(sweep points – 1)) + 1 Hz)
Number of sweep (trace) points	default value	1001
	range	101 to 32001
Marker tuning frequency step size	marker step size = sweep points	span/(sweep points – 1)
	marker step size = standard	span/(default sweep points – 1)
Frequency counter resolution		0.001 Hz
Count accuracy		±(frequency × reference accuracy + ½ (last digit))
Display range for frequency axis		0 Hz, 10 Hz to max. frequency
Resolution		0.1 Hz
Max. span deviation		±0.1 %

Spectral purity		
SSB phase noise	frequency = 1000 MHz, carrier offset	
	10 Hz, without R&S®FSW-B4 option	–80 dBc (1 Hz) (nom.)
	10 Hz, with R&S®FSW-B4 option	–90 dBc (1 Hz) (nom.)
	100 Hz	< –100 dBc (1 Hz)
	1 kHz	< –125 dBc (1 Hz)
	10 kHz	< –134 dBc (1 Hz)
	100 kHz	< –136 dBc (1 Hz)
	1 MHz	< –145 dBc (1 Hz)
	10 MHz	–155 dBc (1 Hz) (nom.)
Residual FM	frequency = 1000 MHz, RBW = 1 kHz, sweep time = 100 ms	< 0.1 Hz (nom.)

Optical Spectrum Analyzer Yokogawa AQ6370

The technical specifications of this product are available at
https://www.yokogawa.com/pdf/provide/E/GW/Bulletin/0000028273/0/BUAQ6370SR-20EN.pdf

Test&Measurement   YOKOGAWA ◆

The world's
most trusted
OSAs

AQ6370 Series
Optical Spectrum Analyzer

Bulletin AQ6370SR-20EN

Annex 6 Laser Datasheet

1.5 *µ*m External Cavity Tunable Laser (Yenista Optics - Tunics T100S)

The technical information about this device is available at http://yenista.com/IMG/pdf/TUNICS-T100S_DS_201204-2.pdf

TUNICS T100S – Tunable Laser Source High Power with Ultra-Low SSE

YENISTA presents a general-purpose benchtop "work-horse" tunable laser, combining large wavelength range and high output power with SSE suppression. This laser is a must for all optical labs looking for an affordable every day use laser. With TUNICS T100S, the laser is not anymore the limiting factor of your measurement set-up.

Key Parameters

▪ High and SSE-free Output Power: a unique combination ideal for Component Testing
With T100 technology, there is no more trade-off between high output power and SSE suppression. A single laser can be used for all applications from amplifiers/WDM testing to high resolution insertion loss characterization.

▪ 110 / 150 nm Tuning Range with 1 pm Resolution
In one single instrument, the TUNICS guarantees a tuning range of up to 150 nm at 0 dBm (1 mW).

▪ Fast Operation from the Start
The TUNICS laser can be used a minute after turn-up. Scanning time between two wavelengths is around 1 second and sweeping speed is adjustable from 1 nm/s to up to 100 nm/s.

▪ Active Control for Mode-Hop-Free Operation
For ultimate performance, TUNICS T100S features a proprietary active control that ensures perfect mode-hop-free operation and accurate wavelength sweep over its entire tuning range.

▪ Fine Scanning Mode: down to 0.1 pm resolution and frequency modulation
Fine Scanning Mode allows the user to accurately modify the wavelength over ±2 GHz range using the rotary knob on instrument front panel. An external modulation could also be applied to modulate this fine scanning.

▪ Step-by-Step and Sweeping Mode
The TUNICS T100S combines two operating modes. The sweeping ability delivers a continuous variation of the wavelength at a constant rate to enable a fast and uninterrupted measurement. In step-by-step application, the laser exhibits a high wavelength stability suitable for long-term testing.

▪ Internal wavelength reference
Every TUNICS T100S has an internal wavelength reference that leads to a ±30 pm absolute wavelength accuracy. This eliminates the need for an external wavemeter or optical spectrum analyzer.
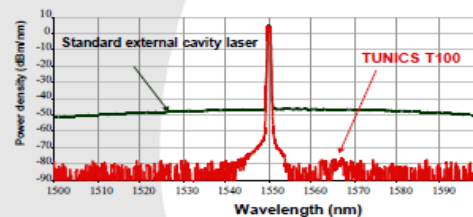
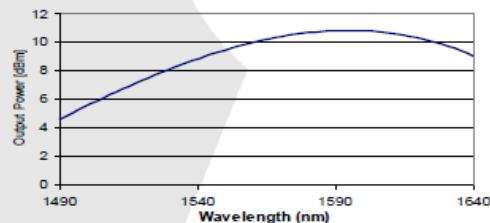Fig.1 TUNICS T100S SSE-free Optical Spectrum

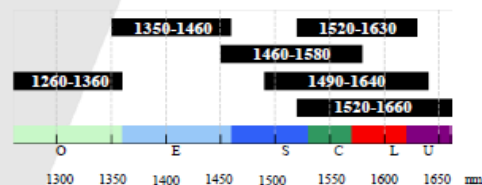Fig. 2 Typical power vs. wavelength (CL-WB Model)

Fig. 3 AvailableT100S Models

yenista OPTICS

April 2012

TUNICS T100S Specifications

	T100S-O	T100S-E	T100S-SC	T100S-CL	T100S-CL-WB	T100S-CLU
Wavelength range						
• P = 0 dBm	1260-1360 nm	1350-1460 nm	1460-1580 nm	1520-1630 nm	1490-1640 nm	1520-1660 nm
• P = 6 dBm	1290-1340 nm	1360-1430 nm	1480-1570 nm	1540-1620 nm	1520-1630 nm	1540-1620 nm
• P = 8 dBm				1560-1600 nm	1540-1610 nm	1560-1600 nm

TUNING CHARACTERISTICS	
Absolute wavelength accuracy [1]	±30 pm
Wavelength stability [2]	±5 pm / h (±3 pm / h typical and ±5 pm / 24h typical)
Tuning repeatability (typ.)	5 pm
Wavelength setting resolution	1 pm
Optical frequency fine tuning	±2 GHz
Tuning speed (typ.)	1s (100 nm)

LASER OUTPUT CHARACTERISTICS		
Power stability [2]	±0.01 dB / h (±0.025 dB / 24h typical)	
Side mode suppression ratio [3]	>40 dB	>45 dB
Signal to source spontaneous-emission ratio [4]	>80 dB	>90 dB
Relative intensity noise [3], [5]	- 145 dB/Hz (typ.)	
Spectral width (FWHM)	400 kHz typical (coherence control OFF) >100 MHz (coherence control ON)	

SWEEPING MODE CHARACTERISTICS	
Mode hop free range	Full specified wavelength and power ranges [8]
Scan speed	Adjustable from 1 to 100 nm/s
Power flatness during scan (typ.)	±0.25 dB
Power repeatability from scan to scan (typ.) [6]	±0.05 dB

INTERFACES	
Optical connector	FC-APC
Output fiber	SMF-28™ (PMF option available)
Output isolation	35 dB
Return loss	60 dB
Remote control	RS-232 C and IEEE-488.1 [7]
Low frequency modulation	10 kHz to 8 MHz
High frequency modulation	30 kHz to 200 MHz

ENVIRONMENT	
Operating temperature range	+15° to +30°C +60° to +85°F
Power supply	100 to 240 V / 50 to 60 Hz
Dimensions(W x H x D) in mm³	448 x 133 x 370
Weight	12.5 kg

Unless otherwise specified, specifications are given after 30 minutes warm-up.
[1]: After self calibration, at +20°C. Over operating temperature range wavelength accuracy is ±40pm for O, E, SC, CL and CL-WB models.
[2]: Over one hour at a constant temperature and after 1 hour warm-up.
[3]: Measured with 0 dBm output power.

[4]: Spontaneous emission measured on a 0.1 nm bandwidth at ±1 nm from the signal.
[5]: Measured at an electrical frequency of 100 MHz.
[6]: Over 100 scans at constant temperature.
[7]: Tested and validated with National Instruments GPIB board.
[8]: 1270-1340 nm at 0 dBm for O band model.

TUNICS T100S and CT400 Component Tester: the perfect match

When used in conjunction with Yenista's CT400 component tester, the TUNICS T100S allows accurate insertion characterization in real time. Refer to CT400 individual data sheet for more details.
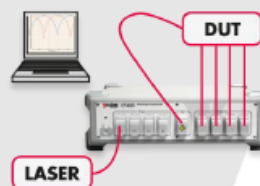
yenista OPTICS

April 2012

1.3 μm Distributed Feedback (DFB) Laser NEL (NEL NLK1B5EAAA)

The Technical information about this device is available at http://www.ntt-electronics.com/en/products/photonics/pdf/NLK1B5EAAA.pdf

NEL Laser Diodes

March2005

NLK1B5EAAA

1290-1360 nm DFB laser diode in a butterfly-type 14 pin package with thermo-electric cooler.
Pigtail fiber is connectorized with an FC/PC connector.

FEATURES
* Wavelength Range   1290 - 1360 nm, ITU-T grid wavelength
* Fiber Output Power   10mW

ABSOLUTE MAXIMUM RATINGS(T_{sub}=25deg.C)

Parameter	Symbol	Ratings	Units
Laser diode reverse voltage	V_R	2.0	V
Laser diode forward current	I_F	150	mA
Operating case temperature	T_{case}	-5 to 70	deg.
Storage temperature	T_{stg}	-40 to 85	deg.
Photodiode reverse voltage	V_{DR}	10	V
Photodiode forward current	I_{DF}	10	mA
Peltier current	I_P	1.4	A

ELECTRICAL/OPTICAL CHARACTERISTICS(T_{sub}=25deg.C)

Parameter	Symbol	Condition	Min.	Typ.	Max.	Units
Forward voltage	V_F	I_F=30mA		1.2	1.6	V
Threshold current	$I_{(TH)}$	CW		10	20	mA
Fiber output power	ϕ_e	CW,I_F=80mA	10			mW
Peak wavelength	λ_p	CW,ϕ_e=10mW	-1	ITU-T	+1	nm
Spectral linewidth[*]	$\Delta\nu$	CW,ϕ_e=10mW		2		MHz
Side mode suppression ratio	SMS	CW,ϕ_e=10mW	35			dB
Monitoring Current(PD)	$I_{R(E)}$	CW,ϕ_e=10mW	0.1			mA
Dark current(PD)	$I_{r(0)}$	CW,V_{DR}=5V			100	nA
Tracking error	E_R	$I_{R(E)}$=constant	-0.5		+0.5	dB
Cooling capacity[*]	ΔT_{PE}	ϕ_e=10mW,T_{case}=70deg	45			deg.
Peltier current	I_{PE}	T_{case}=-5 to 70deg.			1	A
Peltier voltage	V_{PE}	T_{case}=-5 to 70deg.			2	V
Thermister resistance[*]	R	T_{sub}=25deg.		10		kΩ
Isolation[*]	I_s	T_{sub}=25deg.			30	dB

ΔT=| T_{case}-T_{sub} |
[*] Data is not attached.

⚠ **WARNING**

If you plan to use these products in equipment which could endanger lives in the event of a product failure, please consult an NEL engineer before usage. Improper application of these products may endanger life. To avoid possible injury, make certain these products are used in a redundant configuration.

1 These products are subject to export regulations and restrictions set force by the Japanese Government.
2 NTT Electronics Corporation reserves the right to make changes in design,specification or related information at any time without prior notice.
3 The characteristics which are not specified in the data sheet are not guaranteed.
4 The characteristics under the different operation conditions from the ones specified in the data sheet are not guara

1.3 μm Semiconductor Optical Amplifier SOA NEL (INPhenix IPS AD1305)

The technical information about this device is available at http://www.inphenix.com/pro/Semiconductor%20Optical%20Amplifier/IPSAD1305.pdf

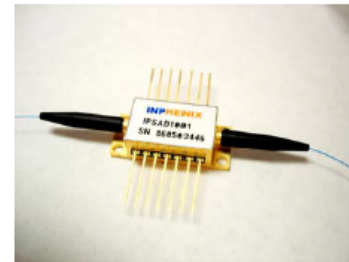Product Specification, Revision 1.50

INPHENIX

Semiconductor Optical Amplifier Device (In-Line Type)

IPSAD1305 (1300nm)

Features

- Wide Optical Bandwidth
- High Gain
- Low Gain Ripple
- Low Noise Figure
- MQW or Bulk Structure

Applications

- In-Line Amplifier
- Loss Compensation
-

Device Specifications

Parameter	Symbol	Min.	Typ.	Max.	Unit
Drive Current	I_F	-	700	-	mA
Operating Wavelength	λ_o	1260	1300	1340	nm
3dB Optical Bandwidth	$\Delta\lambda_{3dB}$	55	60	-	nm
Small Signal Gain at @ - 25dBm Signal	G_{max}	28	30	-	dB
Gain Ripple with Respect to λ	ΔG		0.5	1	dB
Saturation Output Power	P_{sat}	13	15	-	dBm
Noise Figure	NF			7	dB
Polarization Dependent Gain	PDG	-	15	-	dB

INPHENIX

Absolute Maximum Ratings

Parameter	Min.	Max.	Unit
Operating Temperature	− 20	70	°C
Storage Temperature	− 40	85	°C
SOA Forward Current	-	1000	mA
SOA Reverse Voltage	-	2.5	V
TEC Drive Current	-	1.5	A
TEC Drive Voltage	-	3.6	V
Thermistor Resistance	10kΩ @ 25°C		
SOA Chip Temperature Setting	25°C		
Fiber Type	SMF/PMF/MMF ClearCurve Fiber		
Fiber Jacket	250μm tight buffer with/without 900μm loose tube, or 900μm tight buffer		
Package	14-pin Butterfly Type B or C		

Annex 7 Phase Noise Model

1.1 Phase Noise Definition [68]

Assuming a quasi-sinusoidal signal of angular frequency ω_o of amplitude fluctuation $\alpha(t)$, and random phase fluctuation $\varphi(t)$. The mathematical representation of this signal is:

$$v(t) = [1 + \alpha(t)] \cos(\omega_o t + \varphi(t))$$

(207)

It is assumed that $|\alpha(t)| \ll 1$ and $|\varphi(t)| \ll 1$ at the measurement. The phase noise is measured through the power spectral density of the phase noise, this is expressed as,

$$S_\varphi = \langle |\Phi(jf)|^2 \rangle$$

(208)

It has been already shown that the power law describes accurately the oscillator phase noise as follows,

$$S_\varphi(f) = \sum_{n=-4}^{0} b_n f^n$$

(209)

Where,

Coefficient	Noise type
b_{-4}	Frequency random walk
b_{-3}	Flicker of frequency
b_{-2}	White frequency noise, or phase random walk
b_{-1}	Flicker of phase
b_0	White Phase Noise

The power law considers the presence of the white (f^0) and flicker (f^{-1}) are present in the oscillator, the other components of the phase noise are the multiplication of those noise components.

1.2 Oscillator Fundamentals

The most basic oscillator representation is a resonator with an amplifier of gain A in a closed loop that compensate the resonator losses $(^1/_\beta)$ when the Barkhausen condition is satisfied ($A\beta = 1$), as shown in Figure 127.
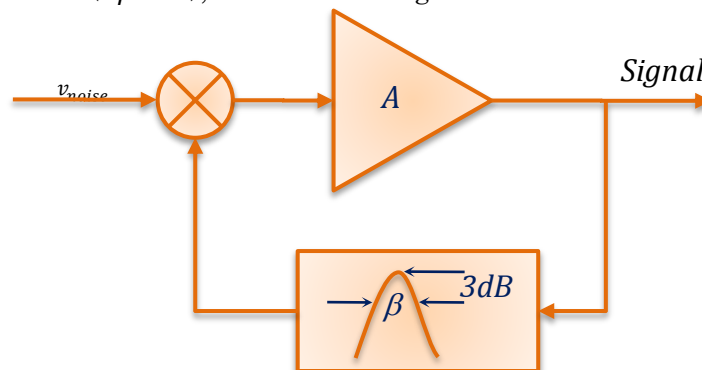

Figure 127 Feedback oscillator model.

The feedback oscillator resonator narrow bandwidth eliminates the harmonic oscillation modes generated by the amplifier non linearities.

Assuming that the resonator relaxation time τ is larger than $1/\omega_o$ by a factor of 10^2, the oscillator behavior can be described in terms of the slow varying complex envelope, as amplitude and phase were decoupled from the oscillation. For this model, just the phase component is considered. In such way, the feedback phase modulation model is represented as in Figure 128.
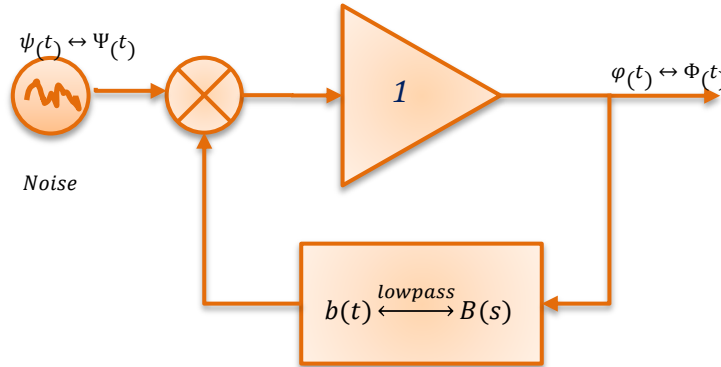

Figure 128 Feedback oscillator phase noise model.

Using a linear approach of the feedback oscillator permits the phase noise modelling as additive noise sources regardless of the physical origin. This analysis models the contribution of each noise process to the oscillator output. This linearization grants the acces to the Laplace-Heavyside formalism. The response $y(t)$ to the input $x(t)$ is given by,

$$y(t) = x(t) * h(t) \quad \leftrightarrow \quad Y(s) = Z(s) * H(s)$$

(210)

Where $h(t)$ is the *impulse response*, $H(s)$ is the transfer function and '*' is the convolution operator, $\leftrightarrow$ is the Laplace transform-inverse pair, and $s = \sigma + j\omega$ is the Laplace complex variable. Using this formalism, the output power spectral density is given by,

$$S_y = |H(jf)|^2 S_x$$

(211)

For the direct modulated VCSEL Based Optoelectronic Oscillator (VBO), the system noise input is represented by the different intrinsic noise sources considered in for their components in Chapter 2, recalling this:

$$S_x = S_{noise}(f) = \left[(RIN_{Laser} + RIN_{DRD} + RIN_{RRD})i_{ph}^2 + 2qI_{ph} + 4k_BTF\right]Z_{eq}$$

(212)

Where,

RIN_{Laser}	Represents de laser relative intensity noise
RIN_{DRD}	Represents the double diffusion Rayleigh scattering
RIN_{RRD}	Represents the reflected Rayleigh scattering
I_{ph}	Represents the photodetected current

Annex 7
Phase Noise Model

q	Represents the fundamental charge
k_B	The Boltzman constant
T	Temperature
F	Amplifier noise factor
Z_{eq}	Equivalent impedance load

1.3 Amplifier Noise

Additive White Noise

The amplifier noise is considered a random process. It is influenced by the operation temperature (T) and the internal configuration of the amplifier. The white noise contribution of the amplifier por a given sinusoidal carrier of power P is

$$S_\varphi(f) = b_0 = \frac{Fk_bT}{P} \tag{213}$$

The noise factor (F) for cascaded amplifier is computed through the Friis formula, for N cascaded amplifiers it is expressed as,

$$F = F_1 + \frac{F_2 1}{G_1^2} + \frac{F_3 1}{G_1^2 G_2^2} + \cdots \tag{214}$$

Flicker Noise

It has been shown by several authors [100]–[102]that the phase flickering noise relapses in a narrow value range. For this reason, a table with typical values is proposed. These are shown in the following table,

Quality	Microwave Amplifier
Fair	-100
Good	-110
Best	-120

1.4 Phase Noise Model for the Delay Line Oscillator

As shown in Chapter 1 and 2, the delay line optoelectronic oscillator is a variation of the optoelectronic oscillator that uses a delay line of delay τ_d as a resonator, so the oscillation frequency is an integer multiple of $1/\tau_d$. Extending the Leeson effect for this oscillator, the delay line equivalent quality factor (Q) is,

$$Q = \pi\tau_d f_{oscillation} \tag{215}$$

As long as the delay line is a wideband resonator, a filter is necessary to select one frequency and reduce the amplitude of the other modes (see Figure 4 Chapter 1) for this reason the transfer function of the resonator is split into two functions, one corresponding to the delay line and the second one to the filter named τ_{delay} and τ_{filter}. Using the Laplace-Heavyside formalism, both transfer functions of the feedback path are as follow,

$$b_{filter}(t) = \frac{1}{\tau_{filter}} e^{-\frac{t}{\tau_{filter}}} \leftrightarrow B_{filter}(s) = \frac{1/\tau_{filter}}{s + 1/\tau_{filter}} \qquad (216)$$

$$b_{delay}(t) = \delta(t - \tau_{delay}) \leftrightarrow B_{delay}(s) = e^{-s\tau_{delay}} \qquad (217)$$

$$b(t) = b_{filter}(t) * b_{delay}(t) \leftrightarrow B(s) = B_{filter}(s) B_{delay}(s) \qquad (218)$$

From this,

$$B(s) = \frac{1/\tau_{filter}}{s + 1/\tau_{filter}} e^{-s\tau_{delay}} \qquad (219)$$

Once inserted into the feedback loop, the transfer function is:

$$H(s) = \frac{1}{1 - B(s)} = \frac{s + 1/\tau_{filter}}{s + (1 - e^{-s\tau_{delay}})/\tau_{filter}} \qquad (220)$$

1.5 Close in Noise Spectra

As mention at the beginning of this Annex, the phase noise spectrum is expressed as,

$$S_\varphi = |H(jf)|^2 S_\psi \qquad (221)$$

At low frequencies, it holds that [103],

$S_\varphi(f)$	Remark
$\approx \dfrac{1}{4\pi^2 \tau_{delay}} \dfrac{1}{f^2} S_\psi(f)$	$\omega \ll \dfrac{2\pi}{\tau_{delay}}$
$= \dfrac{f_{oscillation}^2}{4\pi^2 m^2} S_\psi(f)$	$f_{oscillation} = \dfrac{m}{\tau_{delay}}$ Where m is a integer multiple of the oscillation frequency
$= \dfrac{f_{oscillation}^2 b_0}{4\pi^2 m^2} \dfrac{1}{f^2} + \dfrac{f_{oscillation}^2 b_{-1}}{4\pi^2 m^2} \dfrac{1}{f^3}$	Amplifier noise

1.6 Predicted Spectra

The predicted spectra of the oscillator phase noise is as shown in Figure 129. The first element to analyze is the amplifier phase noise, see Figure 129a. This noise is turned inside the oscillator phase noise by its transfer function $H(s)$.

If a low Q resonator is used, the phase noise type 1 is seen (Figure 129b), where $f_L > f_c$ ($f_L = \frac{1}{2\pi\tau}$). This oscillator type presents the $^1/_{f^3}$, $^1/_{f^2}$ and f_0. If a high Q resonator is used, $f_L < f_c$, a type 2 spectrum is observed. This is characterized by the presence of $^1/_{f^3}$, $^1/_f$ and f^0 slopes, as observed in Figure 129c.
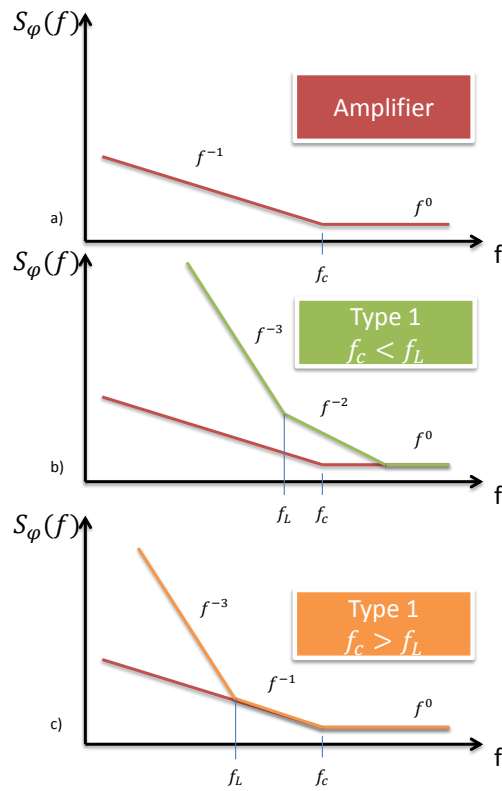
Figure 129 Oscillator phase noise spectra.